

**Final Report: Intelligent Network-Centric Sensors  
Development Program**

*University of Memphis*

*Department of Electrical and Computer Engineering*

*31 July 2012*

Principal Investigator: Dr. Eddie L. Jacobs

Co-principal Investigators: Drs. David J. Russomanno, Carl Halford, and Aaron  
Robinson

**DISTRIBUTION STATEMENT A. Approved for public release. Distribution is  
unlimited.**

20121018097



THE UNIVERSITY OF  
**MEMPHIS**

Department of Electrical and  
Computer Engineering

206 Engineering Science Bldg  
Memphis, Tennessee 38152-3180

Voice: 901.678.2175  
Fax: 901.678.5469  
eljacobs@memphis.edu

Defense Technical Information Center  
8725 John J. Kingman Road, Suite 0944  
Fort Belvoir, VA 22060-6218

To Whom It May Concern:

Please find enclosed one copy of the final technical report for cooperative agreement number W911NF-10-2-0071, "Intelligent Network-Centric Sensor Systems". The report includes a detailed account of all major advances accomplished under this agreement along with copies of all published and un-published reports generated as a result of the effort.

Sincerely,

Eddie Jacobs, D.Sc.  
Director, Center for Advanced Sensors

## 1.0 Executive Summary

The University of Memphis conducted basic research into techniques for advancing network-centric sensors for eventual deployment in Department of Defense (DoD) applications. This basic research included the following focus sub-areas: i) feature fusion/feature-based sensor system design techniques; ii) sensor ontologies for problem-solving architectures; iii) profiling sensor improvement through the use of innovative classification algorithms and data visualization techniques; iv) alternative sensing modalities; v) turbulence mitigation techniques; and vi) development of a feature sensing laboratory.

Under the topic of feature fusion/feature-based sensor system design, techniques known as Lasso, Group Lasso, and Sparse Multiple Kernel Learning were applied to break beam profiling sensor design. The results indicate that the Group Lasso technique is effective for feature quality maximizing sensor design because of its ability to provide both inter-group and intra-group feature sparsity.

Under the topic of sensor ontologies for problem-solving architectures, a framework that matches sensors to compatible algorithms to form synthesized systems was developed and applied to improved forms of the beam-break profiling sensor. This work resulted in several publications.

Under the topic of profiling sensor improvement, various algorithms for improving the classification performance of a pyro-electric based profiling sensor were investigated and tested using data from field collections. Results indicated that Logistic regression with a simple height to width ratio provide good performance.

Under the topic of alternative sensing modalities, a model for micro-resonator based sensors was developed, research toward the improvement and refinement of a novel technique for forming terahertz images was performed, and the use of compressive sensing in a profile type detector was investigated. This work resulted in several publications.

Under the topic of turbulence mitigation techniques, lucky imaging, blind deconvolution, spectral techniques, and frame averaging were examined using turbulence simulation against their ability to perform in a wide variety of tactical situations. The strengths and weaknesses of each were discussed in a publication. In addition, the applicability of turbulence mitigation techniques to sparse array sensors such as profiling sensors was investigated.

Under the topic of a feature sensing laboratory, the design and implementation of an infrastructure to support long-term sensor network emplacements in a laboratory like environment was pursued. To date, key features of the design have been implemented with final integration of the initial deployment likely to happen in September 2012.

The execution of this contract has resulted in some significant scientific and technical progress in support of intelligent, network-centric, sensors. We believe that this work has been of immediate benefit to the Army and will continue to pay dividends in technical achievement into the near future. Further publications will result directly and indirectly from this work.



## 2.0 Introduction

The University of Memphis conducted basic research on the subject of Intelligent Network Sensors in support of US Army basic research needs in the areas of perimeter security and force protection. This research covered a broad range of research topics and has resulted in several conference and journal publications.

The topics of research pursued under this effort were: i) feature fusion/feature-based sensor system design techniques; ii) sensor ontologies for problem-solving architectures; iii) profiling sensor improvement through the use of innovative classification algorithms and data visualization techniques; iv) alternative sensing modalities; v) turbulence mitigation techniques; and vi) development of a feature sensing laboratory. A detailed description of each research topic pursued in this effort is given below. Further details and copies of published papers may be found in the Appendices.

## 3.0 Feature Fusion/Feature Based Sensor Design

**Task 3.1: Demonstrate sensor optimization based on enhancement of feature quality.**

**Task 3.2: Develop a feature fusion quality metric to serve as a cost function for optimizing sensor design.**

To demonstrate the procedure to accomplish the above stated objectives, the design of a sparse trip wire sensor for human versus animal classification is used as a case study. The sensor consists of two poles that can be placed on either side of a bottleneck along a trail. One pole is lined with NIR transmitters and receivers, while the other pole is lined with reflectors. As an object passes between the two poles, it blocks the path between the trans-receiver (Tx-Rx) and reflector (Rr). The shape of the moving object is thus traced at the output of the sensor system. The choice of number of sensors and their positions on the poles are important design parameters. This effort investigates techniques to optimize these parameters with the objective of enhancing the quality of shape features that distinguish humans from animals. Each Tx-Rx and Rr pair generates '0' based on the amount of time they have been blocked by the moving object. The count of the number of '0's generated by a pair can be used one feature. The sensor system used in this research has 16 such pairs, generating 16 features for each object (hence forth a Tx-Rx and Rr pair will be referred to as a detector in this report). This means a feature fusion technique that assigns weights to features based on their importance also assigns weights to the corresponding detector. This means that a detector with negligible weights can be removed from the sensor during subsequent design iterations. Three feature fusion techniques, namely Lasso [Tibshirani1996], Group Lasso[Friedman2010] and Sparse

Multiple Kernel Learning[Subramanhya2010] are investigated for feature quality based sensor design.

### Sparse Multiple Kernel Learning (SMKL)

In many cases, two classes, not separable linearly in their native dimensions, can be made linearly separable in higher dimensions. In algorithms such as Support Vector Machines (SVM), the inner product operation on the data is an important step. This process becomes computationally challenging in higher dimensions. The Kernel trick allows the dot product to be implemented in the lower dimensions itself, but gives the effect of a dot product in the higher dimension. Let  $\phi(x)$  represent the mapping or projection of  $x$  on to a higher dimension. The Kernel trick allows for the inner product  $\langle \phi(x)\phi(x') \rangle$  in the higher dimensional feature space to be represented by a Kernel in the input (low dimension) space  $K(x, x')$ . For example the radial basis function Kernel given by

$K(x, x') = \exp\left(-\frac{\|x - x'\|^2}{2\sigma^2}\right)$  corresponds to an inner product in an infinite dimensional space.

SMKL is a non-linear group selection technique that weights groups of features. In the context of this report, the technique assigns weights to groups of detectors. SMKL consists of a composite  $K(x, x')$  kernel generated by the weighted sum of primitive kernels  $k(x, x')$ .

$$K(x, x') = \sum_{g=1}^G \beta_g k(x, x')$$

where  $G$  is the total number of group and  $\beta_g$  are the kernel weights. If different groups of features are assignment to different kernels then the kernel weights become weights for the groups. The process of estimation of the weights follows the technique described in [Subramanhya2010]

### Lasso

Least Absolute Selection and Shrinkage Operator, known more by its acronym Lasso is a linear technique for solving a sparse regression problem. Lasso minimizes objective function  $\|X\beta - y\|_2^2 + \lambda \|\beta\|_1$  to find the optimum weighting parameters  $\beta$  for the features  $X$  given the corresponding class predictions  $y$ .  $\lambda$  is the regularization parameter that can be varied to change the sparsity of the solution.

### Group Lasso

Group Lasso as proposed by Friedman et al. is regression technique that introduces sparsity at both the group level and at the individual feature level. The sparsity is achieved by minimizing the cost function given by:

$$\left\| y - \sum_{g=1}^G X_g \beta_g \right\|_2^2 + \lambda_1 \sum_{g=1}^G \|\beta_g\|_2 + \lambda_2 \|\beta\|_1$$

$G$  is the number of groups,  $N_g$  is the number of features in the  $g$ th group,  $X_g$  corresponds to the features of the  $g$ th group,  $\beta = [\beta_1 \beta_2 \dots \beta_G]$  and  $\beta_g = [\beta_{g1} \beta_{g2} \dots \beta_{gN_g}]$ . The process of solving the optimization problem is described in [Friedman2010] The second term in the cost function can cause very few weights in  $\beta_g$  to be non-zero introducing sparsity within a group. A combination of the second and third term in the cost function can cause all the weight in a particular  $\beta_g$  to be set to zero. This results in discarding an entire group, leading to sparsity at the group level. In summary, Group Lasso provides both inter-group and intra-group sparsity. It should be noted that the SMKLL technique only provides group level sparsity and not intra-group sparsity.

### Results

The algorithms were applied to a version of the trip wire sensor, which has 16 detectors. In the case of Group Lasso, three groups were formed with detectors 1 through 5 forming group 1, detectors 6 to 11 forming group 2 and detectors 12 through 16 forming group 3. A total of 135 human profiles and 96 animal profiles collected through various data collections were used for the analysis.

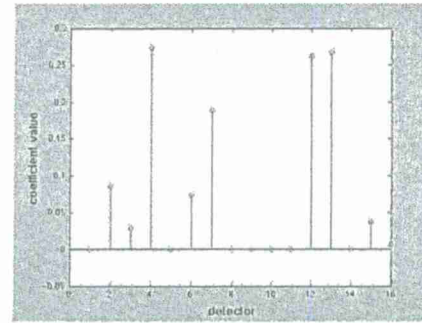


Figure 3.1. Weights assigned to detectors through Lasso

The graphs shown in Figures 3.1 and 3.2 show the weights assigned to detectors of the trip wire sensor using Lasso and Group Lasso respectively.

The results indicate Lasso and Group Lasso assigns non-zero weights to only 7 out of the total of 16 detectors. In this particular case, it can be hypothesized that Group Lasso does not provide group level sparsity since at least one detector in each group is essential to minimizing the first term in the cost function. SMKLL provides weights of 0.3804, 0.305 and 0.3.144 respectively for groups 1, 2 and 3. This confirms with the results of Lasso and Group Lasso, since every group has detectors that contribute toward minimizing the error.

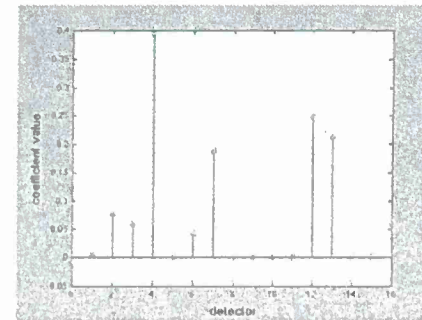


Figure 3.2. Weights assigned to detectors using group Lasso

The investigation indicates that the Group Lasso technique is an effective for feature quality maximizing sensor design because of its ability to provide both inter-group and intra-group feature sparsity. Future effort will entail research into multi-modal sensor network design using the techniques described above.

## References

[Tibshirani1996] R. Tibshirani, "Regression shrinkage and selection via the lasso," J. Royal. Statist. Soc. B, vol. 58, no. 1, pages 267-288, 1996.

[Friedman2010] J. Friedman, T. Hastie, and R. Tibshirani, "A note on the group lasso and sparse group lasso," technical report, 2010 [online: <http://www-stat.stanford.edu/~tibs/ftp/sparse-grlasso.pdf>]

[Subrahmanya2010] N. Subrahmanya and Y. Shin, "Sparse multiple kernel learning for signal processing applications," Pattern Analysis and Machine Intelligence, IEEE transactions, vol. 32, no. 5, May 2010.

## 4.0 Sensor Ontologies

**Task 4.1: Conduct basic research to a) advance sensor ontologies for problem-solving architecture; and b) advance profiling sensors through the use of innovative classification algorithms and data-visualization techniques**

The deployment of ubiquitous sensor systems and algorithms has led to many challenges, such as matching sensor systems to compatible algorithms which are capable of satisfying a task. Compounding the challenges is the lack of the requisite knowledge models needed to discover sensors and algorithms and to subsequently integrate their capabilities to satisfy a specific task. Basic principles for an ontological problem-solving framework have been researched and a proof-of-concept framework was implemented in support of Task 4.1.

The proof-of-concept framework matches sensors to compatible algorithms to form synthesized systems, which are capable of satisfying a task and then assigning the synthesized systems to high-level missions. The approach designed for the ontological problem-solving framework has been instantiated in the context of a persistence surveillance prototype environment, which includes profiling sensor systems and algorithms to demonstrate proof-of-concept principles. Even though the problem-solving approach was instantiated with profiling sensor systems and algorithms, the ontological framework may be useful with other heterogeneous sensing-system environments. Work in support of Task 4.1 was published in J. Qualls and D.J. Russomanno (2011) "Ontological Problem-Solving Framework for Dynamically Configuring Sensor Systems



and Algorithms,” *Sensors*, Volume 11, Number 3, 3177-3204. This paper is provided as a supplement to this report.

The work of the previous paragraph was extended, also in support of Task 4.1. This work leverages knowledge models describing sensors, algorithms, and high-level missions to facilitate automated inference of assigning systems to subtasks that may satisfy a given mission specification. To demonstrate the efficacy of the ontological problem-solving architecture, a family of persistence surveillance sensor systems and algorithms has been instantiated in a prototype environment to demonstrate the assignment of systems to subtasks of high-level missions. This work extends the results of the previously cited journal paper and was published as J. Qualls and D.J. Russomanno (2011) “Ontological Problem-Solving Framework for Assigning Sensor Systems and Algorithms to High-Level Missions” *Sensors*, Volume 11, Number 9, 8370-8394. This paper is provided as a supplement to this report.

To advance profiling sensors through the use of innovative data-visualization techniques work was completed in support of Task 4.1 to port existing data visualization software for creating silhouettes from data obtained from the vertical array detector version of a profiling sensor to a platform-independent architecture. The silhouette viewer was subsequently integrated into the ontology problem-solving framework where it can be described using the web ontology language (OWL) and subsequently discovered and tasked. The integration of the silhouette viewer into the ontology-based framework is described in the context of data fusion in the paper C. Kothari, J. Qualls and D.J. Russomanno (2012) “An Ontology-Based Data Fusion Framework for Profiling Sensors,” *IEEE International Conference on Electro/Information Technology*, IEEE Press, Indianapolis, Indiana. The research in this paper was also in direct support of Task 1 and is provided as a supplement to this report.

Additional work was completed in support of Task 4.1 in classification algorithm development. A back-propagation neural network was created to classify data from a novel, wireless profiling sensor developed in support of Task 4.3. The wireless version of the profiling sensor allows the detectors to be placed in custom configurations, versus the traditional vertical detector array. The results of the classification algorithm were published in the paper: A. Galvis, D.J. Russomanno and C. Kothari (2012) “A Wireless Near-IR Retro-Reflective Profiling Sensor,” *Proceedings SPIE: Ground/Air Multi-Sensor Interoperability, Integration and Networking for Persistent ISR III*, Volume 8389, Baltimore, Maryland. This paper is also provided as a supplement to this report.

**Task 4.2: Conduct research to help define a means by which sensor specifications, capabilities, and properties can be published and discovered in a computer-readable format**

The ontology work described in support of Task 4.1 also directly supports Task 4.2 by using ontologies to define and make available in a computer-readable format sensor specifications, capabilities, and properties. In addition to the two *Sensors* journal papers

previously listed, additional research was conducted in support of Task 2 to provide a proof-of-concept illustration about how sensor specifications, capabilities, and properties can be published in an ontology and used to support ontology-based fusion. The paper published as C. Kothari, J. Qualls and D.J. Russomanno (2012) "An Ontology-Based Data Fusion Framework for Profiling Sensors," *IEEE International Conference on Electro/Information Technology*, IEEE Press, Indianapolis, Indiana, which was first cited above in support of the visualization subtasks of Task 4.1, describes the details of this work in support of Task 4.2.

Additional activity and accomplishments in support of Task 4.2 include a concept paper researching the role of an ontology to support data-to-decision sensing environments that assess human intent from external stimuli. The paper published as C. Kothari, D.J. Russomanno, R.B. Sartain and R. Frankel (2012) "Toward Data-to-Decision Sensing Environments to Assess Human Intent from Responses to Stimuli," *Proceedings SPIE: Ground/Air Multi-Sensor Interoperability, Integration and Networking for Persistent ISR III*, Volume 8389, Baltimore, Maryland, is also provided as a supplement to this report.

**Task 4.3: Assess research theories and concepts through the construction of laboratory sensors, algorithm development and implementation, implementation of novel visualization software, and hardware and software architectural considerations that could ultimately be integrated into network-centric architecture**

Profiling sensors were advanced in support of Task 4.3 through the construction of novel laboratory sensors, algorithms, and visualization tools. Three laboratory profiling sensors were created in support of Task 4.3, including a traditional vertical array (and wired) profiling sensor, a wired profiling sensor with offset detectors, and a novel, wireless profiling sensor in which each detector comprises a node in a wireless sensor network. The wireless sensor network approach allows the detectors of a profiling sensor to be deployed in custom configurations. Software to classify and visualize data acquired from the novel, wireless profiling sensor was also developed in support of Task 4.3.

The notion of a profiling sensor was first implemented as a near-IR, retro-reflective prototype consisting of a vertical column of sparse detectors by a team led by Dr. Russomanno at the U. of Memphis in support of cooperative agreement W911NF-05-2-0019 between the University of Memphis and the U.S. Army's Research Laboratory (ARL). Alternative arrangements of detectors were researched and implemented in support of Task 4.3 in which a subset of the detectors were offset from the vertical column and placed at arbitrary locations along the anticipated path of the objects of interest. The paper published by R.K. Reynolds, S. Chari and D.J. Russomanno (2011) "Embedded Real-Time Classifier for Profiling Sensors and Custom Detector Configuration," *Proceedings SPIE: Ground/Air Multi-Sensor Interoperability, Integration and Networking for Persistent ISR*, Volume 8047, Orlando, Florida, pp. 80470E-1-80470E-9, is also provided as a supplement to this report and describes accomplishments in support of Task 4.3.

All prior work with the near-IR, retro-reflective profiling sensors has consisted of wired detectors, including the work cited in the previous paragraph. Research was conducted in support of Task 4.3 to advance this prior work by designing and implementing a wireless prototype version of a near-IR, retro-reflective profiling sensor in which each detector is a wireless sensor node. In this architecture, a base station is responsible for collecting all data from the detector sensor nodes and coordinating all pre-processing of data collected from the sensor nodes, including data re-alignment, before subsequent classification algorithms are executed. Such a wireless detector configuration advances deployment options for near-IR, retro-reflective profiling sensors. This work, which was in support of Task 4.3, is detailed in the paper: A. Galvis, D.J. Russomanno and C. Kothari (2012) "A Wireless Near-IR Retro-Reflective Profiling Sensor," *Proceedings SPIE: Ground/Air Multi-Sensor Interoperability, Integration and Networking for Persistent ISR III*, Volume 8389, Baltimore, Maryland. This paper is also provided as a supplement to this report.

#### **Task 4.4: Undertake field data collection with profiling sensors and emulators to build an extensive signature library to support algorithm development**

In support of Task 4.4, field data collections were limited to expanding the profiling sensor library with data captured from the new profiling sensors that were developed in support of Task 4.3. The data was used to support the classification algorithm and visualization algorithm development referenced in support of Tasks 4.1 through 4.3. Additional field data collections would improve the robustness of the various classifiers.

#### **Papers Published in Support of Project (Copies provided in Appendix X)**

1. R.K. Reynolds, S. Chari and D.J. Russomanno (2011) "Embedded Real-Time Classifier for Profiling Sensors and Custom Detector Configuration," *Proceedings SPIE: Ground/Air Multi-Sensor Interoperability, Integration and Networking for Persistent ISR*, Volume 8047, Orlando, Florida, pp. 80470E-1-80470E-9.
2. J. Qualls and D.J. Russomanno (2011) "Ontological Problem-Solving Framework for Dynamically Configuring Sensor Systems and Algorithms," *Sensors*, Volume 11, Number 3, 3177-3204.
3. J. Qualls and D.J. Russomanno (2011) "Ontological Problem-Solving Framework for Assigning Sensor Systems and Algorithms to High-Level Missions" *Sensors*, Volume 11, Number 9, 8370-8394.
4. A. Galvis, D.J. Russomanno and C. Kothari (2012) "A Wireless Near-IR Retro-Reflective Profiling Sensor," *Proceedings SPIE: Ground/Air Multi-Sensor Interoperability, Integration and Networking for Persistent ISR III*, Volume 8389, Baltimore, Maryland.
5. C. Kothari, J. Qualls and D.J. Russomanno (2012) "An Ontology-Based Data Fusion Framework for Profiling Sensors," *IEEE International Conference on Electro/Information Technology*, IEEE Press, Indianapolis, Indiana.
6. C. Kothari, D.J. Russomanno, R.B. Sartain and R. Frankel (2012) "Toward Data-to-Decision Sensing Environments to Assess Human Intent from Responses to Stimuli," *Proceedings SPIE: Ground/Air Multi-Sensor Interoperability, Integration and Networking for Persistent ISR III*, Volume 8389, Baltimore, Maryland.

### **5.0 Profiling Sensors: classifiers, visualization techniques, and network-centric integration**

#### **Background**

Conventional electro-optical systems have been used extensively in Intelligence Surveillance and Reconnaissance (ISR) applications. These systems have typically been



based on using two dimensional focal plane arrays. The disadvantage of such systems for applications of interest, namely deployment in inaccessible terrains for border security, is power consumption and cost. If the discrimination task is narrowed down to specific classes such as distinguishing between humans, animals and vehicles at ranges not exceeding few tens of meters, high resolution, high bit depth imaging systems may not be required. This scenario is true especially in the terrains in which objects can only travel through specific routes consisting of narrow trails. In this research, object recognition algorithms are developed for a pyroelectric detector based linear array to classify humans and animals. Initial testing on a smaller set of data point showed promising results [White2010] . The current report presents findings based on a more extensive data collection effort and new algorithmic approaches.

### Sensor Description

A schematic of the pyroelectric linear array (PLA) sensor is shown in Figure 5.1 and a photo of the sensor package is shown in Figure 5.2. The PLA sensor uses a Dias 128 element linear array of pyroelectric detectors along with a F/0.86 germanium lens. The size of each detector is  $90\mu\text{m} \times 100\mu\text{m}$  with a pitch of  $10\mu\text{m}$ . With a focal length of 50 mm, the detector instantaneous FOV (IFOV) is  $1.8\text{mrads} \times 2\text{mrads}$ . The extent of the spatial sample at range of 30 meters is  $5.4\text{cm} \times 6\text{cm}$ , providing about 17 samples over the height of a 2m tall human. A 18F4550 pic microcontroller is used for A/D conversion and communication. The sensor system operates at a sampling rate of 20Hz.

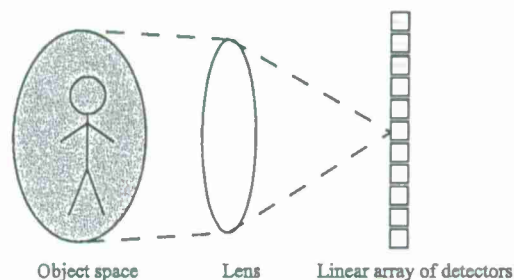


Figure 5.1. Schematic of PLA sensor.

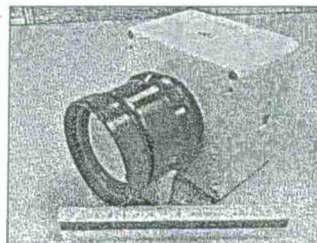


Figure 5.2. Photo of PLA sensor

### Data collection effort

Data collection using the PLA sensor was performed in two geographically distinct locations. One location was near the US-Mexico border which is typically has an arid terrain with thorn bushes forming significant portions of the vegetation. The other location was at a petting zoo near Memphis, Tennessee where the terrain was covered with grass and trees. The human category was represented by males and females of with varying physical built. Large, medium and small horses, cows, lamas, donkeys and dogs formed the animal class. The humans and animals moved in the field of view of the system at various speeds at ranges varying from 10 meters to 20 meters. Animals had handlers directing their movements during the data collection. Figure 5.3 shows the output of the PLA sensor with three horses, Figure 5.4 shows six humans and Figure 5.5 shows a human followed by a miniature cow.



Figure 1.3. Image of three horses generated by the PLA sensor



Figure 5.4. Image of six humans generated by PLA sensor

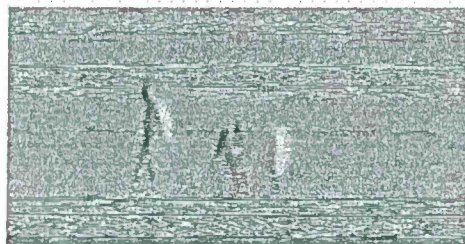


Figure 5.5. Image of a human followed by a miniature cow generated by PLA sensor

### Object Recognition algorithms

A statistical threshold was estimated for each detector output for segmenting the targets from background. The AC couple nature of the pyroelectric detector suppresses static objects in the background and only responds to the moving targets. If a target does not show variations in sections of its body, then the detectors do not respond. This can lead to fragmentation of an object. When a hot object enters and leaves the FOV of the sensor, the step response properties of the pyroelectric detector generate large output up swings and down swings at the instants of entry and exit of the object respectively. Fragmented objects can be regrouped by tracking these bipolar swings. The statistical threshold used for segmentation was also used to binarize objects with object set to 1 and background set to 0 for extracting geometrical features such as height to width. On the other hand, the segmented objects were retained in gray scale form for extracting texture based features using Log-Gabor filter bank. These features are then classified using one of three different classification algorithms, namely Mahalanobis distance classifier, Gaussian mixture classifier and Logistic Regression.

### Results

A total of 315 human profiles and 182 animal signatures were collected using the pyroelectric sensor at two locations at the US Mexico border in Arizona (ArzData) and at a petting zoo near Memphis (PzData). The number of samples of at each location for the three data collection sites is shown in Table 5.1. The data was separated into testing and training data using in two ways as shown in Table 5.2. The training and testing choices described in Table 5.2 were made because PzData has too few samples to form a training set in itself. On the other hand, including PzData in the test set increased the variance of the test set, making the test robust. This is because the animal samples in ArzData were horses but the petting zoo data, apart from horses, also contained cows, lamas, donkeys.

Table 5.1: Number of data points collected using PLA sensor

	ArzData location 1	ArzData location 2	PzData
human signatures	140	145	41
animal signatures	73	84	41

Table 5.2: Training and testing data

Data set	Training data	Test data
1	ArzData location 1	ArzData location 2 + PzData
2	ArzData location 2	ArzData location 1 +

	PzData
--	--------

Classification rates are shown in Tables 5.3 and 5.4. It is observed that Logistic regression using height and width features achieves the highest classification rate of over 89% for data set 1 and classification rate of over 90% classification rate for data set 2. The GMM classifier using height to width ratio also performs well coming with classification rates over 85% in both cases. The main cause of error was the incorrect grouping of fragments of objects during the object detection phase. Another cause of error was animals running at high speeds. The profile height and width feature of a galloping horse is similar to that of a tall human walking slowly. The Gabor features performed poorly and using dimensionality reduction techniques such as linear discriminant analysis only provided marginal improvement in the classification accuracy. Though results of the classification rates are not reported here for wavelet packet based features, their classification performance was significantly lower.

Table 5.3. Classification rates for data set 1

Feature extraction	Classifier	Classification rate
Gabor features	Mahalanobis distance	75.3%
Height and width	Logistic Regression	89.6%
Height to width ratio	GMM	85.7%

Table 5.4. Classification rates for data set 2

Feature extraction	Classifier	Classification rate
Gabor features	Mahalanobis distance	73.6%
Height and width	Logistic Regression	90.8 %
Height to width ratio	GMM	86.4%

### Future Work

The results from this research effort will be submitted to the IEEE Sensors Journal in August 2011.

Several tasks are foreseen in future efforts to further refine and improve the sensor system. The first one includes implementing the software on low resource computing platforms for real time performance. The second task is incorporating this system into a multi-modal sensor network. It is hypothesized that fusion of features from the PLA sensor with sensors such as acoustic and seismic sensors will further increase the discrimination rates. Another goal is to overcome misclassification of galloping animals as humans. For this a two columns array is currently being developed. The time of



appearance of an object in each of the columns can be used to estimate speed of objects, which can be used to address the above-mentioned errors. Further, a more sensitive detector array is being used for the development of a long range PLA with ability to discriminate well beyond the 30-meter range limit of the current PLA system. This long range PLA system will provide greater sensor to object standoff distance and thus expanding the utility of the sensor beyond trail monitoring into other tactical and military applications. The higher sensitivity detector system can reduce the fragmentation effect at the sensor output that has also been a source of classification errors.

### **Papers Published in Support of Project (Copies provided in Appendix X)**

[White2010] W. E. White III, J. B. Brown, S. Chari, and E. L. Jacobs, "Real-time assessment of a linear pyroelectric sensor array for object classification," D. A. Huckridge and R. R. Ebert, Eds., vol. 7834, no. 1. SPIE, 2010, p.783403. [Online]. Available: <http://link.aip.org/link/?PSI/7834/783403/1>

## **6.0 Alternative Sensing Modalities**

### **Task 6.1: Develop alternate modalities of operation for beam break profiling sensors.**

An alternative to beam-break sensors for border and perimeter security is the use of micro-mechanical resonators. These types of sensors could be used to produce seismic or acoustic versions of profiling sensors. A detailed analysis of this mode of sensing was conducted and is presented in Appendix X.

### **Task 6.2: Map the feature space of an "atomic" sensor and relate the features to profile classification performance.**

Sensor atoms are fundamental units of sensing. This concept was explored as part of the overall effort of this contract. Some basic properties of a particular type of sensor atom, the Bernoulli sensor atom, were derived. A brief paper (unpublished) on the concept of sensor atoms and the Bernoulli sensor atom was produced and is provided in Appendix X. Publication of this work will require implementation and refinement of the concept of atoms in groups, which is an ongoing area of research.

**Task 6.3:** Further research into a University of Memphis concept for terahertz and sub-millimeter wave imaging for concealed weapons/contraband detection.

**Task 6.4:** Investigate the use of compressive sensing techniques in improving profile classification.

THz/sub-millimeter wave sensing provides a “see through” capability without the use of ionizing radiation. This capability is important in many types of security problems where the potential threat posed by an individual must be assessed prior to entry into a secured area. Sensors of this type have been under development for some time and low cost solutions remain elusive. Several sub-millimeter wave active and passive imaging systems for detection of hidden threats have been demonstrated but they all suffer from the low frame rate (i.e. active imagers) or high size and power consumption associated with cooled detection (i.e. passive imagers). Our effort is focused toward a solution to these problems using image plane coded aperture imaging techniques in active configurations with single pixel detectors. Different aspects of the work have been published in peer reviewed conferences and journals. Invited talks on this approach have been presented at IEEE and OSA conferences.

At the beginning of the effort sub-millimeter wave imaging using a single pixel detector and an image plane coded aperture had been demonstrated by our group. The image plane coded aperture was implemented using a spinning disk with holes separated in a pseudo-random fashion on a perimeter line. The proof of concept device could reconstruct line images of a masked source placed ten meters away from the aperture of a reflective optic. These simple images consisted of two point sources. The work was published in the paper O. Fuxhi and E. L. Jacobs (2010) “A Sub-Millimeter Wave Line Imaging Device,” Proceedings of SPIE, Volume 7670, Orlando, Florida, USA. This paper is provided as a supplement to this report.

In continuation of the effort described in the previous paragraph, a scanning line imager was built and imaging of an extended metallic object was demonstrated. Each line of the image was acquired in 300ms as the target was scanned across the field of view. The images were reconstructed offline using linear measurement techniques. The linear measurement techniques are computationally efficient and the image reconstruction reduces to a simple matrix vector multiplications. This work was published in the paper O. Fuxhi and E. L. Jacobs (2010) “A sub-millimeter wave line scanning imager,” Proceedings of SPIE, Volume 7837, Toulouse, France. This paper is provided as a supplement to this report.

The image plane coded aperture used in the previous work is suitable for building a compressive sensing (CS) imager. CS imagers make linear measurements on the image of the scene. The number of measurements is usually smaller than the desired number of pixels in the image and therefore the image reconstruction is realized using non-linear iterative algorithms. We used the CS algorithms on measurements collected with the image plane coded aperture line imager and were able to reconstruct line images with half the number of measurements used with linear measurement techniques. The line imager

configuration of this sensor is in essence a THz profiling sensor. This work was summarized in the paper Imama Noor, Orges Furxhi and Eddie L. Jacobs (2011) "Compressive sensing for a sub-millimeter-wave single pixel imager", Proceedings of SPIE, Volume 8022, Orlando, Florida, USA. This paper is provided as a supplement to this report.

In continuation of the effort, a two-dimensional version of the image plane coded aperture imager was built and demonstrated. The image plane coded aperture was implemented using a spinning disk with holes placed pseudo randomly across the surface of the disk. A square aperture was placed in front of the disk to indicate an image window. This device could scan a two-dimensional image of the scene every 20ms (50Hz). The images that were reconstructed consisted of 64x64 pixels and were reconstructed in real time as the data was collected. Initially the two-dimensional coded aperture was used to form images at visible light wave lengths. For this purpose an N-type silicon PIN photodetector was used instead of the sub-millimeter wave detector. And a collimated red laser was used as an illumination source instead of the sub-millimeter wave source. The reason for visible light implementation was two-fold. First, it helped with the debugging of the issues related to the spinning disk coded aperture (elimination issues with the sub-millimeter wave optics) and second, it demonstrated the wavelength independence of the spinning disk coded aperture. This work was published in the paper O. Furxhi and E. Jacobs, "Spatially Selective Mask for Single Pixel Video Rate Imaging," in Imaging Systems and Applications, OSA Technical Digest (CD) (Optical Society of America, 2011), paper ITuA3, in Toronto, Ontario, Canada. This paper is provided as a supplement to this report.

The spinning disk coded aperture device was then used to implement a two-dimensional, real-time, sub-millimeter wave imager. This device could scan a two-dimensional reflection mode image of a metallic target positioned 10 meters away, every 20ms (50Hz). The target was illuminated with sub-millimeter waves and its reflection was imaged on the coded aperture. The images that were reconstructed consisted of 64x64 pixels and were reconstructed in real time as the data was collected. Imaging was also demonstrated in transmission mode (imaging the transmission of a sample/target). This work was published in Orges Furxhi, Eddie L. Jacobs and Robert Hewitt (2011), "Two-dimensional, real-time, sub-millimeter-wave imaging using a spatially selective mask", Proceedings of SPIE, Volume 8022, Orlando, Florida, USA. This paper is provided as a supplement to this report.

An analysis comparing various modes of active imaging in terms of signal to noise ratio (SNR), including the image plane coded aperture approach, was conducted. The purpose of the analysis was the identification of advantages and disadvantages of the image plane coded aperture approach compared to more traditional ways of forming images in active configurations. The analysis concluded that the measurement SNR performance of the image plane coded aperture approach rests between the conjugate point imager configurations (best SNR) and focal plane array configurations (worst SNR) provided equal illumination power. The SNR approached the best SNR case when compressive sensing reconstruction techniques could be realized. However, the image SNR for the

coded aperture approach is also related to the reconstruction method. The analysis identified the need for further analysis with regards to methods for the generation of hole patterns on the spinning disk that lead to independent codes (independent codes lead to better reconstructions). Another approach that could be pursued is the identification of other implementation of the coded aperture different from the spinning disk. This work was published in Orges Furxhi and Eddie L. Jacobs (2011), "Comparison of schemes for active sub-millimeter wave imaging", Proceedings of SPIE, Volume 8188, Prague, Czech Republic. This paper is provided as a supplement to this report.

Further analysis concerning the image reconstruction technique that is utilized by the two dimensional sub-millimeter wave imager was conducted and a journal paper was published in the Journal of Optical Engineering summarizing the imager and the mathematical analysis associated with the reconstruction techniques. The publication Orges Furxhi, Eddie L. Jacobs and Chrysanthé Preza, "Image plane coded aperture for terahertz imaging", Opt. Eng. 51, 091612 (Jun 15, 2012), is provided as a supplement to this report.

Other approaches of implementing an image plane coded aperture imager were investigated and an effort was put forward to formalize the concept of image plane coded aperture (IPCA) detectors. IPCA detectors are used as substitutes for focal plane arrays in frequency regimes where focal plane arrays are impractical, expensive, or non-existent. IPCA detectors are composed of a single element detector sensitive to the radiation frequency of interest, a reconfigurable spatial light modulator (SLM), and a mechanism such as a lens or a horn that is used to collect the radiation past the SLM and focus it on the sensing element. The IPCA detector is placed in the image plane of an imager and is used to make linear measurements on the image by modulating the information on the image plane spatially and/or temporally in amplitude, frequency, phase, or polarization. The image is then reconstructed computationally using inverse imaging techniques. In this work the spinning disk IPCA detector for sub-millimeter waves was used to illustrate the concept. Also, an IPCA detector with a phase modulating SLM was proposed as an alternative. This work was published in O. Furxhi, E. L. Jacobs (2012), "Image Plane Coded Aperture Detectors for THz Imaging" 2012 IEEE MTT-S International Microwave Symposium Digest, Montreal, Quebec, Canada. This paper is provided as a supplement to this report.

Another effort was also put forward to further understand and model the behavior of the spinning disk IPCA with respect to the codes that it generates. The generation of a procedure for producing hole patterns that lead to independent codes are of interest as independent codes improve the image quality. Initial work in this regard was published in E. Jacobs and O. Furxhi, "Image Plane Coding for Terahertz Imaging," in Optical Sensors, OSA Technical Digest (online) (Optical Society of America, 2012), paper SW3C.3, Monterey, CA, USA. This paper is provided as a supplement to this report.

In summary, the research effort has advanced the terahertz/sub-millimeter wave imaging device from a line imager with offline image reconstructions to a two-dimensional, real-time imager with 50Hz image scan rates and real-time reconstructions. The effort has also



generated further analysis on this imaging approach and has identified aspects of the approach that need improvement.

### **Papers Published in Support of Project (Copies provided in Appendix X)**

1. Orges Furxhi and Eddie L. Jacobs, "A sub-millimeter wave line imaging device," Proc. SPIE 7670, 76700L (2010), DOI:10.1117/12.850152
2. Orges Furxhi and Eddie L. Jacobs, "A sub-millimeter wave line scanning imager," Proc. SPIE 7837, 78370D (2010), DOI:10.1117/12.865100
3. Imama Noor, Orges Furxhi, and Eddie L. Jacobs, "Compressive sensing for a sub-millimeter-wave single pixel imager," Proc. SPIE 8022, 80220K (2011), DOI:10.1117/12.884147
4. O. Furxhi and E. Jacobs, "Spatially Selective Mask for Single Pixel Video Rate Imaging," in Imaging Systems and Applications, OSA Technical Digest (CD) (Optical Society of America, 2011), paper ITuA3.
5. Orges Furxhi, Eddie L. Jacobs, and Robert Hewitt, "Two-dimensional, real-time, sub-millimeter-wave imaging using a spatially selective mask," Proc. SPIE 8022, 80220J (2011), DOI:10.1117/12.883994
6. Orges Furxhi and Eddie L. Jacobs, "Comparison of schemes for active sub-millimeter wave imaging," Proc. SPIE 8188, 81880M (2011), DOI:10.1117/12.901821
7. Orges Furxhi, Eddie L. Jacobs, and Chrysanthé Preza, "Image plane coded aperture for terahertz imaging," Opt. Eng. 51, 091612 (2012), DOI:10.1117/1.OE.51.9.091612
8. O. Furxhi, E. L. Jacobs, "Image Plane Coded Aperture Detectors for THz Imaging" 2012 IEEE MTT-S International Microwave Symposium Digest, paper TU4D-4, Montreal, Canada.
9. E. Jacobs and O. Furxhi, "Image Plane Coding for Terahertz Imaging," in Optical Sensors, OSA Technical Digest (online) (Optical Society of America, 2012), paper SW3C.3.

## **7.0 Turbulence Mitigation**

### **Task 7.1: Investigate the functional applicability and limitations of current turbulence mitigation techniques and algorithms.**

In support of Task 7.1 a thorough review of the most common mitigation techniques was completed, their respective algorithms implemented, and the results compared. The comparison resulted in the discovery of a number of advantages and disadvantages related to the implementation of each. They may be summarized as follows. Lucky/synthetic imaging is based on the finite probability that an uncorrupted frame and will eventually propagate through the turbulent atmosphere. It has of the advantage of automatically handling isoplanatic restriction that plagues most of the other turbulent mitigation techniques and enables diffraction limited imaging. The disadvantages of the algorithm lie in that it depends on short exposure imagery, calculation of image quality metrics, and dependence on a mosaic procedure for best results even though isoplanatism is handled inherently in the algorithm. Blind deconvolution has the advantage that it can be implemented for correction of a wide variety of turbulent atmospheres even when little

detail of the intervening atmosphere is provided. The disadvantages include the enormous computational complexity, no guarantee of convergence to the optimal solution, and dependence on isoplanatic patch size. Higher order spectral techniques have the advantage of being spectrally intuitive, resistant to corruption from white Gaussian noise, capable of identifying nonlinear relationships between phase components and therefore enabling a better representation of the degraded object. The drawbacks to its implementation are the significant data storage requirement, trial and error determination of the intervening atmosphere's spectral amplitude, the dependence on isoplanatic patch size, and the inherent fundamental frequency linear phase corruption. Finally, frame averaging was the final mitigation technique investigated. It has the advantage of being simple, computationally efficient, and effective in the removal of the jitter associated with a turbulent atmosphere. The drawbacks to its implementation are that it effectively prevents diffraction limited imaging and is not suitable for targets traveling with considerable speed. These results appear as an unpublished paper and further details related to the implementation can be found in Appendix X.

**Task 7.2: Examine the turbulent effects as a function of range, atmospheric effects, imaging band, optical design, and detector type.**

In support of Task 7.2, an efficient turbulence simulation algorithm was developed to reproduce the turbulent atmosphere effects on a pristine image or video of an applicable target. The algorithm is based on visible wavelength statistics captured from various turbulent atmospheres. This effort extended those results to include infrared wavelengths. Additionally, the simulation tool allows the user to input range, strength of turbulence, imaging band, short or long exposure detector integration times, and other optical design characteristics. The result is a simulated image or image sequence representing the effects of the atmosphere, the optics, and the detector. The degraded imagery is suitable for most types of turbulence mitigation algorithm development. It should be noted that the simulation algorithm has not undergone strenuous comparison to real collected data. That effort is currently underway. The details of the implementation and the result results from this effort have been published and can be found in Appendix X.

**Task 7.3: Explore the effects of turbulence on hyper-spectral data, fusion and metric development and the effects of mitigation on feature discrimination.**

The following efforts were undertaken to determine the effects of turbulence on feature extraction techniques applied to a sparse detector sensor arrays. Video data of humans and animals was captured using a long wave infrared imaging sensor array. That data was subsequently processed to extract profile data, determine applicable height to width ratios, and classified based on the extracted features. The turbulence simulation algorithm developed in support of Task 7.2 was then used to corrupt the same imagery. The height to width ratio of the resultant imagery was examined to determine the quantitative differences when compared to the uncorrupted sequences. The results show that for coarse-grained classifications such as human versus animal determination, even the strongest levels of turbulence only minimally affect the height to width ratios. Thus, we

can conclude that for human versus animal classification, turbulence should not be much of an issue. However, as noted above, the turbulence simulation algorithm is not undergone strenuous data verification and thus the application of these results should be limited until such time that verification has been completed. These results appear as an unpublished paper and further details related to the implementation can be found in Appendix X.

**Task 7.4: Consider the effects of the extension of current turbulence mitigation techniques to sparse detector sensor arrays.**

The efforts in support of Task 7.4 include the consideration of current turbulence mitigation techniques and their application to the profile extraction system. Implementation of a turbulence mitigation algorithm cannot be considered apart from the processing platform. Therefore, the recommendations derived under this section reflect the fact that a low power sparse detector array makes up our sensing platform. Given these constraints lucky/synthetic imaging and single frame or multi-frame de-convolution cannot be considered due to their dependence on short exposure imaging and high computational complexity. Higher order spectral techniques must also be excluded due to the large amount of data storage require for their implementation and their heavy computational complexity as well. Therefore we are left with only frame averaging as applicable mitigation technique for the sensing platform. Frame averaging represents a simple and straightforward method of improving the captured imagery for human consumption and can be implemented quite easily on most low power platforms.

**Papers Published in Support of Project (Copies provided in Appendix X)**

[Robinson 2012] "An efficient turbulence simulation algorithm", A. L. Robinson, J. Smith, and A. Sanders, Proc. SPIE 8355, 83550K (2012), DOI:10.1117/12.919541

## 8.0 Feature Sensing Laboratory

**Task 8.1:** Characterize the existing campus sensor system including a formal knowledge model captured in an ontology. This will involve learning what is currently present on campus with regard to sensing systems, instrumenting them so that they produce data instead of just pictures, and establish a means for archiving this data.

**Task 8.2:** Supplementing the existing campus sensor system. These sensors will either be sensors operating in non-visible wavebands or sensors designed to provide new sensing capabilities such as profiling sensors.

**Task 8.3:** Experiment design. We will design multi-use experiments in which scenarios are created to stimulate events of interest.

An important question in the development of unmanned ground sensors (UGS) is what the field performance will be long term and under different environmental conditions. It would be desirable to have a long-term emplacement of sensors that could be monitored 24/7 in order to gain data on real world performance of these systems. As part of an Army sponsored program on Intelligent Network-Centric Sensors, we have begun building an UGS field test laboratory. When fully built, studies as outlined in the tasks above could be carried out.

Although initially planned as an on-campus facility, it was decided, in consultation with the government technical POC, to implement this laboratory in an environment more typical for border and perimeter security applications. The site we have chosen is a biological field station owned by the University. The site chosen is the University of Memphis Meeman Biological Field Station. The site covers 623 acres and is located approximately twenty five miles northwest from the main university campus. The University of Memphis operates an earthquake monitoring station which includes a microwave link back to the campus (see Figure 8.1).

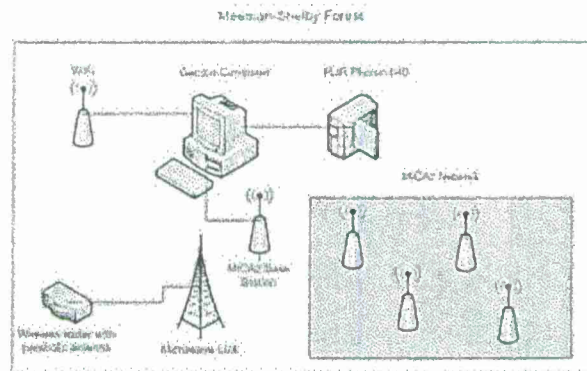
Our design allows the status and information collected by sensors to be reviewed at the monitoring station in near real time. The data collected is moved through routing hardware and piped through a local network to a the microwave link. This RF link consists of a 300 ft antenna and a robust 4.2 GHz Freewave link direct to the campus network. The antenna and RF equipment are located approximately 900 ft from the test site. Once the information arrives at the main campus it is routed to the appropriate destination via secure links.



Figure 8.1. RF antenna - Meeman forest



The laboratory is configured to allow deployment of static and mesh sensor networks. This configuration is centered on a base station that is in charge of routing stand alone and mesh-network data to the RF link. The base stations can also act as sensor test point. The implemented architecture also has the flexibility to accommodate multiple base stations if necessary. This means that any desired combination of sensor network can be easily implemented and deployed. A diagram of the network layout is shown in Figure 8.2.



Mesh networks based on XBee ZigBee modules and static nodes using XBee Wi-Fi modules were tested. These modules were chosen because they offer a simple standard interface and their low power usage (see Figure 8.3). The drawback is the speed limitation imposed by the serial interface. A maximum speed of 240Kbaud limits the amount of usable information that can be transmitted. On average, a 1.2MB data file will take 1 minute to transfer.

This makes this configuration ill suited for video but highly efficient to monitor low data rate sensors, such as profiling sensors. The network can be configured to use standard Wi-Fi in order to achieve higher speeds. This change however, requires that additional steps be taken to maximize power efficiency of deployed sensor modules in order to extend their up-time.

Several types of local hardware configurations for sensor control were evaluated. They range from the simplest "sensor atom" composed of an Arduino microcontroller, a pyroelectric detector and an XBee radio to a base station. The basic base station is single board computer. This computer is typically based on an Atom processor and runs Linux. This provides the flexibility and power of a full fledged PC computer but drawing a maximum power of 40Watts. If higher power efficiency is required this can be scaled down to an Arm processor computer such as a beagle board.

Preliminary test indicate that with line of sight or near line of site placement of sensor nodes communications at over 1500ft can be easily maintained. This suggests that for practical deployment inter sensor node spacing of 300 to 500 feet is sustainable. The clear implication is that a substantial amount of terrain can be monitored with relatively few sensor nodes. On the other hand base stations deployed as direct gateways to the RF link must be deployed within line of site of it to maintain reliable communications.

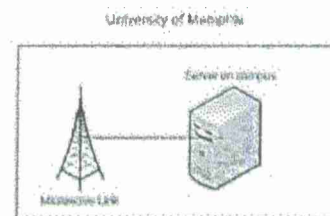


Figure 8.2. Network layout

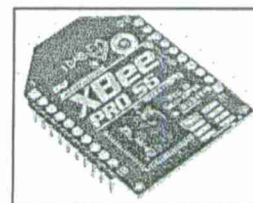


Figure 8.3. Xbee module

Our initial deployment of the systems is shown in this diagram. We have chosen to use an open source Gentoo based platform for the sensor base station. This will provide control of most of the Meeman based communications. To this will be connected high bandwidth sensors such as forward-looking infrared camera and a low bandwidth sensor network. For this project, two FLIR Photon 640 sensors were obtained for configuration in the sensor network. The low bandwidth network will be a ZigBee sensor network consisting of MICAz motes with attached pyroelectric motion sensors deployed along a trail to monitor movement of animals and people. The MICAz motes allow for basic processing and present the possibility of just transferring the results of classifications. A distributed array of motion detecting sensors has been shown in some of our research to be highly effective in classifying humans and animals. We will deploy a PIR based version of this array along the trail. The initial array will consist of only three sensors but can be expanded. Studies have shown that very limit classification can be made with a single sensor. Our hope is to develop a three-sensor system with better performance.

Many of the stated tasks for this portion of the research were not achieved due to delays and complications in implementing the network involved. Significant time was spent tracking down communication interference between our network router and the earthquake sensors. This interference was resulting in false reports of earthquake activity. A significant effort at providing additional shielding for our router seems to have solved the problem and we have made significant progress this summer.

We expect to have our initial version of the network up and running by the first of September 2012. Over time we expect to expand the number, variety, and coverage of sensors in the network. This ultimately may require a dedicated landline or additional microwave link to support the bandwidth necessary. We plan to use this facility to perform testing of new sensors and algorithms, energy harvesting research, and smart tasking of sensors via intelligent networks.

## 9.0 Conclusions

The execution of this contract has resulted in some significant scientific and technical progress in support of intelligent, network-centric, sensors. We believe that this work has been of immediate benefit to the Army and will continue to pay dividends in technical achievement into the near future. Further publications will result directly and indirectly from this work.

## **Appendix A. Published papers in support of this contract.**

Copies of all published papers completed as part of this cooperative agreement are provided following this page.

# A Wireless Near-IR Retro-Reflective Profiling Sensor

Alex Galvis\*, David J. Russomanno, and Cartik R. Kothari

Department of Electrical and Computer Engineering  
Purdue School of Engineering and Technology  
Indiana University-Purdue University Indianapolis  
Indianapolis, IN, USA 46202

## ABSTRACT

The notion of a profiling sensor was first realized by a near-IR, retro-reflective prototype consisting of a vertical column of sparse detectors. Alternative arrangements of detectors have been implemented in which a subset of the detectors have been offset from the vertical column and placed at arbitrary locations along the anticipated path of the objects of interest. All prior work with the near-IR, retro-reflective profiling sensors has consisted of wired detectors. This paper advances this prior work by designing and implementing a wireless prototype version of a near-IR, retro-reflective profiling sensor in which each detector is a wireless sensor node. In this novel architecture, a base station is responsible for collecting all data from the detector sensor nodes and coordinating all pre-processing of data collected from the sensor nodes, including data re-alignment, before subsequent classification algorithms are executed. Such a wireless detector configuration advances deployment options for near-IR, retro-reflective profiling sensors.

**Keywords:** Wireless profiling sensor, wireless sensor, neural network, object classification.

## 1. INTRODUCTION

The original notion of a profiling sensor was proposed by Ronnie Sartain of the U.S. Army Research Laboratory, in which objects traversing the field of view of a crude imaging sensor, consisting of a collection of sparse detectors, could be classified by examining their silhouettes.<sup>1</sup> A vertical array, consisting of sixteen pairs of transmitters and reflectors, was first developed to produce sixteen parallel near-IR beams (Figure 1). A silhouette was then generated if the object traversing the specified trail would break the beams<sup>1-5</sup> (Figure 2). It was proposed that a low-cost sensing device of this form would be useful for providing security surveillance for several applications, including the U.S.-Mexican border, to detect illegal activity and in other areas where the classification of objects is highly relevant.<sup>6</sup> Because of the extent of the U.S.-Mexican border, using low-cost surveillance equipment would make it economically feasible to cover more areas than using traditional imaging sensing devices.

The first profiling sensor involved a vertical array of sixteen near-IR retro-reflective sensors that generated a crude image.<sup>7</sup> Each sensing element produced a near-IR retro-reflective beam perpendicular to a pairing reflecting surface mounted on an opposing pole.<sup>3,8,9</sup> A classification algorithm would then take the raw data (broken or unbroken beam) generated by the profiling sensor to produce and classify an object's silhouette into one of three categories of interest (i.e. human, animal, or vehicle).<sup>8,9</sup> As a next step to improve this prototype's versatility, a low-resource microcontroller was interfaced with this profiling sensor. The Digi International BL4S200 single-board-computer was used to store and classify data of the profiling sensor.<sup>10</sup> Other hardware improvements, such as an interface handheld I/O box, were added later on to facilitate data access to the microcontroller without the need of a computer.<sup>9</sup> Furthermore, an additional improvement included the arrangement of sensing elements into a custom arrangement<sup>9</sup> (Figure 3) while still generating similar raw data that could be discriminated among the three classifications groups of interest.<sup>11</sup> This new offset arrangement of detectors may provide a means by which the sensor could be more easily concealed.

---

\*Further author information:

E-mail: agalvis@iupui.edu, Telephone: 1 317 274 9726



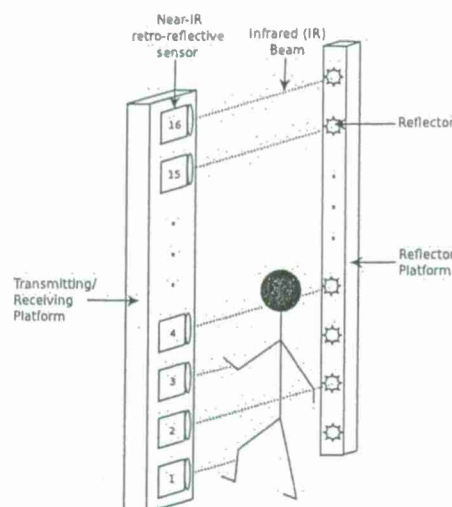


Figure 1. Object passing through the parallel beams of a vertical array of a near-IR retro-reflective profiling sensor.

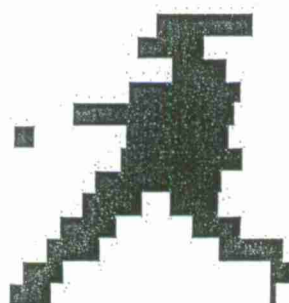


Figure 2. Generated silhouette of a human after traversing through the profiling sensor.

This paper focuses on a wireless near-IR retro-reflective profiling sensor that can be thought of as a set of sixteen wireless sensing nodes that comprise the overall profiling sensor. Previous profiling sensor prototypes have used CX-RVM5<sup>12</sup> active near-IR detectors that depend on their own pairing reflector. Each node in the wireless profiling sensor uses a Sharp GP2Y0D02YK0F<sup>13</sup> (Figure 4) as the sensing element with a similar field of view to the CX-RVM5 but does not require a reflector to sense a change-of-state event. The Sharp GP2Y0D02YK0F sensing element can thus be thought as a touch-less switch that turns on (digital high) if an object obstructs the path of its infrared beam and turns off (digital low) if there is no obstruction. Additionally, to make the sensing node wireless, each sensing element has been hardwired to its own wireless transmitter: an OEM Radio Frequency (RF) board<sup>14</sup> (Figure 5). A sensing node sends one packet containing the state and node identification data to a USB gateway receiver only if a change of state occurs (high-to-low or low-to-high) as an object passes through its field of view. The computer recording the data can then assign a binary value to each state and generate a silhouette representation of the object or process it by the classification algorithm described in the subsequent sections.

The focus of this paper is to present the architecture and the interaction of a wireless profiling sensor with a computer. The computer software developed for this work integrates useful tools, such as object classification and object silhouette previews, which can be provided in a test scenario immediately after each passing object is detected. A trained classifier implemented by a back-propagation neural network is also introduced and shown to provide classification results of 94% accuracy in testing to date.

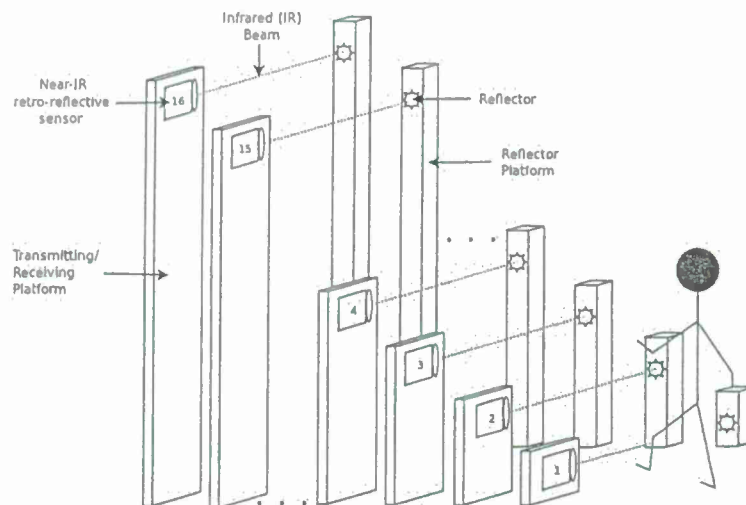


Figure 3. Object passing through the beams of a custom array near-IR retro-reflective profiling sensor.

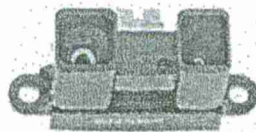


Figure 4. Sharp GP2Y0D02YK0F distance measuring sensor unit.

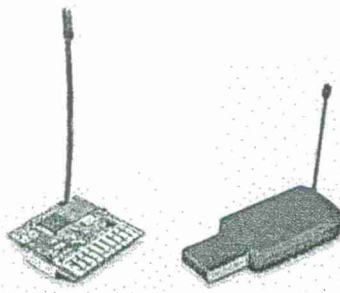


Figure 5. OEM RF board (Left) and USB gateway receiver (Right).

## 2. DATA LIBRARY

In previous work done by Russomanno et al. at the University of Memphis, a near-IR profiling sensor was used to capture profiles of over 1000 objects in the field, including humans, animals, and vehicles.<sup>15</sup> Each sample was captured at approximately 1 kHz and stored as a matrix of 16 binary strings corresponding to each of the 16 sensing elements in the array.<sup>10</sup> The length of each binary string depended upon the velocity at which the

object traveled through the specified field of view.<sup>9,16,17</sup> In other words, a vehicle traveling at a higher velocity would correlate to shorter binary strings, while a vehicle traveling at a lower velocity would yield longer strings.

Since the profiling sensor generates outputs comprised of zeroes and ones, it is especially convenient to use a back-propagation neural network as it preferably processes data that has been normalized. However, the architecture of the back-propagation neural network requires a fixed number of input arguments; therefore, it is necessary to compress all data into a fixed column dimension size. Thus, for this approach, an algorithm has been used to achieve this defined length without significantly altering the data in the sample library. Figure 6 shows silhouette images before and after the compression algorithm has been applied. After analyzing the same compression results in the remainder of the library samples, it was determined that no major resolution loss occurs if these are compressed to 256 columns. Therefore, a new database of silhouettes was generated with the compressed samples to use as the training and testing data set of the back-propagation neural network.

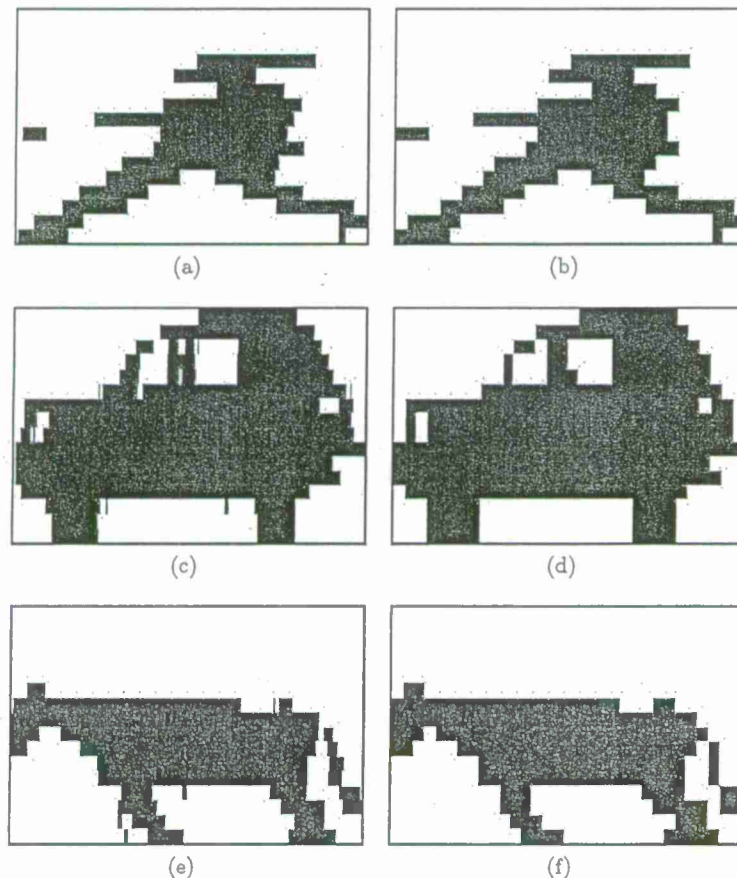


Figure 6. Silhouettes before compression and after compression: (a) Human silhouette before compression, (b) Human silhouette after compression, (c) Vehicle silhouette before compression, (d) Vehicle silhouette after compression, (e) Animal silhouette before compression, (f) Animal silhouette after compression

In the original near-IR retro-reflective profiling sensor, each sensor recorded one bit per sampling cycle.<sup>16,17</sup> This generated a real-time recording of the obstruction and restoration of each sensor beam. In the wireless near-IR retro-reflective profiling sensor, individual transmitters send one packet for each change of state in a sensing node (object or no object obstruction) instead of frequently sampling the current state of each sensing element. This method reduces power consumption<sup>14</sup> compared to the current model, which extends the useful life of the device. A wireless sensor node only sends a packet at each change of state: one packet for obstruction and one

packet for restoration of the beam. Using the time difference between changes of states, a computer algorithm generates the zeros and ones correlating to the obstruction and restoration, forming the 16 binary strings by a previously defined length (256 bits). Though the recording method is different than the original sensor in this new prototype, each of the sensing nodes has a comparable field of view as the original wired prototype, which does not affect the resolution of the recording and results in similar silhouette data as presented in Figure 7.

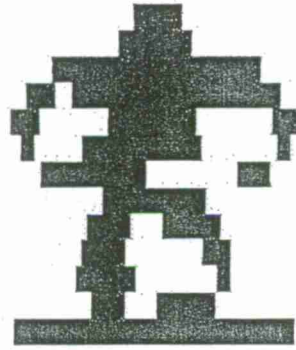


Figure 7. Human silhouette generated by the wireless near-IR retro-reflective profiling sensor.

### 3. WIRELESS SENSING NODE HARDWARE

In an effort to make the new profiling sensor independent from a pairing reflective surface, a near-IR distance sensing device was used to detect objects along the path of each sensing element. This sensing element is a single point distance module, which measures the distance from the emitting infrared diode to the reflecting surface of the object. Furthermore, the design of the sensing element used in this prototype is not considerably affected by environmental light or the reflective properties of the object up to a guaranteed distance of 80cm.<sup>13</sup> The near-IR distance sensor module utilizes the triangulation principle: the laser path is initiated at the near-IR beam emitter, reflects off of the object, and is captured by the imager. When this event occurs, the output line of the sensor is set to a logical high, otherwise is set to low. The relationship between the emitter, object, and imager is shown in Figure 8. The horizontal distance from the emitter to the object relies on the following: 1) the angle created between the emitted laser path to the object and the reflected laser path to the imager; and 2) the distance between the IR beam and the imager. The horizontal distance can be easily calculated by Equation 1, while Equation 2 utilizes the sine of the angle alpha to determine the horizontal distance.<sup>18</sup>

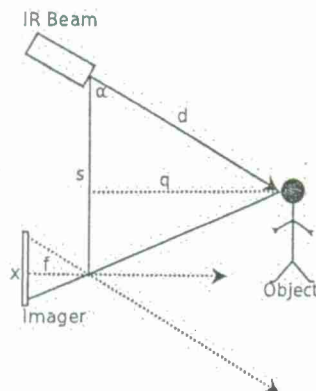


Figure 8. Relative distances and angle between object and individual elements in the distance sensor.

$$q = \frac{(f)(s)}{x} \quad (1)$$

$$d = \frac{x}{\sin(\alpha)} \quad (2)$$

To support wireless data transmission, each of the 16 distance sensing elements has been interfaced to their own OEM wireless transmitter. The OEM wireless transmitter has been programmed to send a packet of data when a change of logic state is received by the distance sensing element. A base station then gathers the data packets from the 16 wireless near-IR retro-reflective sensing nodes and processes them for object classification and silhouette image generation. Figure 9 shows the wireless near-IR retro-reflective profiling sensor system made up of 16 near-IR wireless sensing nodes and one base station that receives the packets from each node. However, specific I/O requirements between the OEM wireless transmitters and the near-IR distance sensing device required additional hardware that would not only need to regulate the voltage to each device, but the signal going from the sensing element to the transmitter. Figure 10 shows a block diagram representation of one near-IR wireless sensing node.

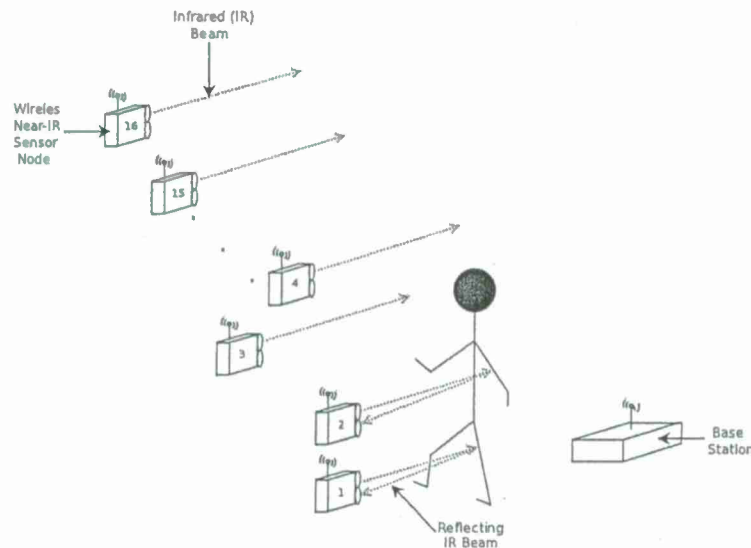


Figure 9. Wireless near-IR retro-reflective profiling sensor made up of 16 near-IR sensor nodes. A base station collects the packets from each change of state event as an object crosses through the IR beams.

The OEM wireless transmitters have been used in this wireless profiling sensor because they can be easily interfaced with external digital and analog devices. Finally, each transmitter supports multiple transmission frequencies options:<sup>14</sup> the ISM Band 902-928MHz has been used in the complete wireless near-IR retro-reflective profiling sensor.

#### 4. DATA ACQUISITION

To gain adequate data to identify a passing object, the status of each node must only be known at two stages: when the object first obstructs the beam and when the beam is restored. Previous profiling sensor prototypes utilize a constant collection of data at a set frequency for its method of data acquisition.<sup>16,17</sup> As previously mentioned in section 2, a similar data acquisition method would quickly drain the battery of the wireless profiling sensor since the transmitter needs to pull current for every packet transmission.<sup>14</sup> Therefore, we have implemented a data acquisition method that not only uses the battery more efficiently, but only uses one data packet per change of state from each sensing element to generate the necessary raw data.



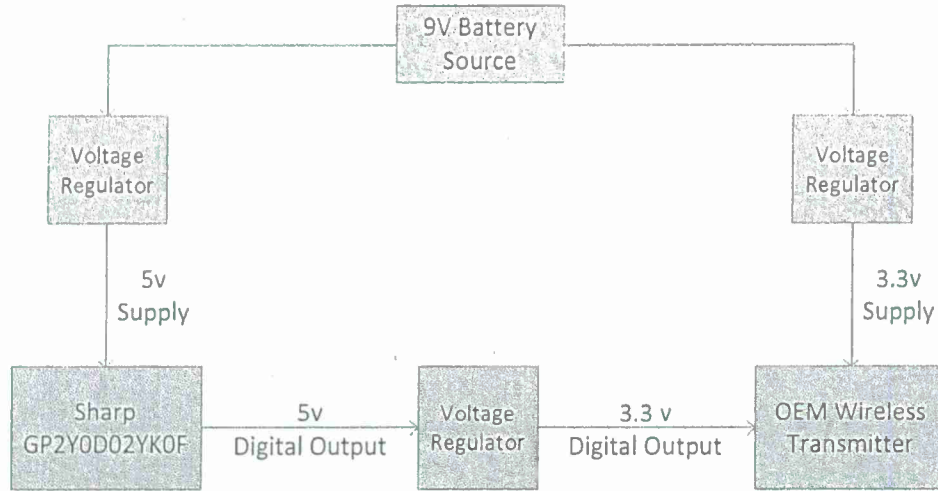


Figure 10. Wireless near-IR retro-reflective sensor node block diagram.

In the wireless profiling sensor, there is a designated trigger node that alerts the base station to the presence of an object. When this node detects an obstruction, the base station will begin recording data from all sensing nodes for a period of time specified in sensor's configuration setup. This packet contains the state of the node and the source node identification number. The state of the node is a binary code in which zero (0) indicates an unbroken beam and one (1) indicates an obstructed beam. As the base station gathers data packets, it will also record the time in milliseconds of when each packet is received. After the specified recording time expires, the base station ceases to record data. The recording of one object during this period of time is denoted as one recorded event. The base station sorts the collected transmission records of the recorded event by source node identification numbers. Then an algorithm determines the time length of the recorded event by calculating the difference between the time stamp of the final packet received and the time stamp of the initial packet received. In previous prototypes, time stamps were unnecessary because of the continuous data recording, but since this new prototype collects data only when a change of state occurs, we must generate the frequency of data acquisition for our non-constant rate to develop a binary matrix representation of this data.

The resulting binary matrix is a  $16 \times m$  matrix in which every entry corresponds to a low or a high bit reading at a point in the sampling. To generate this matrix with the collection of time samples received, the total time length of the recording  $\Delta t$  is calculated by subtracting the time of the first packet received  $t_0$  from the time the last packet is received,  $t_f$ . Equation 3 is then used to find the length of a time segment that will eventually be replaced by a binary value corresponding to the node state in that time interval. Additionally,  $t_b - t_a$  is the time difference from a change of state within  $\Delta t$ . As shown in Equation 4,  $t_b - t_a$  is divided by the result in Equation 3 so that this time interval can be interpreted as a sequence of bits describing the constant state of the  $(t_a, t_b)$  interval. Figure 11 is a visual representation of this procedure. Repeating this procedure for each sensing node generates the 16 necessary binary rows making up the entire binary matrix of the silhouette. Finally, this matrix is then used to generate a silhouette image of the passing object, as well as input data to a back-propagation neural network for its classification.

$$s = \frac{\Delta t}{256} \quad (3)$$

$$N = \frac{t_b - t_a}{s} \quad (4)$$

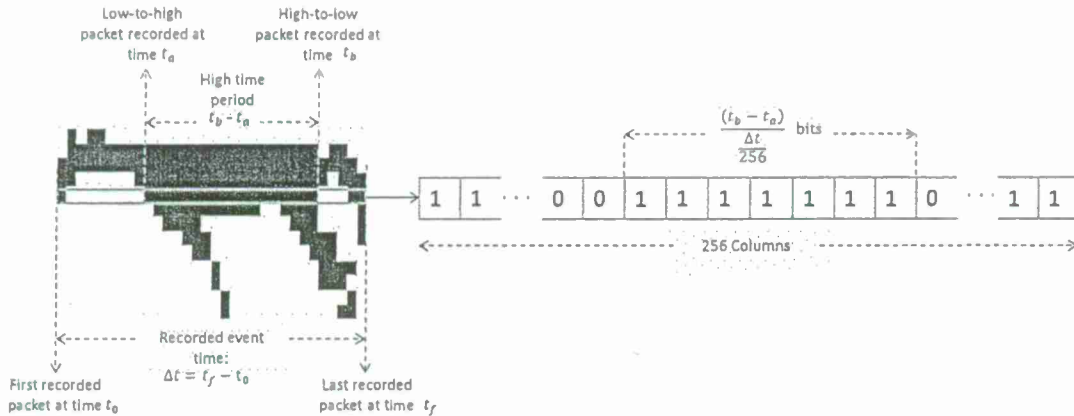


Figure 11. Populating a binary row by using a change-of-state-time-segmentation method.

## 5. CLASSIFICATION AND RESULTS

Although the original raw data had varying column dimensions, it has been shown that compressed data with a fixed number of columns produces virtually no alterations in the silhouette resolution in the analyzed library. Since a back-propagation neural network is used to classify the data, a fixed number of inputs were required to obtain a classification result. After normalizing the data to 256 columns, the back-propagation neural network was trained with half the data set within the compressed library. This neural network is comprised of  $256 \times 16 = 4096$  processing elements in the input layer, 20 processing elements in the hidden layer, and 3 processing elements in the output layer. This configuration was observed to provide the best classification results compared with other back-propagation neural networks with differing numbers of processing elements within the hidden layer. The method used to train the neural network was from Ebehart and Shi.<sup>19</sup>

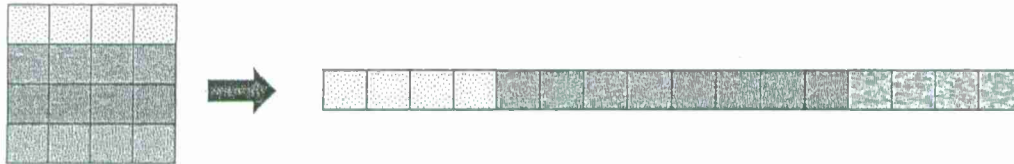


Figure 12. Matrix vectorization: all rows from a two-dimensional matrix are put sequentially into a linear array.

To make the matrix easier to handle by the neural network, the binary matrix has been vectorized, a process in which all rows are combined sequentially (Figure 12). Each processing element in the input layer uses each bit entry in the vector matrix as the argument to a sigmoid function (Equation 5), which will generate a real value between 0 and 1. The output values from each processing element in the previous layer become the input values for each of the processing elements in the subsequent layer. The edges connecting the processing elements from one layer to its subsequent layer have a weight value which is generated during the training process of the neural network. The weight of the edge is then multiplied by the input for each processing element in the hidden layer. The sum of these 4096 products becomes the argument for the sigmoid function of the hidden layer. This process is repeated from the hidden layer to the output layer to generate 3 output values. A schematic of this neural network is shown in Figure 13. Equations 6 and 7 are used to calculate the input values to the processing elements in the hidden and output layer. The values  $v_{ih}$  and  $w_{ji}$  denote the weight values from the input to the hidden layer and from the hidden to the output layer, respectively, all which are generated during the training of the neural network. Furthermore, notice that the sum of products begin from  $h = 0$  and  $i = 0$ , the bias processing elements, which take an input value of 1.

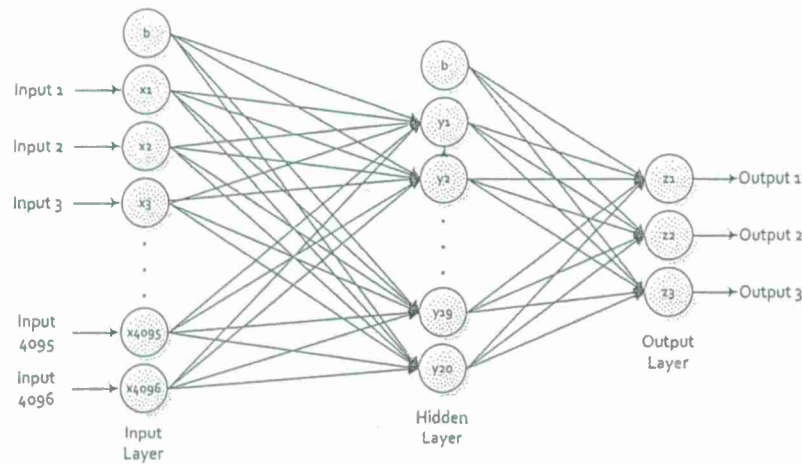


Figure 13. Back-propagation neural network with 4096 input processing elements, 20 hidden processing elements, and 3 output processing elements. Bias processing elements are denoted by  $b$  and these take an input value of 1.

$$f(x) = \frac{1}{1 + e^{-x}} \quad (5)$$

$$y_{ki} = f \left( \sum_{h=0}^n ((x_{kh})(v_{ih})) \right) \quad (6)$$

$$z_{ki} = f \left( \sum_{i=0}^h ((y_{ki})(w_{ji})) \right) \quad (7)$$

The output values in the output layer are positive real numbers between 0 and 1; the output processing element with the highest value indicates the classification of the input. A total of 577 test samples from three classes were classified by the back-propagation neural network. The distribution of the test samples from each class is shown in Figure 14. When the neural network assesses the entire set of testing data, 94% of the data is properly sorted into the correct classification groups (Figure 15). All of this data was previously collected by the vertical sparse array profiling sensor.

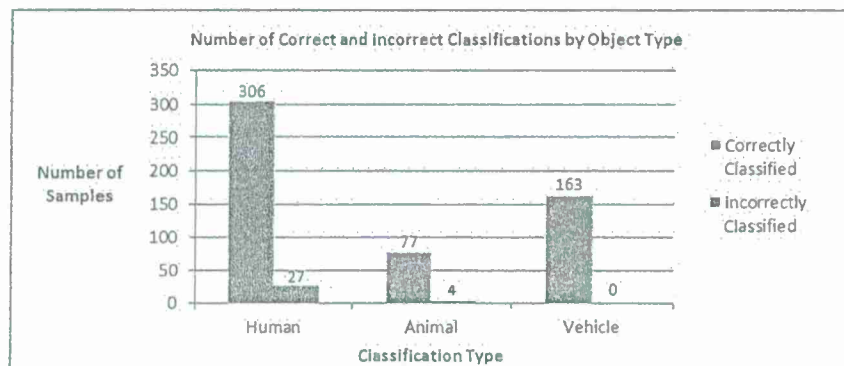
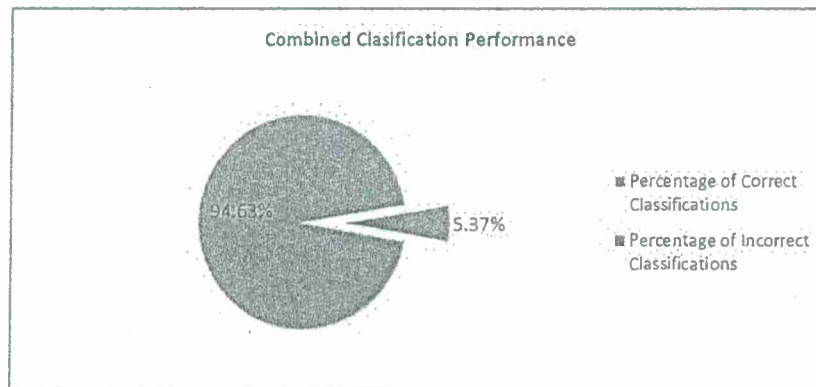


Figure 14. Distribution of number of samples per class within the testing data set.

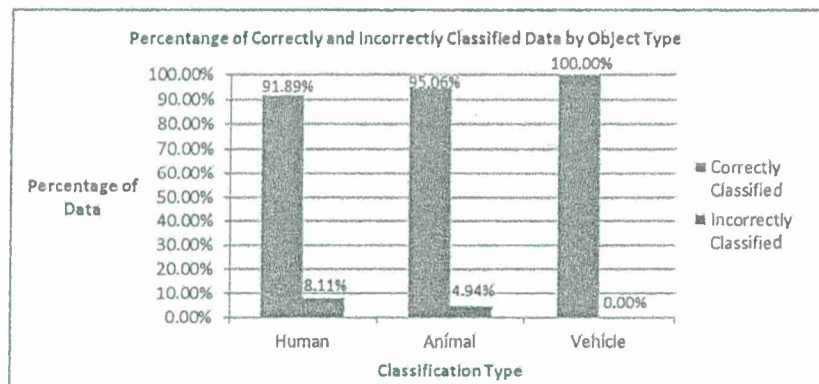
Unlike the vertical sparse array profiling sensor, the new wireless prototype allows for a small horizontal offset of approximately 5-10 inches. This offset is achieved without significantly diminishing the classification accuracy.



However, to maintain this high level of accuracy, passing objects must have an approximately constant velocity.<sup>9</sup> When a passing object changes its velocity in the horizontal space between each sensing node, the silhouette will be significantly distorted and classification results can be affected. Therefore, increasing the horizontal spacing between these nodes increases the risk of incorrectly classifying the passing object. It was determined that keeping horizontal distances within 5 inches will correctly classify the data close to 94% accuracy. For convenience, the existing data library, comprised of data collected using a vertical sparse array profiling sensor, was used to train the back-propagation neural network in this experiment. However, for any configuration of sensing nodes, a new data library can be populated and used to retrain the neural network to evaluate its classification performance. Finally, the confusion matrix that shows the performance of the classification algorithm in this test is shown in Table 1.



(a)



(b)

Figure 15. Classification results (a) Overall combined percent of correct and incorrect classification results, (b) Correct and incorrect classification results by object classes.

Table 1. Confusion matrix of classification results.

		Predicted Class		
		Human	Animal	Vehicle
Actual Class	Human	306	20	7
	Animal	4	77	0
	Vehicle	0	0	163

## 6. CONCLUSION

By combining the Sharp GP2Y0D02YK0F with an OEM RF board, a wireless profiling sensor prototype was designed and tested with highly accurate results in classifying passing objects at close range. As shown in these experiments, the Sharp GP2Y0D02YK0F proximity sensor can be used to collect data in a similar way to the CX-RVM5 IR based profiling sensor. The data collected by the proximity sensors is generated by using only two packets of data, one for a broken beam and one when the beam is restored. There is no significant loss of silhouette resolution when the normalized binary matrix is generated. Furthermore, this input into the back-propagation neural network is used to train and classify data, producing correct classifications with up to 94% accuracy. In addition to the increasing processing capabilities, the flexibility to deploy these sensors in the field is increased by allowing each sensing node to have a horizontal offset. Overall, this new design of the profiling sensor is an incremental improvement as compared to the original, wired profiling sensor prototype.

In continuing this work, we plan to collect data using the wireless profiling sensor using several different sensing node placement configurations. This information will be used to retrain the back-propagation neural network and test the classification performance of different arrangements of sensing nodes. Additionally, we will modify the OEM wireless transmitter software to allow each sensing node to calculate the relative position of all of the other sensing nodes; thus eliminating the need to train the neural network for each new configuration of elements. This will ideally allow for completely randomized configurations, rather than positioning the nodes in set and tested patterns.

## ACKNOWLEDGMENTS

Funding for this work was provided in part by the U.S. Army Research Laboratory (ARL) award number: W911NF-10-2-0071, as well as support from Indiana University-Purdue University Indianapolis. The findings and opinions expressed in this paper do not necessarily reflect the views of ARL or the U.S. government.

## REFERENCES

- [1] E. Jacobs, D. J. Russomanno, and C. Halford, "Profiling sensors for border and perimeter security," *SPIE Newsroom*, August 2009.
- [2] S. Chari, C. Halford, E. Jacobs, F. Smith, J. Brown, and D. Russomanno, "Classification of humans and animals using an infrared profiling sensor," *Unattended Ground, Sea, and Air Sensor Technologies and Applications XI 7333*(1), p. 733310, SPIE, 2009.
- [3] R. B. Sartain, K. Aliberti, T. Alexander, and D. Chiu, "Long-wave infrared profile feature extractor (pfx) sensor," *Unattended Ground, Sea, and Air Sensor Technologies and Applications XI 7333*(1), p. 733311, SPIE, 2009.
- [4] S. Chari, F. Smith, C. Halford, E. Jacobs, and J. Brooks, "Range and velocity independent classification of humans and animals using a profiling sensor," *Ground/Air Multi-Sensor Interoperability, Integration, and Networking for Persistent ISR 7694*(1), p. 76941K, SPIE, 2010.
- [5] W. E. White III, J. B. Brown, S. Chari, and E. L. Jacobs, "Real-time assessment of a linear pyroelectric sensor array for object classification," *Electro-Optical and Infrared Systems: Technology and Applications VII 7834*(1), p. 783403, SPIE, 2010.
- [6] J. B. Brown, S. K. Chari, and E. L. Jacobs, "An assessment of a 360-degree profiling sensor for object classification," *Ground/Air Multisensor Interoperability, Integration, and Networking for Persistent ISR II 8047*(1), p. 80470F, SPIE, 2011.
- [7] D. J. Russomanno, S. Chari, and C. Halford, "Sparse detector imaging sensor with two-class silhouette classification," *Sensors* 8(12), pp. 7996–8015, 2008.
- [8] D. J. Russomanno, S. Chari, E. Jacobs, and C. Halford, "Near-IR sparse detector sensor for intelligent electronic fence applications," *Sensors Journal, IEEE* 10, pp. 1106–1107, June 2010.
- [9] R. K. Reynolds, S. Chari, and D. J. Russomanno, "Embedded real-time classifier for profiling sensors and custom detector configuration," *Ground/Air Multisensor Interoperability, Integration, and Networking for Persistent ISR II 8047*(1), p. 80470E, SPIE, 2011.

- [10] R. K. Reynolds, D. J. Russomanno, S. K. Chari, and C. E. Halford, "Profiling sensor classification algorithm implementation on an embedded controller," *Ground/Air Multi-Sensor Interoperability, Integration, and Networking for Persistent ISR* 7694(1), p. 769413, SPIE, 2010.
- [11] R. K. Reynolds, "Real-time object classification using a custom sparse array profile sensor on an embedded microcontroller," Master's thesis, The University of Memphis, May 2011.
- [12] Anon, "CX-RVM5/D100/ND300R data sheet," 2007. Ramco Innovations.
- [13] Sharp Corporation, "GP2Y0D02YK0F distance measuring sensor unit," December 2006. Sheet No. E4-A00501EN.
- [14] Monnit Corporation, "Monnit WIT wireless temperature sensor," 2012. Sheet No. MD-001-1A.
- [15] D. J. Russomanno, S. Chari, K. Emmanuel, E. Jacobs, and C. Halford, "Testing and evaluation of profiling sensors for perimeter security," *The ITEA Journal of Test and Evaluation* 31(1), pp. 121-130, 2010.
- [16] M. Yeasin, D. J. Russomanno, M. S. Sorower, M. Smith, and J. S. Shaik, "Robust classification of objects using a sparse detector sensor," in *IC-AI*, pp. 742-748, 2008.
- [17] J. B. Brown, S. Chari, J. Hutchison, J. Gabonia, and E. Jacobs, "Assessment of a linear pyroelectric array sensor for profile classification," *Unattended Ground, Sea, and Air Sensor Technologies and Applications XII* 7693(1), p. 76930O, SPIE, 2010.
- [18] K. Konolige, J. Augenbraun, N. Donaldson, C. Fiebig, and P. Shah, "A low-cost laser distance sensor," in *Robotics and Automation, 2008. ICRA 2008. IEEE International Conference on*, pp. 3002-3008, May 2008.
- [19] R. Eberhart and Y. Shi, *Computational Intelligence: Concepts to Implementations*, Morgan Kaufmann, Burlington, August 2007.

# An Ontology-based Data Fusion Framework for Profiling Sensors

Cartik Kothari<sup>1</sup>, Joseph Qualls<sup>2</sup> and David Russomanno<sup>1</sup>

<sup>1</sup>Purdue School of Engineering and Technology  
Indiana University-Purdue University  
Indianapolis, IN, U.S.A.  
[ckothari@iupui.edu](mailto:ckothari@iupui.edu), [drussoma@iupui.edu](mailto:drussoma@iupui.edu)

<sup>2</sup>Research and Engineering  
RenderMatrix, Inc.  
Memphis, TN, U.S.A.  
[iqualls@rendermatrix.com](mailto:iqualls@rendermatrix.com)

**Abstract**—Data-to-decision systems must fuse information from heterogeneous sources to infer a high-level understanding of a situation. A high degree of confidence in the inferred knowledge is necessary for appropriate actions to be taken based upon the assessment of a situation. This paper presents an extensible Semantic Web compatible framework that uses rich ontological descriptions for the autonomous and human-aided fusion of heterogeneous sensors and algorithms to create evidence-based hypotheses of a situation under persistent surveillance. Raw data acquired from profiling sensors is combined with the output of visualization and classification algorithms, yielding information with a higher degree of confidence than what would be obtained without the fusion process. The framework can readily accommodate other data sources and algorithms into the fusion process.

**KEYWORDS:** Semantic Web, Ontology, Sensor Network, Data Fusion, Situation Awareness, Data to Decision Framework, Autonomous Decision Systems

## I. INTRODUCTION

The fusion of data from heterogeneous sources, such as sensors and intelligence reports, is integral to the inference of highly reliable, evidence-based knowledge of a situation. The degree of confidence in the inferred knowledge improves with further acquired evidence, that is, fusion of data from more sources. This paper describes an extensible Semantic Web compatible framework for the autonomous fusion of data from heterogeneous sensors and algorithms, allowing a human operator receiving the fused data to assess a situation with an increased confidence in the context of persistent surveillance.

Situation awareness has been defined by Endsley [1] as follows: “the perception of elements in the environment within a volume of time and space, the comprehension of their meaning, and the projection of their status in the near future.” Situation awareness is critical to decision making in many applications, such as, patient monitoring, emergency response, military command control, and border surveillance.

Systems for situation awareness require the fusion of a myriad of data and knowledge sources, including disparate sensor systems, algorithms, and intelligence reports. Semi-automated and automated inference using fused data may lead to an enhanced knowledge about the entities of interest in a situation, as well as an increased confidence in interrelationships, enabling situation awareness. End user

confidence in the inferred knowledge is critical to timely and appropriate actions.

Integration of sensor data with algorithmic processes and human-controlled information systems poses a significant challenge for network-centric sensor frameworks. Fig. 1 is a summary of the classical Joint Director of Laboratories (JDL) fusion levels [2], augmented with a knowledge management component [3]. These six fusion levels cover both automated and “human in the loop” processing of data and knowledge. The model supports the concept of autonomous algorithms and human users contributing to an evolving solution state in which fused information may enable the identification and assessment of strategies and tactics for counterintelligence [3-5]. The JDL model is useful for describing the conceptual framework within which a particular fusion process occurs and it also provides a reference for describing the level of fusion in an overall process.

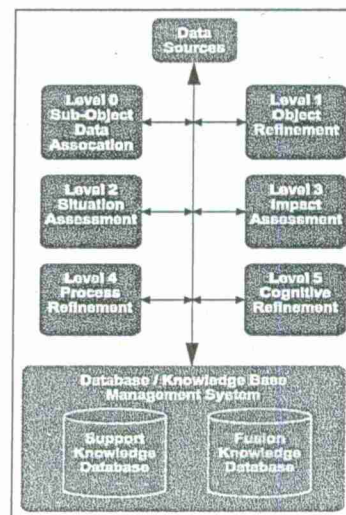


Fig. 1. Six levels of the data fusion model augmented with a data and knowledge management system.

Multi-sensor data integration has been limited primarily by the lack of standards for data exchange and for describing sensor capabilities and specifications, which would enable their automated discovery, invocation, and composition with other sensors as part of process workflows [6-7]. The XML-based



data formats and standards, such as SensorML (Sensor Markup Language)<sup>1</sup> and the Observations and Measurements (O&M) Schema<sup>2</sup> have been adopted by the Sensor Web Enablement (SWE) [8] initiative of the Open Geospatial Consortium (OGC)<sup>3</sup> to mitigate these deficiencies. The SWE initiative aims to bring together Web connected sensors of all types in a common framework for discovery, invocation, and tasking. The advent of the Semantic Web initiative [9] and its associated representational standards, such as the Web Ontology Language (OWL)<sup>4</sup> and the Resource Description Framework (RDF)<sup>5</sup>, has led to the development of sensor specific ontologies, such as OntoSensor [10] and the Sensor Data Ontology [11]. These ontologies contain computable descriptions (definitions) of sensors and sensor data, their properties, capabilities, and relationships.

In this paper, we present an ontology-based framework that is capable of fusing raw data with the output of machine learning algorithms that process the given raw data; yielding further knowledge about a monitored situation. The framework is robust and flexible to accommodate a variety of algorithms and heterogeneous sensors by providing ontological descriptions of their input and output capabilities. Descriptions of these components, which use ontologically defined terms, allow capability-based matching of sensors and algorithms creating a plug-and-play architecture while eliminating the hurdles to their interoperability.

## II. PROFILING SENSORS FOR SURVEILLANCE

Persistence surveillance environments can contain a wide variety of sensor systems and algorithms. One such family includes profiling sensors, which are denoted by the nomenclature PFx. The PFx sensors are often regarded as crude 'imaging' devices and typically use a sparse detector array, as compared to a large focal plane array found in traditional cameras [12]. PFx sensors may be active or passive sensors that capture data about objects that pass through their field of view. For example, Fig. 2-a shows an active near-infrared version of a profiling sensor (PF<sub>i</sub>) with a sparse array of detectors in a vertical geo-location placement.

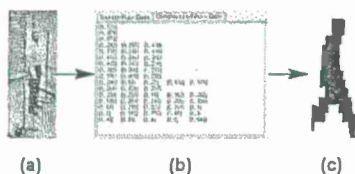


Fig. 2. PF<sub>i</sub> sensor system comprising (a) near infrared detectors in a vertical geo-location placement (b) sensor output formatted using run-length encoding and (c) output of an algorithm that produced a silhouette of the object.

One algorithm that operates on PFx data has the objective of visualizing the raw data as a crude profile or silhouette for human-aided classification. In addition, other algorithms operate on the PFx raw data and attempt to classify the data autonomously. For example, one approach is to attempt to classify the data into one of three classes: human, animal, or vehicle. Extensions of such algorithms may attempt a more refined classification, such as, human with backpack, light truck, etc. The PFx algorithms may use a variety of classification techniques, such as the naïve Bayesian classifier [13], naïve Bayesian with Linear Discriminant Analysis (NB-LDA) for dimensionality reduction [14], K-Nearest Neighbor (K-NN) classifier [15], Soft Linear Vector Quantization (SLVQ) [16], and Support Vector Machines (SVM) [17] for autonomous classification. A comprehensive set of papers on profiling sensors appears in [18-24].

### A. Application Scenario

Consider a border patrol agent remotely monitoring an area for activity of interest. The agent may be interested in detecting humans attempting to cross a border with or without weapons and drugs using deployed PFx sensor systems. In many scenarios, there is a low tolerance for false positives, given the remoteness of a location under surveillance or the possible hostile environment. The raw data output of the sensor as seen in Fig. 2b contains very little information about the sensed entity to an end user. The silhouette generated from this data, shown in Fig. 2c, provides more information to an end user as to the outline of the detected entity. The agent is likely to recognize the silhouette in Fig. 2-c as that of a human. However, some silhouettes are much less informative to an end user as in Fig. 3. In such cases, the silhouette needs to be supplemented with other information to increase the agent's confidence that the object is indeed human or a truck, animal, etc. A classification algorithm capable of processing the raw data or the silhouettes may yield such supplemental information. As a rudimentary fusion scenario, the agent could be provided with the silhouette in addition to the output of the classification algorithm. In many instances, the combined information may increase the agent's confidence in a given hypothesis.



Fig. 3. Examples of less informative silhouettes to end users

## III. FUSION FRAMEWORK

The ontology-based framework facilitates the integration of raw data from sensor systems and the output of algorithms that process either the raw data or other intermediary data formats to create high-level knowledge of the sensed environment. The current fusion framework described in this paper is an extension to previous work of the authors that focused on autonomous matching of sensor systems to algorithms which in turn were assigned to missions [25-26].

<sup>1</sup><http://www.opengeospatial.org/standards/sensorml>

<sup>2</sup><http://www.opengeospatial.org/standards/om>

<sup>3</sup><http://www.opengeospatial.org/>

<sup>4</sup><http://www.w3.org/TR/2009/WD-owl2-primer-20090611/>

<sup>5</sup><http://www.w3.org/TR/rdf-primer/>



### A. Ontology and Rule Framework

The framework was implemented using Description Logic (DL) ontologies in preference to conventional relational databases because of the machine interpretable formal logic based semantics and the inference capabilities of the former. The ontology (excerpt as an UML diagram in Fig. 4) was created using TopBraid Composer<sup>6</sup>.

The *DataFusion* instance has been defined as an aggregate of exactly one or more *DataFusionComponent* instances which may be either an *Image* instance or an *AlgorithmOutput* instance. The *Image* instance is the product of a *SimpleSensorSystem* instance, which comprises a *Sensor* instance and an *Algorithm* instance. The *AlgorithmOutput* instance is the product of an *Algorithm* instance. Both the *Sensor* and *Algorithm* classes are the root of an extended hierarchy (not shown here, refer to [25] and [26]) that covers many different sensor system types, such as electromagnetic, chemical, and radar, as well as algorithmic processes, such as profile generators, visualizers, classifiers and neural networks.

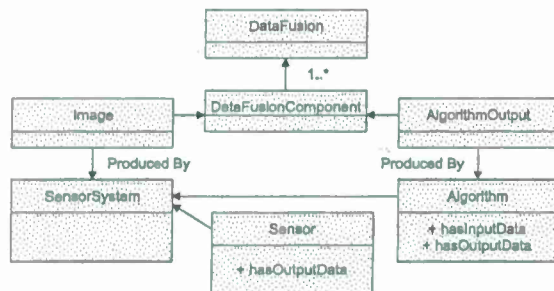


Fig. 4. Core ontology for sensor data fusion represented in UML

The philosophy behind the class diagram is explained in Figs. 5-8, by the object diagrams adjoining each of the outputs. Fig. 5 shows a simple silhouette that has been generated by a sensor system comprising a PF<sub>1</sub> sensor and a visualizing algorithm. A human user may be able to recognize this image as that of a human. In comparison, Fig. 6 shows the silhouette in addition to the output of a simple classifier algorithm, implemented by a Support Vector Machine, which classifies the image as a human with 90% certainty. Fig. 7 shows the silhouette supplemented by the output of a Bayesian classifier, which categorizes the silhouette as that of a human with 93% certainty. Lastly, Fig. 8 illustrates the fusion of the outputs of both classifiers and presents all the results together with the silhouette. The image and the classifier(s) outputs are modeled as components of the Data Fusion instance.

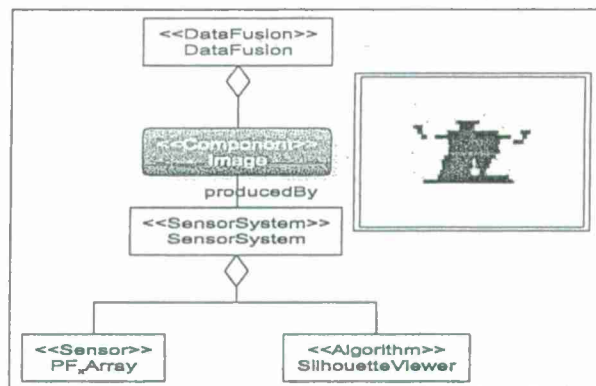


Fig. 5. An image from a sensor system

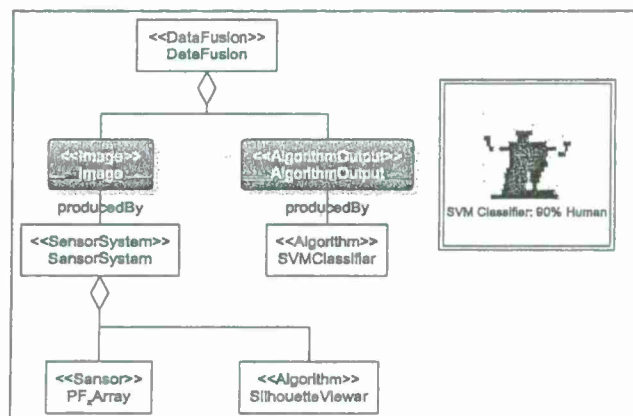


Fig. 6. Fusion of the image with the output from another component, an SVM classifier algorithm

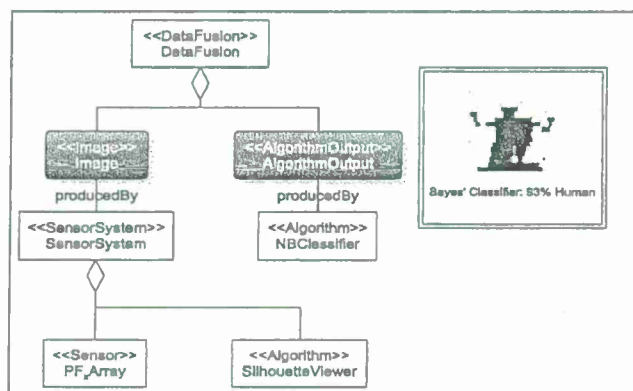


Fig. 7. Fusion of the image with the output from another component, an NB classifier algorithm

<sup>6</sup> [http://www.topquadrant.com/products/TB\\_Composer.html](http://www.topquadrant.com/products/TB_Composer.html)

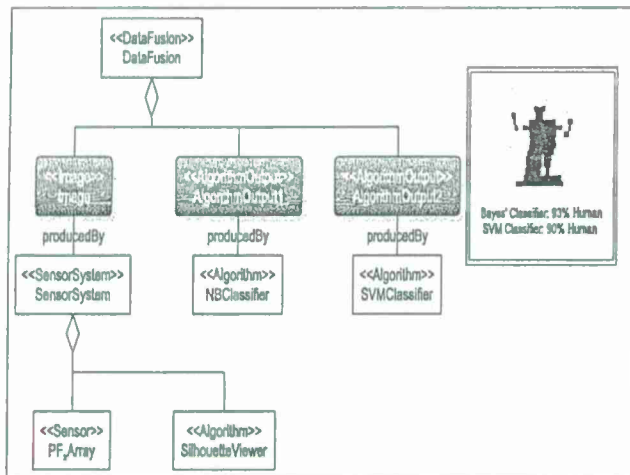


Fig. 8. Fusion of the image with the output from multiple classifiers

### B. PFx Example

We have developed an application in a persistence surveillance context to demonstrate the utility of the ontology-based framework for the fusion of data from sensor systems and algorithms. The purpose of the mission is to provide raw surveillance data with algorithmically derived profiles and classifications to a human observer in a remote location. Given the ontological definitions of the components shown in Fig. 9, the framework generated a *DataFusion* instance to detect human activity in an area under surveillance.

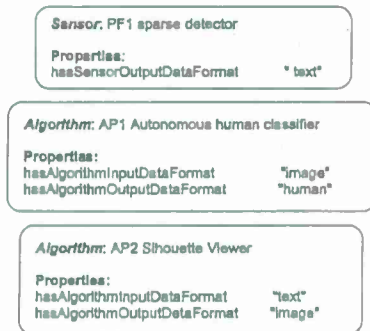


Fig. 9. Components with associated properties to be used in a surveillance mission

Fusion of data from a profiling sensor and a classifier algorithm is accomplished with a SPARQL<sup>7</sup> query. The algorithms (Java functions) are invoked using a feature, which is part of the SPARQL library, called the SPARQL Inferencing Notation (SPIN)<sup>8</sup> developed by TopQuadrant Inc. Fig. 10 shows an example of the SPARQL query that is used to generate the *DataFusion* instance that combines a profiling sensor data output to the output of a visualizer. The adjoining object diagram illustrates the ontology instantiation in the CONSTRUCT query.

<sup>7</sup> <http://www.w3.org/TR/rdf-sparql-query/>

<sup>8</sup> <http://spinrdf.org/>

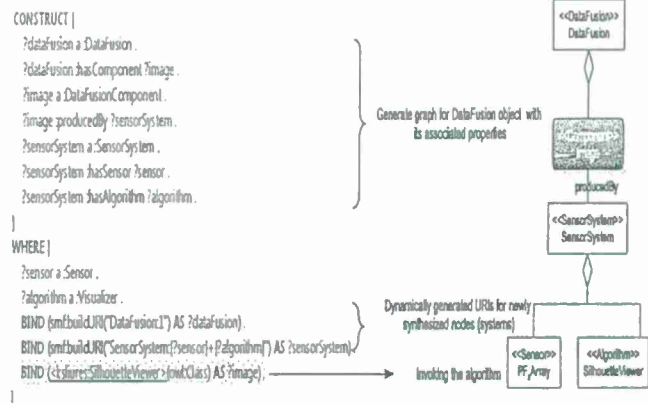


Fig. 10. SPARQL query for invoking an algorithm

In the query, the BIND clause in the last highlighted line contains the invocation to a Java class, which is wrapped as <http://ksl.engr.iupui.edu/resource#SilhouetteViewer> (aliased as `ksliures:SilhouetteViewer`), an RDF resource.

The coupling between sensor system output and algorithm inputs is based upon compatible data formats. Datatype properties such as *hasAlgorithmInputDataFormat* and *hasSensorOutputDataFormat* map the specific component to an enumeration of string literals such as "Text\_Data" or "Static\_Image." To combine this output with the output from a classifier algorithm, the query in Fig. 10 can be extended to add an invocation to a classifier algorithm as shown in Fig. 11. The new invocation has been highlighted in grey in the figure. Note the new component that has been added to the *DataFusion* instance in the object diagram.

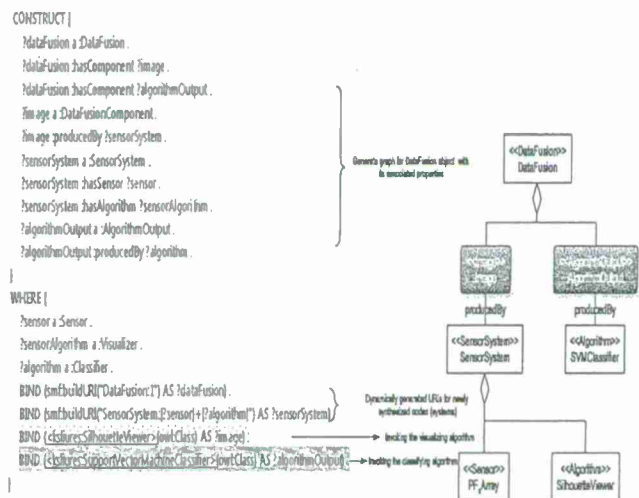


Fig. 11. Extending the SPARQL query in Fig. 11.

#### IV. DISCUSSION

We have presented a simple ontology-based framework which fuses data from multiple sources enabling situation awareness for a human operator. There are two important points to emphasize. First, the ontological framework may facilitate resource control. By having a human operator verify the human activity detected by the sensor systems and algorithmic processes, appropriate decisions can be made in response to the sensed event. The human operator helps the framework avoid false positives from the autonomous algorithmic process, thus managing critical resources optimally, such as deploying unmanned aerial vehicles for further reconnaissance. Second, the ontological framework produces sensor fusion by fusing the two pieces of information from the profile visualizer and the autonomous classifier, which is more valuable to a human operator making decisions than just having access to one piece of information. Therefore, the presented framework is essentially a data-to-decision framework. The framework can also be extended to accommodate heterogeneous sensors, such as vibration and acoustic sensors in addition to the profiling sensors. Fig. 12 shows an extension of the data fusion concept introduced in Figs. 5–8 to include outputs from heterogeneous sensors, such as profiling sensors and vibration sensors, in combination with different classification algorithms to provide much more information about the situation. Outputs from other sensors, such as cameras and acoustic sensors (not shown here) can also be combined in this manner.

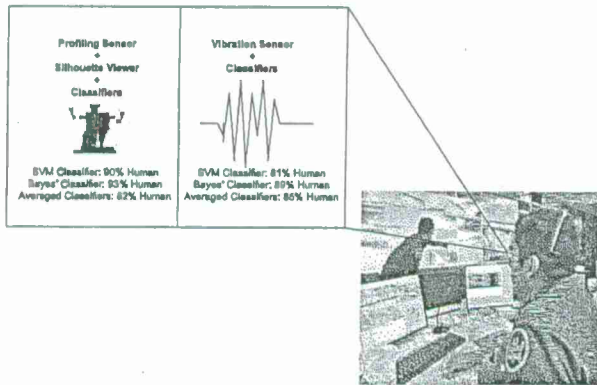


Fig. 12. Data fusion from heterogeneous sensors results in more evidence being presented to a human agent

In terms of the JDL sensor fusion model, the ontological framework performs level 1 object refinement when the *DataFusion* instance fuses the generated profiles to autonomous classifications. Level 5 cognitive refinement (user refinement) also takes place when the synthesized *DataFusion* instance fuses with a human operator's decision to verify the autonomous classification via the visualized profile.

#### V. CONCLUSIONS AND FUTURE DIRECTIONS

The ontology-based framework presented in this paper can be used to present fused information obtained from various

sources to a human observer so as to improve confidence in the perceived situation. Sensor systems can be tasked, algorithms can be dynamically invoked from this framework, and the output data can be assimilated and presented to a human agent enabling situation awareness and appropriate decision making.

A shortcoming of the current framework is the necessity to explicitly specify the matching criteria for the sensor systems in the SPARQL query. Note the SPARQL query example in Fig. 10 invoking the silhouette viewer algorithm. If a classifier algorithm needed to be integrated and invoked as well, an extra constraint would have to be added in the WHERE clause and at least two other unmatched variables would need to be specified in the query. Given the inherent nesting of the sensor systems in the generated system, we are working on an interface for dynamically generating the SPARQL query from the specifications of the selected components. This interface would be the backend for a GUI-based application where each of the components would be displayed on a selection panel.

We are also investigating the use of REST services [27–28] to encapsulate the sensor systems and algorithms in a service-oriented architecture (SOA). Each component would be exposed as an endpoint interface with a specific URI. The specifications of each component would be encoded in a Semantic Web compatible format to enable discovery, invocation, and dynamic composition on an intranet or even the secure Internet.

In the future, the fusion architecture is to be expanded to accommodate multiple profiling sensors in a given area. For example, there may be  $M$  profiling sensors along a path and  $N$  different classification algorithms. The fusion architecture could be tasked to produce an output that combines and appropriately summarizes the outputs of all these components for an end user, as shown in Fig. 13. The next logical step would be to use heterogeneous sensors, such as acoustic and vibration sensors and their corresponding classifying algorithms, to enable situation awareness.

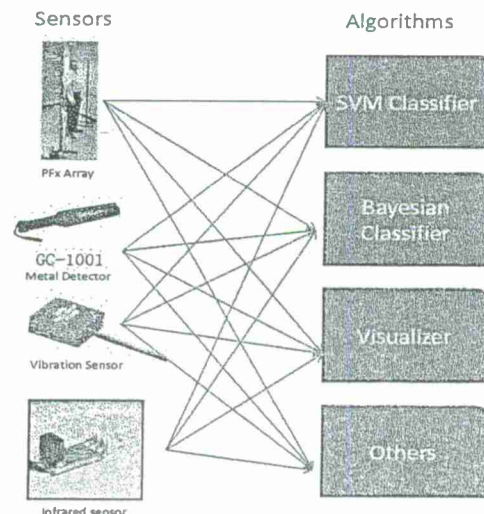


Fig. 13. Data fusion combining output from heterogeneous sensors with multiple algorithms



## ACKNOWLEDGMENTS

Funding for this work was provided in part by the U.S. Army Research Laboratory (ARL) award number: W911NF-10-2-0071, as well as support from the Purdue School of Engineering and Technology, IUPUI. The findings and opinions expressed in this paper do not necessarily reflect the views of ARL or the U.S. government.

## REFERENCES

- [1] M. Endsley, "Toward a theory of situation awareness in dynamic systems," *Human Factors* 37(1), 32–64, 1995.
- [2] A. Steinberg, C. Bowman, and F. White, "Revisions to the JDL data fusion model," *Proceedings of the SPIE 1999*, Orlando, FL, 1999. doi: 10.1117/12.341367
- [3] J. Llinas, C. Bowman, G. Rogova, A. Steinberg, E. Waltz, and F. White, "Revisions and extensions to the JDL data fusion model II," *7<sup>th</sup> International Conference on Information Fusion*, Stockholm, Sweden, pp. 1218–1230, 2004.
- [4] A. Steinberg and C. Bowman, "Rethinking the JDL data fusion levels," *MSS National Symposium on Sensor and Data Fusion*, Baltimore, MD, 2004.
- [5] E. Blasch and S. Plano, "JDL level 5 fusion model: user refinement issues and applications in group tracking," *Proceedings of the SPIE 2002*, Orlando, FL, pp. 270–270, 2002.
- [6] National Research Council (NRC), *Expanding the vision of sensor materials*, National Academy Press, Washington, DC, 2000.
- [7] F. Bergamaschi, D. Conway-Jones, C. Gibson, A. Stanford-Clark, D. Verma, S. Calo, G. Cirincione, and T. Pham, "Policy enabled ITA sensor fabric: A distributed framework for the validation of experimental algorithms using real and simulated sensors," *Proceedings of the IEEE Workshop on Policies for Distributed Systems and Networks*, Washington DC, IEEE Computer Society, 2008. pp. 241–242.
- [8] M. Botts, G. Percival, C. Reed, and J. Davidson, "OGC Sensor Web Enablement: Overview and High Level Architecture," *Proceedings of the 5<sup>th</sup> International ISCRAM Conference*, Washington DC, 2008.
- [9] T. Berners-Lee, J. Hendler and O. Lassila, "The Semantic Web: A new form of web content that is meaningful to computers will unleash a revolution of new possibilities," *Scientific American*, May 2001. pp. 34–43.
- [10] D. Russomanno, C. Kothari and O. Thomas, "Building a sensor ontology: A practical approach leveraging ISO and OGC models," *Proceedings of the 2005 International Conference on Artificial Intelligence*, Las Vegas, NV, 2005. pp. 637–643.
- [11] P. Barnaghi, S. Meissner, M. Presser, and K. Moessner, "Sense and sens'ability: Semantic data modeling for sensor networks," *Proceedings of the International Conference on Mobile and Wireless Communications*, Santander, Spain, 2009.
- [12] D. Russomanno, S. Chari, E. Jacobs, and C. Halford, "Near-IR sparse detector sensor for intelligent electronic fence applications," *IEEE Sensors Journal*, Vol. 10, No. 6, pp. 1106–1107, April 2010.
- [13] I. Rish, "An empirical study of the naïve Bayes classifier," *Proceedings of the Workshop on Empirical Methods in Artificial Intelligence, IJCAI*, 2001.
- [14] D. Duda, P. Hart, and G. Stork, *Pattern Classification*, John Wiley and Sons. pp. 117–121, 2001.
- [15] T. Hastie, R. Tibshirani, and J. Friedman, *The Elements of Statistical Learning*, Springer. pp. 11–16, 2001.
- [16] S. Seo and K. Obermayer, "Soft Learning Vector Quantization," *Neural Computing*, 15:1589–1604, 2003.
- [17] S. Theodoridis and K. Koutroumbas, *Pattern Recognition*. Academic Press. pp. 96–104, 2007.
- [18] S. Chari, C. Halford, and E. Jacobs, "Human target identification and automated shape based target recognition algorithms using target silhouette," *Proceedings of SPIE 2008, Infrared Imaging Systems: Design, Analysis, Modeling, and Testing*, Orlando, FL. Proc. 6941. pp. 69410B–69410B-9, April, 2008.
- [19] S. Chari, C. Halford, E. Jacobs, F. Smith, J. Brown, and D. Russomanno, "Classification of humans and animals using an infrared profiling sensor," *Proceedings of SPIE 2009, Unattended Ground, Sea, and Air Sensor Technologies and Applications XI*. Orlando, FL. Proc. 7333. pp. 733310–733310-9, April, 2009.
- [20] E. Jacobs, S. Chari, D. Russomanno, and C. Halford, "Profiling sensors for border and perimeter security," *SPIE Newsroom*, Bellingham, WA, August, 2009.
- [21] J. Qualls, D. Russomanno, and V. Bollu, "Integration of a profiling sensor onto sensor fabric," *Proceedings of the 2010 International Conference on Information and Knowledge Engineering*, Las Vegas, NV. pp. 250–254, July, 2010.
- [22] D. Russomanno, M. Yeasin, E. Jacobs, M. Smith, and S. Sorower, "Sparse detector sensor: profiling experiments for broad-scale classification," *Proceedings of SPIE 2008, Unattended Ground, Sea, and Air Sensor Technologies and Applications X*. Orlando, FL. Proc. 6963. pp. 69630M–69630M11, March, 2008.
- [23] D. Russomanno, S. Chari, and C. Halford, "Sparse detector imaging sensor with two-class silhouette classification," *Sensors*, Vol. 8, No. 12, pp. 7996–8015, December 2008.
- [24] D. Russomanno, S. Chari, K. Emmanuel, E. Jacobs, and C. Halford, "Testing and evaluation of profiling sensors for perimeter security," *The ITEA Journal of Test and Evaluation*, Vol. 31, No. 3, pp. 121–130, September 2010.
- [25] J. Qualls and D. Russomanno, "Ontological Problem-Solving Framework for Dynamically Configuring Sensor Systems and Algorithms," *Sensors*, 2011; 11(3):3177–3204.
- [26] J. Qualls and D. Russomanno, "Ontological Problem-Solving Framework for Assigning Sensor Systems and Algorithms to High-Level Missions," *Sensors*. 2011; 11(9):8370–8394.
- [27] R. Fielding, "Architectural styles and the design of network based software architectures," Doctoral thesis, University of California Irvine, 2000.
- [28] L. Richardson and S. Ruby, *RESTful Web Services*. O'Reilly Media, 2007.

# Embedded real-time classifier for profiling sensors and custom detector configuration

Robert K. Reynolds<sup>1\*</sup>, S. Chari<sup>1</sup>, and D.J. Russomanno<sup>2</sup>

<sup>1</sup> Department of Electrical and Computer Engineering, University of Memphis, Memphis, TN 38152

<sup>2</sup> Department of Electrical and Computer Engineering, Purdue School of Engineering and Technology, Indiana University-Purdue University, Indianapolis, 46033

## ABSTRACT

A profiling sensor has been realized using a vertical column of sparse detectors with the sensor's optical axis configured perpendicular to the plane of the vertical column of detectors. Traditionally, detectors of the profiling sensor are placed in a sparse vertical column configuration. A subset of the detectors may be removed from the vertical column and placed at arbitrary locations along the anticipated path of the objects of interest, forming a custom detector array configuration. Objects passing through the profiling sensor's field of view have traditionally been classified via algorithms processed off-line. However, reconstruction of the object profile is impossible unless the detectors are placed at a known location relative to each other. Measuring these detector locations relative to each other can be particularly time consuming, making this process impractical for custom detector configuration in the field. This paper describes a method that can be used to determine a detector's relative location to other detectors by passing a known profile through the sensor's field of view as part of the configuration process. Real-time classification results produced by the embedded controller for a variety of objects of interest are also described in the paper.

**Keywords:** Persistent surveillance sensor, profiling sensors, embedded controller, classification, object detection, customizable sensor arrangement

## 1. INTRODUCTION

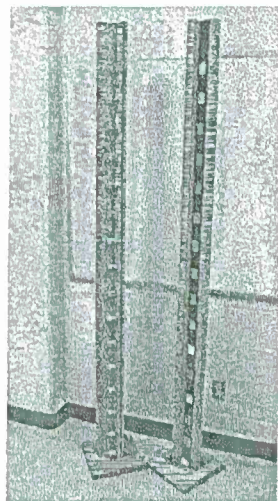
Profiling sensors encompass a family of sensor devices and configurations that are used to acquire profiles or silhouette data of objects of interest for classification purposes<sup>1</sup>. Variations include employing an array of active near-IR trip sensors, a passive pyroelectric approach<sup>2,3</sup>, as well as extracting a subset of pixels from the image of conventional imagers to emulate a sparse detector array<sup>4,5,6</sup>. Deployment scenarios for such profile sensors include border monitoring over open terrain for persistent surveillance. Profiling sensors must be able to automatically distinguish between humans and non-human objects, such as deer, rabbits, horses and other animals that reside in the area of interest. Objects are desired to be classified as either human, vehicle, or animal.

The profile sensor considered for implementation in this paper utilizes a vertically oriented column of sixteen near-IR optical trip wires (OTWs). These detectors are arranged approximately 5 inches apart from one another, forming a sparse array with their optical axes configured perpendicular to the plane of the vertical column as shown in Figure 1 (a). Each detector is coupled with its own reflector mounted on an opposing platform<sup>7,8,9</sup>. Objects that pass through the beams record the 'on' or 'off' state for each detector for a particular time sample, which is then recorded. The object profile is generated by collecting the collection of time samples in which a detector break-beam triggering event occurred, forming a silhouette of the object that passed through the beams of the array as shown in Figure 1 (b). The active IR sensing elements require that a subject pass through the beams to be detected. This requirement limits the OTW to deployments in which objects of interest must pass through a very constricted area.

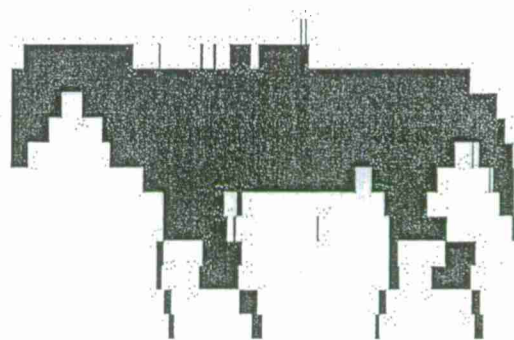
\*rkrynl@s@memphis.edu; phone 1 901 678-2175; fax 1 901 678-5469; www.eece.memphis.edu



Detectors of the profiling sensor are traditionally placed in a sparse vertical column configuration. Since no horizontal spacing exists between the sensing elements, profiles generated by the vertical column are constructed by placing the recorded time samples next to each other.



(a)



(b)

Figure 1 (a) Traditional profile sensor with vertically oriented detectors and (b) example profile of a horse generated by a profile sensor with vertically oriented detectors

Requiring a subject to pass through the sensor to obtain its profile presents a limitation that is easy to counter. If a person recognizes the sensor that is being used to monitor him/her, he/she merely needs to walk around the sensor to avoid detection. Good concealment is therefore essential. Part of the concealment may be done by breaking the vertical array apart, and distributing the detectors along an anticipated path of objects of interest; thereby, reducing the obtrusive size of the single array pole and its reflector<sup>8, 10</sup>. An alternative profiling sensor prototype design is shown in Figure 2. Note that this particular configuration is a prototype with horizontal distances of approximately 15-35 cm between detectors. Actual field implementation would place individual detectors where maximum concealment can be achieved, possibly with significantly greater horizontal separation.



Figure 2: Customized sensor array prototype

Acquiring a profile from the detector elements that are not in the same plane requires that the precise locations of the detector elements be known to synchronize timing between them. Measuring these distances by conventional techniques is particularly time-consuming, especially if the detectors are to be placed at significant horizontal distances from each other. Long setup/measurement time makes the custom configurations impractical for deployment in the field, especially when deployment time is minimal. A quick method of measuring the distance between the detectors is therefore warranted.

## 2. SIMPLE CLASSIFICATION TECHNIQUE USING CUSTOM ARRAY

A simple classifier can be implemented using the custom array by summing the 'on' and 'off' states of the detector along each row as an object passes through the sensor. The summation data along each row is treated as an independent feature and compared to training data sets of human, vehicle, or animal. The object is subsequently classified using Naïve Bayesian classifier. A leave-one-out classification study against the profile sensor's acquired sample library<sup>10</sup> revealed that this technique can obtain a 92% classification rate using Mahalanobis distance. Its ease of implementation makes it particularly appealing for a low-resource microcontroller. However, the technique fails to calculate the object's velocity or its direction of travel, both of which may provide valuable information on a passing subject. Higher-yielding classification algorithms have been developed for profiles generated by the sensor with vertically oriented detectors<sup>7,8,11</sup>. However, to utilize these algorithms, the profile must be reconstructed to appear as if it were generated by the sensor with vertically oriented detectors.

## 3. CUSTOM ARRAY PROFILE RECONSTRUCTION TECHNIQUE

Detector timing for the vertical column configuration is synchronized by the placement of the detectors along the same column, as illustrated by Figure 3. Most subjects passing through the sensor's field of view do not have a flat leading edge; therefore, their profiles will illustrate a non-straight edge. Passing a straight, vertical object through the array will cause all 16 detectors to trip simultaneously, as illustrated by Figure 4.

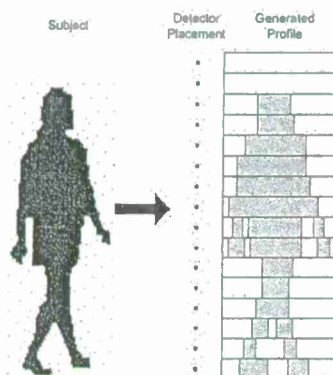


Figure 3: Subject passing through a vertical column sensor

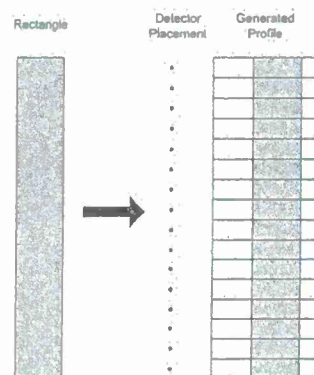


Figure 4: Vertically straight object passing through vertical array

Removing these detectors from the same column destroys the synchronization between them. Passing the straight vertical object through an array in which the detectors are not vertically co-located will create a profile in which the detector elements 'on' and 'off' times are modified by the placement of the detectors. Figure 5 illustrates the passing of a vertically straight object through a modified array. Passing this rectangular 'calibration rectangle' through the sensor is done as part of a calibration routine to define the distances between each detector pair. Since it is known that the leading edge of this rectangular object is vertically straight, the physical location of the detectors can be determined by counting the number of time samples between a detector pair's first transition state. For example, if there are  $X$  time samples

between detectors on row  $i$  and row  $j$ , then it can be assumed that the physical distance between detectors on rows  $i$  and  $j$  for subsequent samples should be offset by the same  $X$  number of time samples. The number of samples between rows is found by searching for the first transition state of each row from 'on' to 'off', corresponding to the leading edge of the passing rectangle. Similarly, the trailing edge may also be used if the calibrating vertical object has a vertical rear edge. Note that the vertical calibration rectangle must be passed through the array at a relatively constant speed to trip the detectors at their correct physical locations.

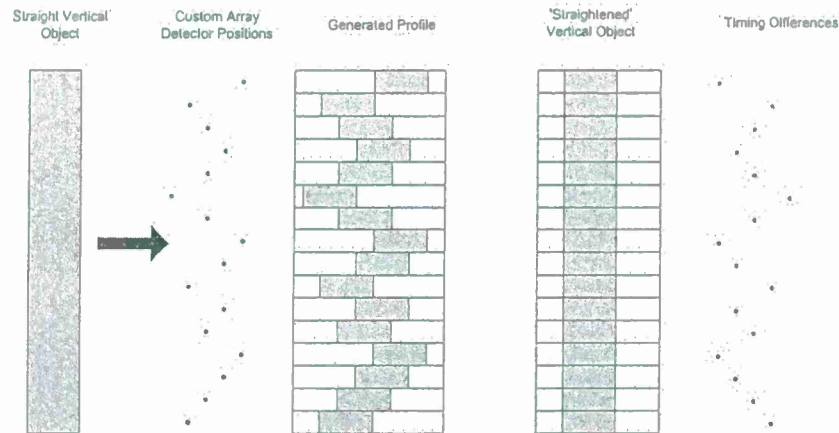


Figure 5: Vertically straight object passing through custom array

These time differences (corresponding to the positions of the individual detectors) are then subtracted from the raw timing profile of each subsequent subject passing through the array to rebuild the proper profile. Figure 6 illustrates a subject passing through the prototype custom array, raw profile generation and the subsequent reconstruction of the raw profile data to form a properly oriented profile.



Figure 6: Subject profile reconstruction after passing through custom array

#### 4. IMPLEMENTATION

Experimentation for the custom array was realized by placing the detector locations at specified heights and random locations. Detectors are placed at random horizontal locations on rows that are vertically separated 5" from each other, consistent with the 5" separation between detectors of the vertical column array profile sensor. This implementation was realized by modifying the single-column array. The single-column array is constructed of PVC pipe sections and is



designed for rapid field data collection deployment. Detectors of the single column array are paired into two-element sections for ease of alignment and to minimize the number of necessary electrical connections. The eight detector pairs are removed from the column array and placed on a section of PVC pipe to set them at their original vertical heights. Horizontal spacing is random.

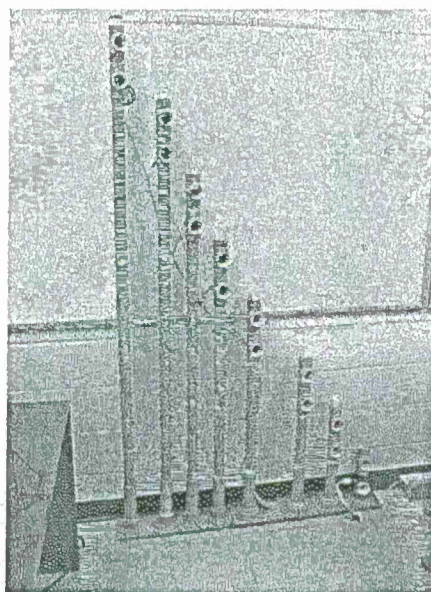
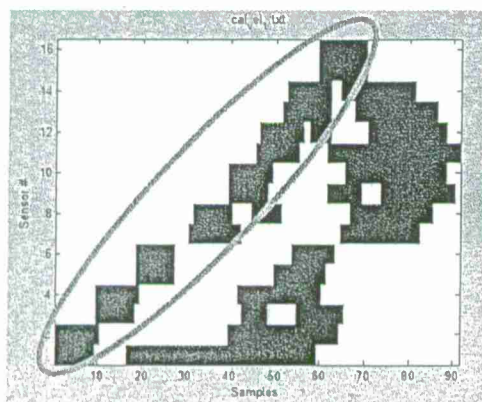
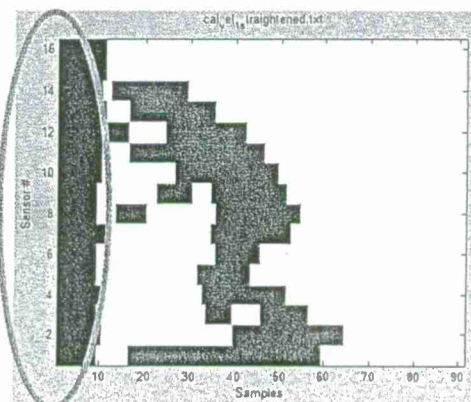


Figure 7: Custom sensor array prototype realized on PVC pipe.

Note that the detector arrangement in Figure 7 shows the detectors in a roughly diagonal pattern. Detector placements do not necessarily require such an arrangement, but may be arranged in any fashion. This particular configuration was merely chosen as an illustration for this paper and to construct the prototype in Figure 7. Also note that the element pairs do not necessarily have to lie on the same vertical plane. Detectors in Figure 7 were left paired together, due to their construction. Figure 8 (a) illustrates a human carrying a 2x4 vertically through the sensor (moving from left to right through the sensor in Figure 7) as part of a calibration routine. The calibration routine determines the first transition state of each detector and finds the time difference between the profile's first detector's trigger event and the first trigger event along each row. The profile is 'straightened' by subtracting these time differences along their respective rows, as shown in Figure 8. Note that the same 2x4 beam is shown again in Figure 8 (b) in a more recognizable format.



(a)



(b)

Figure 8: Person carrying a vertical object through the custom sensor array of Figure 7; (a) uncorrected and (b) corrected. Vertical beam is shown in oval.

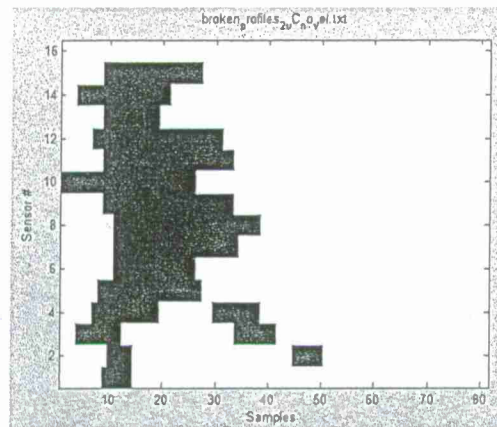
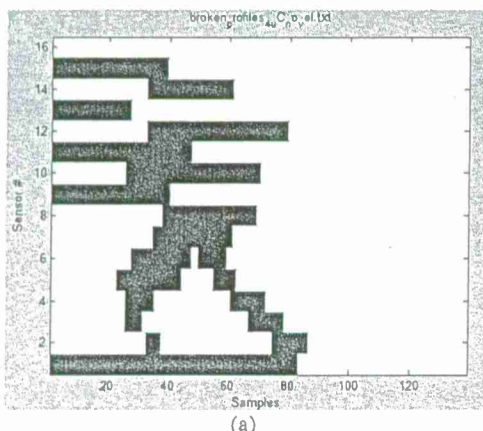


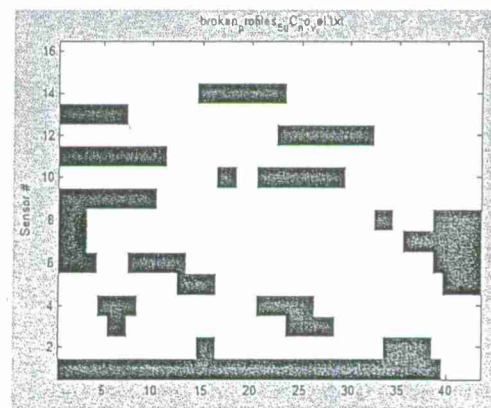
Figure 9: Reconstructed human profile collected with custom array

Subsequent data acquisitions have this same row shifting routine performed on them. Figure 9 shows the corrected profile of a person passing through the array without the 2x4 used for detector timing calibration. This technique of shifting the start position of each of the rows appears to account for the random horizontal placement of detectors. Although the array may be placed in any customized configuration, the specific detector locations must remain fixed after the calibration routine is executed. If the array is modified, the calibration routine must be performed again to find the detectors' positions relative to one another.

Note that data collected from the vertical column array profile sensor consists of timing samples. A slowly travelling subject will generate a profile of greater width than if it were to pass through the sensor quickly. Thus, the number of time samples used to generate a profile alone is not an accurate measurement tool to indicate the physical width of the passing subject. Merely applying the time sample shifting to each of the rows is not an entirely accurate method of realigning a profile since subjects may pass through the array at speeds other than which the detector distances were calibrated. Since  $t = d/v$ , the amount of shift  $t$  applied to each row is a function of the detector element distances  $d$  and the velocity  $v$  of the travelling subject, not merely a count of the number of time samples between rows. Subjects with a speed  $v$ , which may be different than that of objects used in the calibration, will, therefore, have malformed rebuild profiles. Furthermore, correcting the profiles due to time only does not account for the direction of travel that a subject may take through the sensor. Travelling in the direction opposite from what the array was calibrated causes the row data to be shifted in the opposite direction as shown in Figure 10 (b). Although this technique of profile rebuilding may work appropriately if we make the assumption that subjects will always pass at the same speed, it fails when the assumption is violated. Therefore, a more robust calculation technique is required.



(a)



(b)

Figure 10: Incorrect 'corrected' arrays caused by (a) speed other than calibration speed and (b) travelling opposite direction from calibration route.



## 5. VELOCITY CALCULATION AND INCORPORATION

A more accurate method of correctly rebuilding the profiles requires that the physical distances between detectors and the actual velocity of the passing subject be determined. Using these parameters, a more accurate time shifting value may be calculated for each detector state. Timing differences between the detectors are directly proportional to the horizontal distances between them and are determined by passing a vertically oriented object through the array as described earlier. However, the distance between any one pair of detector elements must be known. Ratios of the numbers of time samples recorded between element pairs are computed. Assuming that the calibration rectangle is passed through the sensor at a relatively constant speed, the physical distances are a product of the time ratios between the detectors and the known horizontal distance between the two designated detectors. These distances are calculated several times as part of the calibration routine and averaged along each row.

A subject's velocity through the profile sensor is calculated by averaging the individual velocities  $v_{ij}$  generated between every possible detector pair along the leading and trailing edges of the profile, given by the expression

$$\text{mean velocity} = \frac{2}{M(M-1)} \sum_{\substack{i=\text{lowermost} \\ \text{detector trigger event}}}^{M-1} \sum_{j=i+1}^M v_{i,j} \quad (1)$$

where  $i \neq j$ , and  $M$  = the uppermost detector trigger event<sup>3</sup>. Velocity between each detector pair is defined as  $v_{ij} = d_{ij} / t_{ij}$  where  $d_{ij}$  is the physical distance between detectors  $i$  and  $j$ , and  $t_{ij}$  is the number of samples between the detectors  $i$  and  $j$  to the leading or trailing edge of the profile. Although seemingly computationally intense, the number of detector pair velocity calculations is limited to  $M(M-1)/2$ , where the maximum value of  $M$  is the number of detectors in the array; a maximum of only 120 possible calculations along each edge is possible for a 16 detector array. Combinations where  $t=0$  cause division by zero and are not considered. The implementation of the vertically paired sensor detectors causes horizontal pairings to have a time difference of zero, thereby eliminating those particular detector pair velocity calculations from consideration and further reducing the computational requirements of the microcontroller.

A rectangular-shaped object passing through the sensor would generate constant detector pair velocities. Upright, walking humans are mostly rectangular in shape, generating similar velocities along the horizontal detector pairings for the front and rear edges of the profile. However, not all profiles share this rectangular pattern. The overhanging head of an animal, sloped vehicle windshields, swinging arms, etc., caused by premature detector triggering, can generate abnormal detector pair velocity calculations. These particular velocities are eliminated by setting a threshold of a maximum reasonable velocity for individual calculated velocity values  $v_{ij}$ .

Once an overall subject velocity is calculated, the amount of time required to shift each row  $t_{ij}$  is calculated in samples by  $t_{ij} = d_{ij} / v$ , where  $d_{ij}$  is the physical distance between the detector elements  $i$  and  $j$  found from the calibration routine. Note that this velocity calculation is capable of generating both positive and negative values; with this data a direction of travel through the gates can be determined. Figure 11 illustrates the more properly reconstructed data of the same profiles found in Figure 10 by this more accurate technique.

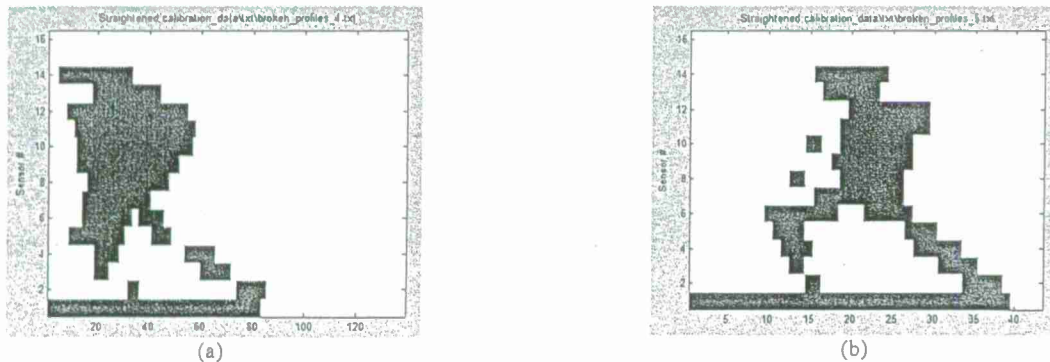


Figure 11: more accurately reconstructed profiles of Figure 10 generated by velocity incorporation.

## 6. RESULTS

The low resource microcontroller has proven to be effective at rebuilding profiles from a custom array when utilizing the passing object's velocity. Figure 12 illustrates the raw and reconstructed profiles for several objects passing through the custom array.

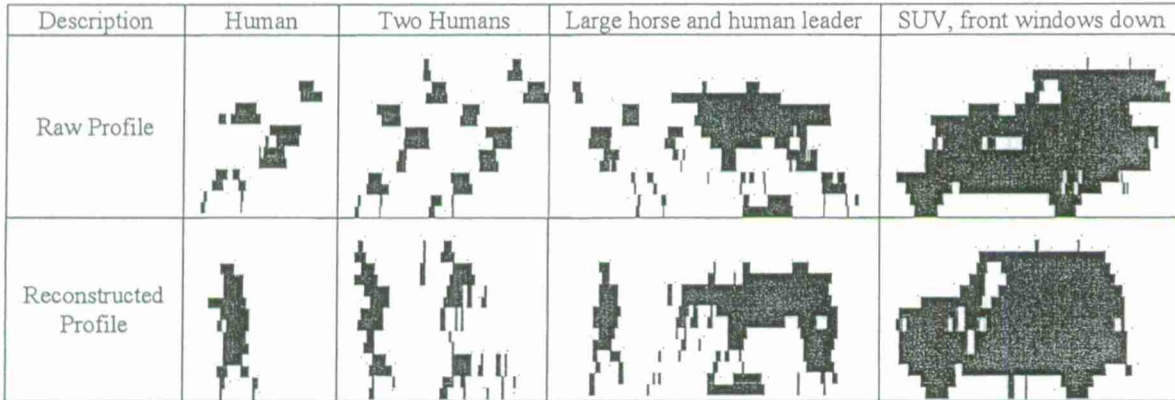


Figure 12: Raw and reconstructed profiles collected by custom array

Incorporation of velocity allows a more accurate profile width to be determined from data acquired from profiling sensors<sup>3</sup>. Classification algorithms, such as the height/width ratio and six-feature technique, are based strongly on the width of the sample<sup>3,11</sup>. Improving the determination of the width of an object will improve the overall classification of objects by profiling sensors. However, to date, there are few samples within our library of profiles<sup>10</sup> that have the physical width derived based on the subject's velocity. This "distance" library is composed of profiles of 30 humans, 32 animals, and 29 vehicles. Comparison of a distance-based width profile to the timing-based width of profiles acquired by the vertical array profile sensor is likely to lead to fallacious results. Take-one-out classification studies were performed on the data within our library utilizing the height-width ratio and six-feature techniques with 54% and 85% results, respectively. Classification confusion matrices for the two classification techniques are displayed in Tables 1a and 1b. Incorporation of a larger training set is hypothesized to increase these classification results.

Table 1a: Height/Width Feature Confusion Matrix

Height/Width Feature Classification	True Classification			
		Human	Animal	Vehicle
	Human	25	4	1
	Animal	4	5	23
	Vehicle	6	3	20

Table 1b: Six-Feature Classification Confusion Matrix

Six-Feature Classification	True Classification			
		Human	Animal	Vehicle
	Human	26	4	0
	Animal	2	28	2
	Vehicle	1	3	25

The simple technique of summing the detector 'off' states is currently utilized as a classification tool on the microcontroller until future data collection events can be performed with the custom array. Detector state events are summed and normalized by the highest number of detector events of the sixteen row features, making this technique particularly appealing: the "timing" library may be compared against the raw timing features of a subject test case. The microcontroller has yielded a real-time 85% classification rate using this feature for a wide variety of humans, vehicles, and animals during field data collection events. Classifications are made by comparing the normalized energy features along each row with a Naïve Bayesian classifier trained against the 'timing' library. These real-time classification results are displayed in the confusion matrix of Table 2:

Table 2: Real-time Row Energy Feature Classification Confusion Matrix

		True Classification		
		Human (30)	Animal (32)	Vehicle (29)
Real-time Row Energy Feature Classification	Human	25	5	0
	Animal	0	32	0
	Vehicle	1	7	21

Implementation of the calibration routine, data collection, velocity calculation, profile reconstruction, and classification algorithm has been completed on a Rabbit BL4S200 microcontroller. Thus far, the microcontroller has shown promising results when coupled to the near-IR profiling sensor array in both vertical and custom detector configurations.

## 7. CONCLUSIONS

Previous work has shown the feasibility of employing the family of profiling sensors to detect objects of interest for wide area surveillance. The focus of this paper is to demonstrate the feasibility of implementing a custom array of random detector placements with minimal setup effort. Efforts show that the system is capable of an 85% classification rate using mutually exclusive features on a sample data set. Future work involves the collection of additional samples and more rigorous testing of the custom array configuration against a more dynamic test subject set.

## REFERENCES

- [1] Sartain, R. B., "Profiling sensor for ISR applications," Proc. SPIE 6963 (2008).
- [2] Jacobs, E. L., Chari, S., Russomanno, D. J. and Halford C. E., "Profiling sensors: a new solution for border/perimeter security," SPIE Newsroom, DOI 10.1117/2.1.
- [3] Brown, J. B., Chari, S. K. and Jacobs, E. L., "Assessment of a linear pyroelectric array sensor for profile classification," Proc. SPIE 7693 (2010).
- [4] Sartain, R. B., Aliberti, K., Alexander T. and Chiu D., "Long-wave infrared profile feature extractor (PFx) Sensor," Proc. SPIE 7333 (2009).
- [5] Chari, S. K., Halford, C. E., Jacobs, E., Smith, F., Brown, J. and Russomanno, D. J., "Classification of humans and animals using and infrared profiling sensor," Proc. SPIE - Defense and Security Symposium: Unattended Ground, Sea, and Air Sensor Technologies and Applications XI, Volume 7333, Orlando, FL, pp. 7333 10-1-733310-9 (2009).
- [6] Chari, S. K., Smith, F. A., Halford C. E., Jacobs, E. and Brooks, J., "Range and velocity independent classification of humans and animals based on object silhouettes," Proc. SPIE 7694 (2010).
- [7] Yeasin, M., Russomanno, D. J., Smith, M., Sorower, M. S. and Shaik, J., "Robust classification of objects from a sparse detection sensor," Proceedings of the International Conference on Machine Learning: Models, Technologies, and Applications, CSREA Press, Las Vegas, NV, 742-748 (2007).
- [8] Russomanno, D. J., Chari, S. K. and Halford, C. E., "Sparse detector imaging sensor with two-class silhouette classification," Sensors, 8(12), pp. 7996-8015 (2008).
- [9] Russomanno, D. J., Chari, S., Emmanuel, K., Jacobs, E. and Halford, C., "Testing and Evaluation of Profiling Sensors for Perimeter Security," The ITEA Journal of Test and Evaluation, 31(1), 121-130 (2009).
- [10] Emmanuel, K., Russomanno, D. J., Jacobs, E. L., Chari, S. K. and Brown, J. B., "Silhouette Data Acquisition for a Sparse Detector Sensor," in Proceedings of Military Sensing Symposia Passive Sensors, SENSIAC (2009).
- [11] Reynolds, R. K., Russomanno, D. J., Chari, S. K. and Halford, C., "Profiling sensor classification algorithm implementation on an embedded controller," Proc. SPIE 7694 (2010).

## ACKNOWLEDGEMENTS

Funding for this work was provided in part by the U.S. Army's Research Office under award number: W911NF-10-2-0071, as well as funds from the Herff College of Engineering at the University of Memphis. This paper does not necessarily represent the position of the U.S. Government. Thanks to Jeremy Brown, Forrest Smith, Yury Tritenko, Jason Brooks, Matthew Smith, Zaher Bunni, Kenny Emmanuel, and Joseph Qualls, for their assistance with the signature collection effort and software development.

*Article*

## Ontological Problem-Solving Framework for Dynamically Configuring Sensor Systems and Algorithms

Joseph Qualls <sup>1,\*</sup> and David J. Russomanno <sup>2</sup>

<sup>1</sup> Department of Electrical and Computer Engineering, Herff College of Engineering, University of Memphis, 3720 Alumni Avenue, Memphis, TN 38152, USA

<sup>2</sup> Department of Electrical and Computer Engineering, Purdue School of Engineering and Technology, Indiana University-Purdue University Indianapolis (IUPUI), 799 W. Michigan St., Indianapolis, IN 46202, USA; E-Mail: drussoma@iupui.edu

\* Author to whom correspondence should be addressed; E-Mail: jqualls@rendermatrix.com; Tel.: +1-901-490-3717.

*Received: 7 January 2011; in revised form: 4 February 2011 / Accepted: 11 March 2011 /*

*Published: 15 March 2011*

---

**Abstract:** The deployment of ubiquitous sensor systems and algorithms has led to many challenges, such as matching sensor systems to compatible algorithms which are capable of satisfying a task. Compounding the challenges is the lack of the requisite knowledge models needed to discover sensors and algorithms and to subsequently integrate their capabilities to satisfy a specific task. A novel ontological problem-solving framework has been designed to match sensors to compatible algorithms to form synthesized systems, which are capable of satisfying a task and then assigning the synthesized systems to high-level missions. The approach designed for the ontological problem-solving framework has been instantiated in the context of a persistence surveillance prototype environment, which includes profiling sensor systems and algorithms to demonstrate proof-of-concept principles. Even though the problem-solving approach was instantiated with profiling sensor systems and algorithms, the ontological framework may be useful with other heterogeneous sensing-system environments.

**Keywords:** sensor networks; sensor ontology; profiling sensors; ontological framework

---



## 1. Introduction

Dynamically matching sensor systems to algorithms to satisfy a task poses a significant challenge in sensor networks. The challenge is made even more difficult because sensor systems and algorithms are not typically designed independently, which often limits their reuse in tasks that may not have been anticipated when the sensors and algorithms were first deployed. Compounding the challenge is the lack of knowledge and data models, which describe sensor and algorithm capabilities, properties, and relationships [1-6]. The focus of this paper is on the reasoning process used in a novel ontological problem-solving framework, which can be leveraged by software agents on sensor networks, to opportunistically match sensor systems to independently designed algorithms to form synthesized systems capable of satisfying a task.

### 1.1. Ontological Problem-Solving Framework

The ontological problem-solving framework (Figure 1) has the overall goal to discover and match sensor systems to compatible algorithms to form a synthesized system, which is capable of satisfying a given subtask. The synthesized systems and other algorithms may then be matched to form more complex synthesized systems, which may then be assigned to tasks of high-level missions (Figure 2). The ontological problem-solving framework will then coordinate all matched and synthesized sensor systems and algorithms to complete the missions. The problem-solving approach could have been developed with standard database technologies and SQL queries. However, one of the issues that makes discovering and matching sensors to algorithms problematic is the lack of knowledge models used to describe those systems.

Figure 1. Overview of ontological problem-solving framework.

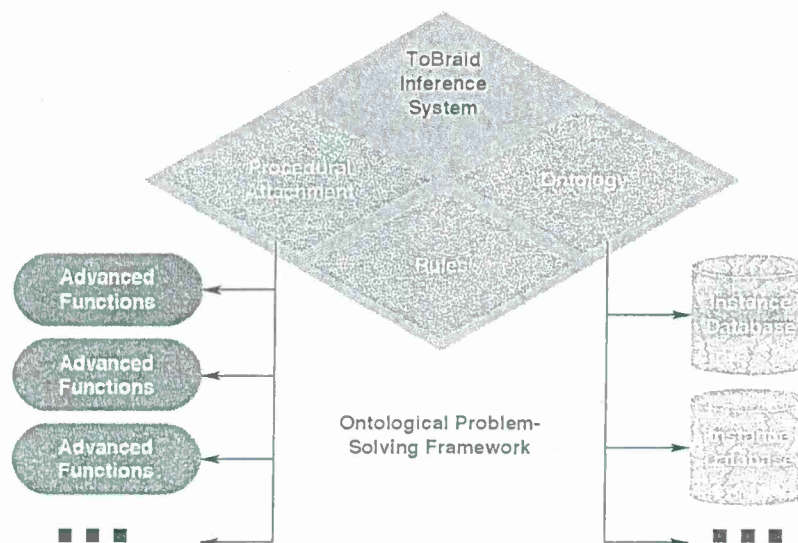
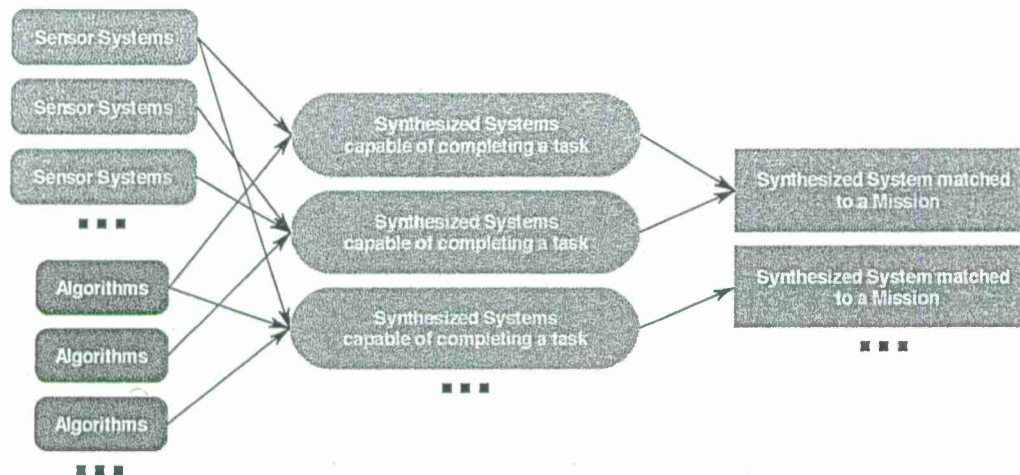


Figure 2. Creation of synthesized systems which are then assigned to subtasks of high-level missions via the ontological problem-solving framework.

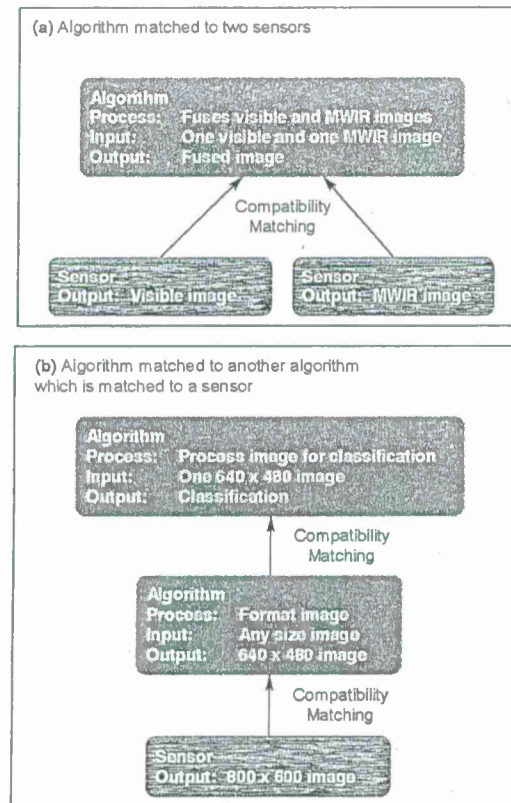


The knowledge models also need to leverage well-defined semantics in a machine-interpretable format so other agents may interact with the described systems. The requirement to opportunistically match sensors to algorithms increased the need to use ontologies (which specify the semantics) and rules based on description logic to infer which components may be used to form synthesized systems. The knowledge models used by the ontological problem-solving framework may then be leveraged by other systems for more complex inference if needed. The ontological problem-solving framework was developed using the TopBraid Maestro software by TopQuadrant [7], which uses the web ontology language (OWL) [1-6] for knowledge capture, SPARQL [8] for specifying rules, and the TopSpin inference engine for interpreting the rules. Other systems, such as Protégé, which uses JESS and SWRL [1-6], could have also been used to develop the ontological problem-solving framework. The main focus of this paper is to detail the reasoning process the ontological problem-solving framework uses to match sensor systems to compatible algorithms to form synthesized systems, which are capable of satisfying a given task.

### 1.2. Matching Sensors to Algorithms

Engineers often design an algorithm for a specific sensor system. This dependence makes the algorithm difficult to use with other sensors opportunistically based on ever-changing persistence surveillance goals. If sensors and algorithms are designed independently, then, a problem-solving approach must enable the matching of a sensor to a compatible algorithm to achieve a task, such as formatting the sensor data for a specific purpose or extracting pixels from an imaging sensor for subsequent processing. The composition of matched sensor systems and compatible algorithms to achieve a task can be made even more difficult if an algorithm requires multiple data sources (Figure 3(a)), or if a chain of multiple sensors and algorithms must be composed to achieve subtasks supporting an overall task (Figure 3(b)). The problem-solving approach must describe the relationship between the preconditions and post conditions of the algorithms, as well as descriptions of the raw data, and possibly features generated by the sensor systems [9-12].

**Figure 3.** (a) Algorithm, which requires data from two sensor systems, matched to two compatible sensor systems. (b) Algorithm matched to a compatible algorithm, which is also matched to a compatible sensor system.



### 1.3. Related Work

There have been several approaches and tools developed to address in part the challenge of matching sensors to compatible algorithms. These techniques and tools include, but are not limited to, Sensor Fabric [9,13-15], Sensor OASiS [16], Agilla [17-19], Semantic Streams and SONGS [20,21], and CIEDETS [22,23]. Other research efforts focused on the development of ontologies that describe sensors and their respective capabilities, such as OntoSensor [2-6], Sensor Network Data Ontology [24], Sensor and Data Wrapping Ontology [25], Stimulus-Sensor-Observation Ontology [26], Sensor Observation and Measurement Ontology [27], Semantic Sensor Network Ontology [28], Disaster Management Sensor Ontology [29], and a survey of sensor ontologies [30] are also efforts relevant to our work. Other work promotes a logical model to follow while developing a problem-solving approach. For example, Sensor Modeling Language (SensorML) [31] describes high-level conceptual models using Unified Modeling Language (UML) of sensors, algorithms, and supporting notions to facilitate interoperability. The Open Geospatial Consortium (OGC) specify draft interoperability interface standards and metadata encodings that integrate sensor systems into information infrastructures, such as Observations and Measurements (O&M) [32,33], SensorML [34], Transducer Model Language (TML) [35], Sensor Observation Service (SOS) [36], Sensor Planning Service (SPS) [37], Sensor Alert Service (SAS) [38], and Web Notification Services (WNS) [39]. Semantic



Streams and OntoSensor are two important efforts because of their use of semantics and ontologies. Semantic Streams and the follow up SONGS effort were developed by Microsoft to facilitate queries to determine capabilities and subsequent tasking of sensors and algorithms. Semantic Streams uses event streams, which are collected raw data from sensor systems with meta information attached, and inference units, which operate on event streams by creating semantic information about the event streams. Queries posted to Semantic Streams are broken down into one or more of the inference units (Figure 4). SONGS adds the use of an ontology to describe the inference units. Instead of queries being directly mapped to inference units, the approach can infer which inference units may satisfy a given query [20,21]. OntoSensor is a semantic-web-compatible ontology that captures knowledge about sensor systems (Figure 5(a)). OntoSensor can be used to create relationships to other sensor instances and to derive properties about sensor systems. Software agents can query the sensor instance data to determine the capabilities of connected sensor systems. Once the capabilities of the sensor systems have been determined, other agents may task the sensor systems, for example, retrieving humidity data for a specified time period (Figure 5(b)) [2-6].

Figure 4. Semantic Streams query.

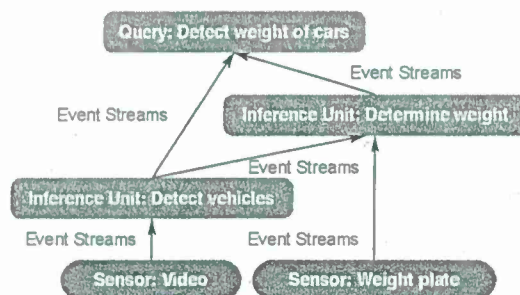
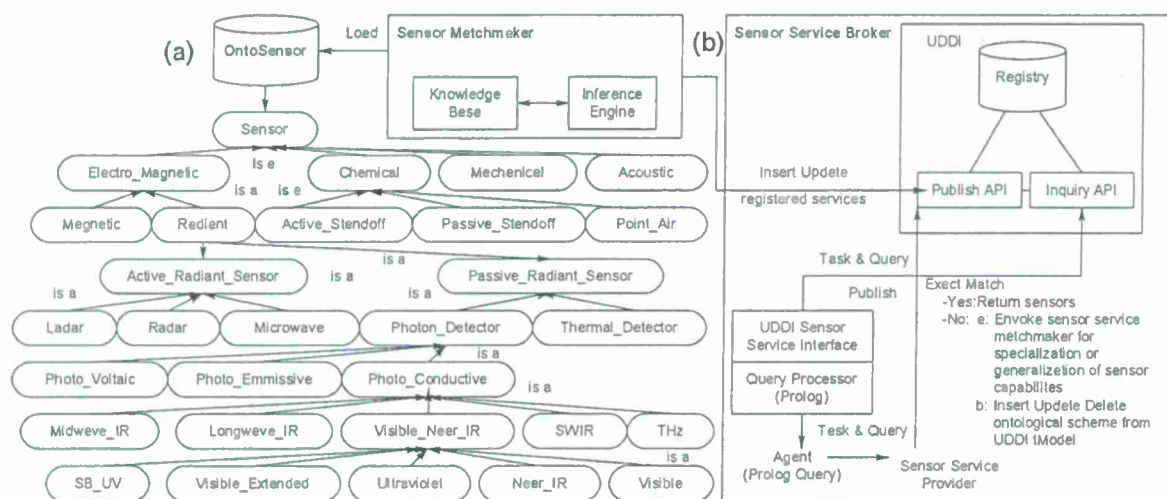


Figure 5. (a) Excerpt of the OntoSensor ontology. (b) Problem-solving for discovering and tasking sensor systems using OntoSensor.





#### 1.4. Profiling Sensor Systems and Algorithms

To show how an ontological problem-solving framework can address the challenge of matching sensor systems to compatible algorithms for a specific task, a family of unattended ground profiling sensors (denoted as PF<sub>x</sub>, in which PF<sub>1</sub>, PF<sub>2</sub>, ..., PF<sub>n</sub> are different types of profiling sensors) and algorithms were deployed in a prototype environment. PF<sub>x</sub> sensor systems provide unique opportunities for dynamic feature extraction through extendable algorithms and subsequent tasking. The main purpose of PF<sub>x</sub> sensors is to capture profiles of objects, which can be subsequently classified by algorithms using a variety of techniques, such as Naive Bayes algorithms, neural networks, or support vector machines. A common theme of all PF<sub>x</sub> sensors is that they are intended to be low cost and provide a profile that can be reliably classified. There are many different types of PF<sub>x</sub> sensors, which exploit various technologies, including a family of PF<sub>x</sub> imaging sensors, which use a sparse detector array. PF<sub>x</sub> sensors include, but are not limited to, novel imaging sensors in the visible, near infrared, short-wave infrared, mid-wave infrared, and long-wave infrared bands. One of the initial and simplest approaches to a PF<sub>x</sub> sensor was a prototype that used a sparse, vertical array of detectors. One configuration was on a vertical pole, as shown in Figure 6(a), while other configurations may include a horizontal displacement among the detectors as shown in Figures 7(a) and 8. Other algorithms may format or compress the raw sensor data produced by PF<sub>x</sub> sensors, as shown in Figure 6(b), or generate profiles into formats such that other algorithms can subsequently process the data, as shown in Figure 7(b). One example is a visualization algorithm, which may generate a silhouette of an object for presentation to a human evaluator for classification. Other algorithms that process PF<sub>x</sub> data may classify silhouettes as humans, animals, or vehicles [12,40-46].

**Figure 6.** (a) Near-IR PF<sub>x</sub> sensor with detectors vertically deployed. (b) Output from an algorithm that formats PF<sub>x</sub> sensor data. (c) Output from an algorithm that produces a silhouette from formatted PF<sub>x</sub> data.

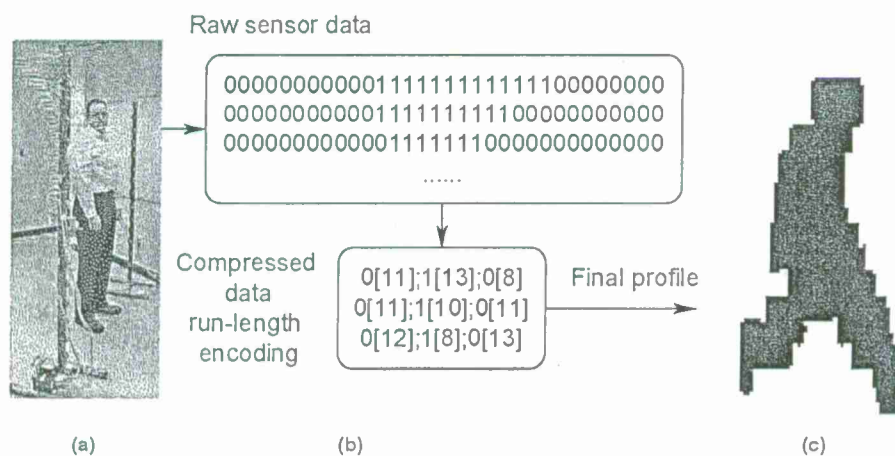


**Figure 7.** (a) PFx sensor with detectors deployed vertically with a horizontal displacement. (b) PFx raw data formatted by an algorithm as a profile.

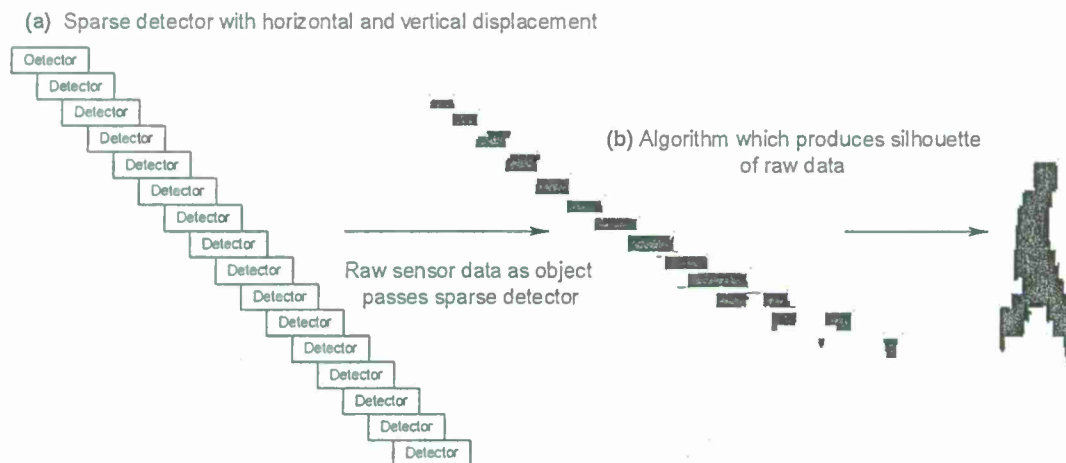
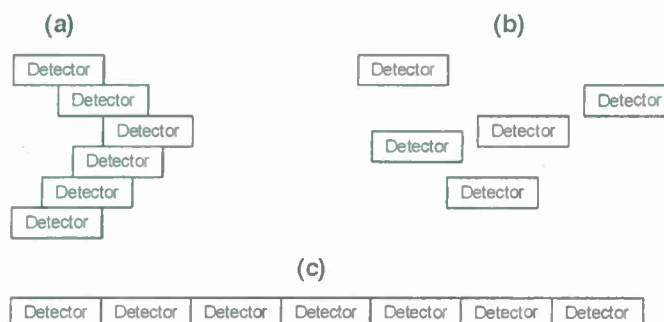
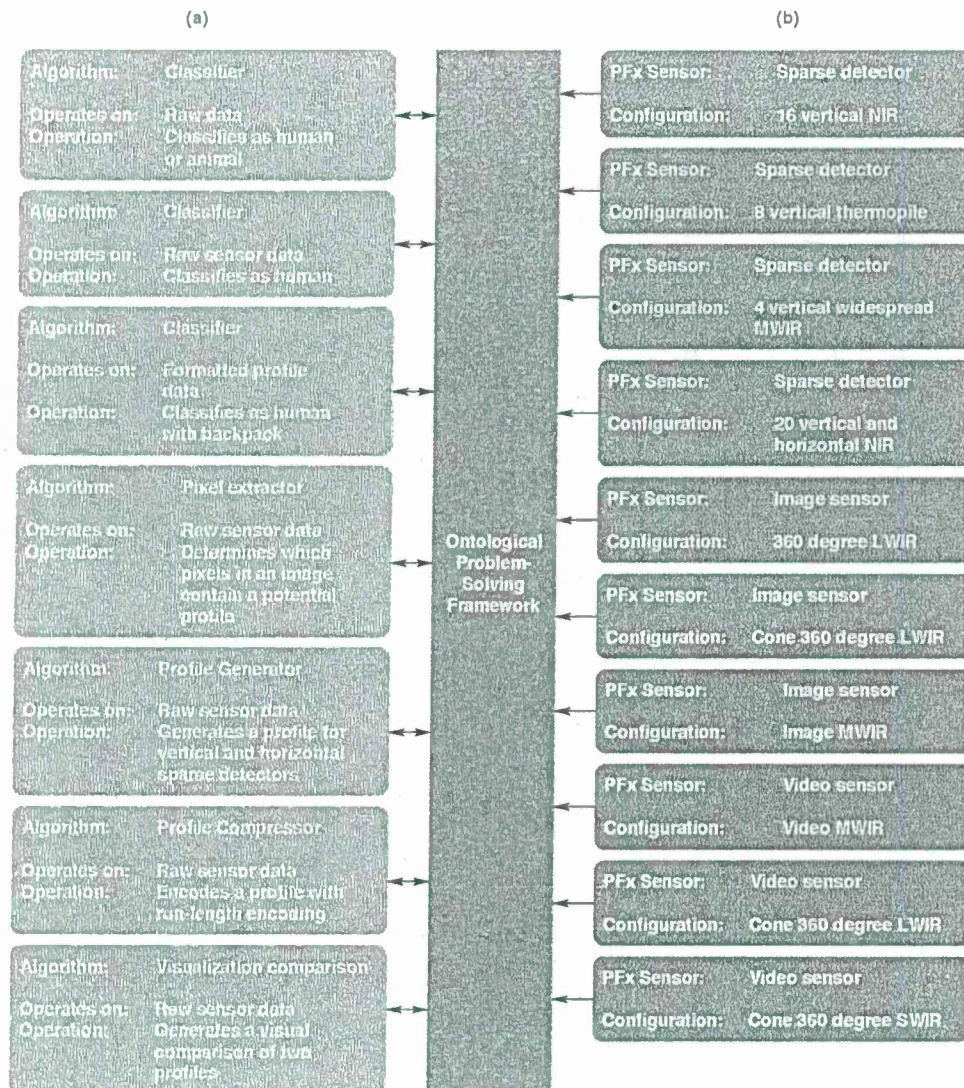


**Figure 8.** (a) PFx sensor with detectors deployed vertically with a specific horizontal displacement. (b) PFx sparse detector with random detector displacement. (c) PFx sparse detector with only horizontal displacement.



The PFx systems, with their various capabilities and relationships, represented a unique opportunity for integration onto the ontological problem-solving framework (Figure 9). The following section describes in detail the novel ontological problem-solving framework using PFx sensors and algorithms to illustrate the matching of sensor systems to independently designed algorithms for a task. The problem-solving approach will illustrate how PFx sensors are matched to compatible algorithms for pixel extraction, profile generation, visualization, and various other tasks. Even though the PFx sensors and algorithms are used for proof-of-principle aspects of the ontological problem-solving framework, the same approach may be extended for use by other types of sensors and algorithms to achieve different tasks.

Figure 9. (a) Representative algorithm types, including classifiers, visualizers, and silhouette generators. (b) Representative PFx sensor types, including sparse detectors and imagers.



## 2. Reasoning Process to Match Sensor Systems to Algorithms

The ontological problem-solving framework uses a reasoning process that leverages knowledge management techniques, such as semantic data modeling with ontologies, to address the challenge of matching sensors to compatible algorithms to form synthesized systems capable of satisfying a task. For this paper, the following definitions are used to describe sensors and algorithms. A sensor is a device that produces raw data while an algorithm uses the raw data for further processing. These definitions are similar to ones put forth by the Open Geospatial Consortium, such as defining sensors as processes and defining sensors and algorithms as services in SensorML [34]. Of note is that low-level algorithms, which may reside on the sensor hardware, are now considered as algorithms, which are not part of the physical sensor. The low-level algorithms may be device drivers or software to process the raw sensor data into a specific format. Separating the low-level algorithms from the



specific sensor systems facilitates a more flexible knowledge representation of the sensor systems and algorithms. With these definitions, meta-data, such as sensor and algorithm properties, network communications, data formats, *etc.*, must be captured to explicitly represent the relationships among sensors and algorithms. The use of models to capture knowledge about sensors and algorithms facilitates inference with rules based on description logic. The knowledge models, rules, and inference engine may then allow other agents using the reasoning process of the ontological problem-solving framework to determine the capabilities of sensors and algorithms to opportunistically discover and form synthesized systems capable of satisfying a task.

### 2.1. Ontological Relationship Structure

In this work, the descriptions of algorithms and sensors are represented in an ontology similar to the approach taken with OntoSensor and CIEDETS, which were developed by knowledge engineers with input from subject sensor matter experts. Using OntoSensor and CIEDETS ontologies as a baseline for the ontological reasoning process, the ontology needed to be extended to allow for the matching of sensors to algorithms to form synthesized systems capable of satisfying a task. The baseline ontology was extended with the following: (1) a class hierarchy for describing algorithms with descriptive properties; (2) additional properties in the sensor class for describing PFX sensors; (3) an additional class hierarchy for matching sensors to compatible algorithms; and (4) additional declarative rules.

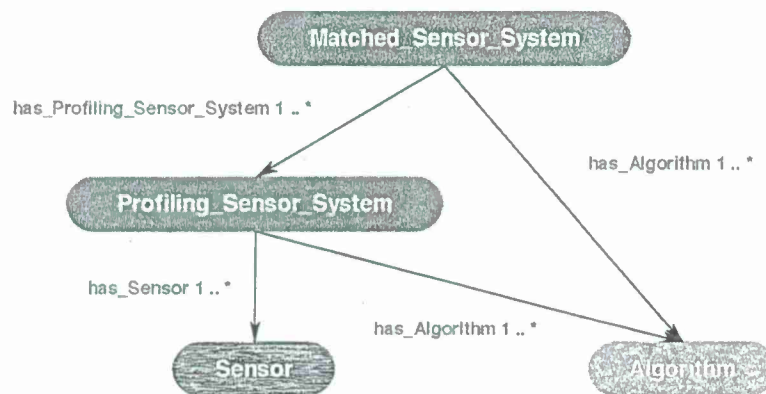
The challenge is to match sensor systems to algorithms to form synthesized systems capable of satisfying a task and then reusing those systems for other tasks. The baseline ontologies already describe sensor systems and various properties of those systems. Since the focus of the ontological problem-solving framework was to use a persistence surveillance sensing environment, properties were added to the sensor classes that describe PFX sensor systems. Generally these systems have properties, such as image resolution, geo-locations of detectors that make up a sparse detector array, and network communications. In order for a PFX sensor system to be described and represented by the ontology, these properties and others were added to various subclasses of the *Sensor* class. Algorithms were not represented by the baseline ontologies so a complete class hierarchy was added along with various attributes, such as data input/output requirements, process capabilities and purposes, descriptions of data, and network communications mapped into many different properties.

If sensor systems and algorithms are matched to perform a task, the ontology must have a way to describe this possible interoperability. This combination is not merely just a sensor and a compatible algorithm, but a combination of systems that may satisfy a given task. To describe this possible combination of systems, the concept of a synthesized system was developed and integrated into the ontology. A synthesized system is a possible combination of a sensor and compatible algorithm that may satisfy a task. When looking at various types of sensor and algorithm combinations in a persistence surveillance environment, generally, a sensor creates raw data of a passing object, a profile of the passing object is created from the raw data, and then the profile has a process applied to it, such as a classification or visualization. This is a two-step process of first generating a profile and second to process this profile. This two-step process can be represented by two different synthesized systems. The first synthesized system matches a sensor to an algorithm for the task of generating profiles, while the second synthesized system is a matching of the first synthesized system to another algorithm,



which has the task of processing the profile for some purpose. To represent the two types of synthesized systems in the ontology, two new classes were created that have object type properties that establish relationships back to established classes and properties. Figure 10 shows the core ontology for matching sensors to compatible algorithms to form synthesized systems, which are capable of satisfying a task, which is made up of four main classes: *Matched\_Sensor\_System*, *Profiling\_Sensor\_System*, *Sensor* and *Algorithm*. A bottom-up approach will be used to explain the purpose of each of the classes, their corresponding relationships, and the following section will describe the rules used to query the ontology instance data for possible synthesized systems.

**Figure 10.** Core ontology of the ontological problem-solving framework that describes the relations of the classes: *Matched\_Sensor\_System*, *Profiling\_Sensor\_System*, *Sensor* and *Algorithm*.



The *Sensor* class describes a sensing device, which generates raw data. The *Algorithm* class describes a process, which requires raw sensor data or data provided by another algorithm as input and then generates output. The *Algorithm* class can include, but is not limited to, PFx data formatters, PFx classifiers, and PFx visualizers. The *Profiling\_Sensor\_System* class is the first synthesized system concept that describes a possible combination of a *Sensor* instance and *Algorithm* instance, which produces a profile of an object in the sensor's field of view. The *Sensor* and *Algorithm* instances are linked to a *Profiling\_Sensor\_System* instance through the two object type properties called *has\_Sensor* and *has\_Algorithm*. A *Profiling\_Sensor\_System* may have many *Algorithm* instances processing the sensor data. For example, one algorithm may extract specific pixels from a raw image while another algorithm generates a profile of the extracted pixels, thus, a chain of algorithms and sensors may be matched in a *Profiling\_Sensor\_System*. The *Matched\_Sensor\_System* class is the second synthesized system concept that describes a possible combination of a *Profiling\_Sensor\_System* instance and *Algorithm* instance, which produces a result, such as a visualization or classification of the profile. The instances *Profiling\_Sensor\_System* and *Algorithm* are linked to a *Matched\_Sensor\_System* instance through the object type property *has\_Profiling\_Sensor\_System* and *has\_Algorithm*. A *Matched\_Sensor\_System* may have many algorithms processing the profile from the *Profiling\_Sensor\_System* instance. For example, one algorithm may convert the profile to a new format, while another algorithm operates on the new profile to generate a classification.

Figure 11. Extended class hierarchy of the ontological problem-solving framework for the *Sensor* and *Algorithm* classes.

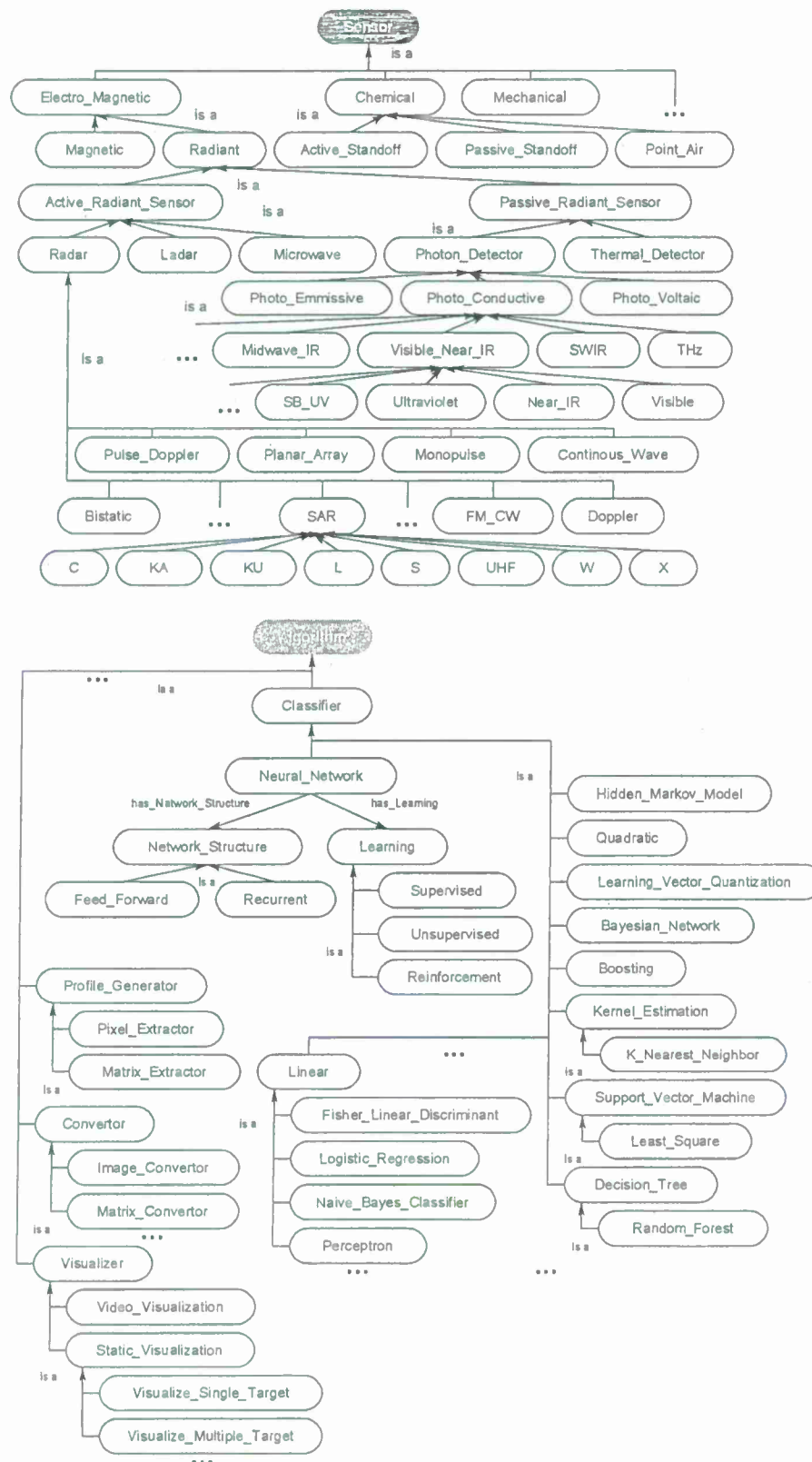


Figure 12. Excerpt of the properties for representative classes and subclasses for the reasoning process in the ontological problem-solving framework.

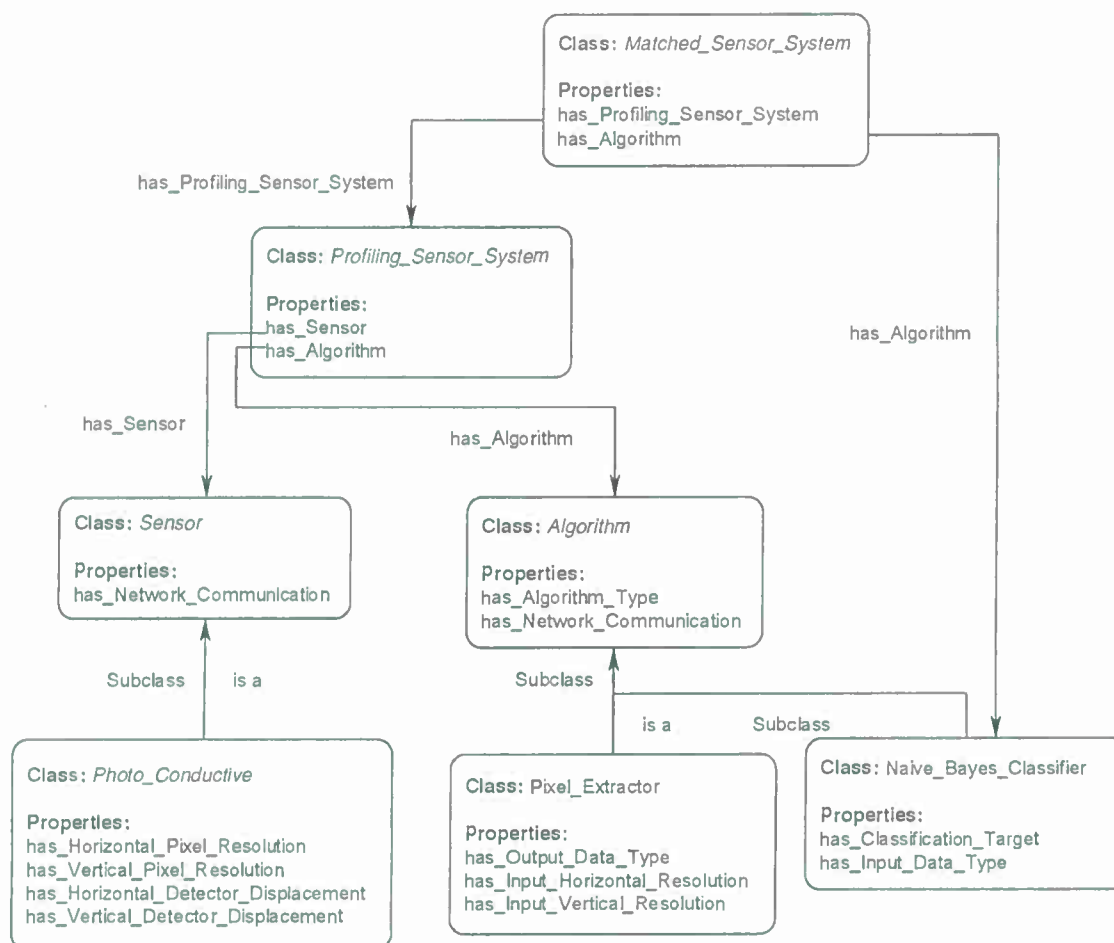


Figure 11 shows the class hierarchy of the *Sensor* and *Algorithm* classes. Each of these classes may have many properties, which are used to describe the instances. Figure 12 shows several of the properties used to describe some of the classes within the ontology. For example, the subclass *Photo\_Conductive* of the *Sensor* class has specific properties describing a sensor's pixel resolution: *has\_Horizontal\_Pixel\_Resolution* and *has\_Vertical\_Pixel\_Resolution* while also inheriting the *Sensor* class property *has\_Network\_Communication*. The subclass *Pixel\_Extractor* of class *Algorithm* has properties describing the resolution of a generated profile: *has\_Input\_Horizontal\_Resolution* and *has\_Input\_Vertical\_Resolution* while also inheriting the property *has\_Network\_Communication* from the *Algorithm* class. Similar in nature is the subclass *Naive\_Bayes\_Classifier* which inherits from the same *Algorithm* class but also adds its own unique properties such as *has\_Classification\_Target*. The *Profiling\_Sensor\_System* and *Matched\_Sensor\_System* classes also have properties, which are derived from the *Sensor* and *Algorithm* classes through rules executed during the inference process. These object and data type properties are only a few of the many describe in the ontology.

## 2.2. Ontological Rules

The graph-matching query language SPARQL [8] was used to create declarative rules for the ontological problem-solving framework. The SPARQL query language has internal functions that will allow for the querying of possible synthesized systems through an inference engine. Once the synthesized systems are returned back from the inference engine the systems can be formed into new instance data to be leveraged by other systems on the ontological problem-solving framework. The rules contain statements that consist of logical constraints among instance data and properties that must be true for subsequent instances and properties to be derived and returned as results back to the ontology. The rules are made up of two components, referred to as the WHERE and CONSTRUCT clauses. The CONSTRUCT (Figure 13(a)) clause is used to return possible object instances and properties based on instance data and properties that satisfy the WHERE clause of the SPARQL rule. The returned instances may include links to established instances (Figure 13(b,c)), as well as links to derived attributes of the returned instances. The WHERE clause contains the logical constraint statements that queried existing instances must satisfy before the CONSTRUCT clause returns the possible instances and establishes links to the pre-existing instances and properties (Figure 14). The WHERE clause constraint statements include preconditions (properties that must exist), and the other descriptive logical constraints, such as FILTER and OPTIONAL statements, that existing queried instances must satisfy before possible instances and properties are returned by the CONSTRUCT clause. Each rule can be regarded as a Horn clause in that each condition is specified in the rule via logical conjunction (logical AND). If all the properties hold true then the specified instance is returned by the rule. Logical disjunction (*i.e.*, logical OR) can be regarded as a collection of rules that create a similar instance, for example, a collection of rules that each bind on different properties which return instances of a *Profiling\_Sensor\_System*.

**Figure 13.** SPARQL CONSTRUCT clause (a) Returned *Matched\_Sensor\_System* instance, *Instance\_Matched\_Sensor\_System*, linked to *Sensor* and *Algorithm* instances. (b) *Instance\_Sensor* and (c) *Instance\_Algorithm* variables instantiated to specific *Sensor* and *Algorithm* instances in the WHERE clause, thereby establishing a link between a matched *Sensor* instance and an *Algorithm* instance. (d) Instance diagram.

```

CONSTRUCT{
  Instance_Matched_Sensor_System a           Matched_Sensor_System      (a)
  Instance_Matched_Sensor_System has_Sensor  ?Instance_Sensor          (b)
  Instance_Matched_Sensor_System has_Algorithm ?Instance_Algorithm      (c)
}

```

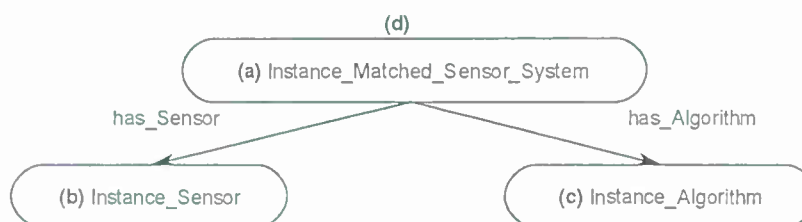
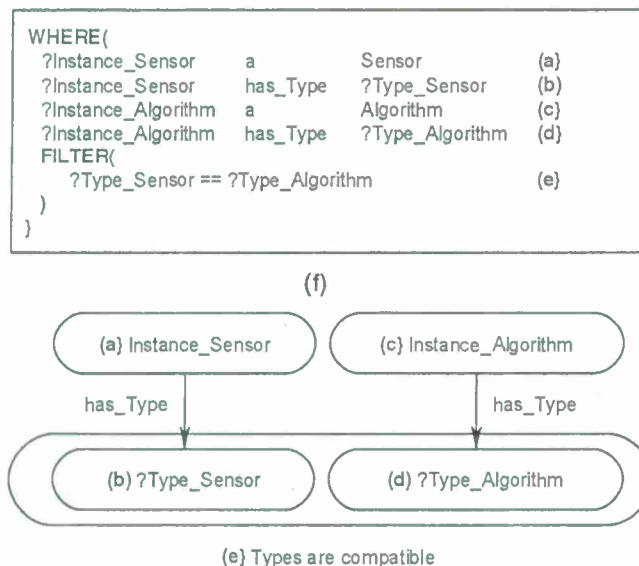


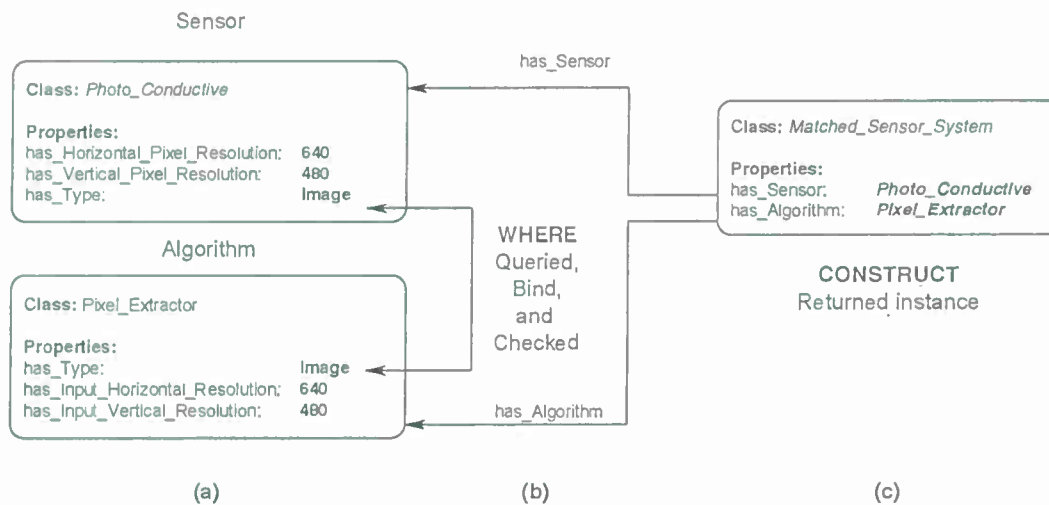


**Figure 14.** SPARQL WHERE clause (a) The variable *Instance\_Sensor* instantiated to an instance of the class *Sensor* with the data property (b) *has\_Type* established to the variable *Type\_Sensor*. (c) The variable *Instance\_Algorithm* instantiated to an instance of the class *Algorithm* with the data property (d) *has\_Type* established to the variable *Type\_Algorithm*. (e) FILTER command comparing *Type\_Sensor* and *Type\_Algorithm* variables for compatibility. (f) Instance diagram.



The inference engine will process the SPARQL rules for all combinations of pre-existing instances. For example, in Figure 14(a,c), these two statements result in the WHERE clause cycling through all *Sensor* and *Algorithm* instances. The statements in Figure 14(b,d) bind the property *has\_Type* value for the instances. The FILTER statement in Figure 14(e) compares the value of *has\_Type* for the *Sensor* and *Algorithm* instances. If the FILTER statement is satisfied, then, the CONSTRUCT clause is subsequently executed to return the specified instance and associated properties. For a simple example, the instance data in Figure 15 will be queried with a complete SPARQL rule with the CONSTRUCT and WHERE clauses in Figures 13 and 14. The *Photo\_Conductive* sensor instance and *Pixel\_Extractor* algorithm instance each have the property *has\_Type* with a value of "Image" (Figure 15(a)). When the complete SPARQL rule of Figures 13 and 14 is executed by the inference engine the WHERE clause will query for a possible *Sensor* and *Algorithm* instances whose property *has\_Type* are the same (Figure 15(b)). Once a possible combination has been found (*Photo\_Conductive* and *Pixel\_Extractor* in this case), the CONSTRUCT clause will be executed by the inference engine to return the possible *Matched\_Sensor\_System* instance with links back to the original *Photo\_Conductive* and *Pixel\_Extractor* instances (Figure 15(c)). The returned *Matched\_Sensor\_System* instance will then be placed into the ontology for further inference and use by other systems. Even though this is a simple example with SPARQL, with additional constructs, such as the FILTER or OPTIONAL commands, far more complex rules may be built.

**Figure 15.** Instance diagram of a SPARQL query binding on specific instance data and returning possible instances (a) Existing *Sensor* and *Algorithm* instances that have *has\_Type* values equal to “Image” (b) WHERE clause binding and checking the *has\_Type* property (c) CONSTRUCT clause returning a possible *Matched\_Sensor\_System* with established links to the found *Sensor* and *Algorithm* instances.



The rules in the ontological problem-solving framework bind on all combinations of *Sensor* and *Algorithm* instances. Their respective properties are then compared in the FILTER statements of the WHERE clause to determine which instances need to be returned and when to establish links between other instances. Figure 16 through Figure 19 each show one of many rules used to return possible *Profiling\_Sensor\_System* instances and *Matched\_Sensor\_System* instances. The WHERE clause in the *Profiling\_Sensor\_System* rules in Figures 16 and 17 bind on the properties of *Sensor* and *Algorithm* instances, such as pixel resolution in Figure 16, number of detectors in Figure 17, and type for both Figures 16 and 17. Further, in the WHERE clause, the FILTER statement now compares specific *Sensor* instance properties to the *Algorithm* instance properties. For example, in Figure 16, the FILTER statement compares the network communication type and pixel resolutions. Once a set of instances for a *Sensor* and *Algorithm* have been queried, which satisfy the constraints of the WHERE clause, the CONSTRUCT clause will then return a *Profiling\_Sensor\_System* instance and establish links to the compatible *Sensor* and *Algorithm* instances. The same process occurs in the WHERE clause in Figure 17, but instead of comparing pixel resolutions, detector properties are compared for compatibility. The rules for *Matched\_Sensor\_System* in Figures 18 and 19 follow a similar logical process as the *Profiling\_Sensor\_System* rule. The only difference between the rules, other than the specific properties of the instances, is in the FILTER statement where an additional statement constrains the WHERE clause to a specific type of *Algorithm*, in this case a “Classifier”. The rules shown in Figures 14 and 19 both return *Matched\_Sensor\_System* instances, which will classify the generated profiles of *Profiling\_Sensor\_System* instances.

Figure 16. Sample rule and instance diagram. The rule returns an instance of a *Profiling\_Sensor\_System* if the *Algorithm* instance and *Sensor* instance are type compatible with respect to the network communication and pixel resolutions properties.

```

CONSTRUCT{
  Instance_Profiling_Sensor_System    a          Profiling_Sensor_System
  Instance_Profiling_Sensor_System    has_Sensor  ?Instance_Sensor
  Instance_Profiling_Sensor_System    has_Algorithm ?Instance_Algorithm
}
WHERE{
  ?Instance_Sensor    a          Sensor
  ?Instance_Sensor    has_Type    ?Sensor_Type
  ?Instance_Sensor    has_Network_Communication    ?Sensor_Network
  ?Instance_Sensor    has_Vertical_Pixel_Resolution    ?Sensor_Vertical_Pixel_Resolution
  ?Instance_Sensor    has_Horizontal_Pixel_Resolution    ?Sensor_Horizontal_Pixel_Resolution

  ?Instance_Algorithm    a          Algorithm
  ?Instance_Algorithm    has_Type    ?Algorithm_Type
  ?Instance_Algorithm    has_Network_Communication    ?Algorithm_Network
  ?Instance_Algorithm    has_Input_Vertical_Pixel_Resolution    ?Algorithm_Vertical_Pixel_Resolution
  ?Instance_Algorithm    has_Input_Horizontal_Pixel_Resolution    ?Algorithm_Horizontal_Pixel_Resolution

  FILTER(
    ?Sensor_Network == ?Algorithm_Network
    ?Sensor_Type == ?Algorithm_Type
    ?Sensor_Vertical_Pixel_Resolution == ?Algorithm_Vertical_Pixel_Resolution
    ?Sensor_Horizontal_Pixel_Resolution == ?Algorithm_Horizontal_Pixel_Resolution
  )
}

```

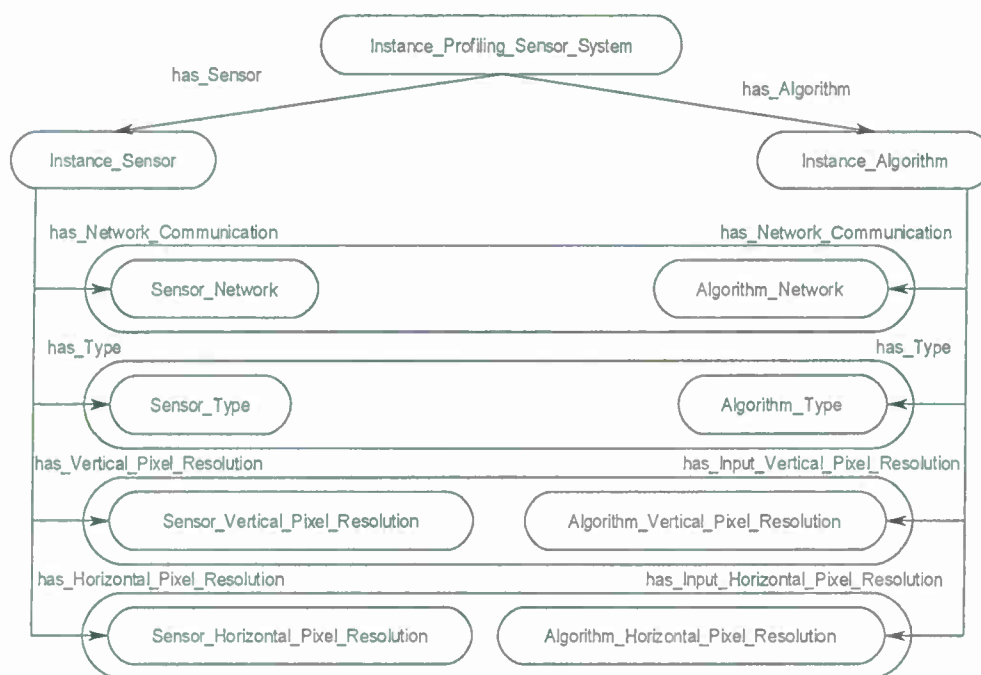


Figure 17. Sample *Profiling\_Sensor\_System* rule and instance diagram. The rule returns an instance if the *Algorithm* instance and *Sensor* instance properties: type, network communication, number of detectors, and displacement properties are compatible.

```

CONSTRUCT{
  Instance_Profiling_Sensor_System    a          Profiling_Sensor_System
  Instance_Profiling_Sensor_System    has_Sensor  ?Instance_Sensor
  Instance_Profiling_Sensor_System    has_Algorithm ?Instance_Algorithm
}WHERE{
  ?Instance_Sensor    a          Sensor
  ?Instance_Sensor    has_Type    ?Sensor_Type
  ?Instance_Sensor    has_Network_Communication ?Sensor_Network
  ?Instance_Sensor    has_Number_Vertical_Detectors ?Sensor_Number_Vertical_Detectors
  ?Instance_Sensor    has_Number_Horizontal_Detectors ?Sensor_Number_Horizontal_Detectors
  ?Instance_Sensor    has_Vertical_Detector_Displacement ?Sensor_Vertical_Detector_Displacement
  ?Instance_Sensor    has_Horizontal_Detector_Displacement ?Sensor_Horizontal_Detector_Displacement
  ?Instance_Algorithm a          Algorithm
  ?Instance_Algorithm has_Type    ?Algorithm_Type
  ?Instance_Algorithm has_Network_Communication ?Algorithm_Network
  ?Instance_Algorithm has_Input_Number_Vertical_Detectors ?Algorithm_Number_Vertical_Detectors
  ?Instance_Algorithm has_Input_Number_Horizontal_Detectors ?Algorithm_Number_Horizontal_Detectors
  ?Instance_Algorithm has_Input_Vertical_Detector_Displacement ?Algorithm_Vertical_Detector_Displacement
  ?Instance_Algorithm has_Input_Horizontal_Detector_Displacement ?Algorithm_Horizontal_Detector_Displacement
  FILTER(
    ?Sensor_Network == ?Algorithm_Network
    ?Sensor_Type == ?Algorithm_Type
    ?Sensor_Number_Vertical_Detectors == ?Algorithm_Number_Vertical_Detectors
    ?Sensor_Number_Horizontal_Detectors == ?Algorithm_Number_Horizontal_Detectors
    ?Sensor_Vertical_Detector_Displacement == ?Algorithm_Vertical_Detector_Displacement
    ?Sensor_Horizontal_Detector_Displacement == ?Algorithm_Horizontal_Detector_Displacement
  )
}

```

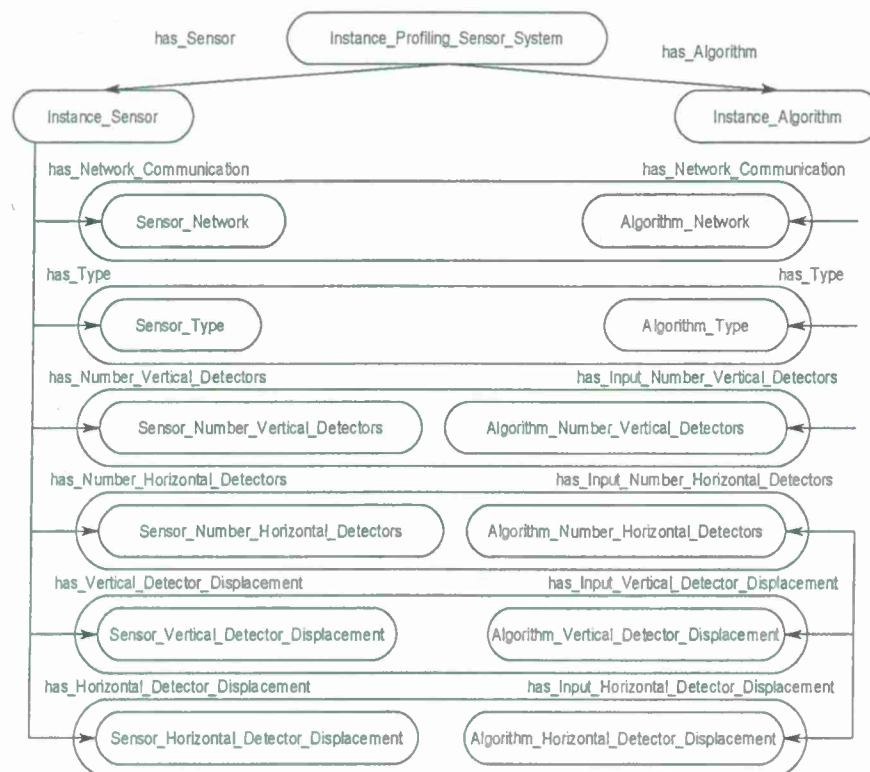




Figure 18. Sample *Matched\_Sensor\_System* rule and instance diagram. The rule returns an instance if the *Profiling\_Sensor\_System* instance and *Algorithm* instance properties: network communication, types, encoding, classification, and pixel resolutions are compatible.

```

CONSTRUCT{
  Instance_Matched_Sensor_System a
  Instance_Matched_Sensor_System has_Profiling_Sensor_System
  Instance_Matched_Sensor_System has_Algorithm
}WHERE{
  ?Instance_Profiling_Sensor_System a
  ?Instance_Profiling_Sensor_System has_Algorithm
  ?Instance_Profiling_Algorithm has_Type
  ?Instance_Profiling_Algorithm has_Profile_Type
  ?Instance_Profiling_Algorithm has_Encoding
  ?Instance_Profiling_Algorithm has_Network_Communication
  ?Instance_Profiling_Algorithm has_Vertical_Pixel_Resolution
  ?Instance_Profiling_Algorithm has_Horizontal_Pixel_Resolution
  ?Instance_Algorithm a
  ?Instance_Algorithm has_Type
  ?Instance_Algorithm has_Network_Communication
  ?Instance_Algorithm has_Operation_Ability
  ?Instance_Algorithm has_Input_Profile_Type
  ?Instance_Algorithm has_Input_Encoding
  ?Instance_Algorithm has_Input_Vertical_Pixel_Resolution
  ?Instance_Algorithm has_Input_Horizontal_Pixel_Resolution
  FILTER(
    ?Profiling_Algorithm_Network == ?Algorithm_Network
    ?Algorithm_Operation_Ability == "Classifier"
    ?Profiling_Algorithm_Type == ?Algorithm_Type
    ?Profiling_Algorithm_Profile_Type == ?Algorithm_Profile_Type
    ?Profiling_Algorithm_Encoding == ?Algorithm_Encoding
    ?Profiling_Algorithm_Vertical_Pixel_Resolution == ?Algorithm_Vertical_Pixel_Resolution
    ?Profiling_Algorithm_Horizontal_Pixel_Resolution == ?Algorithm_Horizontal_Pixel_Resolution
  )
}

```

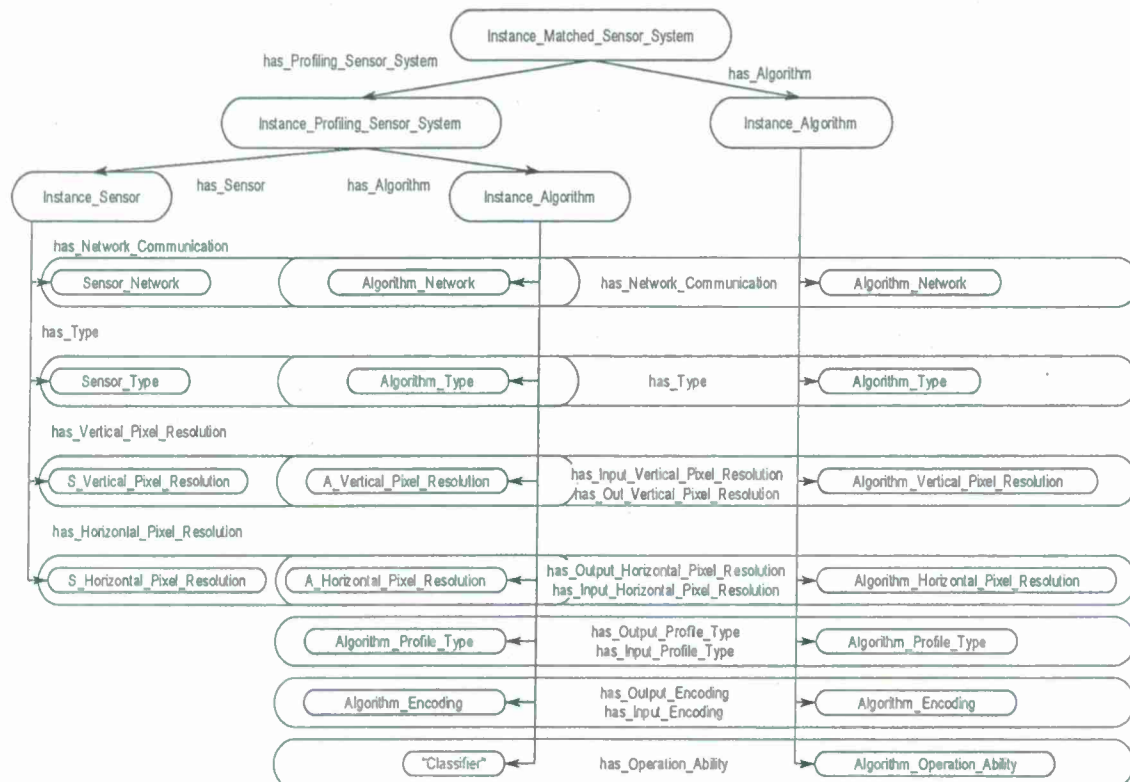
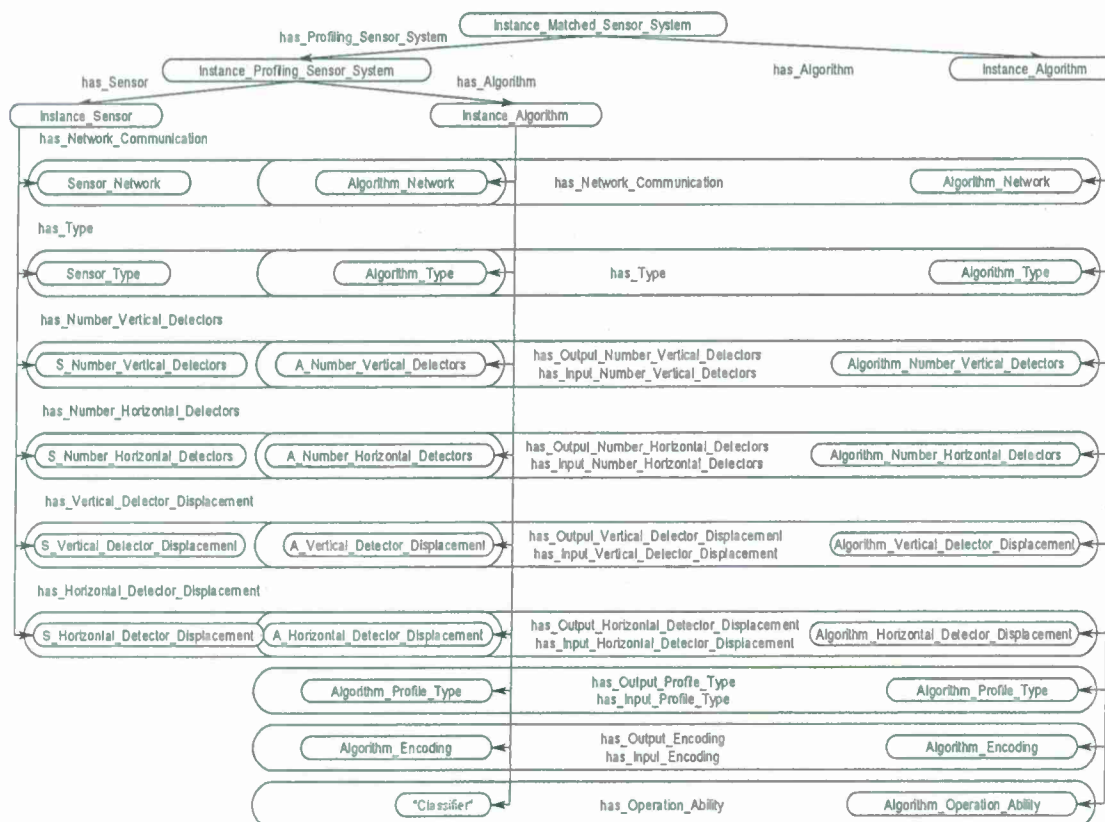


Figure 19. Sample *Matched\_Sensor\_System* rule and instance diagram, which returns an instance if the *Profiling\_Sensor\_System* instance and *Algorithm* instance properties: network communication, types, encoding, classification, data rows, and columns properties are compatible.

```

CONSTRUCT{
  Instance_Matched_Sensor_System a
  Instance_Matched_Sensor_System has_Profiling_Sensor_System
  Instance_Matched_Sensor_System has_Algorithm
}WHERE{
  ?Instance_Profiling_Sensor_System a
  ?Instance_Profiling_Sensor_System has_Algorithm
  ?Instance_Profiling_Algorithm has_Type
  ?Instance_Profiling_Algorithm has_Profile_Type
  ?Instance_Profiling_Algorithm has_Encoding
  ?Instance_Profiling_Algorithm has_Network_Communication
  ?Instance_Profiling_Algorithm has_Number_Data_Rows
  ?Instance_Profiling_Algorithm has_Number_Data_Columns
  ?Instance_Algorithm a
  ?Instance_Algorithm has_Type
  ?Instance_Algorithm has_Network_Communication
  ?Instance_Algorithm has_Operation_Ability
  ?Instance_Algorithm has_Input_Profile_Type
  ?Instance_Algorithm has_Input_Encoding
  ?Instance_Algorithm has_Input_Number_Data_Rows
  ?Instance_Algorithm has_Input_Number_Data_Columns
}FILTER{
  ?Profiling_Algorithm_Network == ?Algorithm_Network
  ?Algorithm_Operation_Ability == "Classifier"
  ?Profiling_Algorithm_Type == ?Algorithm_Type
  ?Profiling_Algorithm_Profile_Type == ?Algorithm_Profile_Type
  ?Profiling_Algorithm_Encoding == ?Algorithm_Encoding
  ?Profiling_Algorithm_Number_Data_Rows == ?Algorithm_Number_Data_Rows
  ?Profiling_Algorithm_Number_Data_Columns == ?Algorithm_Number_Data_Columns
}
}

```



### 2.3. Instances of Profiling Sensor Systems and Algorithms on Ontological Problem-Solving Framework

To illustrate a simple case, Figure 20 shows five sensor instances, including three PFx sensors and two conventional imagers, and six algorithms, including two profile generators and four different classifiers, with different property specifications and requirements. When the inference cycle begins, the rules from Figure 16 through Figure 19 will execute. On the first pass of the inference cycle, five new *Profiling\_Sensor\_System* instances were created, as shown in Figure 21. The two algorithms Profile Image Generator and Profile Matrix Data Generator were matched to multiple sensors based on constraints of the algorithms and specifications of the sensors. For example, the *Algorithm* instance Profile Image Generator was matched to the *Sensor* instance PF<sub>5</sub> Conventional Visible Imager because the constraint of requiring image data for the Profile Image Generator was satisfied.

**Figure 20.** Example instances: (a) Three PFx sensors and two conventional imaging sensors. (b) Two profile generators and four classifiers.

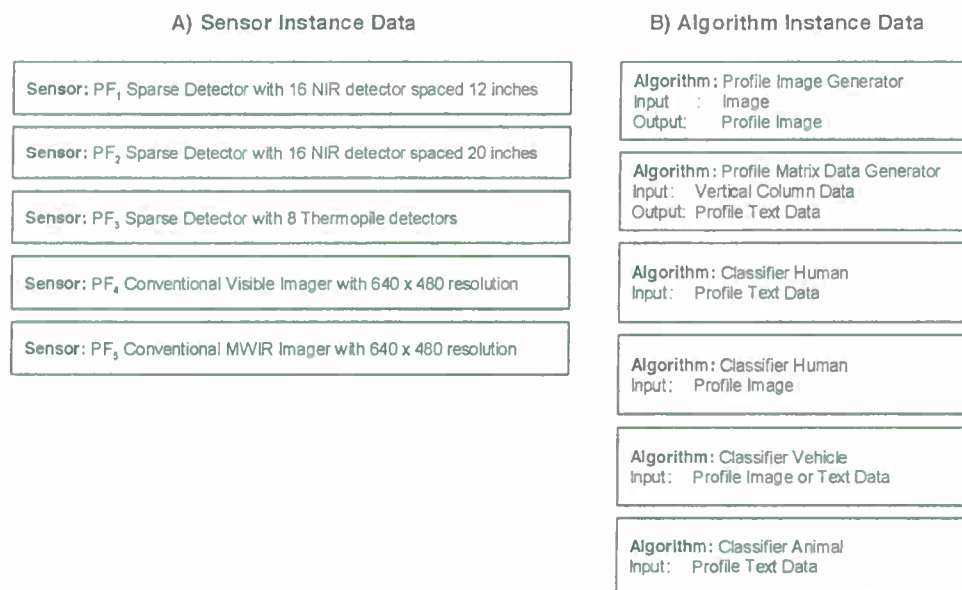


**Figure 21.** Five new *Profiling\_Sensor\_System* instances returned, with derived relationships, after the first pass of the inference cycle.

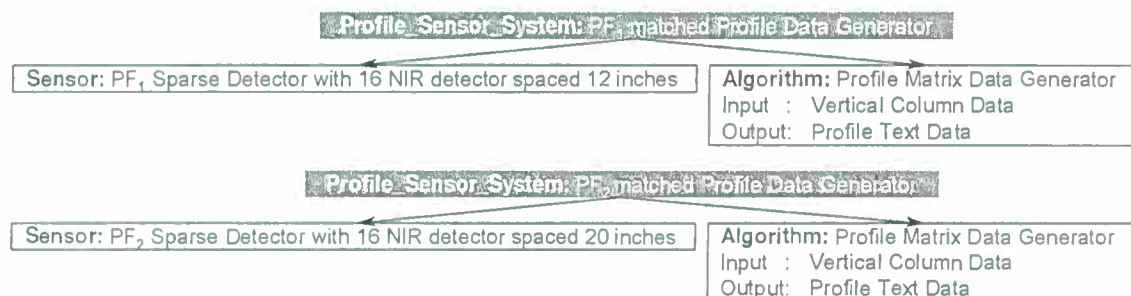
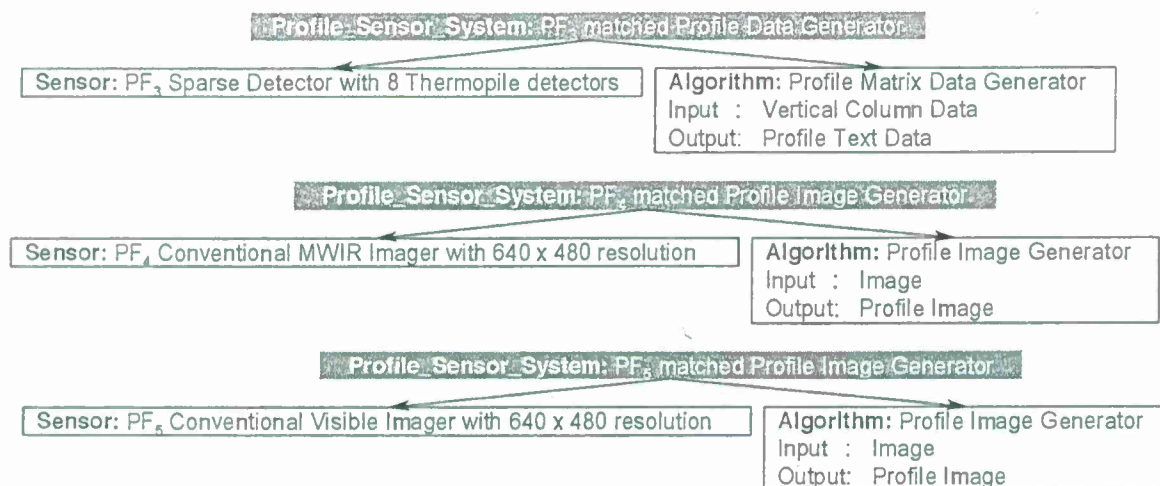


Figure 21. Cont.



During the second pass of the inference cycle, thirteen new *Matched\_Sensor\_System* instances were created, as shown in Figure 22. The four different classifiers were matched to multiple *Profiling\_Sensor\_System* instances based on the type of profile generated and the requirements of the classifiers. For example, the *Profiling\_Sensor\_System* instance PF<sub>1</sub> matched Profile Data Generator was matched to the *Algorithm* instance Human Classifier because the constraint of requiring text data was satisfied for the Human Classifier. On the third pass of the inference cycle, no new instances were created; therefore, the inference cycle halts and returns all matches.

Figure 22. Thirteen new *Matched\_Sensor\_System* instances returned, with derived relationships, after the second pass of the inference cycle.

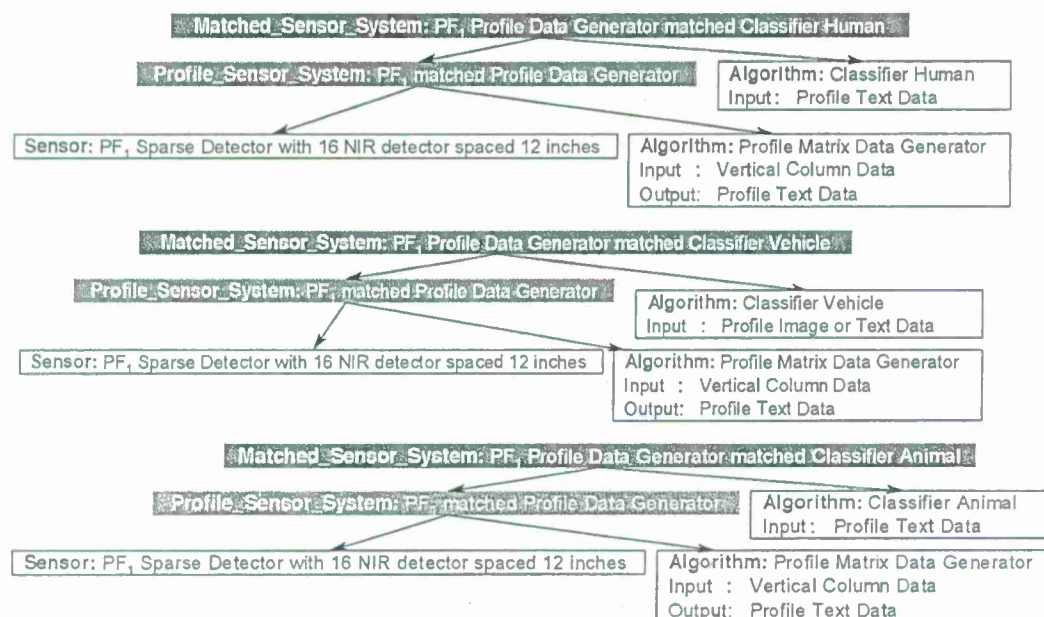




Figure 22. Cont.

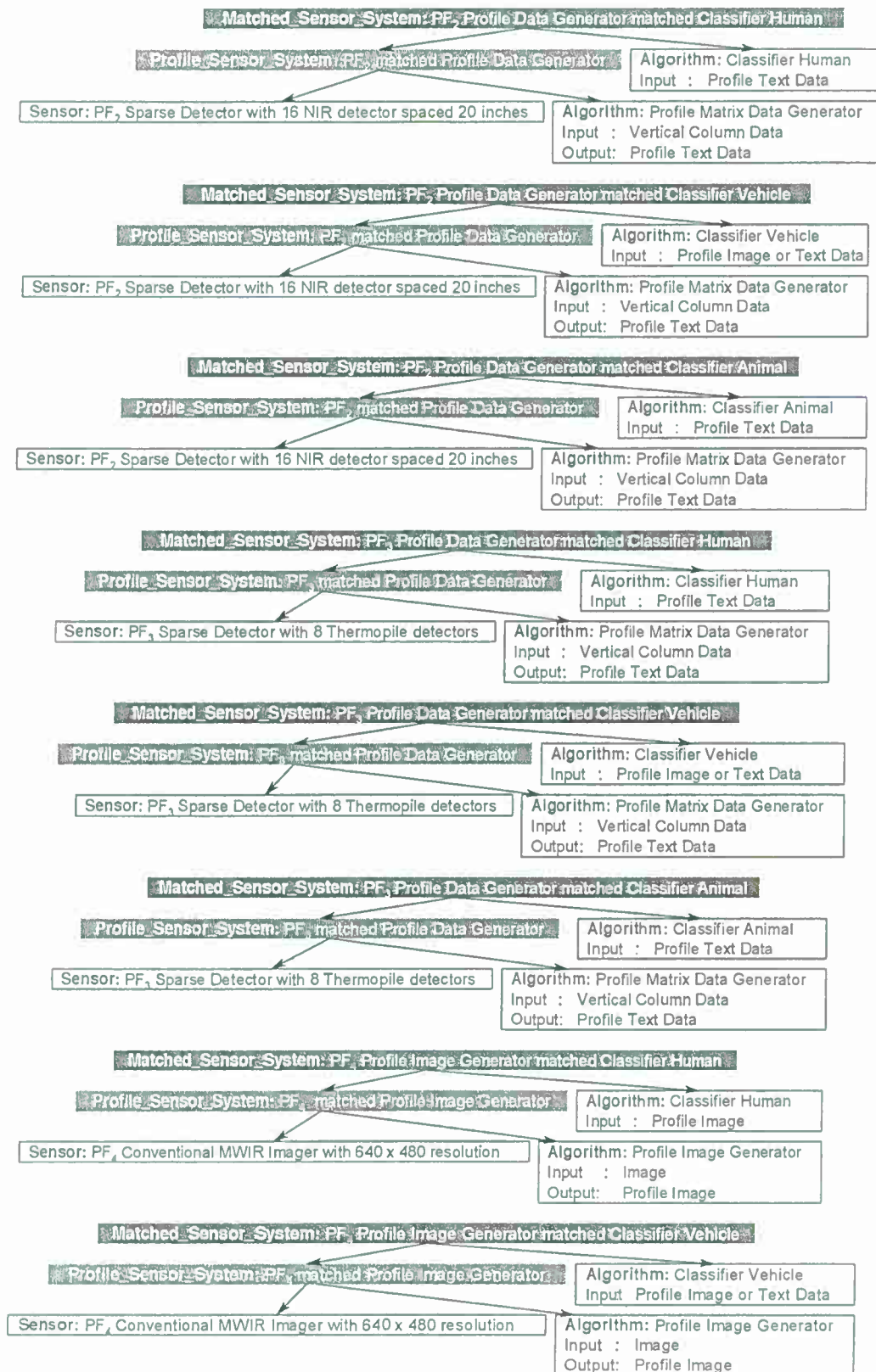
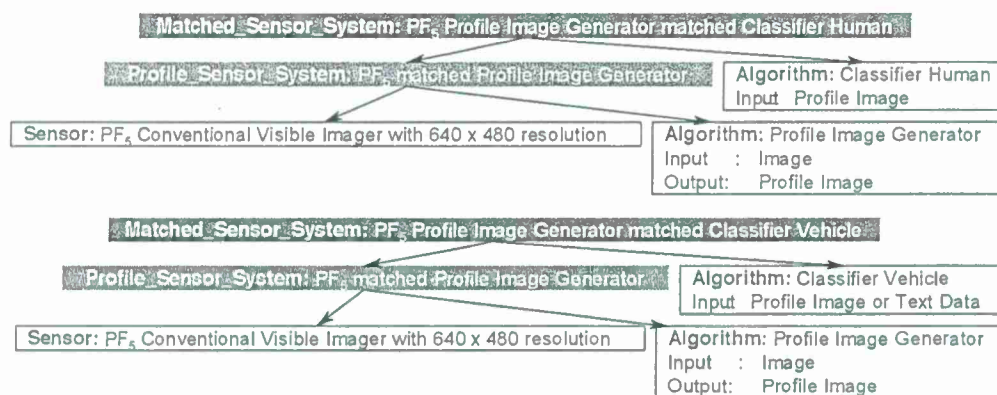


Figure 22. Cont.



### 3. Discussion

The challenge was to match sensor systems to compatible algorithms to form synthesized systems, which are capable of satisfying a task and matching those systems to new systems for other tasks. The sample rules described in this paper specified relatively simple compatibility constraints among sensors and algorithms. However, even with these simple rules, it is noteworthy that the *Algorithm* instances were matched to multiple *Sensor* and *Profiling\_Sensor\_System* instances thus achieving the ability to reuse those systems for tasks that may have not been anticipated at the time the sensors and algorithms were first deployed. For example, of the five synthesized system concept *Profiling\_Sensor\_System* instances that were returned, the algorithm Profile Matrix Generator was matched to three different sensor systems and the algorithm Profile Image Generator was matched to two sensor systems. If not for the matching and return of the *Profiling\_Sensor\_System* synthesized systems, each one of the matched systems would have had to be individually designed.

The same results can be seen in the synthesized system *Matched\_Sensor\_System*, which reused the five *Profiling\_Sensor\_System* synthesized systems in thirteen systems with different tasks, such as visualizing or classifying the profiles. If the original algorithms represented by the *Algorithm* instances had been designed for specific *Sensor* instances, the reasoning process of the ontological problem-solving framework would not have matched the algorithms to new sensors, thus the sensor systems and algorithms would have had to be re-engineered specifically for one another to satisfy a task. It is important to note that the synthesized system concepts *Profiling\_Sensor\_System* and *Matched\_Sensor\_System* capture more than just a *Sensor* matched to an *Algorithm*. The concept synthesized systems, represent new systems which are capable of performing a task. Other rules in the ontological problem-solving framework may operate on far more than just two attributes for establishing interoperability via matching constraints. The rules may determine that multiple matched *Profiling\_Sensor\_System* and *Matched\_Sensor\_System* instances may be formed into new more complex synthesized systems, which may be capable of satisfying more complex tasks, which may include statistical analysis on multiple profiles. With the formation of the synthesized system by the reasoning process, the ontological problem-solving framework may create more complex synthesized systems. These more complex systems may then be assigned to subtasks of high-level missions by other systems on the network coordinating and executing the mission. Without the use of the ontology,

rules, and inference engine these sensors and algorithms would have had to be designed *a priori* as a synthesized system for every new task. However, many of these new tasks are not known at the time the systems are deployed; therefore, opportunistically discovering compatible systems and dynamically creating matched synthesized systems which are capable of satisfying a new task through inference is important.

Currently, the reasoning process of the ontological problem-solving framework is still in a prototype stage so scale-up performance analysis is limited. The problem-solving framework can scale to large numbers of sensors and algorithms, but the time to compute all combinations of sensors and algorithms is based on the computational complexity of the inference engine, which is influenced in part by the reasoning strategy and the expressiveness of the knowledge representation formalism. For the performance to increase, the inference engine must check multiple algorithms in parallel or the ontological problem-solving framework must invoke the inference engine multiple times in parallel with different algorithms and keep track of which instances are being checked to stop redundant bindings. Even though the ontological problem-solving framework is still in the prototype stage, performance issues and solutions are being studied; however, the logical framework is the priority at this stage of research.

#### 4. Conclusions

Challenges, such as matching sensors to compatible algorithms that may satisfy a task, will become even more difficult with the continued development and deployment of new sensor systems and algorithms. Compounding the challenge is the lack of knowledge models used to explicitly capture the design and capabilities of sensor systems and algorithms. By leveraging knowledge models, sensor systems and algorithms can be matched together in real-time without the need to design those matched systems specifically for one another *a priori*, thus facilitating the use of these assets in new and innovative ways not originally anticipated on deployment. To exploit the power of knowledge models, algorithms must become less dependent on any given sensor data source, thus sensor systems and algorithms must describe their respective attributes and capabilities in a machine-interpretable format to allow the reasoning process to infer which systems may be matched together into more complex synthesized systems. The reasoning process of the ontological problem-solving framework discussed in this paper is the first step to achieving this goal and addressing the challenge of matching systems that are capable of satisfying a task. Even though the reasoning process of the ontological problem-solving framework was described in the context of profiling sensor systems and algorithms, the overall approach may be used for other types of sensor systems and algorithms to form different types of synthesized systems capable of satisfying new tasks.

#### Acknowledgements

Funding for this work was provided in part by the U.S. Army Research Laboratory (ARL) award number: W911NF-10-2-0071, as well as funding from the Herff Fellowship program at the University of Memphis and support from Indiana University-Purdue University, Indianapolis. The findings and opinions expressed in this paper do not necessarily reflect the views of ARL or the U.S. government.



## References

1. Bergamaschi, F.; Conway-Jones, D.; Gibson, C.; Stanford-Clark, A. A distributed test framework for validation of experimental algorithms using real and simulated sensors. In *Proceedings of the First Annual Conference of the International Technology Alliance*, Washington, DC, USA, September 2007.
2. Russomanno, D.J.; Kotari, C.; Thomas, O. Sensor ontologies: From shallow to deep models. In *Proceedings of the Thirty-Seventh Southeastern Symposium on Systems Theory*, Tuskegee, AL, USA, 20–22 March 2005.
3. Russomanno, D.J.; Kotari, C.R.; Thomas, O.A. Building a sensor ontology: A practical approach leveraging ISO and OGC models. In *Proceedings of the International Conference on Artificial Intelligence*, Las Vegas, NV, USA, June 2005.
4. Goodwin, C.; Russomanno, D.J. An ontology-based sensor network prototype environment. In *Proceedings of the Fifth International Conference on Information Processing in Sensor Networks*, Nashville, TN, USA, 19–21 April 2006.
5. Goodwin, J.C.; Russomanno, D.J.; Qualls, J. Survey of semantic extensions to UDDI: Implications for sensor services. In *Proceedings of the International Conference on Semantic Web and Web Services*, Las Vegas, NV, USA, 25–28 June 2007.
6. Goodwin, J.C.; Russomanno, D.J. Ontology integration within a service-oriented architecture for expert system applications using sensor networks. *J. Expert Syst.* **2009**, *26*, 409–432.
7. *TopBraid Composer Maestro (Version 3.3.2)*; TopQuadrant: Washington, DC, USA, 2001; Available online: <http://www.topquadrant.com/> (accessed on 7 January 2011).
8. Perez, J.; Arenas, M.; Gutierrez, C. Semantics and complexity of SPARQL. In *Proceedings of the Fifth International Semantic Web Conference*, Athens, GA, USA, 5–9 November 2006.
9. Bergamaschi, F.; Conway-Jones, D.; Gibson, C.; Stanford-Clark, A. Policy enabled ITA sensor fabric a distributed framework for the validation of experimental algorithms using real and simulated sensors. In *Proceedings of IEEE Workshop on Policies for Distributed Systems and Networks*, Palisades, NY, USA, 2–4 June 2008.
10. Gomez, M.; Preece, A.; Mel, G.D. Towards semantic matchmaking in sensor-mission assignment: Analysis of missions and means frameworks. In *Proceedings of First Annual Conference of the International Technology Alliance*, Washington, DC, USA, September 2007.
11. Preece, A.; Gomez, M.; Mel, G.D.; Vasconcelos, W.; Sleeman, D.; Colley, S.; Porta, T.L. An ontology-based approach to sensor-mission assignment. In *Proceedings of First Annual Conference of the International Technology Alliance*, Washington, DC, USA, September 2007.
12. Preece, A.; Gomez, M.; Mel, G.D.; Vasconcelos, W.; Sleeman, D.; Colley, S.; Pearson, G.; Pham, T.; Porta, T.L. Matching sensors to missions using a knowledge-based approach. In *Proceedings of SPIE: Defense Transformation and Net-Centric Systems*, Orlando, FL, USA, March 2008.
13. Qualls, J.; Russomanno, D.J.; Bollu, V.K. Integration of a profiling sensor onto sensor fabric. In *Proceedings of the International Conference on Information and Knowledge Engineering*, Las Vegas, NV, USA, 25–27 August 2010.



14. Wright, J.; Gibson, C.; Bergamaschi, F.; Marcus, K.; Pressley, R.; Verna, G.; Whips, G. A dynamic infrastructure for interconnecting disparate ISR/ISTAR assets (the ITA sensor fabric). In *Proceedings of the Twelfth International Conference of Information Fusion*, Seattle, WA, USA, March 2009.
15. Wright, J.; Gibson, C.; Bergamaschi, F.; Marcus, K.; Pham, T.; Pressley, R.; Verna, G. ITA sensor fabric. In *Proceedings of the SPIE: Unattended Ground, Sea, and Air Sensor Technologies and Applications XI*, Orlando, FL, USA, 13–17 April 2009.
16. Kushwaha, M.; Amundson, I.; Koutsoukos, X.; Neema, S.; Sztipanovits, J. OASiS: A programming framework for service-oriented sensor networks. In *Proceedings of the Second IEEE/Create-Net/ICST International Conference on Communication System Software and Middleware*, Bangalore, India, 9–11 January 2007.
17. Fok, C.L.; Roman, G.C.; Hackman, G. A light weight coordination middleware for mobile computing. In *Proceedings of the Sixth International Conference on Coordination Models and Languages*, Pisa, Italy, 24–27 February 2004.
18. Fok, C.; Roman, G.; Lu, C. Mobile agent middleware for sensor networks: An application case study. In *Proceedings of the Fourth International Symposium on Information Processing in Sensor Networks*, Los Angeles, CA, USA, 2005.
19. Fok, C.; Roman, G.; Lu, C. Rapid development and flexible deployment of adaptive wireless sensor network applications. In *Proceedings of the Twenty-Fourth International Conference on Distributed Computing Systems*, Columbus, OH, USA, 6–9 June 2005.
20. Whitehouse, K.; Zhao, F.; Liu, J. Semantic streams: A framework for composable semantic interpretation of sensor data. In *Proceedings of the Third European Workshop on Wireless Sensor Networks*, Zurich, Switzerland, 13–15 February 2006.
21. Liu, J.; Zhao, F. Towards semantic services for sensor-rich information systems. In *Proceedings of the Second IEEE/CreateNet International Workshop on Broadband Advanced Sensor Networks*, Boston, MA, USA, October 2005.
22. Franken, P.M.; Harrison, A.J.; Holton, J.J.; Macfarlan, L.; Wowczuk, Z.; Capshaw, R.W.; Russomanno, D.J. Development of an ontology-based tool to support the test and evaluation process for rapid acquisition of IED detection capabilities. *ITEA J. Test Eval.* **2009**, *30*, 300–308.
23. Russomanno, D.J.; Qualls, J.; Franken, P.; Robinson, W. Common IED exploitation target set Ontology. In *Proceedings of SPIE, Detection and Sensing of Mines, Explosive Objects, and Obscured Targets XV*, Orlando, FL, USA, 5–9 April 2010.
24. Eid, M.; Liscano, R.; El Saddik, A. A universal ontology for sensor networks data. In *Proceedings of IEEE Conference on Computational Intelligence for Measurement Systems and Applications*, Ostuni, Italy, 27–29 June 2007.
25. Sequeda, J.F.; Corcho, O.; Gómez-Pérez, A. Generating data wrapping ontologies from sensor networks: A case study. In *Proceedings of Second Semantic Sensor Network Workshop at International Semantic Web Conference*, Washington, DC, USA, 25–29 October 2009.
26. Janowicz, K.; Compton, M. The stimulus-sensor-observation ontology design pattern and its integration into the semantic sensor network ontology. In *Proceedings of the Third International Workshop on Semantic Sensor Networks*, Shanghai, China, 7–11 November 2010.

27. Kuhn, W. A functional ontology of observation and measurement. In *Proceedings of the Third International Conference on Geospatial Semantics*, Mexico City, Mexico, December 2009.
28. Neuhaus, H.; Compton, M. The semantic sensor network ontology: A generic language to describe sensor assets. In *Proceedings of AGILE Workshop on Challenges in Geospatial Data Harmonization*, Hannover, Germany, June 2009.
29. Babitski, G.; Bergweiler, S.; Hoffmann, J.; Schön, D.; Stasch, C.; Walkowski, A. Ontology-based integration of sensor web services in disaster management. In *Proceedings of the Third International Conference of GeoSpatial Semantics*, Mexico City, Mexico, December 2009.
30. Compton, M.; Henson, C.; Lefort, L.; Neuhaus, H.; Sheth, A. A survey of the semantic speciation of sensors. In *Proceedings of the Second International Workshop on Semantic Sensor Networks, Eight International Semantic Web Conference*, Washington, DC, USA, 25–29 October 2009.
31. Kobialka, T.; Buyya, R.; Leckie, C.; Kotagiri, R. A sensor web middleware with stateful services for heterogeneous sensor networks. In *Proceedings of the Third International Conference on Intelligent Sensors, Sensor Networks and Information*, Melbourne, Australia, 3–6 December 2007.
32. Cox, S. *Observations and Measurements Part 1—Observation Schema*; OpenGIS Implementation Standard OGC 07-022r1; Open Geospatial Consortium Inc.: Redlands, CA, USA, 2007.
33. Cox, S. *Observations and Measurements Part 2—Sampling Features*; OpenGIS Implementation Standard OGC 07-002r3; Open Geospatial Consortium Inc.: Redlands, CA, USA, 2007.
34. Botts, M.; Robin, A. *Sensor Model Language*; OpenGIS Implementation Standard OGC 07-000; Open Geospatial Consortium Inc.: Redlands, CA, USA, 2007.
35. Havens, S. *Transducer Markup Language*; OpenGIS Implementation Standard OGC 06-010r6; Open Geospatial Consortium Inc.: Redlands, CA, USA, 2006.
36. Na, A.; Priest, M. *Sensor Observation Service*; OpenGIS Implementation Standard OGC 06-009r6; Open Geospatial Consortium Inc.: Redlands, CA, USA, 2006.
37. Simonis, I.; Dibner, P.C. *Sensor Planning Service Implementation Specification*; OpenGIS Implementation Standard OGC 07-014r3; Open Geospatial Consortium Inc.: Redlands, CA, USA, 2007.
38. Simonis, I. *Sensor Alert Service Candidate Implementation Specification*; OpenGIS Implementation Standard OGC 06-028r3; Open Geospatial Consortium Inc.: Redlands, CA, USA, 2006.
39. Simonis, I.; Wytzisk, A. *Web Notification Service*; OpenGIS Implementation Standard OGC 03-008r2; Open Geospatial Consortium Inc.: Redlands, CA, USA, 2003.
40. Jacobs, E.; Chari, S.; Russomanno, D.; Halford, C. Profiling sensors for border and perimeter security. In *Proceedings of SPIE Newsroom*, Bellingham, WA, USA, 20 August 2009.
41. Chari, S.K.; Halford, C.E.; Jacobs, E. Human target identification and automated shape based target recognition algorithms using target silhouette. In *Proceedings of the SPIE: Infrared Imaging Systems: Design, Analysis, Modeling, and Testing XIX*, Orlando, FL, USA, 16–20 March 2008.
42. Chari, S.; Halford, C.; Jacobs, E.; Smith, F.; Brown, J.; Russomanno, D. Classification of humans and animals using an infrared profiling sensor. In *Proceedings of the SPIE: Unattended Ground, Sea, and Air Sensor Technologies and Applications XI*, Orlando, FL, USA, 13–17 April 2009.

43. Russomanno, D.J.; Yeasin, M.; Jacobs, E.; Smith, M.; Sorower, M.S. Sparse detector sensor: Profiling experiments for broad-scale classification. In *Proceedings SPIE-Defense and Security Symposium: Unattended Ground, Sea, and Air Sensor Technologies and Applications X*, Orlando, FL, USA, March 2008.
44. Russomanno, D.; Chari, S.; Halford, C. Sparse detector imaging sensor with two-class silhouette classification. *Sensors* **2008**, *8*, 7996-8015.
45. Russomanno, D.J.; Chari, S.; Emmanuel, K.; Jacobs, E.; Halford, C. Testing and evaluation of profiling sensors for perimeter security. *ITEA J. Test Eval.* **2010**, *31*, 121-130.
46. Russomanno, D.J.; Chari, S.; Jacobs, E.; Halford, C. Near-IR sparse detector sensor for intelligent electronic fence applications. *IEEE Sens. J.* **2010**, *10*, 1106-1107.

© 2011 by the authors; licensee MDPI, Basel, Switzerland. This article is an open access article distributed under the terms and conditions of the Creative Commons Attribution license (<http://creativecommons.org/licenses/by/3.0/>).

*Article*

## Ontological Problem-Solving Framework for Assigning Sensor Systems and Algorithms to High-Level Missions

Joseph Qualls <sup>1,\*</sup> and David J. Russomanno <sup>2</sup>

<sup>1</sup> Department of Electrical and Computer Engineering, Herff College of Engineering, University of Memphis, 3720 Alumni Avenue, Memphis, TN 38152, USA

<sup>2</sup> Department of Electrical and Computer Engineering, Purdue School of Engineering and Technology, Indiana University-Purdue University Indianapolis (IUPUI), 799 W. Michigan St., Indianapolis, IN 46202, USA; E-Mail: drussoma@iupui.edu

\* Author to whom correspondence should be addressed; E-Mail: jqualls@rendermatrix.com; Tel.: +1-901-490-3717.

*Received: 6 July 2011; in revised form: 6 August 2011 / Accepted: 25 August 2011 /*

*Published: 29 August 2011*

---

**Abstract:** The lack of knowledge models to represent sensor systems, algorithms, and missions makes opportunistically discovering a synthesis of systems and algorithms that can satisfy high-level mission specifications impractical. A novel ontological problem-solving framework has been designed that leverages knowledge models describing sensors, algorithms, and high-level missions to facilitate automated inference of assigning systems to subtasks that may satisfy a given mission specification. To demonstrate the efficacy of the ontological problem-solving architecture, a family of persistence surveillance sensor systems and algorithms has been instantiated in a prototype environment to demonstrate the assignment of systems to subtasks of high-level missions.

**Keywords:** sensor networks; Sensor Ontology; profiling sensors; mission tasking

---

### 1. Introduction

Dynamically discovering, matching, and integrating sensors and compatible algorithms to form a synthesis of systems that are capable of satisfying subtasks of high-level missions poses a significant challenge for network-centric architectures. Compounding the challenge is the lack of knowledge and

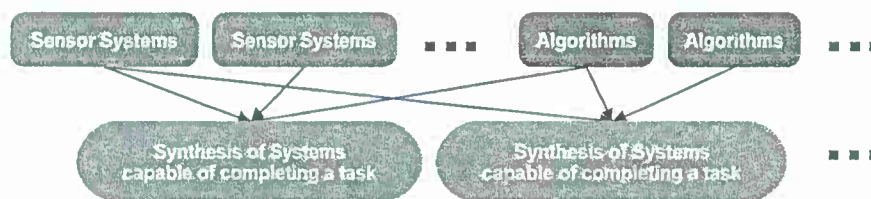


data models used to describe the relationships among sensors, algorithms, and missions. Most algorithms are designed for specific sensor systems in anticipation of performing a specific task. Designing and deploying tightly integrated systems limits their potential reuse for new, unanticipated tasks without re-engineering the systems [1-6]. This paper will review the authors' prior work [7], which addresses the issue of autonomously matching sensor systems to compatible algorithms. Section 2 of the paper will review the challenges of assigning the matched systems to subtasks of missions. Section 3 will review related work of systems and frameworks that assign systems to missions. The remainder of the paper will focus on the authors' extension of their previous work to now include assignment of the synthesis of systems to subtasks of missions in the context of a persistence surveillance sensing environment. Section 4 discusses the operation of the persistence surveillance environment and Sections 5, 6, and 7 discuss the extended ontological problem-solving framework laboratory prototype for mission assignment and execution.

#### *Previous Work by Qualls and Russomanno*

Matching sensor systems to compatible algorithms to form a synthesis of systems poses a significant challenge to problem-solving frameworks. Frameworks must be able to match the systems together and then reuse the same systems in new matches as depicted in Figure 1. In prior work, Qualls and Russomanno [7] focused on the reasoning process of matching sensor systems and algorithms to form a synthesis of systems capable of satisfying a task.

**Figure 1.** Process for matching sensor systems to compatible algorithms to form a synthesis of systems capable of satisfying a task.



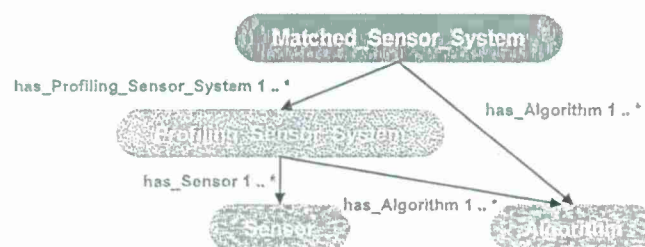
The prior work by the authors included developing a laboratory prototype ontological problem-solving framework that leveraged knowledge engineering techniques to opportunistically infer the discovery and matching of sensor systems to compatible algorithms. The knowledge engineering techniques included an ontology, rules, and inference engine to autonomously form the synthesis of systems. Standard database technologies and SQL queries could have been used for the prototype development, but one of the main shortcomings limiting the matching of systems together is the lack of knowledge models to describe and represent the systems. The knowledge models themselves must leverage well-defined semantics in a machine-interpretable format for autonomous matching. The use of knowledge models also provides the added benefit of more readily transferring the knowledge to other systems as compared to other techniques.

To autonomously form the synthesis of systems, the prototype framework used ontologies to describe properties and relationships among sensor systems, algorithms, and possible synthesis of systems. The ontologies have two parts: (i) the class hierarchy for describing relations among different

types of sensor systems; and (ii) algorithms and properties for describing specific properties of each class. Data-type properties, which may be regarded as attributes, are used to describe sensor system and algorithm parameters, such as pixel resolutions, field of view, data format, algorithmic process, and network connections. Object-type properties, which may be regarded as associations, were used to link specific sensor systems and algorithms together during the inference process for the synthesis of systems. With the properties in the ontology, instance data may then be created to represent actual sensor systems and algorithms.

Figure 2 shows a small excerpt of the ontology including four main classes for synthesis: *Matched\_Sensor\_System*, *Profiling\_Sensor\_System*, *Sensor*, and *Algorithm*. The *Sensor* class describes a sensing device and the *Algorithm* class describes an algorithmic process. The process can either operate on data generated by the sensing device or data generated by other processes. The *Profiling\_Sensor\_System* class represents a synthesis of systems that describes possible combinations of *Sensor* and *Algorithm* instances which produce formatted signal profiles of objects as they pass through a sensor system's field of view. The class *Matched\_Sensor\_System* describes a synthesized system that contains possible combinations of *Profiling\_Sensor\_System*, *Algorithm*, and *Sensor* instances, which produce results, such as visualizations or classifications of the generated signal profiles. Not shown is the class hierarchy for the *Target* class, which contains further subclasses of *Human*, *Animal* and *Vehicle*. These subclasses are further refined and include subclasses, such as of *Bird*, *Large\_Animal*, and *Bear* for *Animal* and subclasses of *Car*, *Light\_Truck*, and *Heavy\_Truck*, for *Vehicle*, and so on. Also not shown is a class hierarchy of the *Object\_Of\_Interest*, which includes subclasses and properties describing accessories, such as backpacks and an extensive description of weapons, which include bladed, non-bladed weapons, and projectile weapons, such as small and heavy arms including pistols, machine guns, and rocket-propelled grenades. Each of the further subclasses has its own respective data-type properties describing those classes. Rules in the form of queries with conditional actions were developed to be processed by an inference engine to search the instance data for possible synthesis of systems. For further information on the development of the ontology in Figure 2, class hierarchy, and rule design please refer to Qualls and Russomanno [7].

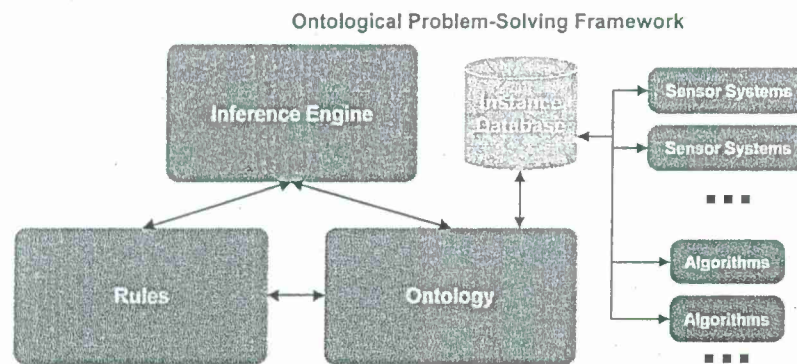
Figure 2. Excerpt of the ontology in the ontological problem-solving framework for matching sensors to algorithms to form a synthesis of systems.



The ontological problem-solving framework with the knowledge engineering techniques discussed above was developed with the TopBraid Composer Maestro software environment by TopQuadrant [8]. TopBraid uses the Web Ontology Language (OWL) [9] for authoring ontologies; rules with logical conditions were developed with SPARQL [10]; and the TopSPIN inference engine was used for

processing the SPARQL rules. The authors chose TopBraid Composer Maestro due to their familiarity with this platform from other research projects. OWL is based upon one specific description logic (DL) with the main difference being the naming nomenclature. For example, in OWL a class is a concept in DL, an OWL property is a role in DL, and an OWL object is an individual in DL. The rules developed by the authors in the ontological problem-solving framework are expressed as SPARQL queries with additional constraints on RDF triples. In addition, some of the rules include actions implemented by invoking Java functions via procedural attachment [11]. Other ontological development environments could have been used for the prototype development, such as Protégé with JESS and SWRL [1-7]. Figure 3 shows the overall framework of the ontological problem-solving system.

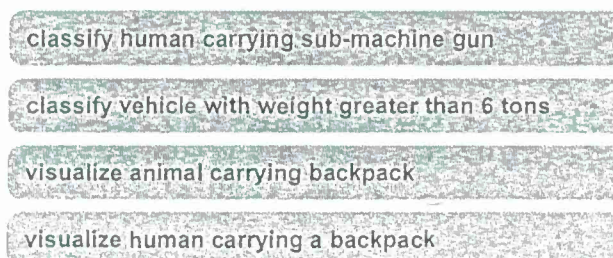
Figure 3. Overview of the laboratory prototype ontological problem-solving framework.



## 2. Assigning Systems to Missions

The prior prototype ontological problem-solving framework developed by the authors only matched sensors and algorithms to form a synthesis of systems [7]. The next logical step was to extend the framework to allow for missions to be instantiated on the framework and then autonomously assign the synthesis of systems to the missions. Before an extension could be made, the concept of a mission must be developed. Knowledge acquired from subject matter experts (SMEs) in the fields of sensor system design, algorithm development, and concept of operations (CONOPS) contributed to the development of the concept of missions. The authors elicited knowledge from the SMEs to first develop missions associated with typical persistence surveillance applications as illustrated in Figure 4.

Figure 4. Typical missions for persistence surveillance.





The authors and SMEs then analyzed the typical missions to yield a set of specifications that could be used to describe the missions. The specifications included a *target* that must be detected, such as a human or vehicle, and a *mission task* for describing a subtask that describes a *process* and *condition* which takes place on the *target*. A *process* describes what must happen on the detected target, such as “classification”, “visualization”, or “signal profile generation”. The process may have ancillary *conditions*, such as target is carrying a “weapon” or “backpack” or even a *condition* of target has “weight greater than six tons”. A specification is shown in Figure 5 via an instance diagram.

Figure 5. Mission decomposed into a specification via an instance diagram.

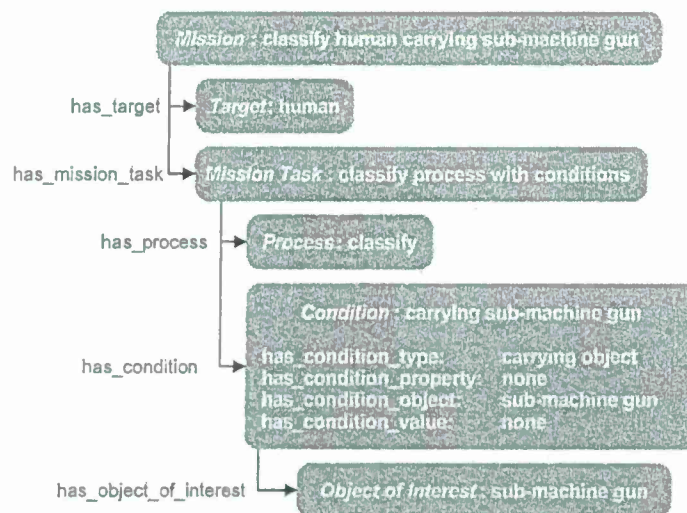
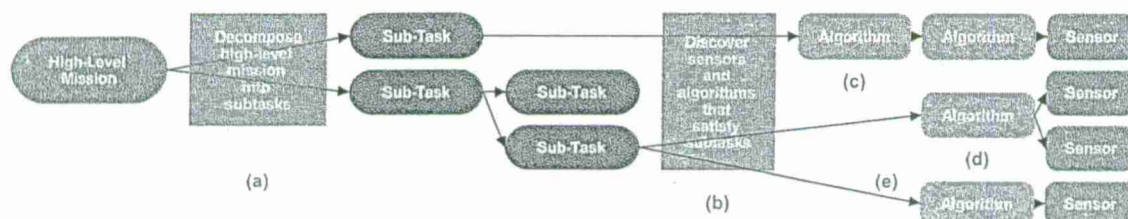


Figure 6. (a) Decompose missions to separate subtasks; (b) Discover sensors and compatible algorithms, which can complete subtasks; (c) Subtask assigned to a chain of algorithms operating on raw data produced by a sensor; (d) Subtask assigned to an algorithm operating on raw sensor data from two different sensors; and (e) Subtask assigned to an algorithm operating on raw data produced by a sensor.



With the high-level missions decomposed into a set of mission specifications, a problem-solving approach must then assign matched sensor systems and algorithms to the subtasks which satisfy the mission specification as indicated in Figure 6. The problem-solving approach must discover which systems can satisfy the given subtasks as illustrated in Figure 6(b). Once systems have been discovered, the interoperation of multiple sensors and algorithms must be coordinated to perform a subtask as indicated in Figure 6(c–e). To perform these operations, the ontological framework must



describe relationships among the sensors, algorithms, and missions in terms of how the subtasks relate to the mission, relationships among subtasks and compatible sensors and algorithms, and the relationships between the sensors and algorithms. Section 5 details how the developed concept of a mission was integrated into the authors' previous work.

### 3. Related Work

Various approaches have been designed and engineered to assign sensors and algorithms to missions or task specifications, such as Semantic sensor mission assignment [12], Ontological sensor mission assignment [13], Knowledge base for sensors to missions [14], GloServ [15], Ontology Centric sensor mission assignment [16], Resource management [17], Sensor Mission Matching [18], Semantic-aware cooperative agents [19], Query Processing for sensor networks [20], Agilla [21-23], Geographic Information System Framework [24,25], Semantic Streams [26,27], and Sensor OASiS [28]. Relevant to our work is the development of ontologies that represent and describe sensor systems such as OntoSensor [2-6], Sensor Network Data Ontology [29], Sensor and Data Wrapping Ontology [30], Stimulus-Sensor-Observation Ontology [31], Sensor Observation and Measurement Ontology [32], Semantic Sensor Network Ontology [33], and Disaster Management Sensor Ontology [34]. Also of importance to the authors' work are other examples of relevant sensor ontologies [35]. There are many logical models and standards to follow and adapt, such as the Sensor Modeling Language (SensorML) [36], that leverage the Unified Modeling Language (UML) to conceptualize sensor systems and algorithms to facilitate interoperability. Also, the Open Geospatial Consortium (OGC) [37] drafts standards that may be used to define metadata encodings and interoperability interface standards to facilitate problem-solving frameworks that can integrate sensor systems and algorithms into information infrastructures. The OGC includes many standards, such as Observations and Measurements (O&M) [38,39], SensorML [40], Transducer Model Language (TML) [41], Sensor Observation Service (SOS) [42], Sensor Planning Service (SPS) [43], Sensor Alert Service (SAS) [44], and Web Notification Services (WNS) [45].

One example system, Agilla [21-23], is a framework used to monitor sensor systems connected to a sensor network. Agilla uses protocols with specific conditions that, when met, will perform a specific action or actions. For example, the actions and conditions may be to activate other protocols when a sensor reports a temperature above a specific threshold. The newly activated protocols may then coordinate other sensors to collect data, invoke algorithms for further analysis, or even activate more protocols to perform a specific action or actions. Figure 7(a) shows an Agilla network with a fire detection protocol on one sensor node. The fire detection protocol has the task of detecting a temperature above a specific threshold. Once the temperature threshold is reached, the protocol will activate other fire detection protocols on more sensors nodes, Figure 7(b). As the protocols activate on the other sensor nodes, the protocols will determine the perimeter of the fire and then send the perimeter data to a new protocol, Figure 7(c), which then activates fire services [21-23]. Another example system, Geographical Information System Framework [24,25], leverages several different frameworks in the overall management of sensor systems and algorithms on a sensor network as depicted in Figure 8. The framework includes knowledge models, such as ontologies, for describing sensors, algorithms, and tasks. Service-oriented architectures are used to handle communications

among all systems, and geographic information system placement logic is used for tasking. The different frameworks operating together allow end users or autonomous systems to query the framework for available sensor systems and then task the sensor systems to retrieve data or to perform specific actions based on sensor data [24,25].

Figure 7. (a) Fire detection protocol on a node in an Agilla sensor network that detects a fire; (b) Protocol activates other protocols on different nodes to determine the perimeter of the fire and then activates other protocols for fire services; and (c) Activation of fire services.

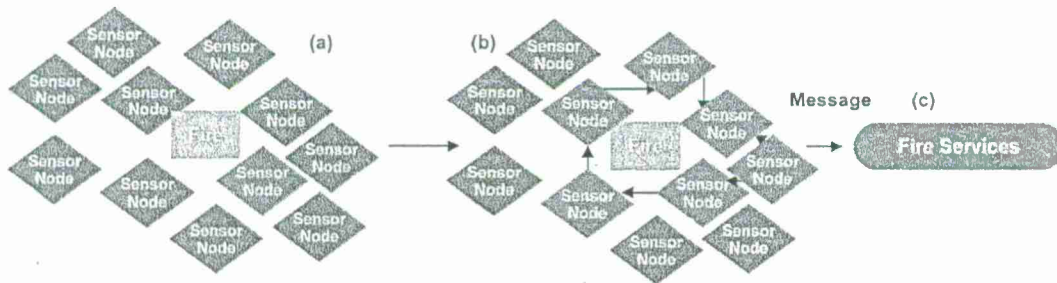
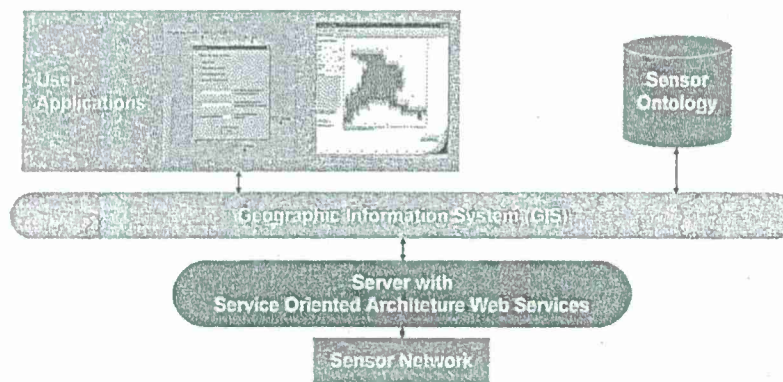


Figure 8. Geographical Information System Framework displaying interconnections among the geographic information system, service-oriented architecture, ontologies and end user software applications.

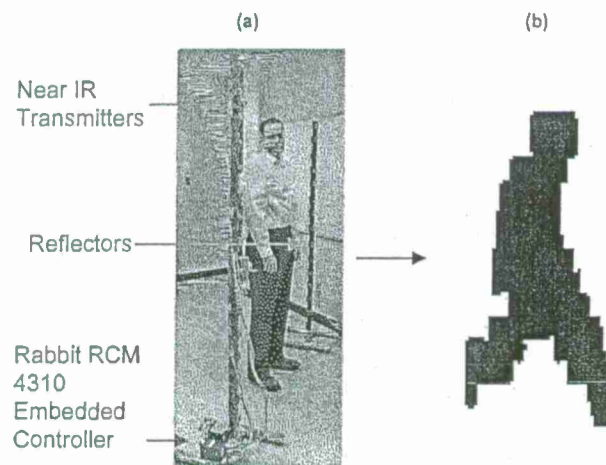


#### 4. Persistence Surveillance Sensing Environment

To demonstrate the efficacy of the extended ontological problem-solving framework, a persistence surveillance sensing environment was constructed from a family of emulated unattended ground profiling sensor systems and algorithms. The profiling sensors provide a means for capturing signals of objects which pass through a profiling sensor's field of view. The signals are then passed to algorithms which create profiles of the signals, which are then sent to other algorithms for further processing, such as object classification or visualization. The profiling sensors have a common theme in that they are low cost and provide a signal that can be classified. The profiling sensors are denoted by the nomenclature PFx [46]. The PFx sensors may use a variety of sensing bands, including visible, near infrared, short-wave infrared, mid-wave infrared, and long-wave infrared bands. They typically share a common design principle of using a sparse detector array.

Figure 9(a) shows a sparse detector PFx sensor consisting of sixteen near-infrared detectors in a vertical deployment with no relative horizontal displacement and a reflector pole. When an object passes between the two poles, which is the field of view of the sensors, the resulting signal will be recorded. An algorithm then processes the signal by formatting the raw sensor data using run-length encoding. The formatted sensor data may be used by other algorithms to visualize the acquired data as a silhouette shown in Figure 9(b). Other possible configurations of a vertical near infrared sparse detector may include a horizontal displacement, which may be used to determine the velocity of an object [46-53]. The chain of creating raw sensor data, generating profiles, and then processing the profiles for visualization or classification provides a unique opportunity to show how the prototype ontological framework can autonomously assign the PFx sensors and algorithms to the subtasks of various missions based on their relationships and capabilities.

Figure 9. (a) PFx sensor system using sixteen near-infrared detectors deployed vertically with no horizontal displacement; and (b) Silhouette generated by an algorithm operating on the sensor data.



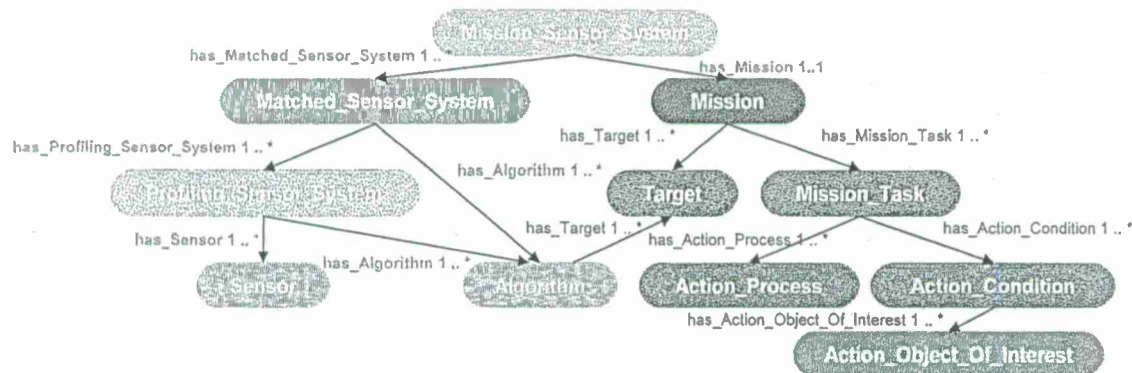
## 5. Reasoning Process for Assigning Sensor Systems and Algorithms to Missions

### 5.1. Problem-Solving Framework for Assigning a Synthesis of Systems to Mission Specifications

To address the challenge of assigning sensor systems and algorithms to high-level missions the previous work by Qualls and Russomanno [7] was extended with the concept of a mission developed from eliciting knowledge from SMEs. Figure 10 shows the original ontology of the problem solving-framework, as seen in Figure 3, extended with an ontology for describing mission specifications. The extended ontology is shown here with two additional classes: *Mission\_Sensor\_System* in gray, and *Mission* in red. The *Mission* class has five supporting classes, also in red, to describe mission specifications: *Target*, *Mission\_Task*, *Action\_Process*, *Action\_Condition*, and *Action\_Object\_Of\_Interest*. The primary goal of the ontology in the prototype ontological framework is to support the synthesis of the *Mission\_Sensor\_System*, which is a synthesis of systems assigned to a mission.



Figure 10. Extension of the prototype ontological problem-solving framework for matching sensor systems to algorithms to form a synthesis of systems that may now be assigned to subtasks of missions.



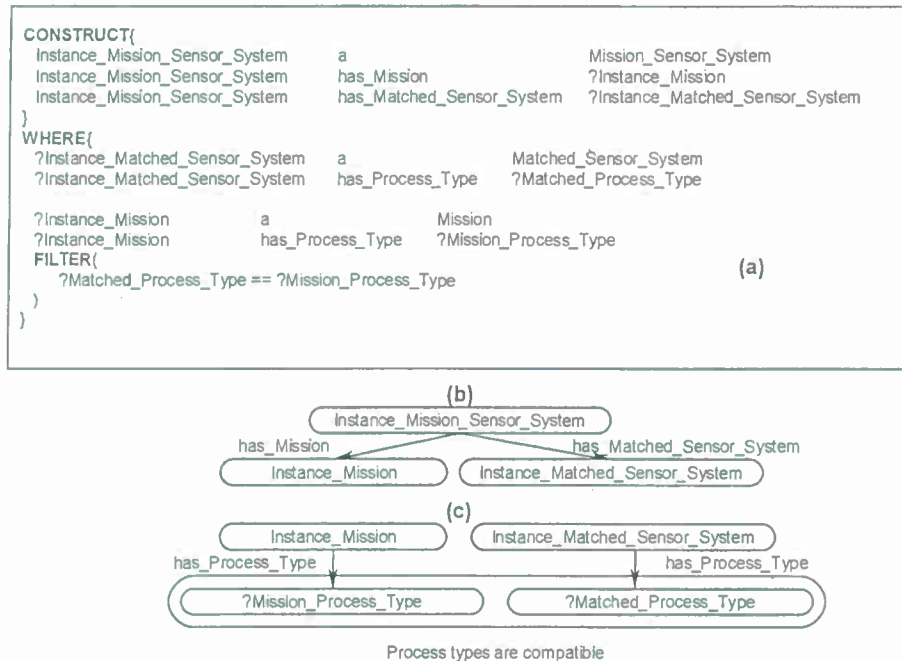
A *Mission\_Sensor\_System* class describes a possible combination of *Matched\_Sensor\_System* instances and a *Mission* instance through the two object type properties *has\_Matched\_Sensor\_System* and *has\_Mission*. A *Mission\_Sensor\_System* may have many *Matched\_Sensor\_System* instances but one only *Mission* instance. The *Mission* class describes the various specifications of a mission. The *Mission* class leverages two other classes, *Target* and *Mission\_Task*, to define mission specifications. The *Target* class describes the object that the mission needs to detect, such as human or animal. The *Mission\_Task* class describes the process and condition which must take place on the *Target* instance. To define the process specification, the *Mission\_Task* leverages two other classes: *Action\_Process* and *Action\_Condition*. The *Action\_Process* class describes a specification process, such as “classify” or “visualize” for the detected *Target* instance. The *Action\_Condition* class describes further specifications that the *Action\_Process* might require. Last, the class *Action\_Object\_Of\_Interest* describes objects that a *Target* instance may be associated with, for example, objects that may be carried by a human or animal.

## 5.2. Ontological Framework Rules

The original prototype ontological problem-solving framework used SPARQL [10], a graph-matching query language to implement the rules to query the instance data and return possible synthesis of systems. SPARQL rules can be regarded as Horn clauses with addition logical constraints. The rules contain the following two components; CONSTRUCT and WHERE clauses. First, the CONSTRUCT clause returns possible object instances, which contain new properties, derived properties, and links to other class instances and their corresponding attributes. Second, the WHERE clause contains statements that specify constraints. The constraints include the properties that must exist and the logical constraints that properties of a class instance must satisfy before the rule will execute. Each of the constraints in a single rule are connected via a logical conjunction (logical AND), whereas a collection of rules of a common theme are connected via a logical disjunction (logical OR). Once all properties and logical constraints of the WHERE clause are satisfied, the corresponding CONSTRUCT clause will return the possible object instance or instances.



Figure 11. (a) Example SPARQL rule with CONSTRUCT and WHERE clauses, which returns a possible *Mission\_Sensor\_System* instance; (b) Instance diagram of CONSTRUCT clause; and (c) Instance diagram of WHERE clause.



New rules were developed for assigning the synthesis of systems to missions, thus returning possible *Mission\_Sensor\_System* instances. Figure 11 shows an example SPARQL rule that queries the existing instance data and returns a *Mission\_Sensor\_System* instance in the CONSTRUCT clause when the properties and logical constraints are satisfied in the WHERE clause. The CONSTRUCT clause in Figure 11(a) contains three statements. The first statement declares the object instance *Instance\_Mission\_Sensor\_System* to be of class type *Mission\_Sensor\_System*. The second two statements establish links to the possible existing instances through the two properties: *has\_Mission* and *has\_Matched\_Sensor\_System*. To establish these two links, the two properties are linked to two variables *Instance\_Mission* and *Instance\_Matched\_Sensor\_System*, respectively. The WHERE clause in Figure 11(b) contains five statements. In the first two statements, the object variable *Instance\_Matched\_Sensor\_System* is instantiated with an instance of class type *Matched\_Sensor\_System* and the variable *Matched\_Process\_Type* is instantiated with the value from the data type property *has\_Process\_Type* from the same *Matched\_Sensor\_System* instance. In the second two statements, the object variable *Instance\_Mission* is instantiated with an instance of class type *Mission* and the variable *Mission\_Process\_Type* is instantiated with the value from the data type property *has\_Process\_Type* from the same *Mission* instance. The final statement in the WHERE clause contains the FILTER command which appears as a simple logical constraint that compares two variables. This particular FILTER command compares the two data type variables *Matched\_Process\_Type* and *Mission\_Process\_Type* for equality. When the inference engine processes this rule, the CONSTRUCT clause will return a possible *Mission\_Sensor\_System* instance with links to a *Matched\_Sensor\_System* instance and links to an assigned *Mission* instance if the two instances and properties exist and if the

two properties are equal in the WHERE clause. Once a *Mission\_Sensor\_System* instance has been returned by the rules, the ontological framework can then execute the mission by coordinating all synthesized systems, sensors, and algorithms assigned to that mission and returning the results of the mission via a procedural attachment statement.

One note of interest is the subsumption qualities of the logical constraint for the FILTER command. For example, if the *Matched\_Process\_Type* variable is set to a subclass of the *Process\_Type* and the *Mission\_Process\_Type* variable is set to a superclass of the *Process\_Type*, the rule will need to return true or false depending on a set threshold for the semantic distance between the variables. To set this threshold the authors decided to set the mission as a priority. The reason for this selection is based on feedback from the SMEs in terms of CONOPs. For example, a mission may be created for a specific target but no synthesis of systems can complete that exact mission. Forcing the framework to assign systems only to exact matches of missions would severely limit the capabilities of the framework. So the authors decided to allow the framework to return possible best matches between a synthesis and a mission. For the ontological framework the semantic distance threshold has been set as follows for the prototype. There are two basic conditions: if the property of the mission is a subclass of the matched system or if the property of the mission is a superclass of the match system. First, if a mission property such as *has\_Action\_Object\_Of\_Interest* is set to a value that is a subclass of the same property of the matched systems, the framework will assign the matched system to the mission up to the top-level superclass that property may have. For example, if the mission *has\_Action\_Object\_Of\_Interest* variable is set to pistol, the framework would assign matched systems up to highest class domain of the property in this case *has\_Action\_Object\_Of\_Interest*, which is the class *Object\_Of\_Interest*. Second, if the *has\_Action\_Object\_Of\_Interest* variable of the matched system is set to a value that is a subclass of the same property of the mission then an assignment will take place. For example, if the mission *has\_Action\_Object\_Of\_Interest* property is set to pistol, the framework would assign matched systems that are subclasses of pistol.

The rules in the ontological problem-solving framework all follow a similar structure outlined in Figure 11. The rules bind on all combinations of *Mission* and *Matched\_Sensor\_System* instances and return possible *Mission\_Sensor\_System* instances in the CONSTRUCT clause when the corresponding properties exist and logical constraint statements are met in the WHERE clause. Figures 12 and 13 each show one of many different kinds of rules that return possible *Mission\_Sensor\_System* instances and their resulting instance diagrams. These rules bind on properties of the *Matched\_Sensor\_System* instance that link back to other instances, such as the type of process the system can accomplish, and additional properties, such as conditions on the process that may or may not be optional. The rules also bind on properties of a *Mission* instance, which, as previously discussed, include *Target*, *Mission\_Task*, *Action\_Process*, and *Action\_Condition*. Figure 12 shows a rule which binds on a simple mission to process a target with no conditions, such as “classify human male”. Figure 13 shows a rule that binds on more advanced missions that processes a target with conditions, such as “visualize horse carrying backpack” or “classify human male with height greater than six feet”, respectively.

Figure 12. Rule and instance diagram showing how a *Mission\_Sensor\_System* is returned for a simple *Mission* if a *Matched\_Sensor\_System* can accomplish the mission based on *Action\_Process* and *Target* properties.

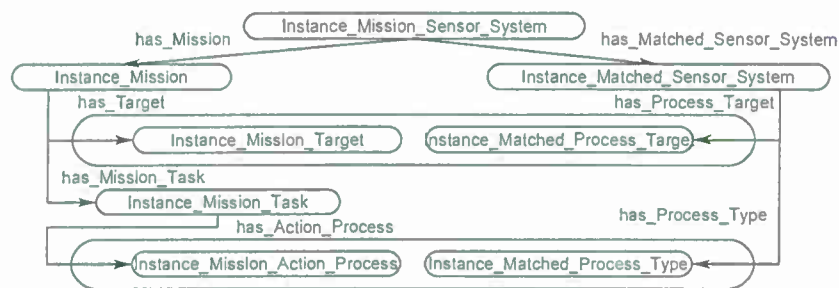
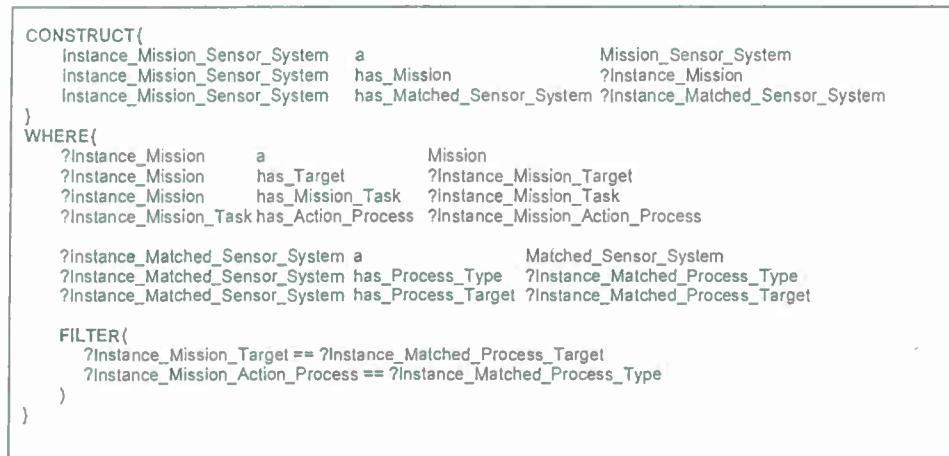


Figure 13. Rule and instance diagram showing how a *Mission\_Sensor\_System* is returned for an advanced *Mission* if a *Matched\_Sensor\_System* can accomplish the mission based on *Action\_Process*, *Action\_Condition*, and *Target* properties.

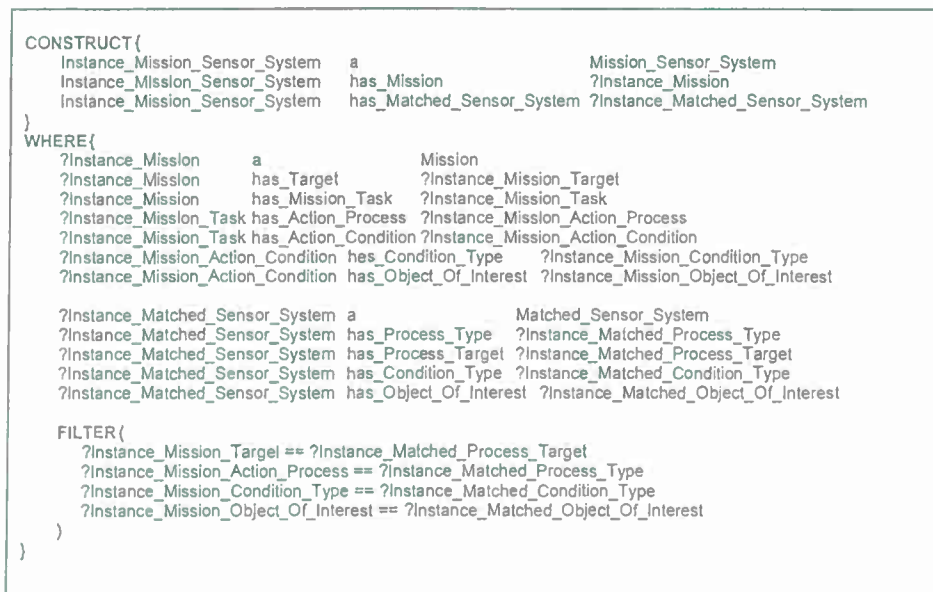
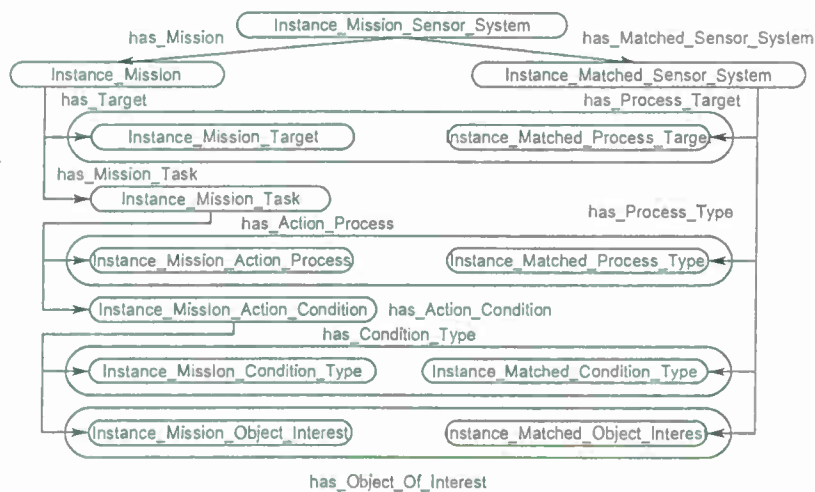


Figure 13. Cont.



## 6. Example of Assigning a Synthesis of Systems to Mission Specifications

To show how the prototype ontological problem-solving framework operates, a small example has been created. Figure 14 shows an overview of all emulated assets instantiated and the resulting synthesis of systems and assignment to a mission instance. To begin, the ontological framework was instantiated with: (i) one emulated sensor systems *Photo\_Conductive* (Figure 14(a)); (ii) two algorithms, *Pixel\_Extractor* (Figure 14(b)) and *Naive\_Bayes\_Classifier* (Figure 14(c)); and (iii) one mission instance (Figure 14(d)). The following section will detail how the sensor system and algorithms are matched together to form a synthesis of systems that are assigned to a mission. Each of the instances has many different data-type properties, but for this example only a few relevant properties are shown in Figure 14.

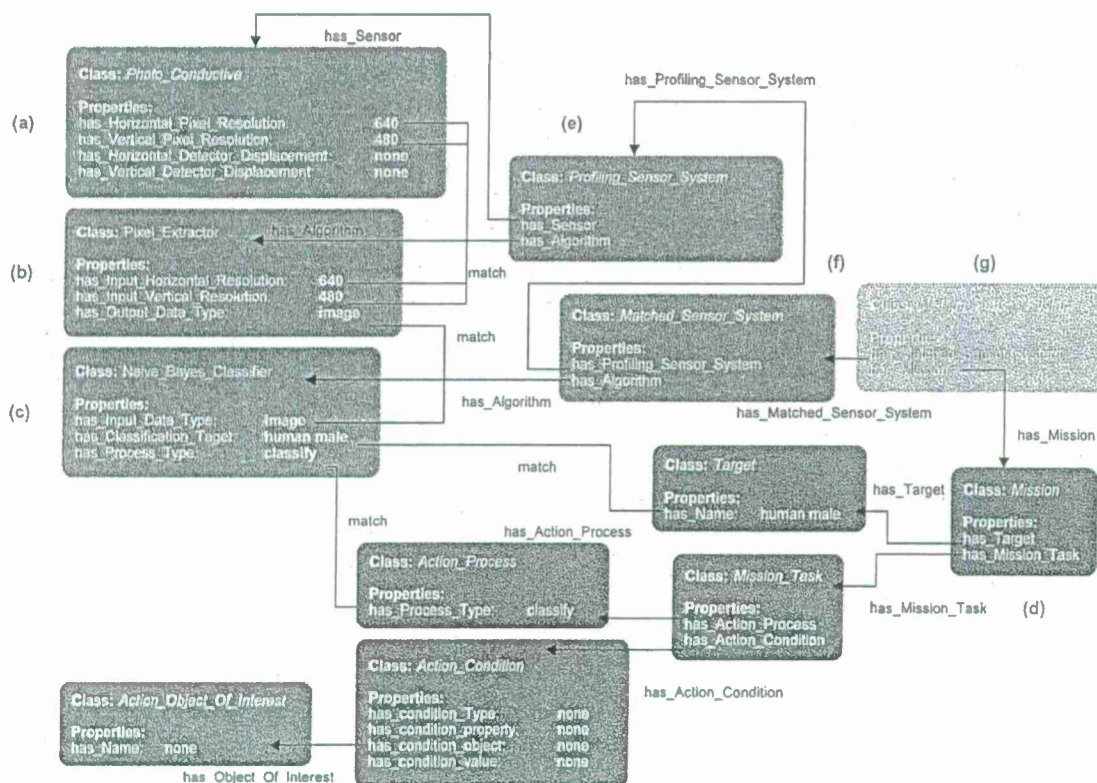
The *Sensor* instance *Photo\_Conductive* has four properties; *has\_Horizontal\_Pixel\_Resolution* set to 640 pixels, *has\_Vertical\_Pixel\_Resolution* set to 480 pixels, *has\_Horizontal\_Detector\_Displacement*, and *has\_Vertical\_Detector\_Displacement* both set to none. The *Photo\_Conductive* instance represents a sensor capable of generating a signal profile of a passing target. The *Algorithm* instance *Pixel\_Extractor* has three properties; *has\_Input\_Horizontal\_Resolution* set to 640 pixels, *has\_Input\_Vertical\_Resolution* set to 480 pixels, and *has\_Output\_Data\_Type* set to image. The *Pixel\_Extractor* instance represents an algorithm capable of loading a raw signal profile data in 640 × 480 format and then generating a formatted signal profile into an image format. The second *Algorithm* instance *Naive\_Bayes\_Classifier* has three properties: (i) *has\_Input\_Data\_Type* set to image; (ii) *has\_Classification\_Target* set to human male; and (iii) *has\_Process\_Type* set to classify. The *Naive\_Bayes\_Classifier* instance describes a classifier that operates on features of an image and then classifies the image as a human male or not a human male.

The *Mission* instance represents a mission that requires the detection of human males, *i.e.*, classify human male. The *Mission* instance has two object-type properties, *has\_Target* and *has\_Mission\_Task*, which link to the *Target* instance and *Mission\_Task* instance. The *Target* instance describes a human male instance that has many properties, such as *has\_Name* and not shown *has\_Height*, and *has\_Weight*.



The instance *Mission\_Task* has two object-type properties *has\_Action\_Process* which links to the instance *Action\_Process* “classify” and the property *has\_Action\_Condition* which links to the *Action\_Condition* instance “none”. The *Action\_Process* instance has many data-type properties, such as *has\_Process\_Type*, which can have the values *classify*, *profile\_generator*, *convertor*, and *visualizer*. For this case, the data-type property is set to *classify*. The *Action\_Condition* instance “none” has three data-type properties, *has\_Condition\_Type*, *has\_Condition\_Property*, and *has\_Condition\_Value*, each set to “none” and one object-type property, *has\_Condition\_Object*, which links to the instance *Action\_Object\_Of\_Interest* “none”. The instance *Action\_Object\_Of\_Interest* “none” is of type *Object\_Of\_Interest* which describes a possible object the *Target* may be holding or wearing, but in this example, the mission does not specify if the human male is carrying an object, so all values are set to none.

**Figure 14.** *Mission\_Sensor\_System* instance diagram showing a linked *Mission* instance “classify human male” matched to a synthesized system capable of satisfying the high-level mission. (a) *Sensor* instance *Photo\_Conductive*; (b) *Algorithm* instance *Pixel\_Extractor*; (c) *Algorithm* instance *Naive\_Bayes\_Classifier*; (d) *Mission* instance “classify human male”; (e) *Profiling\_Sensor\_System* instance; (f) *Matched\_Sensor\_System* instance; and (g) *Mission\_Sensor\_System* instance.



With all systems and a mission instantiated on the prototype ontological framework, rules such as those in Figures 12 and 13 will process the instance data to form a synthesis of systems and assign the synthesis to the mission. The first synthesis of systems to be returned is a *Profiling\_Sensor\_System*

instance shown in Figure 14(e). The *Profiling\_Sensor\_System* instance was returned because the properties of *Photo\_Conductive* and *Pixel\_Extractor* matched, i.e., the output pixel resolutions of the *Photo\_Conductive* and input pixel resolutions of the *Pixel\_Extractor* matched to  $640 \times 480$ . The synthesized *Profiling\_Sensor\_System* instance contains two derived object-type properties that link to the *Sensor* instance *Photo\_Conductive* and the *Algorithm* instance *Pixel\_Extractor*, called *has\_Sensor* and *has\_Algorithm*. The *Profiling\_Sensor\_System* instance represents a synthesis of systems capable of formatting a raw signal profile into a formatted "image" profile.

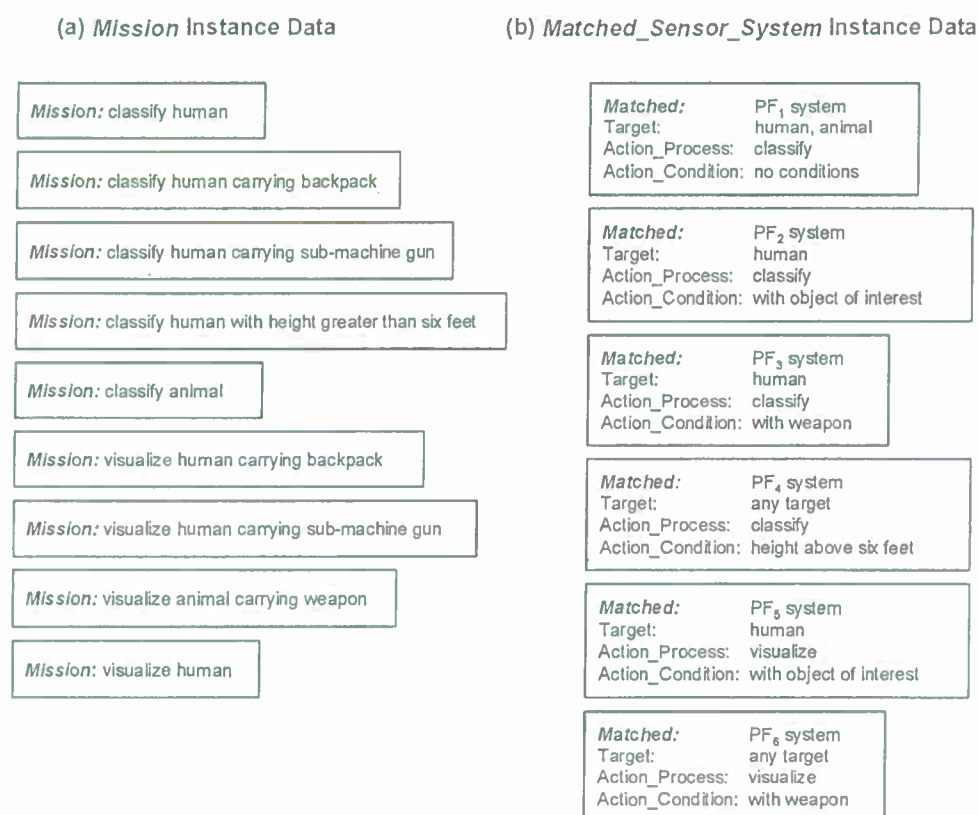
The next pass of the inference cycle will produce the second synthesis of systems; the *Matched\_Sensor\_System* instance shown in Figure 14(f). The *Matched\_Sensor\_System* instance contains the two object-type properties *has\_Profiling\_Sensor\_System*, which links to the synthesized *Profiling\_Sensor\_System* instance, and *has\_Algorithm*, which links to the *Naive\_Bayes\_Classifier* instance. The algorithm *Naive\_Bayes\_Classifier* was matched to the *Profiling\_Sensor\_System* instance because the data-type property *has\_Output\_Data\_Type* set to "image" matched the data-type property *has\_Input\_Data\_Type* set to "image", respectively. The new *Matched\_Sensor\_System* instance represents a synthesized system, which generates raw signal data that can then be classified as a human male or not a human male.

On the next inference cycle, the rules return a possible *Mission\_Sensor\_System* instance, shown in Figure 14(g), which assigns the synthesized system *Matched\_Sensor\_System* instance to the simple *Mission* instance because of two sets of properties. First, the data-type property *has\_Classification\_Target* value "human male", which is linked to the *Matched\_Sensor\_System* through the *has\_Algorithm* object-type property, matches to the data type property *has\_Name* "human male" in the *Target* instance, which is linked to the instance *Mission* through the object-type property *has\_Target*. Second, the *Naive\_Bayes\_Classifier* instance has the data-type property *has\_Process\_Type* set to the value "classify". The *Naive\_Bayes\_Classifier* instance is linked to the *Matched\_Sensor\_System* instance through the object-type property *has\_Algorithm* because the data-type property *has\_Process\_Type* of the instance *Action\_Process* is set to "classify". *Action\_Process* is linked to the instance *Mission\_Task* through the object-type property *has\_Action\_Process*, which in turn is linked to the *Mission* instance through the object-type property *has\_Mission\_Task*. The synthesized *Mission\_Sensor\_System* instance links to the synthesized *Matched\_Sensor\_System* instance through the object-type property *has\_Matched\_Sensor\_System* and links to the *Mission* instance through the object-type property *has\_Mission* and represent synthesized systems ready to be coordinated to complete the mission classify human male. The returned *Mission\_Sensor\_System* system is added as an instance in the ontology so further inference can leverage the synthesis of systems and mission for further complex mission tasking or for actual coordination to execute the mission. Although Figure 14 shows relatively simple properties, and the rules in Figure 12 and Figure 13 bind on simple compatibility constraints, further properties and more complex uses of the SPARQL, FILTER, and OPTIONAL commands may allow for more complex synthesized systems to be returned and assigned to increasingly sophisticated missions.

## 7. Instantiated Emulated Profiling Sensor Systems and Algorithms

To show the efficacy of the ontological problem-solving framework, several emulated profiling sensor systems and algorithms were instantiated as complete *Matched\_Sensor\_System* instances in the ontological problem-solving framework as a prototype environment for testing. In the prototype environment, nine different *Mission* instances and six different *Matched\_Sensor\_System* instances were instantiated, Figure 15. Each of the various *Matched\_Sensor\_System* instances contained *Profiling\_Sensor\_System* instances made up of matched emulated sensor systems and algorithms, with some of the emulated systems shared between different *Matched\_Sensor\_System* instances.

Figure 15. Instantiated examples on the ontological framework: (a) Nine different *Mission* instances consisting of detection and classification of targets and visualization of targets; and (b) Six different *Matched\_Sensor\_System* instances with links to *Profiling\_Sensor\_System*, *Sensor* and *Algorithm* instances matched together to form a synthesized system capable of performing a task.



When the ontological problem-solving framework begins, the inference cycle processes the rules similar to those in Figures 12 and 13. When the inference cycles terminate, sixteen new *Mission\_Sensor\_System* instances were returned as shown in Figure 16. From Figure 16, multiple *Matched\_Sensor\_System* instances were matched to a single *Mission* instance while in some cases a single *Matched\_Sensor\_System* instance was matched to multiple *Mission* instances. For example, the *Mission* instance “classify human carrying sub-machine gun” can be completed by two different



*Matched\_Sensor\_System* instances: “PF<sub>2</sub> system” and “PF<sub>3</sub> system” because the *Action\_Process* “classify” of the *Mission* matched the *Process\_Type* “classify” of both PF<sub>x</sub> systems and each of the *Mission* instance *Action\_Object\_Of\_Interest* “sub-machine gun” matched the *Action\_Condition* of both PF<sub>x</sub> systems. This particular assignment also represents how the authors chose to handle subsumption with a semantic distance threshold in that the *Action\_Condition* of both PF<sub>x</sub> systems were not “sub-machine gun” but “object of interest” and “weapon”, which are each super classes of “sub-machine gun”. Assigning matched systems in this way allows the ontological framework to “best fit” a mission to a synthesis of systems. Also the *Matched\_Sensor\_System* instance “PF<sub>5</sub> system” can complete three different *Mission* instances: “visualize human carrying backpack”, “visualize human carrying sub-machine gun”, and “visualize human”.

Once the assignments have been completed, *i.e.*, the *Mission\_Sensor\_System* instances have been returned by the inference engine, the prototype ontological framework selects a single completed *Mission\_Sensor\_System* instance through a rule and then coordinates all sensor systems and algorithms associated with the instance via a procedural attachment within the rule to complete the mission and return the results. Once the mission has been completed, the ontological framework will then select the next *Mission\_Sensor\_System* instance to coordinate, complete, and return the results. Since the ontological problem-solving framework is in a laboratory prototype stage, only a single mission is completed at a time. Also, if the *Mission* instance is matched to several *Matched\_Sensor\_System* instances, the same mission will be completed for each assignment regardless if it was previously completed. Improved systems can be developed that allow for simultaneous mission coordination, completion, and avoidance of repeating a mission, but the focus here is on proof-of-concept.

Figure 16. Sixteen new *Mission\_Sensor\_System* instances were returned with derived relationships after the inference cycle completed.

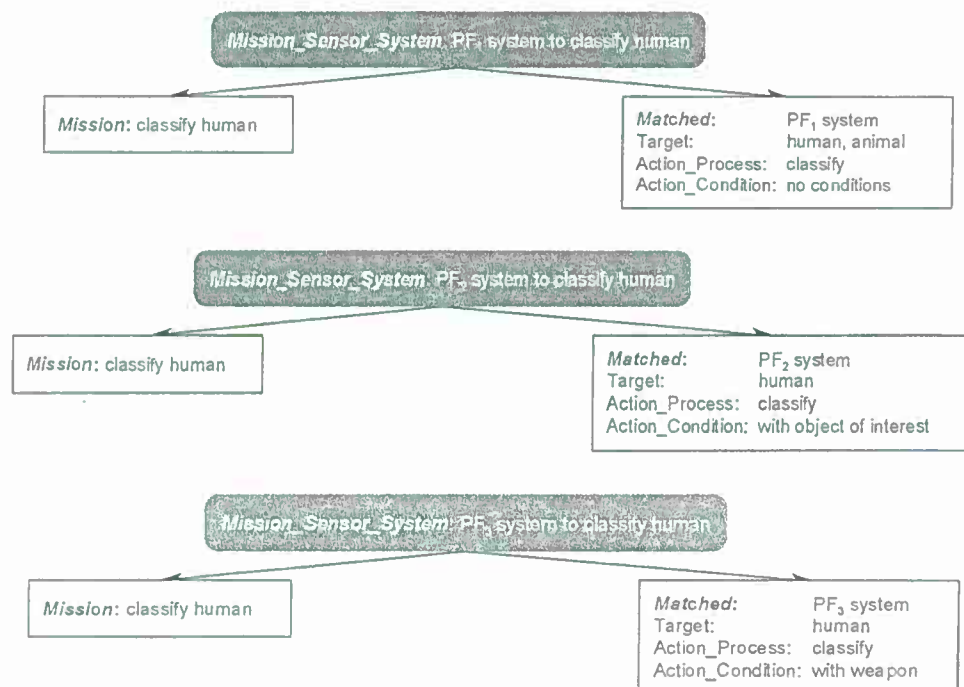




Figure 16. Cont.

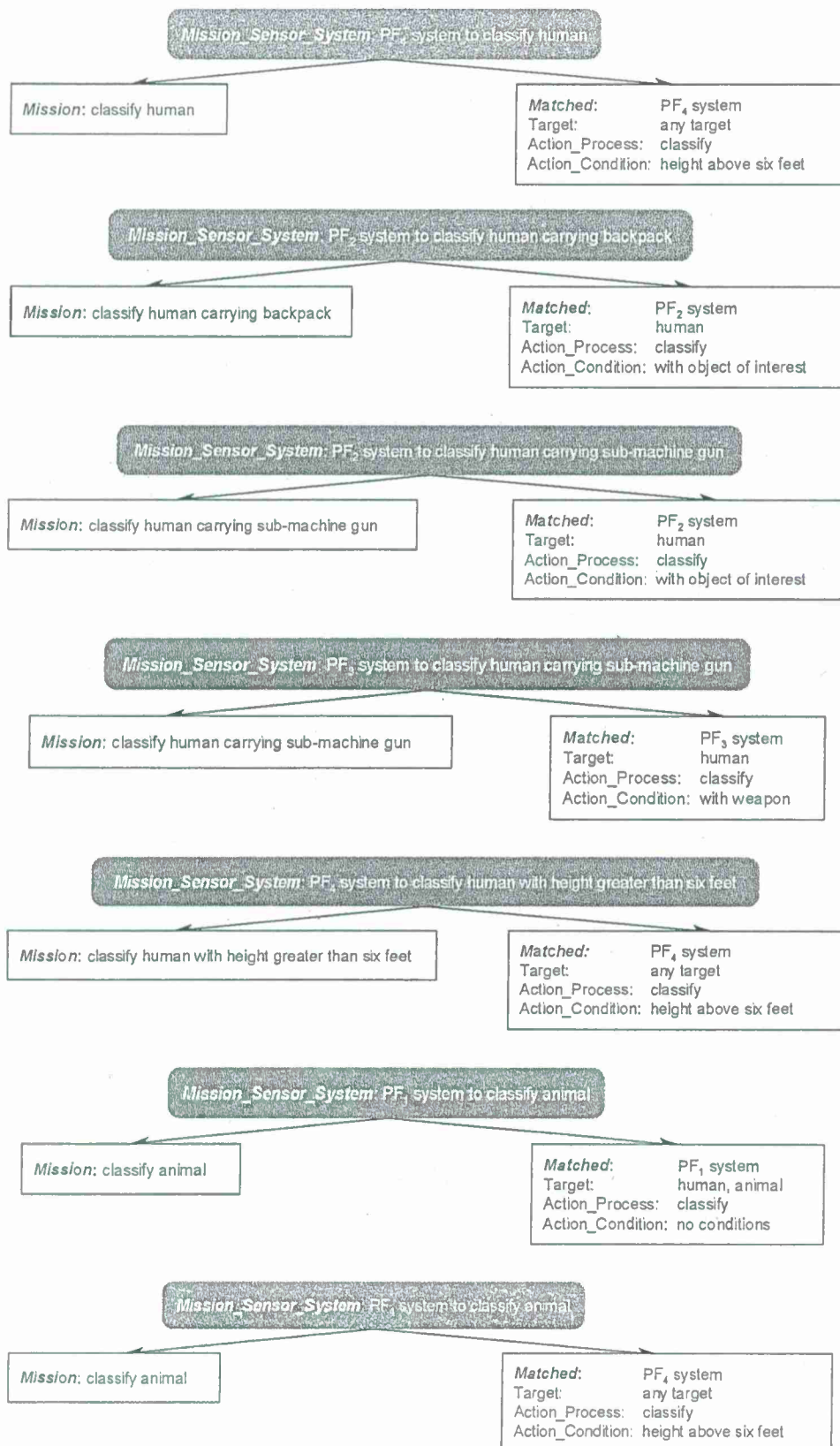
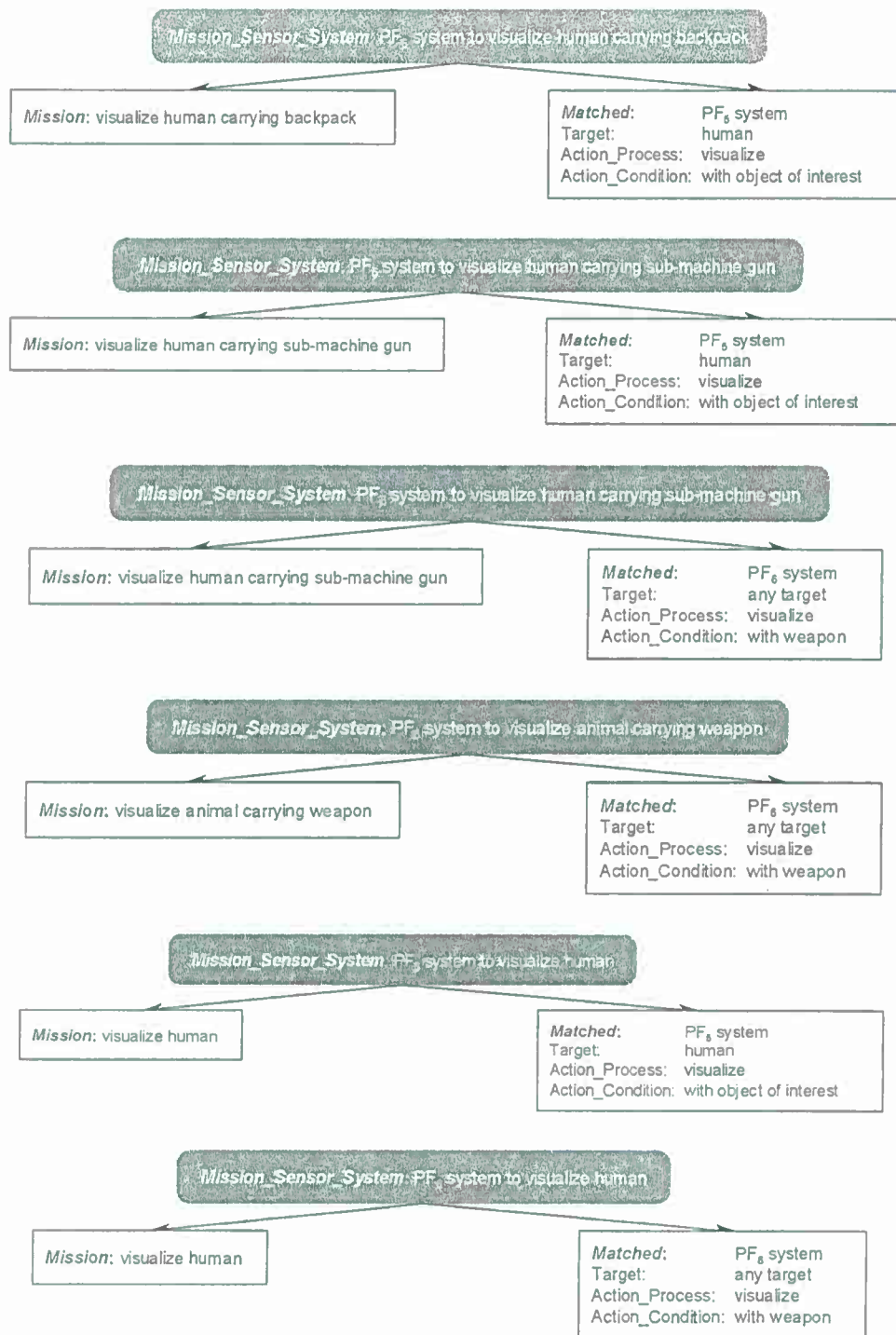


Figure 16. Cont.



## 8. Discussion

The challenge for the ontological problem-solving framework was to assign a synthesis of systems to subtasks of mission specifications. Even though the rules described in this paper contain relatively simple compatibility constraints among sensors, algorithms, and missions, these rules illustrate an

important proof-of-concept. Namely, a problem-solving approach to matching *Sensor* and *Algorithm* instances to form synthesized *Matched\_Sensor\_System* and *Profiling\_Sensor\_System* instances which are then assigned to high-level *Mission* instances to form a *Mission\_Sensor\_System* instance that is ready to be executed by the ontological framework or other autonomous systems for mission completion. It is important to note that multiple *Matched\_Sensor\_System* instances were reused and assigned to different *Mission* instances, which the *Matched\_Sensor\_System* instances were capable of satisfying. For example, the *Matched\_Sensor\_System* PF<sub>3</sub> instance, which is capable of visualizing a human carrying an object, was assigned to three different *Mission* instances that required the detection of “humans” with and without various objects, such as “weapons” or “backpacks”. It is important to realize that the *Mission\_Sensor\_System* is more than just sensors and algorithms assigned to a mission, the *Mission\_Sensor\_System* is a synthesized system, which is capable of performing the assigned subtasks to satisfy the overall mission specification and returning results for further analysis or more complex missions.

Rules in the ontological framework may operate on more than just properties of the various instances. For example, more complex rules may determine that certain *Mission\_Sensor\_System* instances may be composited together to satisfy more complex mission specifications. Possible complex *Mission* instances may include the detection of multiple targets and the tasking of other complex synthesized systems to monitor the targets for a specific time, which could be represented as a single *Mission\_Sensor\_System* instance. Other rules may even generate new missions or decompose missions into specifications for subtask assignment. Without leveraging ontologies, rules, the inference engine, and the concept of synthesized systems, all of the sensors and algorithms would need to be configured *a priori* for the anticipated missions and reconfigured for unanticipated missions. Most missions and subtasks are not known at the time of system deployment, therefore, a problem-solving approach may opportunistically assign synthesized systems to subtasks of high-level missions in real-time, which is an extremely important capability for dynamically changing requirements in a particular environment.

As discussed in the related work, many framework and middleware systems have been researched and developed to assign systems to missions. Some of the middleware systems used *a priori* matching of assets to mission tasks, such as Agilla [21-23], which limits the reuse of assets for other tasks without new matching occurring *a priori*. Other systems that use knowledge bases for sensor mission assignment [12-19] leveraged ontologies and other techniques for automated sensor mission assignment. As stated previously, the reasoning and use of knowledge engineering techniques by the authors for the prototype ontological framework is similar to other efforts in some aspects. The work described in this paper differs from these other works in that the domain of the missions and assets were limited to a persistence surveillance sensing environment. By limiting the domain, the research of the prototype ontological problem-solving framework could focus on providing a complete solution that not only assigns assets to missions but also includes a coordination system that connects to emulated assets and completes the mission.

Although the priority at this stage of this research is the logical problem-solving framework, another important aspect is performance. Performance can be analyzed along several dimensions, including scale-up analysis with solution finding, mission operation time, and mission completion rates. First, scale-up performance analysis is limited at this point, but the ontological framework can

scale to a very large number of instantiated sensors, algorithms and missions, limited only by physical memory constraints. The reasoning strategy used by the inference engine, along with the features expressible in the knowledge representation language, dictate the overall computational complexity, which in turn determines the time for the ontological framework to infer all combinations of sensors, algorithms, and missions. Performance can be increased by enabling the inference engine to check multiple sensors, algorithms, and missions in parallel or by invoking the inference engine multiple times in parallel, while having a strategy in place to eliminate redundant bindings.

Currently, the prototype ontological framework has been tested with fifty systems not detailed in this paper. The ontological framework takes less than two seconds to find all possible combinations, which equates to over 500 new combinations after the inference cycle completes. As more sensor systems and algorithms are added to the ontological framework, combinatorial explosion becomes an issue. Combinatorial explosion may be somewhat mitigated once asset resource control and time constraints are taken into account in the rules. First, as the number of systems increase, new systems for the ontological framework will need to be researched and developed that limit the number of solutions found and to determine the correctness of the proposed solution. Second, mission operation time is determined by how the ontological framework or other systems can execute and complete missions. To increase performance, the framework needs to operate missions in parallel and prioritize matched sensors and algorithms, which are assigned to different missions. Third, the prototype ontological framework described in this paper does not take into account competing missions, *i.e.*, resource management. New research is focusing on designing systems that provide information to the ontological framework for priority of missions, such as time constraints, availability of sensor systems and algorithms, *i.e.*, resource control and time difference between collection of data and mission time completion. Other mechanisms will need to be established that prevent a mission from never completing. For example, a mission may be to classify humans, but humans may never be detected thus locking the resources for that mission indefinitely. Placing time constraints on active missions may prevent the never ending mission.

## 9. Conclusions

Although the paper only shows PFx sensors, algorithms, and missions related to operation of those sensors and algorithms instantiated on the ontological framework, the principles and techniques that have been demonstrated may be appropriate for other types of sensors, algorithms, or missions. Development and deployment of new sensor systems and algorithms will continue to create challenges, such as discovering appropriate sensor systems and algorithms to satisfy tasks which may then be assigned to subtasks of mission specifications. The lack of explicit knowledge models used to describe the capabilities of sensor systems and algorithms and the specifications on high-level missions compounds the challenge even further. To allow the flexibility of assigning systems to unanticipated missions, the framework must leverage knowledge models, such as ontologies, rules, and inference engines, in a machine-interpretable format to perform automated synthesis and assignment of sensor systems and algorithms. The use of ontologies facilitates inference with rules allowing the prototype ontological problem-solving framework to autonomously reason about how a synthesis of systems may be formed and then assigned to missions. New research for the prototype is focusing on addressing the



issues raised in the discussion section, such as combinatorial explosion, resource constraints, mission completion time, and other areas. The problem-solving approach developed in this paper for the laboratory prototype ontological framework is the first step towards achieving reuse of systems without an *a priori* configuration, flexible assignment of synthesized systems to mission subtasks through automated inference, and addressing further issues affecting a framework's ability to autonomously coordinate assets.

### Acknowledgements

Funding for this work was provided in part by the U.S. Army Research Laboratory (ARL) award number: W911NF-10-2-0071, as well as funding from the Herff Fellowship program at the University of Memphis and support from Indiana University-Purdue University, Indianapolis. The findings and opinions expressed in this paper do not necessarily reflect the views of ARL or the U.S. government.

### References

1. Bergamaschi, F.; Conway-Jones, D.; Gibson, C.; Stanford-Clark, A. A distributed test framework for validation of experimental algorithms using real and simulated sensors. In *Proceedings of the First Annual Conference of the International Technology Alliance*, Washington, DC, USA, 25–27 September 2007.
2. Russomanno, D.J.; Kotari, C.; Thomas, O. Sensor ontologies: From shallow to deep models. In *Proceedings of the Thirty-Seventh Southeastern Symposium on Systems Theory*, Tuskegee, AL, USA, 20–22 March 2005.
3. Russomanno, D.J.; Kotari, C.R.; Thomas, O.A. Building a Sensor Ontology: A practical approach leveraging ISO and OGC models. In *Proceedings of the International Conference on Artificial Intelligence*, Las Vegas, NV, USA, 27–30 June 2005.
4. Goodwin, C.; Russomanno, D.J. An ontology-based sensor network prototype environment. In *Proceedings of the Fifth International Conference on Information Processing in Sensor Networks*, Nashville, TN, USA, 19–21 April 2006.
5. Goodwin, J.C.; Russomanno, D.J.; Qualls, J. Survey of semantic extensions to UDDI: Implications for sensor services. In *Proceedings of the International Conference on Semantic Web and Web Services*, Las Vegas, NV, USA, 25–28 June 2007.
6. Goodwin, J.C.; Russomanno, D.J. Ontology integration within a service-oriented architecture for expert system applications using sensor networks. *J. Expert Syst.* **2009**, *26*, 409–432.
7. Qualls, J.; Russomanno, D.J. Ontological problem-solving framework for dynamically configuring sensor systems and algorithms. *Sensors* **2011**, *11*, 3177–3204.
8. *TopBraid Composer Maestro (Version 3.3.2)*; TopQuadrant: Washington, DC, USA, 2001. Available online: <http://www.topquadrant.com/> (accessed on 6 July 2011).
9. Patel-Schneider, P.; Hayes, P.; Horrocks, I. *OWL Web Ontology Language Semantics and Abstract Syntax*; Available online: <http://www.w3.org/TR/owl-semantics/> (accessed on 6 July 2011).
10. Perez, J.; Arenas, M.; Gutierrez, C. Semantics and complexity of SPARQL. In *Proceedings of the Fifth International Semantic Web Conference*, Athens, GA, USA, 5–9 November 2006.

11. Steels, L. Procedural attachment. In *Proceedings of the Artificial Intelligence Memo 543*, Boston, MA, USA, 5–9 August 1979.
12. Gomez, M.; Preece, A.; Mel, G.D. Towards semantic matchmaking in sensor-mission assignment: Analysis of missions and means frameworks. In *Proceedings of the First Annual Conference of the International Technology Alliance*, Washington, DC, USA, September 2007.
13. Preece, A.; Gomez, M.; Mel, G.D.; Vasconcelos, W.; Sleeman, D.; Colley, S.; Porta, T.L. An ontology-based approach to sensor-mission assignment. In *Proceedings of the First Annual Conference of the International Technology Alliance*, Washington, DC, USA, September 2007.
14. Preece, A.; Gomez, M.; Mel, G.D.; Vasconcelos, W.; Sleeman, D.; Colley, S.; Pearson, G.; Pham, T.; Porta, T.L. Matching sensors to missions using a knowledge-based approach. In *Proceedings of the SPIE: Defense Transformation and Net-Centric Systems*, Orlando, FL, USA, 18–20 March 2008.
15. Arabshian, K.; Schulzrinne, H. Combining ontology queries with key word search in the GloServ service discovery system. In *Proceedings of the International Conference on Middleware*, Newport Beach, CA, USA, 26–30 November 2007.
16. Gomez, M.; Preece, A.; Johnson, M.P.; Mel, G.D.; Vasconcelos, W.; Gibson, C.; Bar-Noy, A.; Borowiecki, K.; Porta, T.L.; Pizzocaro, D.; *et al.* An ontology-centric approach to sensor-mission assignment. In *Proceedings of the Sixteenth International Conference on Knowledge Engineering and Knowledge Management*, Acitrezza, Italy, 29 September–2 October 2008.
17. Mel, G.D.; Sensoy, M.; Vasconcelos, M.; Preece, A. flexible resource assignment in sensor networks: A hybrid reasoning approach. In *Proceedings of the First Annual Workshop on the Semantic Sensor Web*, Crete, Greece, June 2009.
18. Rowaihy, H.; Johnson, M.; Brown, T.; Bar-Noy, A.; Porta, T.L. Sensor-mission matching: Centralized and distributed approaches. In *Proceedings of the First Annual Conference of the International Technology Alliance*, Washington, DC, USA, September 2007.
19. Sensoy, M.; Vasconcelos, W.; Mel, G.D.; Norman, T. Selection of sensors for missions using semantic-aware cooperative agents. In *Proceedings of the Third International Workshop on Agent Technology for Sensor Networks*, Budapest, Hungary, 8–12 May 2009.
20. Yao, Y.; Gehrke, J. Query processing for sensor networks. *IEEE Pervasive Comput.* **2004**, *3*, 46–55.
21. Fok, C.L.; Roman, G.C.; Hackman, G. A light weight coordination middleware for mobile computing. In *Proceedings of the Sixth International Conference on Coordination Models and Languages*, Pisa, Italy, 24–27 February 2004.
22. Fok, C.; Roman, G.; Lu, C. Mobile agent middleware for sensor networks: An application case study. In *Proceedings of the Fourth International Symposium on Information Processing in Sensor Networks*, Los Angeles, CA, USA, 25–27 April 2005.
23. Fok, C.; Roman, G.; Lu, C. Rapid development and flexible deployment of adaptive wireless sensor network applications. In *Proceedings of the Twenty-Fourth International Conference on Distributed Computing Systems*, Columbus, OH, USA, 6–9 June 2005.
24. Russomanno, D.J.; Trittenko, Y. A geographic information system framework for the management of sensor deployments. *Sensors* **2010**, *10*, 4281–4295.

25. Tritenko, Y.; Russomanno, D.J.; Qiu, Q. Managing sensor deployments with geographic information systems. In *Proceedings of the Sensors Applications Symposium*, New Orleans, LA, USA, 17–19 February 2009.
26. Whitehouse, K.; Zhao, F.; Liu, J. Semantic streams: A framework for composable semantic interpretation of sensor data. In *Proceedings of the Third European Workshop on Wireless Sensor Networks*, Zurich, Switzerland, 13–15 February 2006.
27. Liu, J.; Zhao, F. Towards semantic services for sensor-rich information systems. In *Proceedings of the Second IEEE/CreateNet International Workshop on Broadband Advanced Sensor Networks*, Boston, MA, USA, October 2005.
28. Kushwaha, M.; Amundson, I.; Koutsoukos, X.; Neema, S.; Sztipanovits, J. OASIS: A programming framework for service-oriented sensor networks. In *Proceedings of the Second IEEE/Create-Net/ICST International Conference on Communication System Software and Middleware*, Bangalore, India, 9–11 January 2007.
29. Eid, M.; Liscano, R.; El Saddik, A. A universal ontology for sensor networks data. In *Proceedings of IEEE Conference on Computational Intelligence for Measurement Systems and Applications*, Ostuni, Italy, 27–29 June 2007.
30. Sequeda, J.F.; Corcho, O.; Gómez-Pérez, A. Generating data wrapping ontologies from sensor networks: A case study. In *Proceedings of Second Semantic Sensor Network Workshop at International Semantic Web Conference*, Washington, DC, USA, 25–29 October 2009.
31. Janowicz, K.; Compton, M. The stimulus-sensor-observation ontology design pattern and its integration into the semantic sensor network ontology. In *Proceedings of the Third International Workshop on Semantic Sensor Networks*, Shanghai, China, 7–11 November 2010.
32. Kuhn, W. A functional ontology of observation and measurement. In *Proceedings of the Third International Conference on Geospatial Semantics*, Mexico City, Mexico, December 2009.
33. Neuhaus, H.; Compton, M. The semantic sensor network ontology: A generic language to describe sensor assets. In *Proceedings of AGILE Workshop on Challenges in Geospatial Data Harmonization*, Hannover, Germany, 2–5 June 2009.
34. Babitski, G.; Bergweiler, S.; Hoffmann, J.; Schön, D.; Stasch, C.; Walkowski, A. Ontology-based integration of sensor web services in disaster management. In *Proceedings of the Third International Conference of GeoSpatial Semantics*, Mexico City, Mexico, December 2009.
35. Compton, M.; Henson, C.; Lefort, L.; Neuhaus, H.; Sheth, A. A survey of the semantic specification of sensors. In *Proceedings of the Second International Workshop on Semantic Sensor Networks, Eight International Semantic Web Conference*, Washington, DC, USA, 25–29 October 2009.
36. Kobialka, T.; Buyya, R.; Leckie, C.; Kotagiri, R. A sensor web middleware with stateful services for heterogeneous sensor networks. In *Proceedings of the Third International Conference on Intelligent Sensors, Sensor Networks and Information*, Melbourne, Australia, 3–6 December 2007.
37. Open Geospatial Consortium; OGC: Wayland, MA, USA, 1994. Available online: <http://www.opengeospatial.org/> (accessed on 6 July 2011).
38. Cox, S. *Observations and Measurements Part 1—Observation Schema*; OpenGIS Implementation Standard OGC 07-022r1; Open Geospatial Consortium Inc.: Redlands, CA, USA, 2007.

39. Cox, S. *Observations and Measurements Part 2—Sampling Features*; OpenGIS Implementation Standard OGC 07-002r3; Open Geospatial Consortium Inc.: Redlands, CA, USA, 2007.
40. Botts, M.; Robin, A. *Sensor Model Language*; OpenGIS Implementation Standard OGC 07-000; Open Geospatial Consortium Inc.: Redlands, CA, USA, 2007.
41. Havens, S. *Transducer Markup Language*; OpenGIS Implementation Standard OGC 06-010r6; Open Geospatial Consortium Inc.: Redlands, CA, USA, 2006.
42. Na, A.; Priest, M. *Sensor Observation Service*; OpenGIS Implementation Standard OGC 06-009r6; Open Geospatial Consortium Inc.: Redlands, CA, USA, 2006.
43. Simonis, I.; Dibner, P.C. *Sensor Planning Service Implementation Specification*; OpenGIS Implementation Standard OGC 07-014r3; Open Geospatial Consortium Inc.: Redlands, CA, USA, 2007.
44. Simonis, I. *Sensor Alert Service Candidate Implementation Specification*; OpenGIS Implementation Standard OGC 06-028r3; Open Geospatial Consortium Inc.: Redlands, CA, USA, 2006.
45. Simonis, I.; Wytzisk, A. *Web Notification Service*; OpenGIS Implementation Standard OGC 03-008r2; Open Geospatial Consortium Inc.: Redlands, CA, USA, 2003.
46. Jacobs, E.; Chari, S.; Russomanno, D.; Halford, C. Profiling sensors for border and perimeter security. In *Proceedings of the SPIE Newsroom*, Bellingham, WA, USA, August 2009.
47. Chari, S.K.; Halford, C.E.; Jacobs, E. Human target identification and automated shape based target recognition algorithms using target silhouette. In *Proceedings of the SPIE: Infrared Imaging Systems: Design, Analysis, Modeling, and Testing XIX*, Orlando, FL, USA, 16–20 March 2008.
48. Chari, S.; Halford, C.; Jacobs, E.; Smith, F.; Brown, J.; Russomanno, D. Classification of humans and animals using an infrared profiling sensor. In *Proceedings of the SPIE: Unattended Ground, Sea, and Air Sensor Technologies and Applications XI*, Orlando, FL, USA, 13–17 April 2009.
49. Qualls, J.; Russomanno, D.J.; Bollu, V.K. Integration of a profiling sensor onto sensor fabric. In *Proceedings of the International Conference on Information and Knowledge Engineering*, Las Vegas, NV, USA, 25–27 August 2010.
50. Russomanno, D.J.; Yeasin, M.; Jacobs, E.; Smith, M.; Sorower, M.S. Sparse detector sensor: Profiling experiments for broad-scale classification. In *Proceedings SPIE-Defense and Security Symposium: Unattended Ground, Sea, and Air Sensor Technologies and Applications X*, Orlando, FL, USA, 17 March 2008.
51. Russomanno, D.; Chari, S.; Halford, C. Sparse detector imaging sensor with two-class silhouette classification. *Sensors* **2008**, *8*, 7996–8015.
52. Russomanno, D.J.; Chari, S.; Emmanuel, K.; Jacobs, E.; Halford, C. Testing and evaluation of profiling sensors for perimeter security. *ITEA J. Test Eval.* **2010**, *31*, 121–130.
53. Russomanno, D.J.; Chari, S.; Jacobs, E.; Halford, C. Near-IR sparse detector sensor for intelligent electronic fence applications. *IEEE Sens. J.* **2010**, *10*, 1106–1107.



# Toward Data-to-Decision Sensing Environments to Assess Human Intent from Responses to Stimuli

Cartik R. Kothari<sup>a</sup>, David J. Russomanno<sup>a\*</sup>, Ronald B. Sartain<sup>b</sup>, and Ronald Frankel<sup>c</sup>

<sup>a</sup>Department of Electrical and Computer Engineering  
Purdue School of Engineering and Technology, Indiana University-Purdue University  
Indianapolis, IN 46202 USA

<sup>b</sup>Primal Innovation LLC, Sanford, FL 32771 USA

<sup>c</sup>Army Research Laboratory, Adelphi, MD 20783 USA

## ABSTRACT

Remote detection of harmful intent is necessary for effective and appropriate countermeasures and will reduce risks to life and property. Trained human observers and sensor systems typically use facial expressions, gaits, gestures, perspiration, and a number of other observable characteristics as possible indicators of harmful intent with mixed results. It is proposed that responses of human subjects to external stimuli can be used as additional indicators of harmful intent in surveillance contexts. A variety of alerting stimuli, possible responses to the stimuli, features to be sensed by sensors, and the utility of these sensed features as indicators of harmful intent are discussed in this paper. An ontology-based data-to-decision framework for assessing human intent, which would leverage the formal representations of the alerting stimuli, as well as the variety of possible responses, is proposed in the context of Semantic Web infrastructure.

**Keywords:** Intent Detection, Data-to-Decision Framework, Surveillance, Human Behavior, Ontology.

## 1. INTRODUCTION

The ability to remotely detect the covert intent of humans is very useful from the perspective of security. According to a report by the Army Research Laboratory,<sup>1</sup> such a capability will greatly mitigate the risks involved in military surveillance, especially in hostile environments, and enable the adoption of appropriate and timely countermeasures to threatening situations. These capabilities and benefits can extend to non-military security applications as well, including intelligent border-monitoring applications. Video footage from monitored areas, ranging from border checkpoints to shopping malls, can be used in a preventive capacity in addition to its current primary usage for post-incident investigations. Automated intent detection from video surveillance, as well as from the percepts sensed from other sensors will potentially neutralize the deleterious effects of human observer fatigue. Research studies show even the attention of well-trained security guards drops to unacceptable levels after only 20 minutes of continuously viewing and analyzing video footage.<sup>2</sup>

A number of approaches to human intent detection, using trained human observers, as well as tracking methods in video cameras, have been adopted at various monitored areas, such as airports and border checkpoints with mixed success. These include scrutinizing facial expressions, gaits, movements, and gestures.<sup>3,4</sup> At a basic level, intent detection approaches involve modeling and classification of tracked human movement or expression with certain rules. More advanced approaches involve the use of thermal and infrared imagers that measure pulse and heart rates, or even display patterns of blood circulation and body temperature. The effectiveness of these techniques as indicators of hostile intent is not well established at this time.<sup>5,6</sup>

This paper investigates the use of a novel data-to-decision framework for intent detection, using the responses of human subjects to an alerting stimulus. The responses of the subjects to the stimulus can be used as indicators of harmful intent. Consider the data fusion model proposed by the Joint Directors of Laboratories

---

\*Further author information: (Send correspondence to D.J.R.)

D.J.R.: E-mail: drussoma@iupui.edu, Telephone: 1 317 274 0802, Fax: 1 317 274 4567,  
Department Website: [www.engr.iupui.edu](http://www.engr.iupui.edu)

(JDL),<sup>7</sup> augmented with a knowledge management component in Figure 1.<sup>8</sup> These six fusion levels cover both "automated" and "human in the loop" processing of data and knowledge. The model can be used to frame the concept of autonomous algorithms and human users contributing to an evolving solution state in which fused information may enable the identification and assessment of strategies and tactics for counterintelligence<sup>8-10</sup>

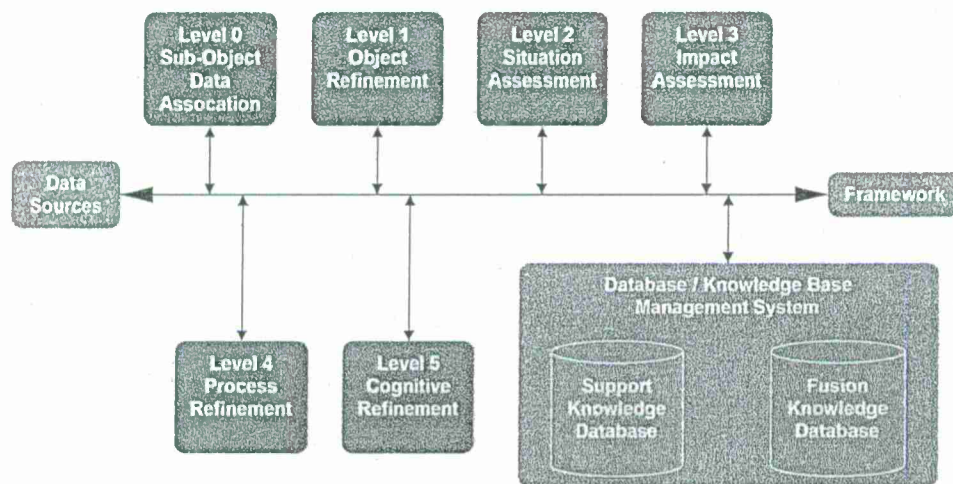


Figure 1. Six levels of the data fusion model augmented with a data and knowledge management system.

## 2. SURVEILLANCE AND INTENT DETECTION

Stimuli can be synthesized and introduced into a sensed environment to assess the reaction of humans. Depending of the background context and environment, a human's reaction to the stimuli may be supportive information that can incrementally contribute to an evolving hypothesis about the intent of the humans. Audible stimuli, such as a recorded human voice reading out a message, or a sound such as the breaking of a twig, or the cocking of a bolt-action rifle, may be used. Flashing lights, a swiveling lamp turning on and tracking the movement of the subject(s), or even an increase in illumination intensity are examples of visual stimuli, which may be more effective at night. The choice of stimulus may be context dependent as well. For example, some stimuli, such as the sound of a rifle being chambered may be more appropriate in a combat zone. The devices that generate stimuli are generally inexpensive and easily camouflaged. However, they may be effective in altering the behavior of the human subjects in many cases, eliciting a variety of responses from individuals and groups, which may be useful in assessing their intent. Let us examine each of the potential stimuli separately.

### 2.1 Alert Stimuli and Responses of Individuals

Suicide bombers are an extreme example of the threat posed by individuals in military installations, airports, and other public places. Every year, security officers trained in profiling passengers on the basis of their general behavior and body language detain thousands of passengers for further screening and questioning at airports around the U.S. and abroad. While arrests and detainment are relatively rare, most of these arrests are for prior convictions that are revealed by background checks and not because of any identified hostile intent.<sup>5</sup> Similarly, security personnel manning secured areas, such as military bases around the world, look for telltale signs in human subjects.

Given the high stakes for suicide bombers and the high levels of anxiety, alert stimuli may be particularly helpful in exposing their intentions. Consider the possible responses of a suicide bomber to an alert message or to flashing lights at night, which may be triggered manually by personnel who observe suspicious behavior. A trained terrorist willing to die for his cause is very unlikely to turn away; instead the response will more likely be a panic stricken rush towards a crowded area in a public space or at least an area manned by security or

defense personnel at a border checkpoint or barrier. In such cases, additional sensors, such as metal detectors and infrared scanners may be deployed to confirm the threat and suitable preventive measures taken to effectively neutralize the threat or at least minimize the destruction to life and property.

Security personnel are also interested in apprehending people attempting to smuggle contraband and prohibited items into the country at international airports, seaports, and borders. Alerting stimuli triggered by suspicious behavior may prompt a smuggler at an airport to attempt to hide or leave the passenger concourse altogether for the aircraft parking areas and taxiways through the secured entry points and ramps. The miscreant can be easily apprehended in such cases. At seaports and at borders, the decision of a suspect to alter course and try an alternate route to evade authorities is a reliable indicator of intention. At land borders, suspects could turn back to the country of origin but still be apprehended by the authorities on their own territory.

Now consider the effect of an alert stimulus on a false positive, a regular benign human subject. Radical changes in behavior such as trying to escape or evade authorities or breaking into a frenzied rush are typically uncommon responses. In most cases, such subjects may stop or adopt similar cooperative behavior patterns. Passengers at an airport rushing to catch a flight or hassled by delays and long or inconvenient travel schedules are more likely to adopt a hostile or defensive attitude in response, but again they are very unlikely to adopt the behavioral patterns of terrorists or felons. At a military checkpoint or barrier, alerting stimuli may inconvenience or irritate a falsely identified subject but again, will not inconvenience the people at large.

Note how alerting stimuli in these examples can positively identify a human subject with malicious or hostile intent from among a crowd even before they approach the security checkpoints. Valuable moments of time, which may mean the difference between destruction and prevention, may be gained by this approach. Inconvenience to the public at large will be minimized; sometimes they may even cooperate in the apprehension of a suspect on the move before the arrival of security personnel. It should be noted because of cost considerations, sophisticated sensors may not be widely deployed in all public spaces except at places of vital importance such as airports, government buildings, and famous monuments and landmarks. In such cases, alert stimuli generated by inexpensive devices alone can be very effective in identifying potential threats to public security.

Across international borders (e.g., U.S.-Canada and U.S.-Mexico) where much of the length of the border is strewn ("dusted") with vibration sensors or profiling sensors, strategically positioned devices that generate alert stimuli may prompt individuals to alter their course and redirect them to selective locations (Section 2.3) where more capable and well-camouflaged sensors, such as metal detectors and infrared cameras are placed. Whether the subjects have benign or malignant intentions, such subjects can be better identified and intercepted as necessary. Course altering behavior can also help in determining the intent of groups of people as discussed in the next subsection.

## 2.2 Alert Stimuli and Responses in Groups of People

Groups of people driven by hostile intent at a militarized zone may be harder to identify if they use very effective concealment techniques. Consider a protesting group of people just outside a military base or at a checkpoint that includes a well-concealed gunman or someone brandishing a Molotov cocktail. Such threats are very hard to identify by conventional surveillance techniques. Alerting stimuli may not be of much use in such situations, except in case someone panics.

At international borders, a variety of stimuli may be used to identify telltale behavioral patterns. A simple audible alert or flashing lights may cause harmless subjects, villagers walking along the border on their way home for example, to call out to identify themselves or stop or similar cooperative behavior. Subjects attempting an illegal crossing may attempt to hide, change course, or damage and destroy any equipment that they can identify. Occasionally, they may even go back the way they came. Diversions from the course may have the desired effect of concentrating a large number of people into a small area (Section 2.3) where more advanced sensing techniques may be deployed to determine if they are wearing uniforms, armed, or carrying contraband. Deployed advanced sensors may be activated opportunistically in such cases to refine the situation assessment.

In a border surveillance context, additional stimuli could be used apart from the auditory and visual stimuli. Trip wires could be raised to cause some members of a group to fall. This may cause a variety of sounds to be detected by a sensitive microphone, such as metallic sounds if the group is carrying guns. An arm in a vertical



position could be caused to drop. Such events can cause predictable responses in the group from which intent may be putatively assessed. An armed group advancing towards a checkpoint with the intention to attack may freeze, scan the area, and wait for other sounds. Or they may decide to press on full speed ahead to try and storm the outpost. In either case, more sensors may be activated to study the group. If additional sensed data confirms the armed status of the group, more aggressive countermeasures can be employed. The choice of stimulus may also decide the type of response from the group. The sound of a rifle being chambered may elicit a more aggressive response from an armed group than the sound of a breaking twig or a birdcall; for example, freeze and scan in the latter case as opposed to war cries and charge in the former.

### 2.3 Constrained Environments for Border Surveillance

Simple devices that alert human subjects can be used in a landscaped environment, effectively diverting human subjects into a small area where state-of-the-art sensing devices have been deployed. For example, consider the harsh desert conditions typical of much of the U.S.-Mexico border. Possible route choices for human subjects at the border can be artificially constrained by a synthesized lake for example, or by the cultivation or transplantation of thorny desert plants, such as cacti that restrict movement through the plants. At night, effective use of lighting can be used to similar effect. The area can be landscaped with lakes, thorny plants, and other artifacts such that human subjects are forced to move towards constrained areas where more advanced sensing devices have been deployed. In the example of the artificial lake, thirsty human subjects in a desert environment are very likely to be drawn to the water. Access to the water itself can be restricted to one (or a few more) points where advanced sensors are deployed. These ideas can leverage existing work in the use of landscaping for crime prevention and surveillance from a criminal justice perspective.<sup>11</sup> Such ideas will also require collaborative work with researchers in behavioral and cognitive science, as well as with experts in ecology and environmental science.

## 3. FORMALIZING CONTEXTS, ALERT STIMULI, RESPONSES, AND INTENTS

The previous section discussed the possible contexts in which alerting stimuli could be applied to determine the intent of human subjects, the variety of stimuli that could be used, the possible responses to these stimuli, and how these could be used as indicators of intent. The purpose of the next section is to begin the presentation of a formal approach to defining these contexts, stimuli, responses, and intents towards inclusion of these definitions in a Semantic Web ontology.<sup>12</sup>

### 3.1 An Ontology for Response-based Intent Detection

Semantic Web ontologies contain formal, logic-based definitions of concepts and inter-concept relationships that are pertinent to a knowledge domain. Each of the defined concepts and relationships is assigned a specific Uniform Resource Identifier (URI), which is an accessible location on the Web. The ontology containing the definitions has a unique Web address and each of the defined concepts and relations corresponds to a specific subsection of this address. An ontology for intent detection will include definitions of contexts, stimuli, behavioral responses, and intents. Each of these concepts is discussed in the following subsections.

#### 3.1.1 Contexts

Response-based intent detection can be used in many contexts. Contexts are defined as combinations of locations and times. Times are simple attributes that can take on a value from a set of values including wartime and peacetime. Locations include international land and sea borders, airports, military bases, seaports, government buildings, national monuments, famous landmarks, and other areas of vital importance. Figure 2 shows a preliminary definition of the *Application\_Context* concept using constructs from the Web Ontology Language (OWL). Note OWL concepts are the same as UML classes. These words, concepts and classes, are used interchangeably in this paper.



```

<owl:Class rdf:about="#Application_Context">
  <rdfs:subClassOf>
    <owl:intersectionOf rdf:parseType="Collection">
      <owl:Restriction>
        <owl:onProperty rdf:resource="#inTime"/>
        <owl:cardinality rdf:datatype="&xsd;NonNegativeInteger"> 1 </owl:cardinality>
      </owl:Restriction>
      <owl:Restriction>
        <owl:onProperty rdf:resource="#atLocation"/>
        <owl:cardinality rdf:datatype="&xsd;NonNegativeInteger"> 1 </owl:cardinality>
      </owl:Restriction>
    </owl:intersectionOf>
  </rdfs:subClassOf>
</owl:Class>

```

Figure 2. OWL definition for *Application\_Context*

### 3.1.2 Alert stimuli

Alert stimuli are broadly categorized into auditory, visual, and others. From the discussion in Section 2, each of these categories may be defined as sub-concepts of the *Stimulus* concept or they may be defined as enumerated values. Given that several types of auditory and visual stimuli can be used, it makes sense to define them as full-fledged sub-concepts of the *Stimulus* concept as shown in Figure 3. The sub-concepts can be instantiated by stimuli, such as flashing lights (*Visual\_Stimulus* instance) and a trip wire being raised (*Others* instance).

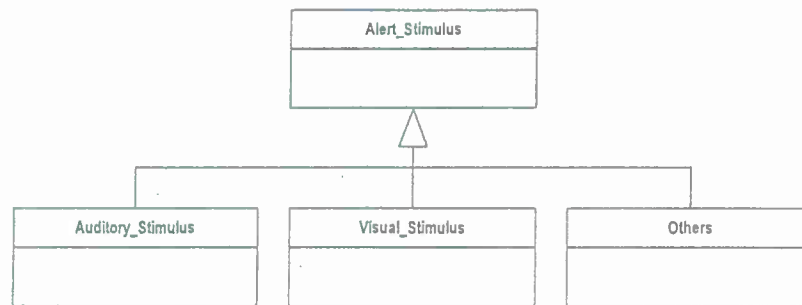


Figure 3. *Alert\_stimulus* class hierarchy.

### 3.1.3 Responses

Possible responses of human targets to alert stimuli include freezing, calling out, charging, war cries, panicking, changing course of movement, hiding, rushing forward, going back the way they came, and attempting to sabotage or destroy surveillance equipment. These actions can all be instances of the *Response* concept in an OWL ontology.

### 3.1.4 Intents

Intents can be classified as hostile or non-hostile at a very high level. Assessment of intent is dependent upon the alert stimulus that was incident upon the human subject(s), the context (the location and time) when it was used, and the recorded behavioral response(s) of the subject(s) to the stimulus. This can be defined as a production rule where each of the parameters that influence the assessed intent is an antecedent while the assessed intent is the consequent. Note the intent can also be defined as a restriction class (named *Assessed\_Intent*) in OWL with three essential associations with the *Application\_Context*, *Alert\_Stimulus*, and *Response* concepts as shown in Figure 4. Figure 5 shows an example of a production rule conforming to these associations shown in Figure 4.

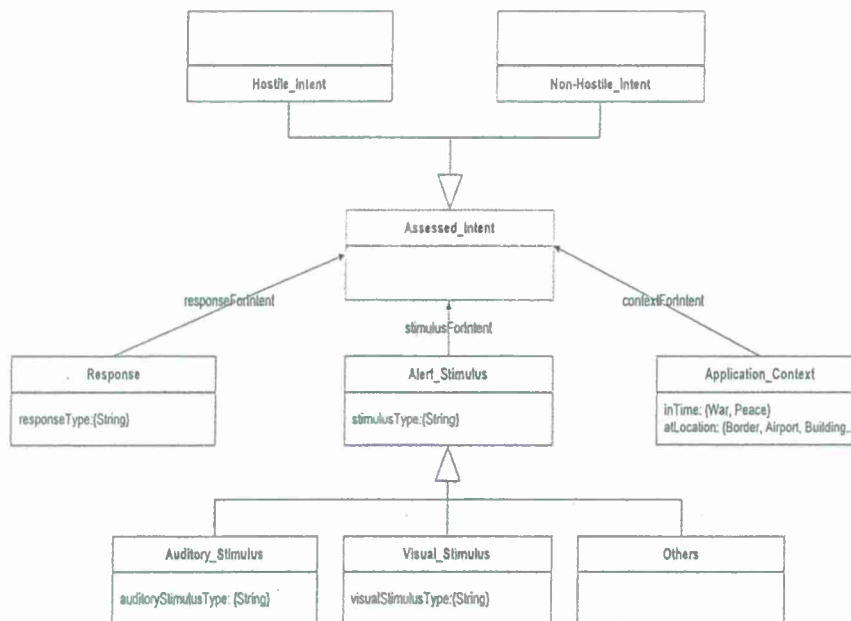


Figure 4. *Assessed\_intent* class.

```

instanceOf(?intent, Assessed_intent), responseForIntent(?charge,?intent),
stimulusForIntent(?sound,?intent), contextForIntent(?appCtx, ?intent),
instanceOf(?appCtx, Application_Context), inTime(?appCtx, "War"),
atLocation(?appCtx, "Border"), instanceOf(?sound, Auditory_Stimulus),
auditoryStimulusType(?sound,"rifle_loaded"), instanceOf(?charge, Response),
responseType(?charge, "charge")
:-
instanceOf(?intent, Hostile_intent).
  
```

Figure 5. Production rule for inferring *Assessed\_intent*

Note each of the attributes in the classes *Response* and *Alert\_Stimulus* can be defined as OWL datatype properties, which take enumerated string values. However, each of these values can be reified into classes of their own in the long term following best practices recommendations.

### 3.2 Automation of Intent Detection

The development of an ontology, with concepts described in the last section, is central to the development of a data-to-decision framework to automatically provide an assessment of the threat posed by human subject(s) under surveillance. The framework would likely use production rules implemented in Jess<sup>13</sup> or other similar rule-based engines to provide a numerical estimate of the likelihood of threat from the human subject(s) under surveillance. In the interest of reusability and interoperability, we propose the use of Semantic Web<sup>14</sup> compatible probabilistic reasoning engines, such as Pronto,<sup>15</sup> an implementation of Semantic Web compatible uncertainty reasoning.<sup>16</sup>

#### 4. RELATED WORK AND CONCLUSIONS

The idea of using human behavior to identify hostile intent and deception is a very old one. A system capable of detecting intent from video surveillance footage was patented in 1997.<sup>17</sup> Cohen et al.<sup>4</sup> have proposed an intent detection system using Point-light Walker (PLW) displays of human motion. This work leverages previous research into identifying the emotional state of humans using motion cues.<sup>18</sup> Tracked human movement is compared with recorded data from actors in a simulated environment as proposed by Frank et al.<sup>19</sup>

Alerting stimuli may significantly impact the efforts to remotely assess the intent of human subjects. In the examples discussed in this paper (Section 2), alert stimuli of different kinds are capable of eliciting predictable responses from individuals and groups under surveillance, all of which may not be possible with conventional sensing methodologies. They have the desirable effect of necessitating the use of more advanced and power consuming sensing techniques only when required and only to refine the assessment of threat. In addition, alert stimuli can potentially evoke telltale responses from suspects well in advance of their approaching a sensitive checkpoint or barrier, improving the prospects of effective countermeasures and threat neutralization. Inconveniences caused to the general public at large by the current practice of security checkpoint profiling will also be significantly reduced.

A data-to-decision framework for estimating the likelihood of hostile intent in human subject(s) based upon the responses of the subjects to an alerting stimulus has been outlined. A number of application contexts, alerting stimuli, and possible responses to the stimuli have been discussed and defined in a formal Semantic Web ontology. This ontology is necessary to automate the process of threat identification and assessment in the future.

#### ACKNOWLEDGMENTS

Funding for this work was provided in part by the U.S. Army Research Laboratory (ARL) award number: W911NF-10-2-0071, as well as support from Purdue School of Engineering and Technology, IUPUI. The findings and opinions expressed in this paper do not necessarily reflect the views of ARL or the U.S. government.

#### REFERENCES

- [1] Bornstein, A., Damarla, T., Lavery, J., Morelli, F., and Schmeisser, E., "Remote detection of covert tactical adversarial intent of individuals in asymmetric operations," Special report. U.S. Army Research Laboratory, Aberdeen, MD. (2010).
- [2] Gouaillier, V., "Intelligent video surveillance : Promises and challenges technological and commercial intelligence report," *Security* (March) (2009).
- [3] Ko, T., "A survey on behavior analysis in video surveillance for homeland security applications," in [*Proceedings of the 2008 37th IEEE Applied Imagery Pattern Recognition Workshop*], *AIPR '08*, 1-8, IEEE Computer Society, Washington, DC, USA (2008).
- [4] Cohen, C., Morelli, F., and Scott, K., "A surveillance system for the recognition of intent within individuals and crowds," in [*Technologies for Homeland Security, 2008 IEEE Conference on*], 559 -565 (May 2008).
- [5] Weinberger, S., "Airport security: Intent to deceive?," *Nature* 465(7297), 412-5 (2010).
- [6] Bond Jr., C. F., "Commentary a few can catch a liar, sometimes: Comments on ekman and O'Sullivan (1991), as well as ekman, O'Sullivan, and frank (1997)," *Applied Cognitive Psychology*, 22(9): 1298-1300 (2008).
- [7] Steinberg, A. N., Bowman, C. L., and White, F. E., "Revisions to the jdl data fusion model," *Sensor Fusion: Architectures, Algorithms, and Applications III* 3719(1), 430-441, SPIE (1999).
- [8] Llinas, J., Bowman, C. L., Rogova, G. L., Steinberg, A. N., Waltz, E. L., and White, F. E., "Revisions and extensions to the JDL data fusion model II," in [*Proceedings of the Seventh International Conference on Information Fusion*], Svensson, P. and Schubert, J., eds., II, 1218-1230, International Society of Information Fusion, Mountain View, CA (June 2004).
- [9] JHAPL, [*Rethinking the JDL Data Fusion Levels*] (June 2004).
- [10] Blasch, E. P. and Plano, S., "Jdl level 5 fusion model: user refinement issues and applications in group tracking," *Signal Processing, Sensor Fusion, and Target Recognition XI* 4729(1), 270-279, SPIE (2002).

- [11] Crowe, T., [*Crime Prevention Through Environmental Design*], Butterworth-Heinemann, 2 ed. (July 1991). ISBN-10: 0750690585.
- [12] Gruber, T. R., "A translation approach to portable ontology specifications," *Knowl. Acquis.* 5, 199-220 (June 1993).
- [13] Friedman-Hill, E., [*Jess in Action: Java Rule-Based Systems*], Manning Publications (July 2003). ISBN-10: 1930110898.
- [14] Berners-Lee, T., Hendler, J., and Lassila, O., "The Semantic Web A new form of Web content that is meaningful to computers will unleash a revolution of new possibilities," (2001).
- [15] Klinov, P., "Pronto: A non-monotonic probabilistic description logic reasoner," in [*The Semantic Web: Research and Applications*], Bechhofer, S., Hauswirth, M., Hoffmann, J., and Koubarakis, M., eds., *Lecture Notes in Computer Science* 5021, 822-826, Springer Berlin / Heidelberg (2008). 10.1007/978-3-540-68234-9\_66.
- [16] Stoilos, G., Simou, N., Stamou, G., and Kollias, S., "Uncertainty and the semantic web," *Intelligent Systems, IEEE* 21, 84-87 (September - October 2006).
- [17] Aviv, D., "Abnormality detection and surveillance system," in [*United States Patent*], (5666157) (1997).
- [18] Montepare, J. M., Goldstein, S. B., and Clausen, A., "The identification of emotions from gait information," *Journal of Nonverbal Behavior* 11, 33-42 (1987). 10.1007/BF00999605.
- [19] Frank, M. G., Menasco, M. A., and O'Sullivan, M., [*Human Behavior and Deception Detection*], John Wiley & Sons, Inc. (2008).



# Optical Engineering

[SPIEDigitalLibrary.org/oe](http://SPIEDigitalLibrary.org/oe)

## Image plane coded aperture for terahertz imaging

Orges Furxhi  
Eddie L. Jacobs  
Chrysanthe Preza



# Image plane coded aperture for terahertz imaging

Orges Furxhi  
Eddie L. Jacobs  
Chrysanthé Preza  
University of Memphis  
Department of Electrical and Computer  
Engineering  
Memphis, Tennessee 38152  
E-mail: ofurxhi@memphis.edu

**Abstract.** In the absence of detector arrays, a single pixel coupled with an image plane coded aperture has been shown to be a practical solution to imaging problems in the terahertz and sub-millimeter wave domains. The authors demonstrate two laboratory, real-time, two-dimensional, sub-millimeter wave imagers that are based on an image plane coded aperture. These active imaging systems consist of a heterodyne source and receiver pair, image forming optics, a coded aperture, data acquisition hardware, and image reconstruction software. In one of the configurations, the target is measured in transmission, while in the other it is measured in reflection. In both configurations, images of the targets are formed on the coded aperture, and linear measurements of the image are acquired as the aperture patterns change. Once a sufficient number of linearly independent measurements are obtained, the image is reconstructed by solving a system of linear equations that is generated from the aperture patterns and the corresponding measurements. The authors show that for image sizes envisioned for many current applications, this image reconstruction technique is computationally efficient and can be implemented in real time. Measurements are collected with these systems, and the reconstruction results are presented and discussed. © 2012 Society of Photo-Optical Instrumentation Engineers (SPIE). [DOI: 10.1117/1.OE.51.9.091612]

**Subject terms:** sub-millimeter wave imaging; terahertz imaging; spatial light modulator; coded apertures; terahertz; compressive sensing.

Paper 120211SSP received Feb. 15, 2012; revised manuscript received Apr. 18, 2012; accepted for publication Apr. 20, 2012; published online Jun. 15, 2012.

## 1 Introduction

The interest in terahertz imaging is motivated by the ability of terahertz (THz) frequencies to penetrate most manmade materials, particularly clothing.<sup>1-3</sup> Additionally, many harmful chemicals and explosives display absorption lines that make them identifiable by THz.<sup>4,5</sup> These characteristics of THz make it attractive for security applications. Unfortunately, THz imaging is one of the last electromagnetic imaging modalities for which focal plane arrays are still impractical and/or too costly to be used in practical security applications. An intermediate solution has been the development of scanning systems. These, however, have their own cost, weight, power, and frame rate limitations.

Our interest is focused in the part of the THz spectrum between 300 GHz and 3 THz, which is referred as the sub-millimeter wave region. This interest is motivated by the availability of mature single detector technologies at these frequencies. Both active and passive imaging configurations at these frequencies have been successfully demonstrated, and now the new frontier in sub-millimeter wave imaging is faster image frame rate and smaller size, weight, power consumption, and cost. Passive systems that operate at close to real time require cooled detectors and tend to have very large form factors.<sup>6,7</sup> Images from these systems are similar to infrared images and provide temperature difference/contrast information. On the other hand, the images acquired with active imagers, that are usually coherent, have very high dynamic range and suffer from the specular reflections and clutter in the scene. However, this phenomenon can be mitigated by using the imager in radar mode

as demonstrated by Cooper.<sup>8</sup> An advantage of active systems is that they operate at room temperature and their form factor is usually limited by the optical aperture rather than the detector and source modules. This makes active systems attractive for applications that require the imager to be portable and operate at stand off ranges.

Awaiting the development of practical and inexpensive focal plane arrays for sub-millimeter wave imaging, other alternatives that exploit the maturity of the single pixel detector have been explored. In particular, we have focused our efforts on spatial light modulators (SLM) for sub-millimeter waves and their application as image plane coded apertures.<sup>9,10</sup> Spatial light modulators work in reflection mode or in transmission mode. Perhaps the most well-known reflective SLM is the Texas Instruments digital micro-mirror device (DMD) known for its use in the Rice University single pixel camera,<sup>11</sup> or in most modern day projectors. A reflective SLM for sub-millimeter waves has been proposed by Lukkanen<sup>12</sup> and entails using an electronically controlled reflect-array that can be used as a beam steerer. However, this work is in its design phase.

An example of transmissive SLM is the liquid crystal optical modulators common in display applications. There have been some efforts to use metamaterials to develop an electronically controlled transmissive SLM<sup>13</sup> for THz, but the modulation depth of that device did not exceed 40%, with a minimum transmission coefficient of 0.3 and maximum of 0.7. Higher modulation depths are preferred for most sub-millimeter wave imaging applications. Another approach that is being investigated for transmissive THz modulators is the use of microelectromechanical systems (MEMS) reconfigurable sub-wavelength metallic slits.



Although this work is promising, but so far only analysis and small scale devices for proof of concept have been demonstrated.<sup>14,15</sup>

The lack of high power illumination sources in the sub-millimeter wave regime and the atmospheric absorption require special consideration for the efficiency of SLMs for sub-millimeter waves. Practical implementations of optical systems for SLMs where the image plane is being modulated favor transmission mode devices. The energy that passes through the SLM transmission mode device can be collected and channeled to the detector, whereas the energy reflected by the SLM reflection mode device will be diffracted away from the detector.

We have developed a mechanically scanned SLM for sub-millimeter waves that serves as an image plane coded aperture. Although a mechanically scanned system, our device has low mechanical complexity, provides high modulation levels and high scanning rates, and has low cost. At the core of this device is a rotating disk with holes that spins at a constant speed. The image is formed on one portion of the disk and is transmitted through the holes onto the single pixel receiver. Linear measurements are made on the image as the disk rotates. An image is reconstructed using the knowledge of the hole patterns and the measured signal from the receiver.

We have previously presented the electromagnetic analysis and design of this device as well as a working example of a line image plane coded aperture as part of a line imager.<sup>9,10</sup> In this paper we describe and demonstrate a two-dimensional version of the device that is used to form  $64 \times 64$  pixel sub-millimeter wave images. Sub-millimeter wave images are formed in transmission mode and in stand-off reflection mode. In transmission mode, a transmissive target is projected onto the device. In stand-off mode, the target is placed 10 m away from the imager and an image of it is formed on the device through an optical system. The next section introduces the image plane coded aperture device and the mathematical formulation of the forward imaging problem with this coded aperture. In Sec. 3, we present an image reconstruction method and discuss the effect of the reconstruction parameters on the relative reconstruction error of the solution. We present results from simulations for two imaging configurations of interest. In Sec. 4 we describe the implementation of the image plane coded aperture and the imaging setups. Images formed using the device are presented and discussed in Sec. 5. Based on the discussion in Sec. 5 and the results from the simulations presented in Sec. 3, we conclude with some recommendations for future work.

## 2 Two-Dimensional Image Plane Coded Aperture

A conceptual sketch of the image plane coded aperture is shown in Fig. 1. The device is placed in the image plane of the imager, and an image is formed over the imaging window. The image is scanned with a spinning disk that is patterned with holes. The detector is sampled continuously and each measurement sample is associated with the pattern of holes in the imaging window at the sample instant. Once the required measurements are recorded, the image is reconstructed. The central component of the coded aperture is the spinning disk with holes located at random positions. The placement of the holes and their sizes depend on the largest imaging wavelength,  $\lambda_{\max}$ . Electromagnetic analysis<sup>10</sup> has shown that for a disk of thickness around three  $\lambda_{\max}$  the

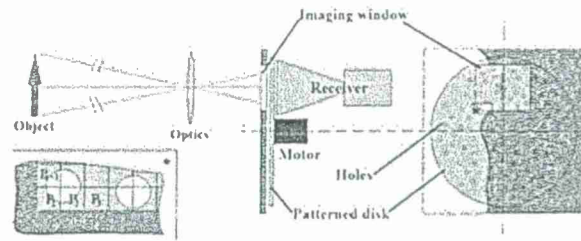


Fig. 1 Conceptual drawing of the coded aperture placed in the image plane of the imaging system. Insert: arbitrary division of the imaging window into pixels.

minimal hole radius should be greater than  $1.4\lambda_{\max}$  and the minimal edge to edge separation between holes should be one  $\lambda_{\max}$ . As long as the radius of the holes and the depth increase proportionally, transmission and linearity are preserved. Because of the assumptions of the image reconstruction method, the transmission of each hole must be unity, and transmission from many holes must be linear.

Another component of importance is the collecting horn placed behind the imaging window and the disk. This collecting mechanism is necessary for coupling all of the energy that makes its way through the holes into the detector. An integrating sphere can also be used when the signal is abundant, but this is rarely the case with active sub-millimeter wave systems. Alternatively, if a horn or integrating sphere is not available, the measured signal should be a good representation of the energy through the holes. By measuring the transmitted field in the far field of the imaging window or by use of a lens, the received signal becomes representative of the total energy in the signal. This effect is a direct result of the forward scattering theorem.<sup>16</sup>

The imaging window is another component. It is an aperture that limits the part of the disk where the image is formed and scanned. The size of the imaging window determines the physical size of the image. It can be of any shape; two shapes that are considered in this paper are square and narrow rectangle (slit).

### 2.1 Mathematical Formulation of the Imaging Problem

For reconstruction purposes, the imaging problem is posed as a linear system of equations and is presented in matrix notation

$$Mp + \eta = \hat{m} = m + \eta. \quad (1)$$

For an image of  $n \times n$  pixels, the column vectors  $\hat{m}$ ,  $m$ ,  $\eta$ , have dimensions  $k \times 1$ , the column vector  $p$  has dimensions  $n^2 \times 1$ , and the matrix  $M$  is a matrix of dimensions  $k \times n^2$ . The vector  $p$  is composed of the values of each image pixel. The vector  $\hat{m} = m + \eta$  is composed of the values of each measurement and is called the measurement vector. The vector  $m$  is the noiseless measurement and  $\eta$  is the measurement noise. The number of measurements is  $k$ . The matrix  $M$  is called the measurement matrix and each of its rows encodes the pattern of holes over the imaging window for each measurement. In this work we consider the case when  $k = n^2$  and the measurement matrix is square. Referring to the insert in Fig. 1, each entry of each row of the measurement matrix is calculated as the fraction of the area of the corresponding

pixel covered by holes. For instance, the measurement matrix entries  $M_{1,1} = 0.23$ ,  $M_{1,2} = 0.27$ ,  $M_{1,3} = 0$ , correspond to image pixel entries  $p_1$ ,  $p_2$ , and  $p_3$  in the insert and represent how much of the area of each pixel is covered by the holes. As the disk rotates and a new measurement is acquired, the measurement matrix entries change to reflect the area of intersection between pixels and holes. Linear equations can be formed using these measurement matrix entry values, the unknown pixel values, and the measurement values or

$$\begin{aligned} M_{11}p_1 + \dots + M_{1n}p_n + \dots + M_{1n^2}p_{n^2} &= \hat{m}_1 \\ \dots &= \hat{m} \dots \\ M_{n^21}p_1 + \dots + M_{n^2n}p_n + \dots + M_{n^2n^2}p_{n^2} &= \hat{m}_{n^2}. \end{aligned} \quad (2)$$

Interpreting these linear equations, the entries of the measurement matrix can also be understood as the contribution of each pixel to the measurement. The sizes of the pixels are arbitrary; therefore, the imaging window can be divided into as many pixels as desired. However, as the number of pixels increases, the rows of the measurement matrix become less linearly independent. The linear independence of the equations whose coefficients are represented in the rows of the measurement matrix is assumed in order to solve Eq. (1). The pixels can also take any shape and are not limited to the square shape shown in the insert of Fig. 1.

Ideally, the mathematical formulation of the imaging problem requires that the measurement samples be associated with the pattern of holes (the measurement matrix row) in the imaging window at the sample instant. In the actual implementation the precise location of the holes is only known to within a constant offset angle. Equations (1) and (2) can be interpreted as a matrix representation of the correlation of the disk hole pattern with the image discretized in pixels. By empirically testing assumed offset angles in the formulation of the measurement matrix and checking the resulting image registration for a calibration image (a point source), this unknown can be found.

In constructing the measurement matrix in Eq. (1) we make the following assumptions. Each measurement is collected as the pattern of holes in the imaging window is stationary. All the energy that passes through the holes is collected and measured by the detector. The measured energy is the sum of the energy passing through all the holes. However, all of these assumptions are violated by the actual implementation. The disk is rotating at a constant speed, and each measurement is collected as the disk rotates. The majority, but not all, of the energy that goes through the holes is collected and measured. However, in the current implementation the error introduced by the approximate measurement model is overshadowed due to the measurement noise. Both the noise and error due to the measurement model approximation are mitigated by the regularization that is introduced in solving Eq. (1).

### 3 Image Reconstruction

The unknown pixel values are obtained by solving Eq. (1). In the presence of noise and inaccuracies in the coefficients of the measurements matrix only an approximate solution,  $\hat{p}$ , can be obtained because the problem is ill-conditioned. A number of solution methods can be borrowed from the inverse imaging literature as well as from the compressive

sensing literature.<sup>17</sup> Most methods however, are iterative in nature and therefore not suited for real-time systems. For real-time systems, closed form solutions are preferred. One method for finding the approximate closed form solution is the regularized least squares<sup>18</sup>

$$\hat{p} = \left[ M^T M + \sum_i \mu_i H_i^T H_i \right]^{-1} M^T \hat{m} = R(\mu_i) \hat{m}, \quad (3)$$

where  $\mu_i$  are regularization parameters,  $H_i$  are linear operators applied on the solution, and the superscript  $T$  denotes the matrix transpose. Borrowing notation from Bertero and Boccacci,<sup>18</sup> the resulting matrix multiplication and additions are all grouped together into  $R(\mu_i)$  for notational ease. In the absence of any regularization  $R(\mu_i = 0) = M^{-1}$ , is the inverse of  $M$ . The linear operators  $H_i$  are modeled using *a priori* knowledge of the solution. For example, if the minimal norm solution is desired, the linear operator is the identity matrix. If the solution is smooth, the linear operator could be the Laplacian so that sharp transitions are minimized.

From Eqs. (1) and (3) we can write the approximate solution in terms of a noiseless approximation term and a propagated noise term

$$\hat{p} = R(\mu_i)m + R(\mu_i)\eta. \quad (4)$$

In the absence of noise and regularization the approximate solution reaches the exact solution

$$\lim_{\eta \rightarrow 0, \mu_i \rightarrow 0} R(\mu_i)m + R(\mu_i)\eta = M^{-1}m = p. \quad (5)$$

The exact solution is defined by Eq. (5) and should be interpreted as the "model limited" reconstruction of the image plane, not the object plane. The term "model limited" refers to the fidelity of the measurement model represented by the measurement matrix  $M$ . With the approximate and exact reconstructions defined, we can express the reconstruction error  $\epsilon$  as

$$\epsilon = \hat{p} - p \quad \epsilon = [R(\mu_i)m - p] + R(\mu_i)\eta. \quad (6)$$

The relative reconstruction error is a more useful quantity and it is given as

$$\text{RRE} = \frac{\|\epsilon\|}{\|p\|}. \quad (7)$$

For the regularized least squares solution, the relative reconstruction error depends on the measurement noise,  $\eta$ , and on the regularization parameters,  $\mu_i$ .

The reconstruction error of Eq. (6) is composed of two terms: the approximation error  $[R(\mu_i)m - p]$  and the noise propagation  $[R(\mu_i)\eta]$ . Expanding  $R(\mu_i)$  as in Eq. (3), one observes that the approximation error is directly related to the regularization parameters, and the noise propagation term is inversely related to the regularization parameters. When the measurement matrix is only mildly ill-conditioned and the regularization parameters are small, the noise propagation term dominates the reconstruction error.<sup>18</sup> Ideally we require measurement matrices to have low condition numbers or to be mildly ill-conditioned. Real-time imaging is more forgiving of noise propagation



than approximation error. The noise will appear to have high spatial and temporal frequency spectrum and will be integrated out by the eye of the observer while the approximation error will have low spatial and temporal frequency spectrum and will appear as clutter.

### 3.1 Dependence of the Measurement Matrix on Device Implementation

The analysis presented above indicates that low condition number measurement matrices are desired. For the coded aperture described here, the condition of the measurement matrix is strongly related to the size of the disk and the number of measurements that are recorded for each rotation of the disk. High pixel count images require an equally high number of measurements. As the number of measurements increases, the patterns used to form the linear equations represented in Eq. (2) become similar or correlated, and the equations become less independent. This results in an ill-conditioned measurement matrix. Three approaches can be used to mitigate this effect while keeping the resulting image pixel count reasonable. The first approach involves changing the size of the disk. The disk size can be increased while holding the imaging window size constant and positioned toward the perimeter of the disk. This will increase the arc separation between measurements resulting in more variation in pattern between measurements. Increasing the size of the disk increases the form factor and the mechanical and fabrication complexity of the device. Further analysis is required to determine the limits of the disk size that can be used.

Another approach is turning the imager into a line imager and coupling it with a tilting mirror to form two-dimensional images. For this purpose the imaging window can be made into a vertical slit (with respect to the imaging window in Fig. 1). In this case fewer measurements are acquired per rotation and nonsimilar patterns are more abundant facilitating linear independence between measurements and therefore good reconstruction. The tilting mirror would have a small form factor and would be placed immediately before the coded aperture. This approach also increases the mechanical complexity of the system but keeps the form factor of the system unchanged. In addition, a line imager is useful in and of itself. For example, it can be used in conjunction with an optical camera in a hallway to scan personnel for concealed objects using self motion of the person to form the THz image. The system could then superimpose the THz images on the optical images as personnel pass through the hallway.

A third approach is the use of compressive sampling (CS) reconstruction methods.<sup>17</sup> In the CS approach the number of measurements in one rotation of the disk can be less than the number of pixels or  $k < n^2$ . This allows larger spacing between measurements and hence less correlation between measurement matrix entries. Our preliminary analyses with the random hole patterns have indicated that the resulting measurement matrices are still correlated even when half the number of measurements are used and they do not satisfy the restricted isometry property (RIP). However, combinations of different hole and pixel shapes might result in measurement matrices that satisfy the RIP. In addition, the identification of a sparsity basis could allow the use of even fewer measurements resulting in even less measurement correlation. Another implication of using CS reconstruction

methods is the increased measurement integration time for equal measurement frame rates. This results in higher measurement SNR. Further study is required to determine if the information gain in measurement decorrelation and the improvement in SNR outweigh the information loss because of reduced measurements. Also, another application-dependent consideration is the reconstruction time. One disadvantage of CS reconstruction methods over the closed form methods is their iterative nature not suited for real time imaging.

### 3.2 Performance Evaluation with Simulations

To illustrate the effect of the regularization parameters on the reconstruction, we simulated the reconstruction of noisy measurements using Eq. (3). We minimized both the norm and the Laplacian of the solution. The operator for the norm is the identity matrix and the operator for the Laplacian is the one defined in Ref. 19. We sought to reconstruct a  $32 \times 32$  pixel image of a gun shown in Fig. 2(a). An image size of  $32 \times 32$  pixels was chosen to facilitate fast calculation of the relative reconstruction error in Eq. (7). We simulated the reconstruction using both a two-dimensional imaging window and a line or slit imaging window. We did this to support our comments about the advantage of the line imager over the two-dimensional imager with respect to the quality of reconstruction. The hole pattern we used in these simulations is the one we implemented, described in the next section and shown in Fig. 3. The imaging windows that were simulated were a 34 mm by 34 mm square and a 34/32 mm by 34 mm vertical slit (with respect to the imaging window in Fig. 1). The imaging windows were superimposed over the hole pattern to form measurement matrices of size  $1024 \times 1024$  and  $32 \times 32$ , respectively, as the hole pattern is rotated.

For the two-dimensional image reconstruction, the measured signal was simulated by multiplying the measurement matrix with the reshaped ( $1024 \times 1$ ) gun image values. The measured signal was corrupted with zero mean white

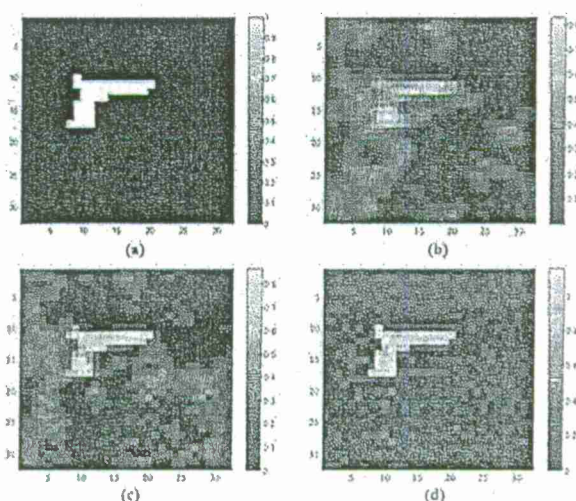


Fig. 2 (a) Target image, (b) two-dimensional imager reconstruction from signal with 20 dB SNR, (c) two-dimensional imager reconstruction from signal with 40 dB SNR, and (d) line imager reconstruction from signal with 20 dB SNR.

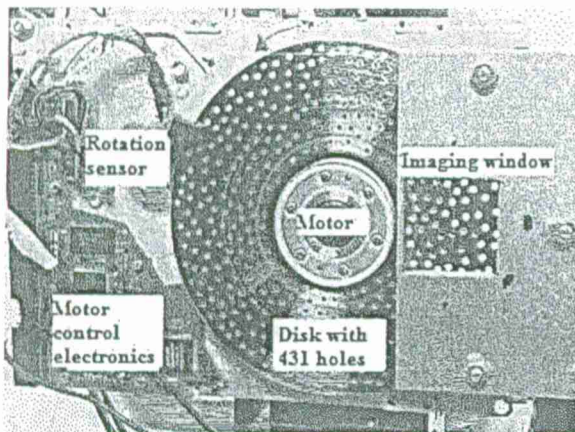


Fig. 3 Implementation of the image plane coded aperture using parts of a 5.25 in. hard drive.

Gaussian noise (using the AWGN function in Matlab) so that the resulting signal to noise ratio of the signal was 20, 30 and 40 dB. The reconstructed image was obtained by multiplying the corrupted signal with the regularized matrix  $R(\mu_i)$ . For the slit image reconstruction, the measured signal for each image column was simulated by multiplying the measurement matrix with each column. Each of the signals was corrupted with zero mean white Gaussian noise so the resulting signal to noise ratio of the signal was 20, 30 and 40 dB. The reconstructed image was pieced together with the reconstructions from each column as the corrupted signals were multiplied with the regularized matrix  $R(\mu_i)$ .

For both imager cases and all the noise cases, the regularization parameters were varied iteratively and the relative reconstruction error (RRE) was calculated using Eq. (7) forming two-dimensional plots of RRE versus the two regularization parameters. The regularization parameters that yielded the minimum RRE were used to calculate the reconstructions shown in Fig. 2. Figure 2 shows the target image [Fig. 2(a)] and the reconstructed images when the imaging window is square and the SNR of the measured signal is 20 dB [Fig. 2(b)] and 40 dB [Fig. 2(c)], and when it is a vertical slit (SNR 20 dB) and the image is scanned across [Fig. 2(d)]. The plots of the RRE for both parameters are shown in Fig. 4. Figure 4(a) shows how the RRE changes with respect to the norm regularization parameter when the Laplacian regularization parameter is optimal (the one yielding minimum RRE). Figure 4(b) shows how the RRE changes with respect to the Laplacian regularization parameter when the norm regularization parameter is optimal. Plots for the two-dimensional and line image reconstruction are shown for measurement signals with 20, 30 and 40 dB SNR. The plots are shown in logarithmic scale with respect to the regularization parameters to display the large dynamic range of the parameters, which depends on noise level and imager configuration.

For the optimal regularization parameters, the RRE for the line imager is lower than for the two-dimensional imager for all noise levels. For example, when the SNR is 20 dB, the minimum RRE for the two-dimensional imager reconstruction is 0.678 and for the line imager reconstruction is 0.191, for SNR 30 dB they are 0.631 and 0.176, respectively, and for SNR 40 dB they are 0.527 and 0.105, respectively. This difference

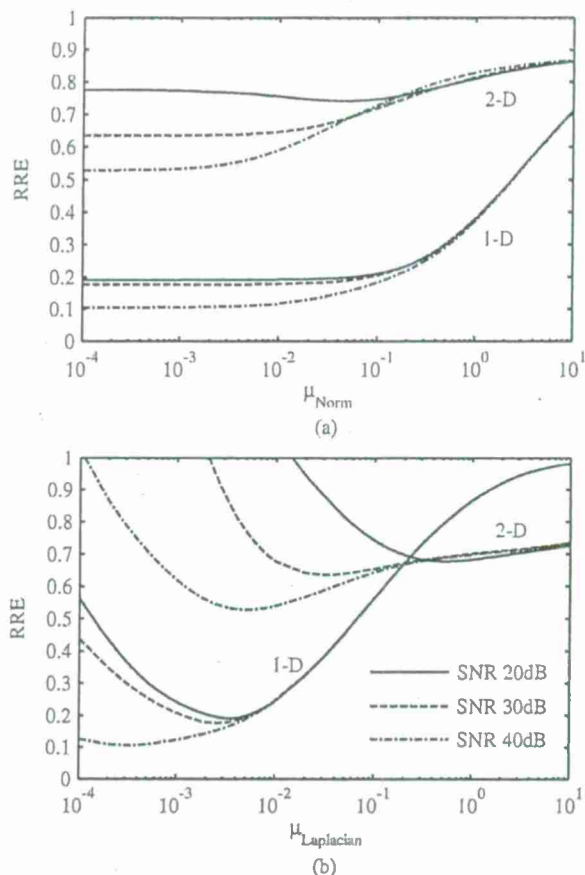


Fig. 4 Relative reconstruction error plotted versus the norm regularization parameter (a) and versus the Laplacian regularization parameter (b) for the two-dimensional (2-D) imager and for the line imager (1-D) when the measurement signal is corrupted by zero mean white Gaussian noise. The lines are slices of the two-dimensional RRE plots when the other parameter is optimal (minimal RRE).

is obvious in the reconstructions in Fig. 2(b) and 2(d). Also, because the two-dimensional imager problem is more ill-conditioned than the line imager problem, higher regularization values are required to reconstruct the best two-dimensional imager image than the best line imager image. As a result the reconstruction error in the two-dimensional imager reconstruction is clutter like (dominated by approximation error) while the line imager reconstruction is noise like (dominated by noise propagation). This effect of the optimal regularization parameter on the reconstruction can also be observed by comparing the two-dimensional imager reconstructions with 20 dB SNR [Fig. 2(b)] and 40 dB SNR [Fig. 2(c)]. As evident from the plots in Fig. 4, the impact on regularization due to the Laplacian regularization parameter is greater than from the norm regularization parameter. However, for values of the Laplacian parameter different than the optimal the impact of the norm parameter becomes more important.

As shown above, the line imager performs better than the two dimensional imager for the particular hole pattern that we have implemented. One assumption that was made however, is that the SNR for the measurement is the same for the two-dimensional and line configurations. This assumption is justified if proper optics are used for both imagers while the



power of the illumination source is held constant. A proper optical system would illuminate and image only the region of the object being measured by the aperture.

The condition number of the line imager can be lowered even further if a different pattern is implemented on the disk. A pattern that implements a simplex code mask (SCM) is possible with the line configuration. The measurement matrix that results from an SCM consists of 1s and 0s. According to Harwit,<sup>20</sup> the SCM measurement matrix is the matrix with the lowest condition number when only entries of 0 and 1 can be used. The condition of the two-dimensional imager can also be lowered using a different disk pattern, and such patterns will be investigated in the future.

#### 4 Implementation of the Image Plane Coded Aperture and Imaging Setups

The two-dimensional image plane coded aperture was implemented using parts of a 5.25 in. hard drive. One of the platters of the hard drive was used as the spinning disk. The radius of the holes and their minimal separation were designed for operation at 640 GHz. A hole radius of 1 mm and a minimal separation of 2 mm were chosen to guarantee unity transmission, linearity, the structural integrity of the disk, and because of the availability of standard tools in these sizes. With these parameters as restrictions, a random pattern of 431 holes was generated, and the holes were drilled on a CNC mill. The case of the hard drive was cut and modified for access to the disk and for mounting on the optical stages. The electronics of the motor driver were also modified so that the disk could be rotated at 3000 rotations per minute (RPM). An emitter diode and phototransistor pair were placed in the proximity of the disk to register the measurement samples with the corresponding hole patterns in the imaging window. A 34 mm × 34 mm imaging window aperture was machined on two slabs of aluminum, and they were mounted to sandwich the disk. Figure 3 shows a picture of the front and back of the device with all the components described above labeled.

The coded aperture was used in two imaging configurations. In the first configuration the device was paired with the sub-millimeter wave receiver to form images in transmission mode. A sketch and picture of this setup are shown in Fig. 5. We use a heterodyne source and receiver pair from Virginia Diodes. The source and receiver operate at 640 GHz. In this configuration, the 640 GHz source is placed 1 m in front of the device and is flood illuminating the imaging window. An object mask is placed right before the imaging window, and the projected image is scanned by the spinning disk. The 640 GHz receiver is placed behind the disk and measures the energy passing through the holes. The intermediate frequency (IF) of the receiver was down converted from 4.8 to 2.2 GHz and this new IF was supplied to a spectrum analyzer. The spectrum analyzer was used to band-pass filter and amplify the signal. A time sweep of the signal triggered for each rotation was generated, and the video output of the spectrum analyzer was sampled at a rate of 250 kHz using a 16 bit data acquisition card from Measurement Computing. The disk rotates at 50 rotations per second and 5000 samples are recorded per rotation. The sampled signal is low-pass filtered in Matlab and 4096 consecutive samples are used to reconstruct a 64 × 64 pixel image using Eq. (3).

In the second configuration, the device was paired with the sub-millimeter wave receiver to form images in

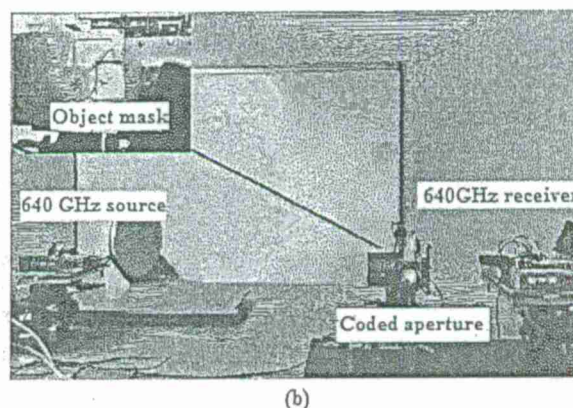
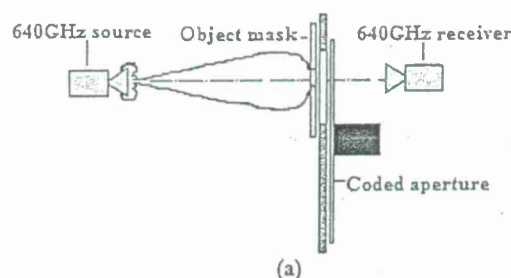


Fig. 5 Sub-millimeter wave setup in transmission mode, (a) sketch and (b) actual implementation.

stand-off mode. A sketch and picture of this setup are shown in Fig. 6. The 640 GHz source is located approximately 2 m from the target and flood illuminates it. The energy reflected by the target is collected by the imaging mirror (in the implementation, the beam is folded by two flat mirrors) 10 m away. This mirror is a section of an ellipsoid of rotation with one focus at 1 m and the other at 10 m. The image is formed on the 1 m side. The system has an effective diameter of 0.305 m (12 in.), effective focal length of 0.909 m, resulting in a F# of 2.983. The magnification of

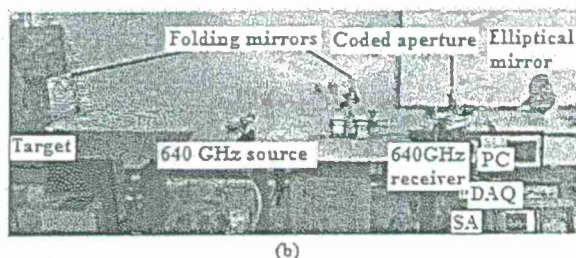
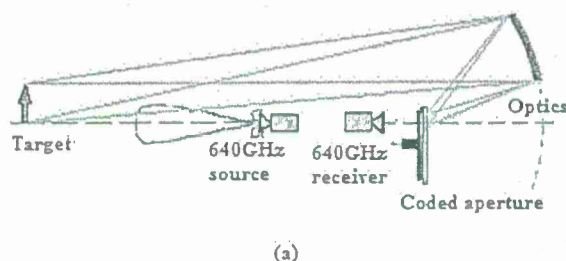


Fig. 6 Sub-millimeter wave setup in stand-off mode, (a) sketch and (b) actual implementation.

the system is 0.1, the depth of focus for coherent radiation is 0.011 m, and the depth of field for incoherent radiation is 1.016 m. The airy disk diameter is 3.75 mm for a wavelength of 468.43  $\mu\text{m}$ , corresponding to the illumination frequency of 640 GHz. The imaging mirror forms an image of the target in the imaging window of the coded aperture. The image is then scanned by the spinning disk, and the energy that goes through the holes is measured by the 640 GHz receiver. The same data collection setup as in the first configuration is used to sample the received signal and reconstruct a  $64 \times 64$  image using Eq. (3).

## 5 Results

For both imager configurations the reconstruction was performed using Matlab software. The Matlab Data Acquisition Toolbox was used to acquire the data from the data acquisition device. Code was written to implement Eq. (3) and to calculate the matrices. The disk is rotated at a rate of 50 rotations per second and therefore allows image formation at 50 frames per second (fps). However, the data acquisition speed of the current implementation is only 10 fps, and when an image is reconstructed and displayed on the screen the image rate is 6 fps. These slower frame rates are due to the implementation in Matlab. On a laptop PC (processor: Intel(R) Core(TM)2 Duo CPU T6670 at 2.2 GHz), the data reconstruction step ( $\text{matrix}_{[4094 \times 4094]} \text{vector}_{[4096 \times 1]}$  product) in the current Matlab implementation takes only 30 ms and the rest of the loop time is occupied by the data acquisition, image reshaping, filtering, and image display. All these steps can be made faster using a compiled implementation and dedicated processing.

For the transmission mode configuration we used the mask shown in Fig. 7(a) as the object. An aperture in the shape of a hand gun was cut on an aluminum sheet, and the sheet was placed in front of the coded aperture as shown in Fig. 5. For the stand-off configuration, an aluminum plate was roughened by sanding and a piece of carpet with an aperture in the shape of a hand gun was placed over it. This target is shown in Fig. 7(b). The target was placed 10 m from the image forming mirror, as shown in Fig. 6, and an image was formed on the coded aperture.

The results of the reconstruction are shown in Fig. 7(c) and 7(d). In both cases the shape of the gun can be distinguished. The image formed in the transmission mode configuration resembles the target more than the image formed in the stand-off configuration. One of the reasons for this difference is the presence of an optical system in the stand-off configuration, which amplifies the effects of coherent imaging because of aberrations. Another reason is the specular nature of active imaging. Both contribute to the nonuniformity of the image intensity on the image plane for the stand-off case. We note that in order to acquire the image in stand-off mode [Fig. 7(d)] the object must be positioned precisely. A slight angular movement, with respect to the optical axis, causes one part of the object to be imaged with higher intensity than the other parts, and only it can be imaged.

The reconstruction error is present in both reconstructions. As discussed in Sec. 3, this is an effect of the ill-conditioned measurement matrix and the measurement noise, the nonlinearity of the measurement, and the assumption of static hole patterns during the detector integration

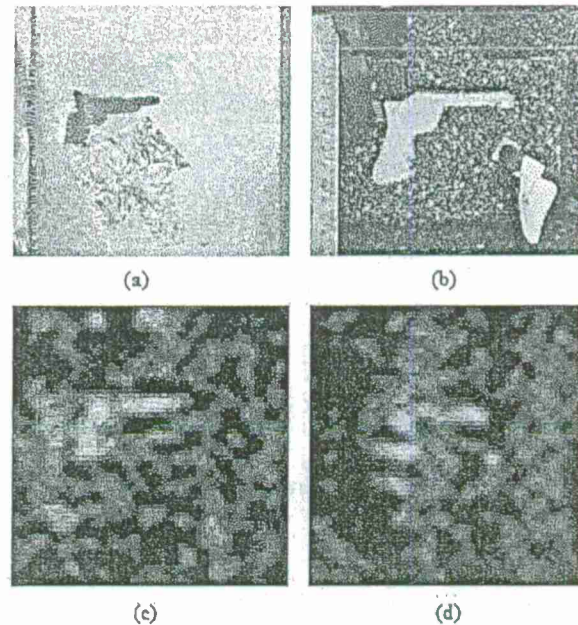


Fig. 7 Imaging targets and image reconstructions from each configuration; (a) target mask used for sub-millimeter wave transmission mode configuration, (b) target for the sub-millimeter wave stand-off mode configuration, (c) reconstruction from the sub-millimeter wave transmission mode configuration, (d) reconstruction from the sub-millimeter wave stand-off mode configuration.

time. The reconstruction noise appears in the form of clutter since the reconstruction required high levels of regularization. In both cases the norm and the Laplacian of the solution were minimized as a result of the regularization.

## 6 Conclusions

We have built an image plane coded aperture device for sub-millimeter wave imaging. This coded aperture has high modulation levels, high scanning rates, low mechanical complexity, and low cost. The design parameters were identified in our earlier publications.<sup>9,10,21</sup> We presented a mathematical formulation for the imaging problem with the image plane coded aperture and a regularized least squares reconstruction method that performs in real time. The effect of the regularization was discussed in terms of the relative reconstruction error and in terms of the nature of the reconstruction error or noise. Low regularization results in high frequency spatial and temporal noise, while high regularization results in clutter type noise. For some coded aperture configurations, e.g., the two-dimensional configuration, high regularization is required because the measurement matrix is very ill-conditioned. For other configurations, e.g., the line imager configuration, low regularization is possible and the reconstructions have low error. The imagers that we implemented and presented here are two-dimensional and can scan images at 50 fps. They can record images at 10 fps. They can scan, reconstruct, and display images at 6 fps. The data acquisition and image reconstruction chains are currently implemented on a personal computer using Matlab interpreted code. The processes of data acquisition, image reconstruction, and image display can be accelerated to produce images at a rate of 50 fps if the code is compiled and a dedicated



computer is used. Our next efforts will be focused on better models of the measurement matrix and the building of a line imager, this will include optics appropriate for line imaging.

## References

1. D. T. Petkie et al., "Active and passive imaging in the THz spectral region: phenomenology, dynamic range, modes, and illumination," *J. Opt. Soc. Am. B* 25(9), 1523-1531 (2008).
2. R. Appleby and H. Wallace, "Standoff detection of weapons and contraband in the 100 GHz to 1 THz region," *IEEE Trans. Antenn. Propag.* 55(11), 2944-2956 (2007).
3. A. J. Gatesman et al., "Terahertz behavior of optical components and commo materials," *Proc. SPIE* 6212, 62120E (2006).
4. R. Appleby and R. Anderton, "Millimeter-wave and submillimeter-wave imagiogr for security and surveillance," *Proc. IEEE* 95(8), 1683-1690 (2007).
5. M. C. Kemp, "Millimetre wave and terahertz technology for detection of concealed threats—a review," *Proc. SPIE* 6402, 64020D (2006).
6. A. Luukanen et al., "Passive real-time submillimetre-wave imaging system utilizing antenna-coupled microbolometers for stand-off security screening applications," in "2010 Int. Workshop on Antenna Tech. (IWAT)," pp. 1-4, IEEE, Lisbon (2010).
7. E. Heinz et al., "Toward high-sensitivity and high-resolution submillimeter-wave video imaging," *Opt. Eng.* 50(11), 113204 (2011).
8. K. Cooper et al., "THz imaging radar for standoff personnel screening," *IEEE Trans. Terahertz Sci. Tech.* 1(1), 169-182 (2011).
9. O. Furxhi and E. L. Jacobs, "A sub-millimeter wave line imaging device," *Proc. SPIE* 7670, 76700L (2010).
10. O. Furxhi and E. L. Jacobs, "A sub-millimeter wave line scanning imager," *Proc. SPIE* 7837, 78370D (2010).
11. D. Takhar et al., "A new compressive imaging camera architecture using optical-domain compression," *Proc. SPIE* 6065, 606509 (2006).
12. A. Luukanen, "Rapid beamsteering reflectarrays for mm-wave and submm-wave imaging radars," *Proc. SPIE* 8022, 80220M (2011).
13. W. L. Chan et al., "A spatial light modulator for terahertz beams," *Appl. Phys. Lett.* 94(21), 213511 (2009).
14. C. W. Berry, J. Moore, and M. Jarrahi, "Design of reconfigurable metallic slits for terahertz beam modulation," *Opt. Express* 19(2), 1236-1245 (2011).
15. M. Jarrahi, "Broadband terahertz modulators based on reconfigurable metamaterials and their potential application to terahertz imaging," in 2010 URSI Int. Symp. Electromagnetic Theory (EMTS), 15, pp. 640-642, IEEE, Berlin.
16. A. Ishimaru, *Electromagnetic wave propagation, radiation, and scattering*, Prentice Hall, Englewood Cliffs, NJ (1991).
17. R. Baraniuk, "Compressive sensing (lecture notes)," *IEEE Signal Process. Mag.* 24(4), 118-121 (2007).
18. M. Bertero and P. Boccacchi, *Introduction to Inverse Problems in Imaging*, Institute of Physics Publishing, Bristol, Philadelphia (1998).
19. R. Gonzales and R. Woods, *Digital Image Processing*, Prentice Hall, Upper Saddle River, NJ (2008).
20. M. Harwit and J. Sloane, *Neil, Hodamard Transform Optics*, Academic Press, New York (1979).
21. O. Furxhi, "Spatially selective mirrors and masks for submillimeter wave imaging," PhD Thesis, The University of Memphis, <http://www.memphis.edu/eid/> (2010).



Orges Furxhi is a post-doctoral fellow in the Department of Electrical and Computer Engineering at the University of Memphis. His research work is concentrated in nonconventional sensors across the electromagnetic spectrum from infrared to microwave. He received his PhD degree in engineering and MS degrees in electrical engineering and in physics from the University of Memphis (PhD 2010, MS physics 2010, MS electrical engineering 2007), and his BS degree in computer engineering from Harding University in 2005.



Eddie L. Jacobs is an assistant professor in the Department of Electrical and Computer Engineering at the University of Memphis. He was previously at the U.S. Army Night Vision and Electronic Sensors Directorate, Fort Belvoir, Virginia, where he led a team of engineers and scientists developing models of the performance of passive and active imaging sensors. His research interests are in novel imaging sensor development, electromagnetic propagation and scattering, and human performance modeling. He received BS and MS degrees in electrical engineering from University of Arkansas, and a DSc in electrophysics from George Washington University.



Chrysanthé Preza is an associate professor in the Department of Electrical and Computer Engineering at the University of Memphis and has a secondary appointment in the Department of Biomedical Engineering. She is also an adjunct faculty at the University of Tennessee Health Science Center in Memphis. She received her degrees from Washington University in St. Louis in both electrical engineering (BS 1987, MS 1990, and DSc 1998) and computer science (BS 1987, MS 1991). Her research focuses on the development of physics-based imaging models and model-based computational methods mainly for biomedical imaging applications utilizing microscopy.

# Image Plane Coding for Terahertz Imaging

Eddie L. Jacobs and Orges Furxhi

Department of Electrical and Computer Engineering, University of Memphis, Memphis, TN,  
USA  
eljacobs@memphis.edu

**Abstract:** Image plane coding is an alternative to focal plane arrays in terahertz imaging devices. A device for terahertz image plane coding is described. Analysis shows that line imaging devices are favored as opposed to two-dimensional imaging.

© 2012 Optical Society of America

OCIS codes: (110.6795) Terahertz imaging; (110.1758) Computational imaging; (100.3190) Inverse problems

## 1. Introduction

The design of imaging sensors operating at millimeter and sub-millimeter wavelengths is complicated by the lack of readily available focal plane arrays. The engineering of focal plane arrays at these wavelengths is challenging due to either cooling requirements for passive sensing or heterodyning for active sensing[1, 2, 3]. To date imaging in these regimes has been dominated by sensors comprised of a single or a few detectors. In order to construct a full size image a mechanical scanning system is often used. Alternatives involving the use of phased array techniques are currently being developed as well[4]. Our approach to this problem has been to pursue the idea of image plane coding. Image plane coding is the process of encoding the information in the image into a series of linear measurements over time which are processed to reconstruct the image. A variety of devices have been employed for visible band image plane coding including liquid crystal spatial light modulators and digital mirror devices. The particular device we have developed is, as far as we know, the only device that is capable of operation at millimeter and sub-millimeter wavelengths and that allows real time image formation.

## 2. Measurements

As mentioned in the introduction, image plane coding is the encoding of an image into a series of linear measurements on the image. Each measurement is a linear combination of many pixels in the image. Mathematically, the process is described by

$$y = Mx + \eta \quad (1)$$

where  $x$  is a vector representing the image,  $M$  is a matrix representing the measurement process,  $\eta$  is a vector representing the noise in the measurement process, and  $y$  is a vector of observed measurements. If  $N$  is the number of pixels in the image  $x$  and  $M$  is the number of measurements in  $y$  then  $M$  is a  $M \times N$  matrix. For  $M < N$ , the solution to equation 1 involves iteration and hence is not suited for real time operation. In addition, images of most objects of interest in the sub-millimeter wave range will be limited in size due to the resolution restrictions of diffraction. Therefore, we only consider the case of  $M = N$ .

Engineering an imaging system from equation 1 requires the co-design of the measurement matrix  $M$  and an algorithm for reconstructing the image  $\hat{x}$  from the measurements  $y$ . Because of measurement noise, the reconstructed image will only be an approximation of the real image  $x$ . Ill-conditioning in the measurement matrix amplifies the noise in most reconstruction algorithms and hence also increases the uncertainty in the estimate of of image. These considerations are addressed in inverse methods employing regularization. The particular method we have to date found most successful with our method of generating measurements is a generalized form of Tikhonov regularization defined by the following[5].

$$\hat{x} = \left[ M^T M + \sum_i \mu_i H_i^T H_i \right]^{-1} M^T y = R y \quad (2)$$

In equation 2, the parameters  $\mu_i$  are Lagrangian multipliers or the regularization parameters and the matrices  $H_i$  define linear operations performed on the results. By appropriate choice of these matrices and multipliers the effects of noise can be minimized in the reconstruction. For our work we use two linear operators: the linear operator and the Laplacian operator. Note that once the measurement matrix has been designed and the linear operators selected, the matrix  $R$  is known so that image reconstruction is simply a matrix multiplication.

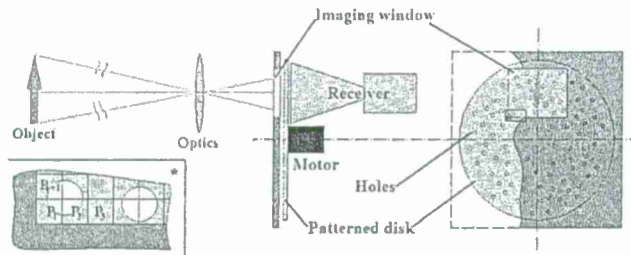


Fig. 1: Schematic representation of spinning disk image plane coding apparatus.

### 3. Device

The device we use for generating measurement matrices consists of a spinning metal disk with a pattern of circular holes coupled with a single heterodyne detector. The device is positioned in the imaging plane of an optical system. The image is restricted to a rectangular section of the disk through the use of a mask. The device is shown schematically in Figure 1. Holes in the metal disk are used for sampling the image. We use hole radii of  $1.4\lambda$  in a  $2.7\lambda$  thick metal disk and achieve a transmission of approximately 100%. In order to achieve independent measurements it is important to avoid hole to hole coupling effects. We have found that a hole spacing of  $\lambda$  or greater achieves this goal. It should be noted that a hole pattern designed for any wavelength will also work well for any smaller wavelength meaning that the hole pattern will preserve the transmission properties and independence properties achieved at the larger wavelength.

The design of the hole pattern and the sampling scheme of the image and detector are the main factors governing the properties of the measurement matrix. Hole patterns are constructed by placing possible hole sites in a hexagonal pattern in a square having side length equal to the diameter of the disk. The side length of each hexagon is selected to be  $3.8\lambda$  which will allow for  $1.4\lambda$  radius holes at  $\lambda$  spacing. The hexagonal pattern results in the closest hole packing density. By selecting an occupation probability and randomly assigning actual holes to each of these sites, a unique hole pattern is generated. Only holes within an annulus defined by the imaging window are actually fabricated on the disk.

Once a hole pattern is determined, the sampling scheme of the image and detector can be used to form the measurement matrix. The imaging window is divided into virtual pixels of rectangular shape (see inset in Figure 1) and arbitrary size. Each pixel is assumed to have a constant intensity and together form the vector  $x$ . The entries in a single row of the measurement matrix are computed as the fractional area of each visible hole on each pixel. The disk is rotated behind the imaging window to produce a new pattern of holes in the imaging window and another row in the measurement matrix is generated. This continues until the  $N \times N$  measurement matrix is filled. As the disk rotates, samples of the energy transmitted through the holes are collected by the receiver. If the disk does not rotate very far between samples by the receiver, there could be significant correlation between adjacent rows in the measurement matrix. The correlation is directly dependent on how long a hole is within the imaging window. Figure 2(a) shows the transit time of a single hole through the imaging window normalized to the sampling time for various image sizes. Sampling time is determined by the size of the image and the speed of rotation of the disk. Since patterns repeat after one rotation of the disk, to avoid correlations due to repeated patterns, the measurement matrix must be filled in one rotation. As a result, the sampling time is simply the number of pixels in an image  $N$  divided into the rotation time. Since each rotation yields an image, the rotation time is the frame time for video.

The vertical axis of Figure 2(a) is the number of samples taken during a transit time. With hundreds of samples being taken for a square image and only one or two for a line image it is clear that avoidance of correlation in the measurement matrix will favor line image scenarios. This can be seen more clearly by viewing measurement matrix condition numbers plotted against normalized transit time (Figure 2(b)). This Figure was produced by making 10 disk realizations and producing measurement matrices for  $64 \times K$  images where  $K = 1, 2, 4, 8, 16, 32, 64$ . The condition numbers for each realization are then averaged at each factor of  $K$ . As the factor  $K$  increases, the logarithm of the condition number of the measurement matrix increases in a power law fashion. This is demonstrated in Figure 3 where simulations of the measurement and reconstruction process are done for both two dimensional imaging and a line imaging scanner. The difference between the two dimensional and line images is that only the vertical dimension is reconstructed in the line image whereas both are reconstructed in the two dimensional image. In practical implementations, the line image would have to be scanned across the target to make an image.



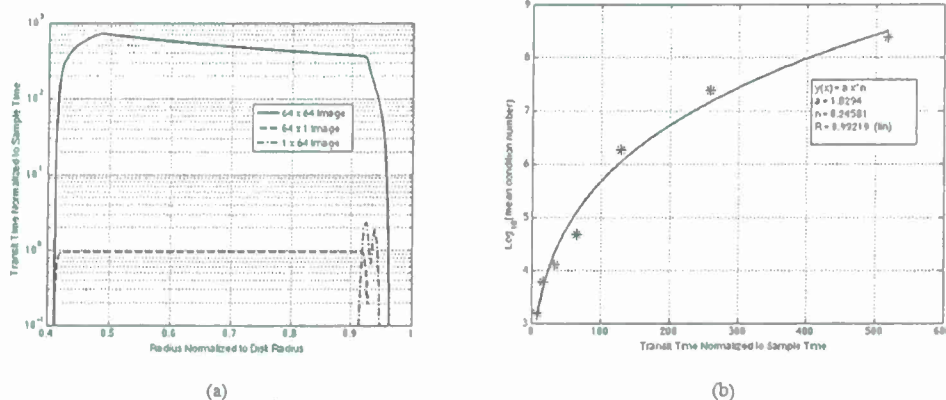


Fig. 2: (a) Transit time of a hole normalized to the sample time for three image sizes/orientations. (b) Measurement matrix condition number as a function of transit time.

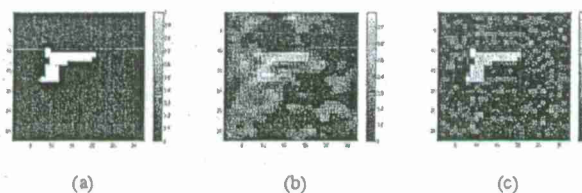


Fig. 3: Target image (a), two-dimensional imager reconstruction (b), and line imager reconstruction (c)

#### 4. Conclusions

To date, we have constructed both line imagers and two dimensional imagers operating at 640 GHz and optical wavelengths using this approach[6, 7]. While we believe we understand the imaging process using this device there are several avenues for improvement that are being pursued. Our primary efforts are being expended on optimizing the measurement matrix/hole pattern design. Our current approach is trial and error and as we refine our models of the imaging process we will improve the procedure for generating hole patterns. We are also improving the optic characteristics of our system. Further efforts at characterizing and reducing measurement noise are also being undertaken.

#### References

- [1] R. Appleby and H.B. Wallace. Standoff detection of weapons and contraband in the 100 GHz to 1 THz region. *IEEE Transactions on Antennas and Propagation*, 55(11):2944–2956, nov. 2007.
- [2] A. Luukanen, M. Aikio, M. Grönholm, M. M. Leivo, A. Mäyrä, A. Rautiainen, and H. Toivanen. Design and performance of a passive video-rate THz system demonstrator. volume 8022, page 802207. SPIE, 2011.
- [3] H. Bruce Wallace. Analysis of rf imaging applications at frequencies over 100 GHz. *Appl. Opt.*, 49(19):E38–E47, Jul 2010.
- [4] Arttu Luukanen, Juha Ala-Laurinaho, David Gomes Martins, Janne Häkli, Päivi Koivisto, Pekka Pursula, Pekka Rantakari, Jussi Säily, Aleksi Tammlinen, Reijo Tuovinen, and Markku Sipilä. Rapid beamsteering reflectarrays for mm-wave and submm-wave imaging radars. volume 8022, page 80220M. SPIE, 2011.
- [5] Mario Bertero and Patrizia Boccacchi. *Introduction to Inverse Problems in Imaging*. Institute of Physics Publishing, Bristol and Philadelphia, 1998.
- [6] Orges Furxhi and Eddie L. Jacobs. A sub-millimeter wave line scanning imager. volume 7837, page 78370D. SPIE, 2010.
- [7] Orges Furxhi and Eddie L. Jacobs. Comparison of schemes for active sub-millimeter wave imaging. volume 8188, page 81880M. SPIE, 2011.



# Image Plane Coded Aperture Detectors for THz Imaging

Orges Furxhi, *Member, IEEE* and Eddie L. Jacobs, *Senior Member, IEEE*

Department of Electrical and Computer Engineering, University of Memphis, Memphis, TN 38152

*Invited Paper*

**Abstract**—Image plane coded aperture (IPCA) detectors are composed of a single element detector sensitive to the radiation frequencies of interest, a reconfigurable spatial light modulator (SLM), and a mechanism such as a lens or a horn that is used to collect the radiation modulated by the SLM and focus it on the sensing element. The IPCA detector is placed in the image plane of an imager and is used to make linear measurements on the image by modulating the signal spatially and/or temporally in amplitude, frequency, phase, or polarization. The image is then reconstructed computationally. In this paper we present an implementation of an IPCA detector that can be used for Terahertz imaging and discuss other possible implementations.

**Index Terms**—Terahertz imaging, Coded apertures, Radar imaging

## I. INTRODUCTION

MUCH of the interest in terahertz imaging is motivated by the abilities of THz frequencies to penetrate most manmade materials particularly clothing [1], [2]. Additionally, many harmful chemicals and explosives display absorption lines that make them identifiable by THz [3]. These characteristics of THz make it attractive for security applications. Unfortunately, focal plane arrays for this regime have not been commercially forthcoming and current offerings either lack sensitivity or are too costly to be used in practical security situations. An intermediate solution has been the development of scanning systems. These, however, have their own cost, weight, power, and frame rate limitations.

Our interest is focused in the part of the THz spectrum between 300GHz and 3THz which is referred as the sub-millimeter wave region. In this region, sensitive detectors are available and the technology is mature. Both active and passive imaging configurations at these frequencies have been successfully demonstrated. Currently, the new frontier in sub-millimeter wave imaging is faster frame rates and smaller size, weight, power consumption, and cost. Passive systems that operate at close to real-time require cooled detectors and are large [4], [5]. Images from these systems are similar to infrared images providing temperature difference/contrast information and therefore are easy to interpret. On the other hand, the images acquired with active imagers, that are coherent, have very high dynamic range and suffer from the specular reflections and clutter in the scene, which makes them difficult to interpret. However, information from active THz radar imaging is easy to interpret [6]. An advantage of active systems is that they operate at room temperature and usually their physical size is limited by the optical aperture rather than the detector and source modules.

One of the most promising sub-millimeter wave systems is the imaging radar system developed by NASA's Jet Propulsion Laboratory [6]. It mitigates clutter and specular reflection from the scene by forming range maps of the scene rather than contrast images. The JPL system is currently limited to 1Hz frame rates. The reported bottlenecks are the mechanical scanning and the signal to noise (SNR) of single pulse detection. The authors of that work acknowledge the practical limitations with speeding the mechanical scanning system and propose the use of transceiver arrays as a solution to faster frame rate. One alternate approach to the mechanical scan has been proposed by Lukkanen [7] and entails using an electronically controlled reflect-array that can be used as a beam steerer. This work is in its design phase. Our substitute for mechanical scanning is the image plane coded aperture (IPCA) detector. In this paper we present the concept of the IPCA detectors, show one implementation, and discuss other possible implementations of such detectors.

## II. IMAGE PLANE CODED APERTURE DETECTORS

Coded aperture detectors are usually envisioned as substitutes for the optical system of an imager when the optical aperture is too large to allow the use of optics. Image plane coded aperture detectors on the other hand, are used as substitutes for focal plane arrays in frequency regimes where focal plane arrays are impractical, expensive, or non-existent. A conceptual sketch showing the place of the IPCA detector in an imaging system and its components is shown in Fig. 1.

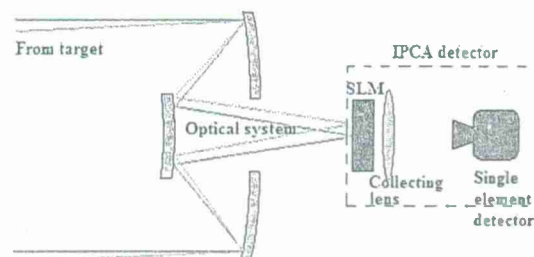


Figure 1. The role of IPCA detectors in an imaging system

IPCA detectors are composed of a single element detector sensitive to the radiation frequency of interest, a reconfigurable spatial light modulator (SLM), and a mechanism such as a lens or a horn that is used to collect the radiation past the SLM and focus it on the sensing element. The IPCA detector is placed in the image plane of an imager and is used to

make linear measurements on the image by modulating the information on the image plane spatially and/or temporally in amplitude, frequency, phase, or polarization. The image is then reconstructed computationally using inverse imaging techniques [8].

Because the IPCA detectors make linear measurements of the image plane a computational reconstruction is necessary. For real-time imaging these computations should happen faster than the required frame rate. Image reconstruction algorithms that satisfy this criterion are closed form solutions that are reduced to simple matrix vector multiplications. However, because of other practical limitations sub-millimeter wave images usually have low resolution (i.e. 64x64 pixels) and iterative solutions can also be used without compromising frame rate. The IPCA detectors can also be used to perform compressive imaging [9].

Depending on the method of modulation the IPCA detectors can be used in active, passive, coherent, or incoherent modes. As such, the use of the detectors is not limited to imaging but can also be used in imaging radar, spectroscopy, or multi-modal imaging. Multi-modal imaging is facilitated by placing a filter in front of the detector or by using several single element detectors responsive to particular wavelengths. Other configurations can be envisioned where the IPCA detectors operate in coherent and incoherent mode (containing a coherent and an incoherent single element detector) to form contrast images as well as range profiles of the scene. An IPCA detector can also be used to make linear measurements of dispersed spectra similar to Hadamard spectroscopy [10].

From the aspect of signal to noise ratio (SNR), the IPCA detectors are favored by active imaging configurations. For similar illumination power, the detector SNR is comparable to a conjugate point imaging system and much higher than focal plane arrays [11]. For passive systems the performance is worse than that of the focal plane arrays but comparable with the conjugate point system [12]. However, the per pixel SNR after the image is reconstructed computationally suffers by an additional factor which can be quite high if the modulation patterns of the SLM are not selected properly.

### III. SPINNING DISK IPCA DETECTOR

One possible realization of an IPCA detector that we have built, is shown in Fig. 2. The SLM consists of a portion (labeled as imaging window in Fig. 2) of a spinning disk with random holes. For each pattern of holes in the imaging window (i.e. a code) a measurement is made by the receiver and it is registered with the pattern. If the holes are designed properly, the measurement will consist of the linear combination of portions of the image. Once the desired number of measurements are made, usually a number equal to the number of desired image pixels, the hole patterns and corresponding measurements are used to decode the image formed in the imaging window.

The insert in Fig. 2 and equation 1 help illustrate this process. The imaging window is divided into pixels ( $n^2$  for this example), not necessarily square or regular. For each pattern of holes or code, we form an equation where the weighted

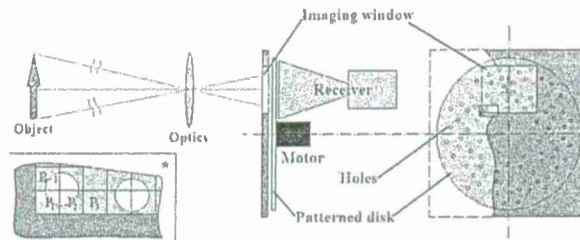


Figure 2. Spinning disk IPCA detector

pixel values (pixel values are the unknowns) add up to the measured value. The weights represent how much each pixel contributes to the measurement and are calculated as the ratio of the hole-pixel intersect area to the total area of the pixel. If the pixels are of equal area, then the equation is complete. If they are not, an additional factor representing the relative sizes of the pixels is computed and multiplied with the other weights. Using the equations from all the measured patterns, a system of equations is formed and solved using linear algebra methods (e.g. regularized linear least squares) [8].

$$\begin{aligned} m_{11}p_1 + \dots + m_{1n}p_n + \dots + m_{1n^2}p_{n^2} &= m_1 \\ &\dots = m_{\dots} \end{aligned}$$

$$m_{n^2 1}p_1 + \dots + m_{n^2 n}p_n + \dots + m_{n^2 n^2}p_{n^2} = m_{n^2} \quad (1)$$

The other parts of the IPCA detector are the collecting horn and single element detector. We use a Schottky diode heterodyne transceiver pair from Virginia Diodes operating at a center frequency of 640 GHz. One possible imaging configuration that we have constructed in our lab is shown in Fig. 3. The optical system consists of a 12 inch diameter elliptical aperture with one focus at one meter (image space) and another at ten meters (target space). The source is pointed directly to the target three meters away and the optical aperture is approximately ten meters away from the target. The disk spins at 50 rotations per second which corresponds to an image frame rate of 50Hz since the necessary measurements are made during one revolution of the disk. The measurements out of the receiver are digitized using a 16-bit data acquisition card. The card is read by a custom Matlab script which also performs the image reconstruction and display. The Matlab part of the system slows down the image formation and display rate to approximately 16Hz when run on a laptop.

Our target was an aluminum plate covered by carpet containing an aperture in the shape of a gun as shown in Fig. 3. The reconstructed image is shown to the right. Three bright spots are clearly distinguishable, the handle, middle part, and barrel. The clutter in the image is due to the reconstruction process which introduces an approximation error and noise propagation from the measurement to the image. The discontinuity of the target image is due to the nature of active imaging, i.e. specular reflections and coherent interference.

Future efforts will be focused towards adapting the spinning disk IPCA detector to an imaging radar system. Also, analysis has shown that a line spinning disk IPCA detector results in lower approximation error and noise propagation during the image reconstruction process. Another one of our efforts will



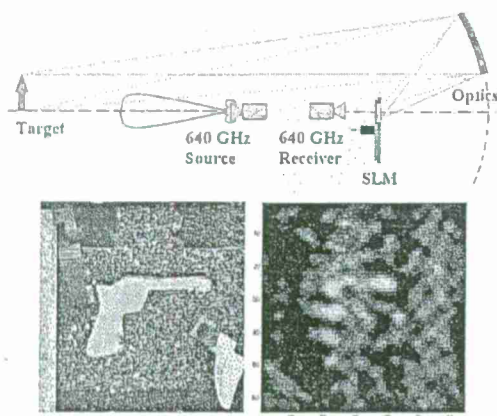


Figure 3. (top) stand-off setup, (bottom left) target, (bottom right) corresponding reconstructed 64x64 pixel image acquired at 50 frames per second and reconstructed at 16 frames per second.

be the development of a line IPCA detector coupled with a single tilting mirror to form two dimensional images.

#### IV. POSSIBLE IPCA DETECTORS

The minimization of approximation error and noise propagation during the image reconstruction process is strongly dependent on the code implemented by the detector. An optimum code is the Hadamard code [10]. The Hadamard code does not propagate noise and also has very low approximation error since it would not require large amount of regularization[8]. The Hadamard code is composed of orthogonal vectors containing values of 1 and -1. One possible implementation of an IPCA detector that realizes the Hadamard code would consist of 180 degree phase modulators, and would be suited for imaging radar systems. A 180 degree phase shift is equivalent to multiplying the incident field by -1.

A group from the University of Virginia has built and demonstrated a broad-band 180 degree phase shifter using integrated sub-millimeter-wave Schottky diodes that operates at 220GHz with a bandwidth of 55GHz within a phase tolerance of  $\pm 15$  degree[13]. The researchers claim that the technology is scalable to sub-millimeter waves in the 640GHz region. If this is possible, these phase shifters would be ideal to implement air to air couplers that can serve as the SLM part of the IPCA detectors. They would allow implementation of Hadamard codes for imaging radar.

#### V. CONCLUSIONS

We have introduced the concept of an image plane coded aperture (IPCA) and briefly discussed some of its applications. An IPCA detector that utilizes a spinning disk with holes as an SLM, was also described and the image of a gun-like target acquired with this IPCA detector was shown. The spinning disk IPCA scans the image plane at 50Hz. The image quality with this system suffers from approximation error and noise propagation artifacts that are introduced during the image reconstruction process. These artifacts can be eliminated if a Hadamard coding scheme is used. We give examples of

existing research that could lead to a device for implementing a Hadamard code with application to a THz imaging radar. The use of an IPCA detector is an alternative to mechanical raster scanning of antennas or mirrors and focal plane arrays. When compared with scanning an imaging antenna or mirror, the IPCA detector has faster scan rates, and possibly low cost and compact form factor.

#### REFERENCES

- [1] D. T. Petkie, C. Casto, F. C. D. Lucia, S. R. Murrill, B. Redman, R. L. Espinola, C. C. Franck, E. L. Jacobs, S. T. Griffin, C. E. Halford, J. Reynolds, S. O'Brien, and D. Tofsted, "Active and passive imaging in the thz spectral region: phenomenology, dynamic range, modes, and illumination," *J. Opt. Soc. Am. B*, vol. 25, no. 9, pp. 1523-1531, Sep 2008.
- [2] R. Appleby and H. Wallace, "Standoff detection of weapons and contraband in the 100 ghz to 1 thz region," *Antennas and Propagation, IEEE Transactions on*, vol. 55, no. 11, pp. 2944-2956, nov. 2007.
- [3] M. Kemp, "Millimetre wave and terahertz technology for detection of concealed threats - a review," in *Infrared and Millimeter Waves, 2007 and the 2007 15th International Conference on Terahertz Electronics. IRMMW-THz. Joint 32nd International Conference on*, sept. 2007, pp. 647-648.
- [4] A. Luukanen, M. Gronholm, P. Lappalainen, M. Leivo, A. Rautiainen, A. Tamminen, J. Ala-Laurinaho, A. Raisanen, C. Dietlein, and E. Grossman, "Passive real-time submillimetre-wave imaging system utilizing antenna-coupled microbolometers for stand-off security screening applications," in *Antenna Technology (iWAT), 2010 International Workshop on*, march 2010, pp. 1-4.
- [5] E. Heinz, T. May, D. Born, G. Zieger, G. Thorwirth, S. Anders, V. Zakosarenko, T. Krause, A. Krüger, M. Schulz, H.-G. Meyer, M. Schubert, and M. Starkloff, "Toward high-sensitivity and high-resolution submillimeter-wave video imaging," *Optical Engineering*, vol. 50, no. 11, p. 113204, 2011.
- [6] K. Cooper, R. Dengler, N. Llombart, B. Thomas, G. Chattopadhyay, and P. Siegel, "Thz imaging radar for standoff personnel screening," *Terahertz Science and Technology, IEEE Transactions on*, vol. 1, no. 1, pp. 169-182, sept. 2011.
- [7] A. Luukanen, J. Ala-Laurinaho, D. G. Martins, J. Häkli, P. Koivisto, P. Pursula, P. Rantakari, J. Säily, A. Tamminen, R. Tuovinen, and M. Sipilä, "Rapid beamsteering reflectarrays for mm-wave and submm-wave imaging radars," D. A. Wikner and A. R. Luukanen, Eds., vol. 8022, no. 1. SPIE, 2011, p. 80220M.
- [8] M. Bertero and P. Boccacci, *Introduction to Inverse Problems in Imaging*. Bristol and Philadelphia: Institute of Physics Publishing, 1998.
- [9] D. Takhar, J. N. Laska, M. B. Wakin, M. F. Duarte, D. Baron, S. Sarvotham, K. F. Kelly, and R. G. Baraniuk, "A new compressive imaging camera architecture using optical-domain compression," C. A. Bouman, E. L. Miller, and I. Pollak, Eds., vol. 6065, no. 1. SPIE, 2006, p. 606509.
- [10] R. D. Swift, R. B. Wattson, J. John A. Decker, R. Paganetti, and M. Harwit, "Hadamard transform imager and imaging spectrometer," *Appl. Opt.*, vol. 15, no. 6, pp. 1595-1609, 1976.
- [11] O. Furrxi and E. L. Jacobs, "Comparison of schemes for active sub-millimeter wave imaging," K. A. Krapels, N. A. Salmon, and E. Jacobs, Eds., vol. 8188, no. 1. SPIE, 2011, p. 81880M.
- [12] J. Lynch, R. Matic, and J. Baron, "Performance limitations of compressive sensing for millimeter wave imaging," D. A. Wikner and A. R. Luukanen, Eds., vol. 7670, no. 1. SPIE, 2010, p. 76700D.
- [13] Z. Liu, J. Midkiff, H. Xu, T. Crowe, and I. Weikle, R.M., "Broad-band 180 deg; phase shifters using integrated submillimeter-wave schottky diodes," *Microwave Theory and Techniques, IEEE Transactions on*, vol. 53, no. 9, pp. 2949-2955, sept. 2005.

# Comparison of Schemes for Active Sub-millimeter Wave Imaging

Orges Furxhi<sup>a</sup>, Eddie L. Jacobs<sup>b</sup>

The University of Memphis, Memphis, TN 38152

## ABSTRACT

Various schemes for active imaging require different allocations of source power and can result in different overall signal to noise ratios. At the University of Memphis we have developed an image-plane scanning device used with a single pixel detector to form video rate images of the scene. Imaging with this device requires flood illumination of the scene. Because sub-millimeter wave sources typically produce low power, it is a common belief that flood illumination results in low detected signal power and therefore low signal to noise ratios (SNR) at the detector. In this work we quantify the SNR at the detector for our system and compare it to conventional imaging systems, conjugate point imaging systems, and focal plane array imaging. Unlike the other two systems, imaging with our device requires an additional pixel formation step; therefore, the SNR at the detector is not the per-pixel SNR. We present the limits of the per-pixel SNR and discuss its dependence on various device components.

**Keywords:** Sub-millimeter waves, terahertz, imaging, spatial light modulator, spatially selective mask, compressive sensing

## 1. INTRODUCTION

In general, an active imaging device consists of an optical system, an illumination system, a detector system, and a signal processing system for image reconstruction and display. There are multiple ways these systems can be configured and the burden each one bears in the image formation process depends on the configuration. One of the simplest schemes is to use a lens or mirror to focus the image of the illuminated scene onto a focal plane array of detectors. Signal processing for this configuration is usually simple as well as each detector in the focal plane array is mapped to an image pixel. For sub-millimeter wave imaging, focal plane arrays of the desired sizes are either expensive or non-existent. Designers of imaging systems are then forced to look at different schemes for forming images. Almost all involve trading image acquisition time/detector integration time for spatial resolution. Also the optimal illumination scheme for each configuration is different. As a result, signal to noise ratios for such systems are different from the focal plane array system.

In this paper we examine the signal to noise ratio (SNR) for the various schemes and compare them. We restrict our study to active imaging where image brightness (signal) is controlled by the strength of the source over an imaged pixel. Five configurations are investigated, namely: conjugate point imaging, conjugate line imaging, conjugate plane imaging, conjugate line-point imaging, and conjugate plane-point imaging. These configurations are described in more detail in the next section, but the conjugates referred to in the system nomenclature are the illuminated region in the object plane and the detector array dimension in the image plane. The last two configurations, conjugate line-point and plane-point, require non-trivial processing of the measured noisy signal to reproduce the image formed on the image plane. The additional processing introduces noise in the final reconstructed image, therefore these two systems require additional analysis.

In the next section we describe each of the active imaging configurations that will be analyzed and compared. Section 3 provides a summary of the derivation of SNR of the detected signal for active heterodyne systems as presented by Brown.<sup>1</sup> The following Sections 4 and 5 provide an analysis of each imaging configuration

---

<sup>a</sup>ofurxhi@memphis.edu, <sup>b</sup>eljacobs@memphis.edu



with respect to incident power on the detector and available integration time per measurement. In Section 6 we summarize the analysis of the previous sections to compare the SNR at the detector for each of the configurations. The analysis of the additional reconstruction noise for the last two configurations is presented in Section 7. In Section 8 we make some final remarks and present our conclusions.

## 2. ACTIVE IMAGING CONFIGURATIONS

Active imagers consist of an illuminating source, illumination optics, image forming optics, and the detector. The detector can be a single or multi-element detector, and more generally it can have a spatial-temporal varying integration aperture. As is usually the case, the imaging and illumination optics are the same, and the source and detector are multiplexed using a beam splitter. Depending on the imager configuration, the optics may contain a beam steering mechanism. The illuminating source might illuminate over regions of various shapes and usually consists of a single point source and beam shaping elements.

Figures 1a through 1e show five possible active imaging configurations. Figure 1a shows a conjugate point imaging configuration. In this configuration the illumination source illuminates a diffraction limited spot in the object plane and the same spot is imaged on a single element detector in the image plane. Spatial resolution is achieved by means of a scanning mechanism that concurrently scans the illumination source and single element detector.

Figure 1b shows a conjugate line imaging configuration. Here the illumination source is projected over a line segment in the object plane; the part of the object that is illuminated is imaged in the image plane on a multi-element detector arranged in a line array configuration. One dimension is resolved by the multi-element array and the other by concurrently scanning the line source and detector across the scene.

Figure 1c shows a conjugate plane imaging configuration. The illumination source is projected over a rectangular area in the object plane; the part of the object that is illuminated is imaged in the image plane on a multi-element detector in a rectangular array configuration. Both dimensions are resolved by the positioning of the detectors on the array. This configuration does not require any scanning.

Figure 1d shows a conjugate line-point imaging configuration. Here the illumination source is projected over a line segment in the object plane; the part of the object that is illuminated is imaged in the image plane on a single element detector with a line-shaped spatial-temporal varying integration aperture. One dimension is resolved by varying the integration aperture of the detector over time and the other by concurrently scanning the line source and detector across the scene. The variable integration aperture is usually implemented by a mask placed over the detector aperture. As shown in the figure, the detector includes a collecting lens and the mask. The lens is used to optically increase the integrating aperture of the detector. Because the mask only lets part of the radiation incident on the aperture to reach the receiving detector we define a fill ratio constant,  $f_r$ . This constant represents the fraction of incident energy that reaches the receiving detector.

Figure 1e shows a conjugate plane-point imaging configuration. Here the illumination source is projected over a rectangular area in the object plane. The part of the object that is illuminated is imaged in the image plane on a single element detector with a rectangular-shaped spatial-temporal varying integration aperture. Both dimensions are resolved by varying the integration aperture of the detector over time. This configuration does not require any image or detector scanning.

## 3. SIGNAL TO NOISE RATIO OF ACTIVE HETERODYNE SYSTEMS

In terms of SNR, the variables of interest for each configuration are integration time and power incident on the detector elements for each measurement. Before examining the integration time and incident power available for each of the five configurations, we present the dependence of the SNR on these two variables. This is a summary of Brown's<sup>1</sup> SNR derivation for an active heterodyne system. A block diagram of the heterodyne receiver analyzed by Brown is shown in Figure 2.

Brown defines the power SNR as the ratio of the average power to the rms fluctuations associated with the noise

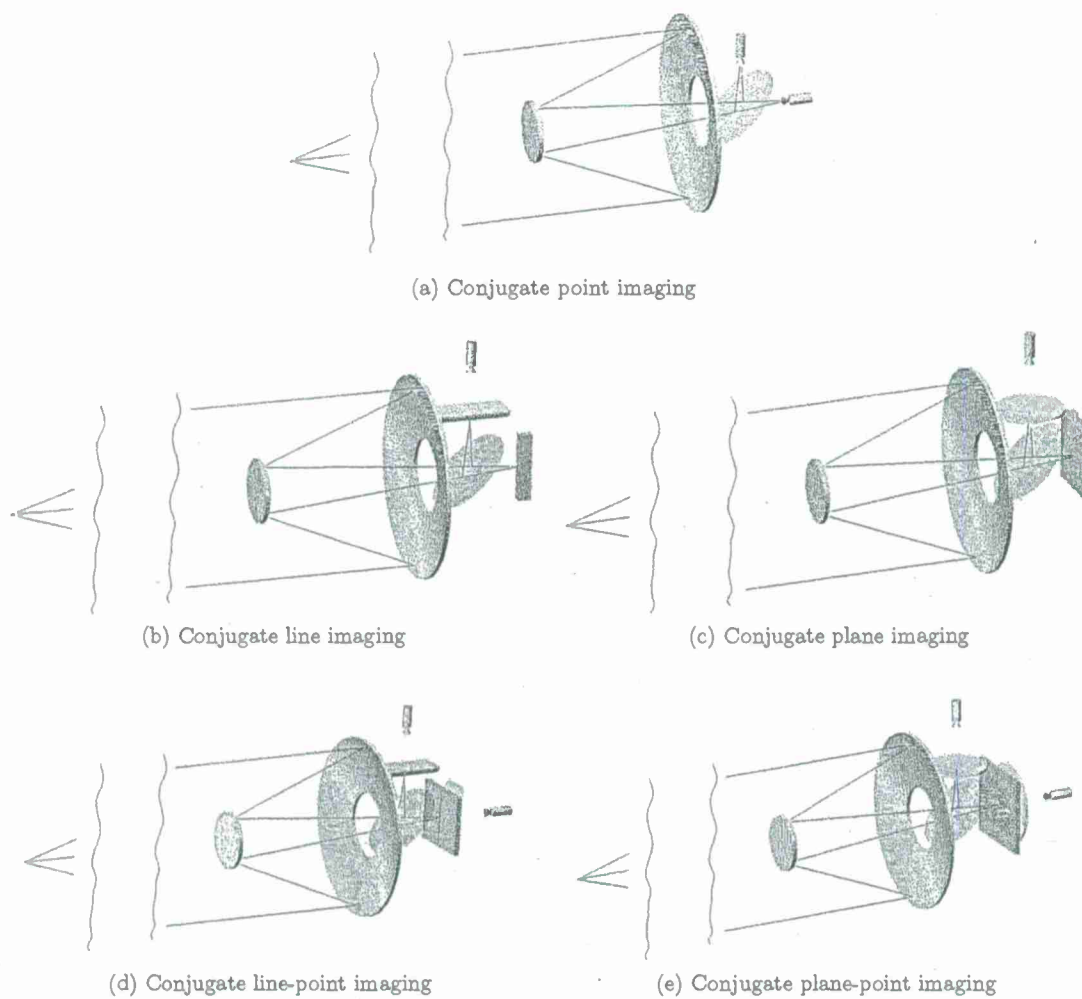


Figure 1. Imager configurations

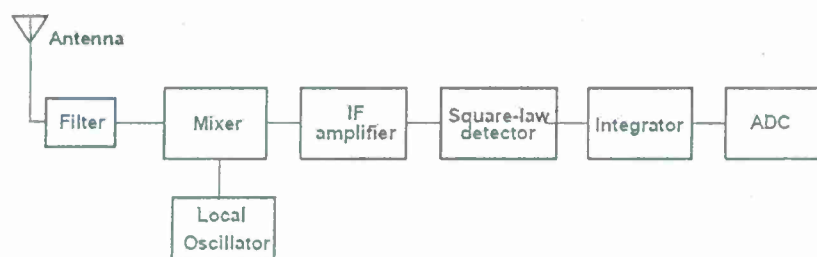


Figure 2. Block diagram of the heterodyne system

$$\frac{S}{N} = \frac{\langle P \rangle}{\sqrt{\langle (\Delta P)^2 \rangle}} = \frac{\langle P \rangle}{S_P B_{ENB}} \quad (1)$$

where  $S_P$  is the power spectral density of the noise and  $B_{ENB}$  is the equivalent noise bandwidth at that point in the sensor.

#### Square-Law detectors:

A square-law detector produces an output proportional to its square

$$X_{out} = AX_{in}^2 = \mathcal{R}P_{abs} \quad (2)$$

For our detectors  $X_{out}$  is usually a voltage,  $P_{abs}$  is the power absorbed by the detector, and  $\mathcal{R}$  is the detector responsivity in units of V/W. Assuming that the input noise to the detector has white noise spectrum and is unrelated to the signal, the SNR at the output of the detector is related to the SNR at the input by

$$SNR_{out} = SNR_{in} \sqrt{\frac{\Delta\nu}{2\Delta f}} \quad (3)$$

where  $\Delta\nu$  is the signal (noise) bandwidth before detection and  $\Delta f$  is the signal (noise) bandwidth after detection. The bandwidth after detection  $\Delta f$ , is determined by the low-pass filter/integrator following the detector. The integration time of the detector (also determined by the low-pass filter/integrator) is  $\tau = 1/(2\Delta f)$ , therefore the SNR relationship above can be expressed as

$$SNR_{out} = SNR_{in} \sqrt{\tau \cdot \Delta\nu} \quad (4)$$

#### Heterodyne conversion:

For the heterodyne conversion the output signal (a voltage) is equal to the product of the input signal and local oscillator signal (LO) times a proportionality constant,  $A$ . Assuming sinusoidal signals ( $X_{in} = B\cos(\omega_{in}t)$  and  $X_{LO} = C\cos(\omega_{LO}t)$ ), the output signal at the intermediate frequency (IF) which is the difference of the input signal frequency and LO frequency will be

$$X_{out} = ABC\cos(\omega_{in} - \omega_{LO})t = 2\eta\mathcal{R}\sqrt{P_{inc}P_{LO}}\cos(\omega_{in} - \omega_{LO})t \quad (5)$$

where  $P_{inc}$  and  $P_{LO}$  are the incident and LO powers, and  $\eta$  is the fraction of each that is absorbed (mixer efficiency). Then the output power at the IF frequency is given by

$$\overline{P}_{out} = D\overline{X_{out}^2} = 4D(\eta\mathcal{R})^2 P_{inc}P_{LO}\overline{\cos^2(\omega_{in} - \omega_{LO})t} = 2D(\eta\mathcal{R})^2 \overline{P}_{inc}\overline{P}_{LO} \quad (6)$$

where  $D$  is the mixer-to-IF circuit matching factor accounting for mismatch between the mixer and IF load impedance and the  $\overline{\phantom{x}}$  represents time averages. Grouping mixer and detector related terms together ( $G_{mix} = 2D\mathcal{R}^2\overline{P}_{LO}$ ), the IF power is rewritten as

$$\overline{P}_{out} = \eta^2 G_{mix} \overline{P}_{inc} \quad (7)$$

The noise consists in the fluctuations of the mixer output signal that are caused by quantum-mechanical fluctuations in the incident and LO signals. Since usually  $P_{LO} \gg P_{inc}$ , the local oscillator noise will dominate and an upper limit on the noise (similar to direct detection noise, since the mixer is a direct detection detector with two arms) will be

$$(\Delta X_{out})^2 = 2\mathcal{R} \cdot (\Delta P_{LO})^2 \cdot \frac{B_{IF}}{\Delta\nu} \quad (8)$$

where  $B_{IF}$  is the IF bandwidth (equivalent to the after detection bandwidth) and  $\Delta\nu$  is the bandwidth over which the mixer accepts radiation. The LO quantum-mechanical noise power is given by

$$\Delta P_{LO} = \sqrt{\eta \cdot h \cdot \nu_{LO} P_{LO} (\Delta\nu)} \quad (9)$$

where  $h$  is Plank's constant and  $\nu_{LO} = \omega_{LO}/2\pi$ . The noise will therefore be

$$(\Delta X_{out})^2 = 2\mathcal{R} \cdot \eta \cdot h \cdot \nu_{LO} P_{LO} B_{IF} \quad (10)$$

or in terms of noise power

$$\Delta P_{out} = D(\Delta X_{out})^2 = 2DR \cdot \eta \cdot h \cdot \nu_{LO} P_{LO} B_{IF} = G_{mix} \eta \cdot h \cdot \nu_{LO} B_{IF} \quad (11)$$

The SNR after the heterodyne conversion will be

$$\left(\frac{S}{N}\right)_{IF} = \frac{\bar{P}_{out}}{\Delta P_{out}} = \frac{\eta^2 G_{mix} \bar{P}_{inc}}{G_{mix} \eta \cdot h \cdot \nu_{LO} B_{IF}} = \frac{\eta \bar{P}_{inc}}{h \cdot \nu_{LO} B_{IF}} \quad (12)$$

**Electrical noise on heterodyne mixers:**

The electrical noise introduced by the IF electronics is accounted for by adding a noise rms term to the IF noise. We call the resulting noise the heterodyne noise and the resulting SNR the heterodyne SNR

$$\left(\frac{S}{N}\right)_{HET} = \frac{\bar{P}_{out}}{\Delta P_{out} + \sqrt{(\Delta P_{IF-e})^2}} = \frac{\eta^2 G_{mix} \bar{P}_{in}}{G_{mix} \eta \cdot h \cdot \nu_{LO} B_{IF} + \sqrt{(\Delta P_{IF-e})^2}} \quad (13)$$

The electrical noise term,  $\sqrt{(\Delta P_{IF-e})^2}$ , will be expressed in terms of the mixer noise equivalent power (NEP). The NEP is found by setting the SNR of the system to unity and solving for the incident power, therefore

$$NEP_{HET} = P_{inc} = \frac{h \cdot \nu_{LO} B_{IF}}{\eta} + \frac{\sqrt{(\Delta P_{IF-e})^2}}{\eta^2 G_{mix}} \quad (14)$$

The specific NEP (NEP per unit bandwidth) is obtained by dividing the NEP by the signal (noise) bandwidth

$$NEP'_{HET} = \frac{NEP_{HET}}{B_{IF}} = \frac{h \cdot \nu_{LO}}{\eta} + \frac{\sqrt{(\Delta P_{IF-e})^2}}{\eta^2 G_{mix} B_{IF}} \quad (15)$$

The first term to the right of the equation is due to the quantum-mechanical noise of the mixer and the second term is due to the electrical noise. If the electrical noise is much larger than the quantum-mechanical noise and the electrical noise is all white Gaussian noise (AWGN), the specific heterodyne NEP reduces to the mixer limited value

$$NEP'_{HET} \approx NEP'_{mixer} = \frac{\sqrt{(\Delta P_{IF-e})^2}}{\eta^2 G_{mix} B_{IF}} \quad (16)$$

therefore we can solve for the electric noise rms term

$$\sqrt{(\Delta P_{IF-e})^2} = \eta^2 G_{mix} B_{IF} \cdot NEP'_{mixer} \quad (17)$$

The heterodyne SNR of Equation 13 is then rewritten as

$$\left(\frac{S}{N}\right)_{HET} = \frac{\eta^2 G_{mix} \bar{P}_{in}}{G_{mix} \eta \cdot h \cdot \nu_{LO} B_{IF} + \eta^2 G_{mix} B_{IF} \cdot NEP'_{mixer}} = \frac{\eta}{h \cdot \nu_{LO} + \eta \cdot NEP'_{mixer}} \cdot \frac{\bar{P}_{in}}{B_{IF}} \quad (18)$$

From this equation we also obtain the specific heterodyne NEP as a function of the specific mixer NEP

$$NEP'_{HET} = \frac{h \cdot \nu_{LO}}{\eta} + NEP'_{mixer} \quad (19)$$



This form of the specific heterodyne NEP is convenient because it is used to define the receiver noise temperature which is usually specified by the manufacturer of the receiver. The receiver noise temperature is also known as noise-equivalent temperature (NET)

$$NET_{HET} = \frac{NEP'_{HET}}{k_B} = \frac{1}{k_B} \left( \frac{h \cdot \nu_{LO}}{\eta} + NEP'_{mixer} \right) \quad (20)$$

where  $k_B$  is the Boltzmann constant. Given the receiver noise temperature,  $NEP'_{mixer}$  can be calculated and then  $(\frac{S}{N})_{HET}$  can be obtained. For example for our 640GHz system,  $\nu_{LO} = 319GHz$ ,  $NET_{HET} = 3000K$ ,  $NEP'_{mixer} = 4.12 \times 10^{-18}[W]$ .

#### Heterodyne detection with Schottky diode mixers:

The SNR after the heterodyne conversion including the contribution of the mixer electrical noise is given by Equation 18. Each term (signal in the numerator and noise in the denominator) is multiplied by the gain of the entire IF amplifier chain  $G_{IF}$ , and the responsivity of the square law detector  $\mathcal{R}_{D^2}$ , that is used to detect the amplified IF signal. The relationship of the SNRs before and after detection for square law detectors is given by Equation 3 and is restated here with the appropriate subscripts

$$SNR_{AD} = SNR_{BD} \sqrt{\frac{B_{BD}}{2B_{AD}}} \quad (21)$$

where the subscript "BD" stands for "before detection" and the subscript "AD" stands for "after detection". In our case  $B_{BD}$  is  $B_{IF}$ , and  $B_{AD}$  is the bandwidth of the integrator,  $\Delta f$ , after the square law detector. The SNR after detection then becomes

$$SNR_{AD} = \frac{\eta^2 \mathcal{R}_{D^2} G_{IF} G_{mix} \bar{P}_{in}}{\mathcal{R}_{D^2} \{ G_{IF} G_{mix} \eta \cdot h \cdot \nu_{LO} B_{IF} + \eta^2 G_{IF} G_{mix} B_{IF} \cdot NEP'_{mixer} \}} \sqrt{\frac{B_{IF}}{2\Delta f}} \quad (22)$$

$$SNR_{AD} = \frac{\eta^2 \bar{P}_{in}}{\eta \cdot h \cdot \nu_{LO} + \eta^2 \cdot NEP'_{mixer}} \sqrt{\frac{1}{2\Delta f \cdot B_{IF}}} \quad (23)$$

Therefore the heterodyne detection the SNR is directly proportional to the incident power and inversely related to the square root of the detection bandwidth,  $\Delta f$ . In terms of incident power and integration time the detected SNR is

$$SNR_{AD} = \left\{ \frac{\eta^2}{\eta \cdot h \cdot \nu_{LO} + \eta^2 \cdot NEP'_{mixer}} \sqrt{\frac{1}{B_{IF}}} \right\} \times \bar{P}_{in} \times \sqrt{\tau} \quad (24)$$

where the integration time is given by  $\tau = 1/(2\Delta f)$ .

#### 4. INCIDENT POWER

Now that the SNR dependence on the incident power and integration time has been stated, we analyze the amount of incident power on the detectors of each imager configuration. This analysis is simplified by introducing the concept of spatial modes. The number of spatial modes,  $M_{S/D}$ , of the source or detector element is defined as the ratio of squares of the sensor (including optics) field of view ( $FOV_{Sensor}$ ) to the source/detector element instantaneous field of view ( $IFOV_{S/D}$ ); equivalently, the ratio of the solid angles. The receiver and transmitter might also include optics or other components.

For conjugate point imaging, source and detector element number of modes is

$$M_S = M_D = \left( \frac{FOV_{Sensor}}{IFOV_S} \right)^2 = \left( \frac{FOV_{Sensor}}{IFOV_D} \right)^2 = 1 \quad (25)$$

This signifies that the source is projected over the region of interest, and that region of interest is imaged by the detector element.

For conjugate line imaging

$$M_S = \left( \frac{FOV_{Sensor}}{IFOV_S} \right)^2 = 1 \quad (26)$$

$$M_D = \left( \frac{FOV_{Sensor}}{IFOV_D} \right)^2 = n \quad (27)$$

where  $n$  is defined as the ratio of the desired linear image size (in the image plane) to the square root of the receiving antenna effective area (assuming a square antenna aperture). The effective area of an aperture antenna can be less than or equal to the physical area of the antenna aperture.<sup>2</sup> We can use the upper limit (max fill factor 100%) and assume the effective and physical areas to be equal. This can also be interpreted as the number of pixels in the linear direction for 100% fill factor. The number source modes is again one because the illumination source in this case is a line segment and is projected over the region of interest. The number of detector element modes however is  $n$  because each of the detector elements only images a fraction of the line segment.

For conjugate plane imaging the reasoning is similar except that each detector element only images  $1/n^2$  part of the image

$$M_S = \left( \frac{FOV_{Sensor}}{IFOV_S} \right)^2 = 1 \quad (28)$$

$$M_D = \left( \frac{FOV_{Sensor}}{IFOV_D} \right)^2 = n^2 \quad (29)$$

where the image is assumed to be square.

For conjugate line-point imaging we have

$$M_S = \left( \frac{FOV_{Sensor}}{IFOV_S} \right)^2 = 1 \quad (30)$$

$$M_D = \left( \frac{FOV_{Sensor}}{IFOV_D} \right)^2 = \frac{1}{f_r} \quad (31)$$

where  $f_r$  is the mask aperture fill ratio defined previously, usually a value less than one. The mask aperture fill ratio represents the fraction of the detector aperture that is transmissive for any pattern. Depending on the mask configuration, practical values for this constant range between  $1/n^2$  and 0.7. For this case the detector element is dependent only on the fill ratio because the image of the illuminated object region is formed on the detector aperture which is then masked with a fill ratio  $f_r$ . For conjugate plane-point imaging we also have the same relationships.

The number of spatial modes for the source is one ( $M_S = 1$ ) in all the configurations because it is assumed that the source power is perfectly projected on the target by the optical system, ignoring diffraction effects. If diffraction effects are accounted for, the number of spatial modes becomes larger than one. The factor of spatial mode increase depends on the  $F\#$  of the system's optical system and the area of the illuminated target space. As the  $F\#$  increases, the spatial mode number increases; illumination projected onto the target is not as selective and the imaged illumination falls outside the aperture of the detector. As the illuminated area increases, the spatial mode number approaches one; in this case the blurred edge to total illuminated area ratio decreases as the area increases. Therefore, accounting for diffraction affects the conjugate point imaging configuration more than the others. For the purposes of the following analysis we will initially ignore diffraction because its effect is usually less than an order of magnitude; but we will pick up the discussion when the various configurations are compared in Section 6.

The relationship between source power and incident power on the detector is calculated using the Friis formula found in many books on radar systems or antennas.<sup>2</sup> Because the source is coupled to an optical system and it is assumed that the optical aperture and source antenna beam width are matched, all the power, attenuated by the atmospheric loss coefficient ( $\tau(r)$ ) and the reflectivity or transmission of the optics ( $\alpha_{Optics}$ ), is projected on the

target. This is true in all of the configurations. If the target is assumed larger than its illuminated sections, the reflected power will be equal to the power density on the target times the radar cross section of the target section and attenuated by the reflectivity of the target ( $R_{Target}$ ). For simplicity, and since the analysis is relative, we assume that the target radar cross-section is equal to the illuminated target area, and any losses associated with target orientation or roughness are absorbed into the reflectivity coefficient. The power reflected by the target will be:

$$P_{Target} = \alpha_{Optics} \tau(r) R_{Target} P_{source} \quad (32)$$

The power collected by the optical aperture is then the power density at the aperture due to the reflecting target (again attenuated by the atmosphere), multiplied by the physical area of the optical aperture ( $A_{Optics}$ ). It is assumed that the optical aperture is large with respect to wavelength and matched to the receiving antenna. The power collected by the optics is then projected in the image plane, and the power integrated across the image plane is

$$\begin{aligned} P_{image} &= \frac{P_{Target} \tau(r) A_{Optics} \alpha_{Optics}}{4\pi r^2} \\ P_{image} &= \frac{R_{Target} P_{source} \tau^2(r) \alpha_{Optics}^2 A_{Optics}}{4\pi r^2} \end{aligned} \quad (33)$$

The power incident on the receiving antenna will be a function of the power in the image plane and the spatial mode number of each configuration

$$P_{inc} = \frac{P_{image}}{M_D M_S} \quad (34)$$

## 5. INTEGRATION TIME

Integration time for the scanning configurations is a function of the picture elements (pixels) required for the image. The number of pixels may or may not be equal to the number of spatial modes. For staring configurations integration time is independent of the number of pixels. Image frame rate affects both staring and scanning systems.

For conjugate point imaging the integration time will be

$$\tau = \frac{1}{F \times (\gamma N)^2} - T \quad (35)$$

where  $F$  is the frame rate in Hz,  $N^2$  is the number of pixels per image or the total number of measurements per image,  $\gamma$  is the pixel oversampling factor, and  $T$  is a scanning delay. The oversampling factor is usually greater or equal to one.

For conjugate line imaging the integration time will be

$$\tau = \frac{1}{F \times \gamma N} - T \quad (36)$$

where it is assumed that the pixelated images will be square.

For conjugate plane imaging the integration time will be

$$\tau = \frac{1}{F} \quad (37)$$

For conjugate line-point imaging and conjugate plane-point imaging the integration time will be the same except that the scanning delay terms might be different

$$\tau = \frac{1}{F \times N^2} - T \quad (38)$$

For these configurations however,  $N^2$  is also interpreted as the number of measurements which can be less than the number of image pixels.

Depending on the implementation of each imaging technique the number of image pixels or measurements,  $N^2$ , and the number of effective antenna areas in the image plane,  $n^2$ , may or may not be equal.

Table 1. Relative SNR expressions for each configuration

Imaging configuration	Relative SNR
conjugate point imaging	$SNR'_{Point} = \sqrt{\frac{1}{F \times (\gamma N)^2} - T}$
conjugate line imaging	$SNR'_{Line} = \frac{\sqrt{\frac{1}{F \times \gamma N} - T}}{n}$
conjugate plane imaging	$SNR'_{Plane} = \frac{\sqrt{\frac{1}{F}}}{n^2}$
conjugate line-point imaging	$SNR'_{Line-Point} = f_r \sqrt{\frac{1}{F \times N^2} - T}$
conjugate plane-point imaging	$SNR'_{Plane-Point} = f_r \sqrt{\frac{1}{F \times N^2} - T}$

## 6. RELATIVE SNR

Given the dependence of the SNR on the incident power and integration time, and the expressions for those variables in terms of number of pixels, frame rate, and imager configuration, we define the relative SNR for each configuration. The relative SNR is the SNR after detection (given in Equation 24) normalized by all the common factors (common between imaging configurations)

$$SNR' = \frac{SNR_{AD}}{\left\{ \frac{\eta^2}{\eta \cdot h \cdot \nu_{LO} + \eta^2 \cdot NEP'_{mizer}} \sqrt{\frac{1}{B_{IF}}} \right\} P_{image}} \quad (39)$$

Using Equations 24 and 34 in 39 we can express the relative SNR as

$$SNR' = \frac{\sqrt{\tau}}{M_D} \quad (40)$$

Using the detector mode number and integration time expressions derived previously we find the relative SNR expressions for each configuration. The expressions are shown in Table 1.

An interesting observation is that conjugate plane-point and line-point imaging perform similarly (differing in the scan delays and mask fill factors). For typical values of  $F = 10Hz$ ,  $n = 1.2N$ ,  $T = 20\%$  delay,  $f_r = 0.5$ , and  $\gamma = 1$ , we plot the relative SNRs as a function of the number of pixels in the linear direction,  $N$ . Figure 3a shows plots of the relative SNRs as given in Table 1. The units of this plot are arbitrary. The best performance is achieved by the conjugate point imaging. The next best performance is achieved by the conjugate line-point and conjugate plane-point systems. The conjugate line system follows and the worst performing system, in terms of SNR, is the conjugate plane system. These results confirm Grossman's result that active systems favor scanning systems with regard to sensitivity.<sup>3</sup> The plots also show that the SNR decreases as the number of image pixels increases for a set frame rate. To compare the rate of decrease with respect to number of image pixels we plot the data from Figure 3a normalized by the relative SNR of the conjugate system. These plots are shown in Figure 3b. The rate of decrease of the conjugate point, conjugate line-point, and conjugate plane-point is the same, while the other two systems suffer a faster decrease. This is expected as the relative SNR for the first group of systems depends only on the integration time while for the second group it depends on the integration time and number of pixels and modes.

The conjugate line-point and plane point systems can also be used in a compressive sensing mode, where the number of measurements required to reconstruct an image can be a fraction of the number of pixels in the image. This is achieved if the measurements satisfy certain conditions and the image is sparse in some domain.<sup>4</sup> The implication is that by decreasing the number of measurements we can account for the loss due to the mask fill ratio and achieve the relative SNR of the conjugate imaging configuration or better. Also, if diffraction effects are considered in the formulation of the mode equations in Section 4, the performance of the conjugate point system will decrease, possibly falling below that of the conjugate line-point and plane-point systems. However, as it is shown in the next section, these two systems suffer by additional noise that is introduced during the image reconstruction process.



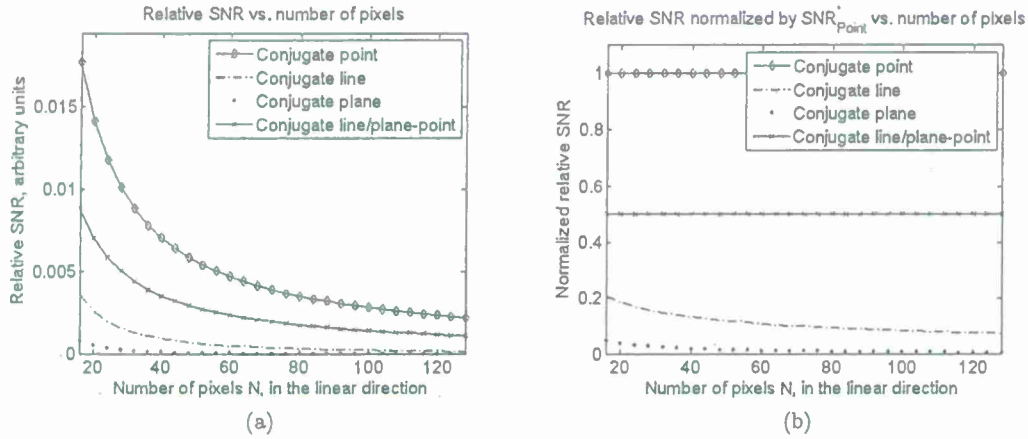


Figure 3. Relative SNR plots

## 7. IMAGE RECONSTRUCTION "NOISE"

The association of measurements with digitized pixels on a screen can be expressed mathematically as

$$Mp + \eta = \hat{m} = m + \eta \quad (41)$$

where  $M$  is a matrix that relates the digitized pixels contained in the vector  $p$  to the noisy measurements  $\hat{m}$ . The noisy measurements are composed of the signal  $m$  and noise  $\eta$ . The matrix  $M$  is called the measurement matrix and is usually calculated based on assumptions on the imaging system. For example, for the conjugate point, line, and plane systems the measurement matrix can resemble a diagonal matrix that may or may not model the point spread function of the optical system. For the conjugate line-point and plane point the measurement matrix will depend on the mask patterns, the point spread function, and possibly other mathematical models of other optical components in the system. Recall from the description of the systems in Section 2 that the mask patterns are used to implement the spatial-temporal varying integration aperture of the detector. The unknown pixel values are obtained by solving Equation 41. In the presence of noise however, only an approximate solution,  $\hat{p}$ , can be obtained because the noiseless measurement is not available. Also, the problem becomes ill-conditioned. One method for finding the approximate solution is the regularized least squares<sup>5</sup>

$$\hat{p} = \left[ M^T M + \sum_i \mu_i H_i^T H_i \right]^{-1} M^T \hat{m} = R(\mu_i) \hat{m} \quad (42)$$

where  $\mu_i$  are regularization parameters,  $H_i$  are linear operators on the solution, and the superscript  $T$  denotes the matrix transpose. Borrowing notation from Bertero,<sup>5</sup> the resulting matrix multiplication and additions are all grouped together into  $R(\mu_i)$  for notational ease. In the absence of any regularization  $R(\mu_i = 0) = M^{-1}$ . The linear operators  $H_i$  are modeled after a priori knowledge on the solution. For example, if the minimal norm solution is desired the linear operator is the identity matrix; if the solution is smooth the linear operator could be the Laplacian so that the sharp transitions are minimized. When constructing the linear operators one must keep in mind the arrangement of the pixel values in the vector  $\hat{p}$ .

From Equations 41 and 42 we can write the approximate solution in terms of a noiseless approximation term and a propagated noise term

$$\hat{p} = R(\mu_i) m + R(\mu_i) \eta \quad (43)$$

In the absence of noise and regularization the approximate solution reaches the exact solution

$$\lim_{\eta \rightarrow 0, \mu_i \rightarrow 0} R(\mu_i) m + R(\mu_i) \eta = M^{-1} m = p \quad (44)$$

The exact solution is defined by Equation 44 and should be interpreted as the "model limited" reconstruction of the image plane, not the object plane. The term "model limited" refers to the fidelity of the measurement model represented by the measurement matrix  $M$ . With the approximate and exact reconstructions defined, we can express the reconstruction error  $\varepsilon$  as

$$\begin{aligned}\varepsilon &= \hat{p} - p \\ \varepsilon &= (R(\mu_i)m - p) + R(\mu_i)\eta\end{aligned}\quad (45)$$

The relative reconstruction error is a more useful quantity and it is given as

$$RRE = \frac{\|\varepsilon\|}{\|p\|}\quad (46)$$

For the regularized least squares solution, the relative reconstruction error depends on the detector noise,  $\eta$ , and on the regularization parameters,  $\mu_i$ . If the image plane is illuminated by a constant intensity the value of the relative reconstruction error can be related to the per pixel signal to noise ratio ( $SNR_P$ ). The relationship is given by

$$SNR_P = \frac{1}{(RRE)^2}\quad (47)$$

The reconstruction error of Equation 45 is composed of two terms, the approximation error ( $R(\mu_i)m - p$ ) and the noise propagation ( $R(\mu_i)\eta$ ). Expanding  $R(\mu_i)$  as in Equation 42, one observes that the approximation error is directly related to the regularization parameters and the noise propagation term is inversely related to the regularization parameters. When the measurement matrix is only mildly ill-conditioned and the regularization parameters are small, the noise propagation term dominates the reconstruction error.<sup>5</sup> For small pixel count images (64x64) high regularization is not desired as it leads to blur spanning several pixels. Therefore, practical measurement matrices have to require only mild regularization. In this case the reconstruction error is approximated by

$$\hat{\varepsilon} = R(\mu_i)\eta\quad (48)$$

The noise in Equation 48 is the detector noise considered in Section 3. We define the reconstruction noise gain as

$$G_\eta = \frac{\|R(\mu_i)\eta\|^2}{\|\eta\|^2}\quad (49)$$

As defined, the reconstruction noise gain is independent of the noise level and can be computed simply by generating all white Gaussian noise of any variance. If the pixel count is not large however, the average of several noise realizations might be necessary.

In a similar manner to the reconstruction noise gain we define the reconstruction signal gain

$$G_S = \frac{\|R(\mu_i)m\|^2}{\|m\|^2}\quad (50)$$

where  $m$  is the noiseless signal. Unlike  $G_\eta$  the reconstruction signal gain is dependent on the signal because  $R(\mu_i)$  tends to filter the spatial frequency components of the signal by different amounts. Also, if the encoding mask is not balanced,  $R(\mu_i)$  might decode the measurements with different gains. An example of balanced encoding is the Hadamard mask.<sup>6</sup> To circumvent this we propose using a gain range rather than a single gain value. One limit of the gain is calculated for a uniform image  $p$  (low spatial frequency, low sparsity) and the other for a one pixel wide impulse image (high frequency limit, high sparsity). Using the noise gain and the signal gain range we can relate the detector noise ( $SNR_{AD}$ ) to the per pixel SNR range ( $SNR_{PR}$ )

$$\frac{SNR_{AD}}{SNR_{PR}} = \frac{G_\eta}{G_{SR}}\quad (51)$$

The gain ratio approximates the ratio of SNRs defined by Equations 24 and 47 as long as the detector noise is the main contributor of the reconstruction error.

For the 64x64 pixel conjugate plane-point system that we have implemented and demonstrated,<sup>7,8</sup> the SNR gain ratio ranges from  $2 \times 10^6$  for the low sparsity image, to  $2 \times 10^3$  for the high sparsity image. For the 32x32 pixel version of the same imager the SNR gain ratio ranges from  $6 \times 10^4$  to  $3 \times 10^2$ . For the 64x1 line imager version of the device the SNR gain ranges between 440 and 20.

The 32x32 pixel imager performs better than the 64x64, and the line imager performs significantly better than the two dimensional imagers. The reason is simply the degree of dependence between measurements. The measurement dependence increases with the number of pixels for a given imager physical dimension. Another important observation is that reconstructions for sparse images have significantly (orders of magnitude) lower gain ratio than the reconstructions for non-sparse images. For more details on our imager the reader can refer to our previous publications.<sup>7,8</sup>

Our imager can be modified to implement a Simplex Code Mask (SCM). The measurement matrix that results from an SCM consists of 1's and 0's. According to Harwit<sup>6</sup> SCMs make the best masks when entries 0 and 1 can be used. For a 64x1 imager with SCM the gain ratio ranges from 64 to 2 without any regularization, and can be even lower if regularization is used.

The analysis presented in this section applies only to the regularized least squares method of image reconstruction. Other reconstruction methods, especially non-linear, exist that provide better immunity to noise. The gain ratio numbers presented above only pertain to the current implementation of our imager and we are investigating methods of breaking the dependence between measurements that results in high noise gain.

## 8. CONCLUSIONS

In this article, a series of imaging configurations for active sensors has been defined. The SNR for each pixel has been calculated. In some of the schemes this SNR differs from the detector SNR due to the necessity of significant computational reconstruction of the image. The noise associated with linear methods of reconstruction has been included in this analysis. The main conclusion of this research is that non-traditional imaging schemes involving coded apertures and computational reconstruction may provide better image quality if reconstruction methods that are robust in the presence of noise can be achieved. This is a very active area of research in computational optics and compressive imaging and is a focus of our ongoing research in this area at the University of Memphis.

## REFERENCES

- [1] Brown, E. R., "Fundamentals of terrestrial millimeter-wave and thz remote sensing," *International Journal of High Speed Electronics and Systems* 13, 995-1097 (2003).
- [2] Balanis, C., [*Antenna Theory: Analysis and Design*], John Wiley & Sons, Inc., New York (1997).
- [3] Grossman, E. N., Luukanen, A., and Miller, A. J., "Terahertz active direct detection imagers," 5411(1), 68-77, SPIE (2004).
- [4] Donoho, D., "Compressed sensing," *IEEE Transactions on Information Theory* 52(4), 1289-1306 (2006).
- [5] Bertero, M. and Boccacci, P., [*Introduction to Inverse Problems in Imaging*], Institute of Physics Publishing, Bristol and Philadelphia (1998).
- [6] Harwit, M. and Sloane, Neil, J., [*Hadamard Transform Optics*], Academic Press, New York (1979).
- [7] Furxhi, O., Jacobs, E. L., and Hewitt, R., "Two-dimensional, real-time, sub-millimeter-wave imaging using a spatially selective mask," 8022(1), 80220J, SPIE (2011).
- [8] Furxhi, O. and Jacobs, E., "Spatially selective mask for single pixel video rate imaging," in [*Imaging Systems Applications*], *Imaging Systems Applications*, ITuA3, Optical Society of America (2011).

# Compressive Sensing for a Sub-millimeter Wave Single Pixel Imager

Imama Noor, Orges Furxhi, and Eddie L. Jacobs

## ABSTRACT

In this paper we demonstrate the use of compressive sensing to form an image with an image plane random mask and a single pixel sub-millimeter wave receiver. This type of imaging device is a practical solution in domains where focal plane arrays do not exist. The imager consists of a heterodyne source and receiver pair, image forming optics, a spatially selective mask, and data acquisition and post-processing hardware and software. The spatially selective mask modulates the signal measured by the receiver which is then sampled by an analog to digital converter and is post-processed to reconstruct the image. The spatially selective mask can produce image samples at full video rates. The post-processing used for this research consists of a sparseness inducing transformation on the measurements and application of compressive sensing reconstruction algorithms. We show several images acquired and reconstructed using this system. While the data acquisition of this system is real time, the processing currently must be done offline. We comment on the performance improvement using compressive sensing methods.

**Keywords:** Compressive sensing, submillimeter wave imaging, dictionary learning, single pixel imager

## 1. INTRODUCTION

Compressive sensing (CS) has been an active research area recently. It exploits the low information rate hidden in a signal. Most signals are sparse in a specific domain. CS uses this hidden information to reconstruct a signal from far less samples than required by a conventional algorithm. There are two main constraints imposed for an exact reconstruction from under sampled data: the sparsity of the signal and the incoherence of the measurement and compression matrices.<sup>1</sup> The number of non zero coefficients in a signal dictates the sparsity index. For an exact reconstruction the number of samples should be approximately four times the sparsity index<sup>1</sup> and the sparsity basis should be incoherent with the measurement matrix. In addition, the measurement matrix should follow the Restricted Isometric Property (RIP) to ensure that a reduction in the number of measurements does not have a significant effect on the information content. This implies that the reduction of dimensions of measurement matrix preserves the distances between the non zero planes of the sparse vector.<sup>2</sup> If a sampling process satisfies these conditions, this problem can be cast into Basis Pursuit Denoising (BPDN) or Lasso. There are different optimization algorithms available to solve BPDN and Lasso. Some widely used algorithms are Dantzig Selector, BPDN and greedy algorithms.<sup>3-5</sup> These algorithms are proven to converge and are tractable.<sup>6</sup>

If the measurement matrix follows the properties mentioned above, then we can use CS methods for reconstruction by using fewer measurements. To reconstruct an undersampled signal using CS theory, we need knowledge of the sparsifying basis for SMMW images. For this purpose we used an online dictionary learning algorithm to find a sparsity basis in which the signal can be represented by fewer atoms and is also incoherent with the measurement matrix.

In this work, we consider the problem of estimating an undersampled sub-millimeter wave line image. Earlier methods solved an inverse problem for signal reconstruction which requires as many or more measurements than the signal dimension. We address the issue of reconstruction from less measurements than required by least square or inverse solution and show that the number of measurements required for optimum reconstruction is less than the dimensions of the signal for a specific error bound.

The measurements obtained are transformed by the sparsity matrix and along with the product of the measurement matrix and sparsity basis are passed to the reconstruction algorithm. We cast the problem as a basis pursuit optimization. The basis pursuit optimization estimates a solution to a set of underdetermined linear Equations. If the objective function used is the  $l_1$  norm minimization and the RIP is satisfied, we are guaranteed



to find the sparsest solution consistent with the measurements.<sup>7</sup> This problem falls into the convex optimization category, ensuring the solution is unique and tractable. As mentioned above there are a lot of libraries available to solve convex optimization problems. We used disciplined convex optimization CVX modeling system to implement BP optimization.<sup>8</sup> CVX uses a base library of convex functions and sets. The solution obtained is an estimate of the coefficients in the sparse basis. The actual signal is obtained by transforming the coefficients back to the spatial domain. We demonstrate this method by reconstructing images from simulations and experimental measurements.

## 2. THEORETICAL BACKGROUND

### 2.1 Compressive sensing

CS is a relatively new approach that provides a mechanism to sample a signal below Nyquist sampling.<sup>2,11</sup> CS imposes some conditions on the characteristics of the signal under consideration and guarantees a reconstruction from fewer samples than required for conventional reconstruction. Consider a signal  $x$  to be reconstructed from the measurements  $y$ . We can express the relationship as

$$y = Ax + \omega \quad (1)$$

where  $y$  is the measurement vector of length  $k$ ,  $x$  is the unknown signal to be reconstructed with  $n$  dimensions. The matrix  $A$  is the measurement matrix and  $\omega$  is Gaussian noise  $(0, \sigma)$ . We consider the under determined problem where  $k < n$ . A signal has to be sparse in a particular domain to get an exact reconstruction using CS methodology. This implies we should be able to represent the signal in that domain by a linear combination of only a few atoms/columns of a dictionary. For instance if  $x$  is sparse in a specific domain  $\phi$  then

$$x = \phi z \quad (2)$$

$$y = A\phi z + \omega \quad (3)$$

where the vector  $z$  is a sparse vector with very few non zero elements. The sparsity index is the number of nonzero elements in the coefficient vector  $z$ . If  $S$  is the sparsity index of a signal in a particular dictionary and  $n$  is the dimension of the signal then the number of measurement required to reconstruct  $x$  should obey<sup>2,12</sup>

$$k \geq CS \log(n) \quad (4)$$

where  $C$  is a positive constant.<sup>2</sup> It depends on the coherence measure of measurement matrix and the sparsity basis. The coherence measure is defined as follows. If  $a_i$  and  $\psi_j$  represent the columns of  $A$  and  $\phi$  respectively then<sup>2</sup>

$$\mu = \frac{1}{\sqrt{n}} \max_{1 \leq i, j \leq n} |(a_i, \psi_j)| \quad (5)$$

The matrices are incoherent if  $\mu$  satisfies the inequality

$$\mu \leq 1 \quad (6)$$

To reconstruct from fewer samples, we need to make measurements such that they are incoherent with the sparsity basis matrix and the product of the measurement matrix with the sparsity basis matrix should satisfy the RIP. The RIP as given by Candès<sup>8</sup> is satisfied if

$$(1 - \delta_S) \|z\|_2^2 \leq \|A\phi z\|_2^2 \leq (1 + \delta_S) \|z\|_2^2 \quad (7)$$

where the product  $A\phi$  is the product of the measurement matrix with the sparsity basis matrix and  $z$  is any sparse vector. The finite constant  $\delta_S$  is the restricted isometry constant and is given by Candès.<sup>8</sup> The RIP

ensures that the transformation  $A\phi$  preserves the distances between the non zero planes of sparse vectors. Said another way, the satisfaction of the RIP is equivalent to the requirement that the largest eigenvalue of  $A\phi(A\phi)^T$  lies in the interval  $[1 + \delta_s, 1 - \delta_s]$ .

If the incoherence and the RIP are satisfied we can use CS reconstruction algorithms for solving this under-determined problem of linear Equations. As mentioned before different optimization techniques such as Dantzig selector, Lasso, or BP can be used for estimating a solution. We formulate the problem as BP and optimize it using Self Dual Minimization (SeDuMi).<sup>14</sup> According to CS Theory if we minimize the  $l_1$  norm, it gives us the sparsest unique solution to this convex problem.<sup>13</sup>

$$\text{minimize } \|x\|_1 \text{ subject to } y = Ax \quad (8)$$

If we decompose  $x$  into  $\phi z$  and minimize the  $l_1$  norm subjected to the constraints below, then

$$\text{minimize } \|z\|_1 \text{ subject to } y = A\phi z \quad (9)$$

We show that solving this optimization problem requires less measurements than the former problem as it decreases the sparsity index by including prior information about the signal structure. The signal  $x$  can be recovered using Equation 2.

In the case of noisy measurements we formulate the problem as BPDN

$$\text{minimize } \|x\|_1 \text{ subject to } \|y - Ax\|_2 < \varepsilon \quad (10)$$

If  $x = \phi z$  then

$$\text{minimize } \|z\|_1 \text{ subject to } \|y - A\phi z\|_2 < \varepsilon \quad (11)$$

where  $\varepsilon > \sigma$  and  $\sigma$  is the noise variance. The signal can be recovered by taking the inverse transform of thresholded coefficients from Equation 2. In this paper we take the transform directly.

## 2.2 Dictionary learning

According to CS theory the signal has to be sparse in a specific domain for exact reconstruction. There are many ways to find a sparsity basis which can represent the signal as a linear combination of a few atoms. In this paper we used an online learning approach for sparse coding.<sup>9</sup> The algorithm considers a finite training set of signals and optimizes an empirical cost function

$$f_n(\phi) \triangleq \frac{1}{n} \sum l(x_i, \phi) \quad (12)$$

In Equation 12,  $\phi$  is the dictionary in  $R^{m \times n}$ , each column of  $\phi$  is called an atom which are the sparse basis vectors,  $x_i$  are the training signals in  $R^{m \times k}$ , and  $l$  is the loss function which is small when  $\phi$  represent  $x_i$  using fewer sparse basis vectors or atoms. The number of training signals  $k$  is typically large and each signal is represented by only a few columns of  $\phi$ . This approach is fast and guaranteed to converge.<sup>9</sup>

### 3. METHODOLOGY

The sub-millimeter wave imager consists of a heterodyne source and receiver pair, image forming optics, a spatially selective mask, and data acquisition and post-processing hardware and software. The compressive sensing measurements are formed by scanning the image with the spatially selective mask. The receiver measures the energy that is transmitted through the spatially selective mask for each pattern of the mask. Those measurements are registered with the mask patterns and a system of Equations describing the measurements in terms of the mask patterns is formulated. This system of Equations is represented in matrix form by Equation 1. A conceptual sketch of for the spatially selective mask considered in this paper is shown in Figure 1. Here we point out only some parameters of interest for the spatially selective mask used. The mask consists of a spinning disk with holes along a constant radius.<sup>10</sup> The holes are of the same size and are placed at random spacings as shown in the figure. We treat the hole diameter and maximum spacings as design parameters and investigate the optimum combination of the two.

A measurement matrix resulting from the spatially selective mask is shown in Figure 2. The hole diameter and spacing affect the matrix in the following way. The thickness of diagonals is related to the diameter of holes and the distance between the diagonals is related to the spacing between holes. We optimized the spacing and diameter of holes over a range of permissible values by minimizing the mean square error calculated from the reconstruction. The optimum value of diameter and spacing was used for further computations and implementation.

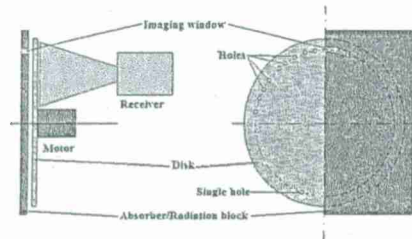


Figure 1. Conceptual diagram of spatial mask and receiver

Sub-millimeter wave images from this system can be well represented by a sum of Gaussians due to their inherent blur. A linear combination from a set of basis functions spanning the entire space can be used to represent any signal. To build this basis for the signals of interest we acquired the image of a point source and translated it over the whole spatial range. Then the set of signals were fed to a dictionary learning algorithm to obtain a transformation.<sup>9</sup> The parameters for algorithm were chosen empirically. The dictionary learning algorithm enforced minimum  $l_1$  norm to obtain a sparse representation.<sup>9</sup> We use the learned dictionary as a sparsifying basis. As mentioned earlier in order to reconstruct a signal from an optimal number of measurements the dictionary, or sparsifying matrix and the measurement matrix should be incoherent. The sum of columns of the gram matrix given in Equation 5 for both matrices was found to be 0.36, which is in range of Equation 6. This implies the incoherence of these two matrices.

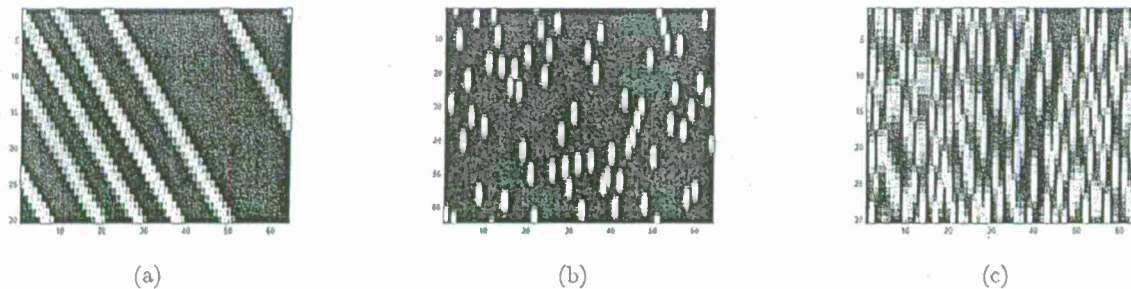


Figure 2. a. 30x64 Matrix M, b. A 64 x 64 Dictionary D, c. Product of D and M

Our problem is expressed as an underdetermined system of linear Equations given by Equation 1. We cast the problem as BP and use the SeDuMi solver for optimization. SeDuMi was chosen due to its lower computation time required and consistent performance compared to other available algorithms. For reconstructions from noiseless measurements we solve by using equality constraints and the problem is formulated by Equation 9. In the case of reconstructions from noisy measurements we first estimate the value of an error bound  $\epsilon$  and formulate the problem as in Equation 11. The value of the error bound is kept greater than the noise variance. For a fixed number of measurements we estimated optimum  $\epsilon$  which minimized the MSE of the reconstructed signal. The optimum value of error bound for a specific number of measurements was used for noisy reconstruction.

#### 4. SIMULATION AND EXPERIMENTAL RESULTS AND DISCUSSION

We simulated 90 signals of length  $64 \times 1$  and a  $64 \times 64$  measurement matrix. Ninety measurement vectors of size  $64 \times 1$  were calculated. A  $64 \times 64$  dictionary was obtained by training the 64 samples of the point spread functions spanning the whole space shown in Figure 2b. The 90 signals were then reconstructed using 30 noiseless measurements and a truncated measurement matrix. The optimum hole size and spacing was found by minimizing MSE of the reconstruction over a range of permissible values of hole sizes and maximum spacing. Figure 3 shows the variation of MSE with hole diameter and maximum spacing.

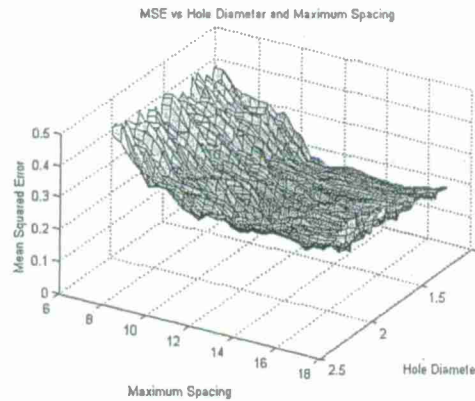
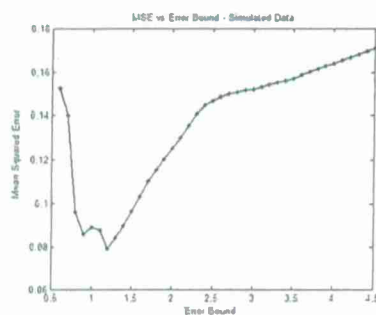
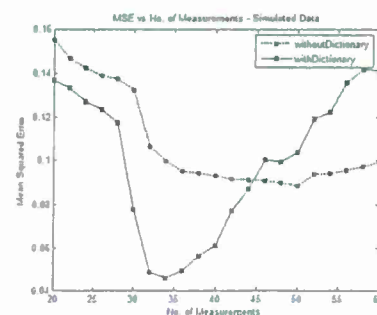


Figure 3. MSE vs Hole Diameter and Maximum spacing in mm

We simulated noisy measurements with  $\sigma = 0.2$  and, using the previous results for the optimized hole size and spacing, we minimized the MSE of the reconstruction over a range of error bound  $\epsilon$  starting from the minimum  $\epsilon = \sigma$ . The error bound against least MSE was found to be 1.2 which is used in further analysis. Figure 4 shows the MSE plotted against a range of error bound for a specific number of measurements.



(a)



(b)

Figure 4. Reconstruction optimization and analysis a. MSE vs Error bound b. MSE vs Measurements



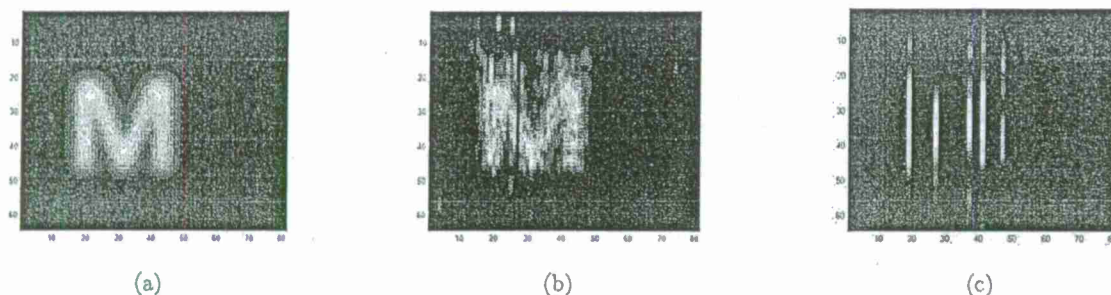


Figure 5. Simulated signal 90 (64x1) vectors a. Object M b. Reconstruction using  $m = 30$  c. Reconstruction using  $m = 60$

Fig. 4b shows the mean square error plot against number of measurements for a fixed  $\epsilon = 1.2$ . We also compare the MSE with and without the aid of a dictionary for reconstruction. The error using the dictionary is lower than without the dictionary when smaller numbers of measurements have been used. After the specified number of measurements is passed the error starts to increase. The specified number of measurements in this case were 30 which shows optimum reconstruction can be achieved by less than half the number of measurements required by a conventional algorithm for a given error bound. Moreover this optimum reconstruction is achieved earlier with the aid of a dictionary in the reconstruction process. Figure 5a shows a simulated signal. Figures 5b & 5c shows the reconstruction using 30 and 60 measurements respectively. As we increase the number of measurements in the presence of noise, quality of reconstruction degrades.

We gathered real data using the imaging device for the "M" object shown in Figure 7a. The value of the optimum error bound  $\epsilon$  is calculated by minimizing MSE over a range of  $\epsilon$  for a specific number of measurements as shown in Figure 6a.



Figure 6. Reconstruction, optimization and analysis of real data a. MSE vs Error bound b. MSE vs no. of Measurements

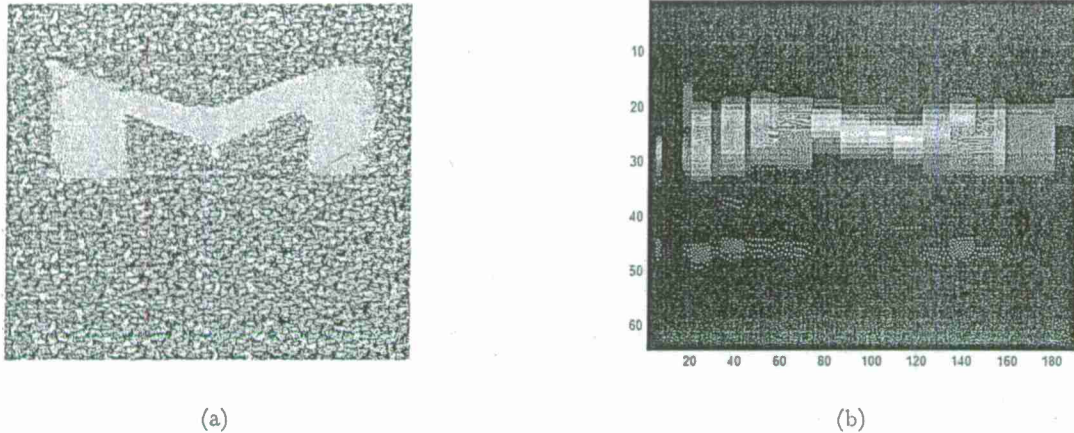


Figure 7. Real Data 191 (64x1) vectors a. Object M, b. Reconstruction using  $m = 30$

The mean square error increases after exceeding the specific number of measurements as shown in Figure 6b. The error is lower initially when the dictionary is used in the reconstruction process before the specified number of measurements. Figure 7b shows the reconstructed "M" from 30 measurements for each vector. The reconstruction from 60 measurements produced no solution. The results were consistent with simulations.

## 5. CONCLUSION AND FUTURE WORK

Compressed sensing provides the capability of reconstructing an image using fewer measurements than would otherwise be required. It does this by pushing the compression and encoding processes into the measurement process itself. This makes it attractive for imaging devices that need to reproduce a lot of pixels with very few detectors. It should be noted that SMMW imagers do not strictly fall into this category. While it is true that focal plane array detectors do not exist in this regime it is also true that relatively few pixels are needed for most security applications. This is due to the wavelengths involved, the targets of interest (concealed weapons), and the ranges involved (a few to a hundred meters). Under these conditions, images will never be terribly large. However, there are other advantages to using compressive sensing reconstruction.

The SMMW imager described in this paper and other papers by the authors currently makes the same number of measurements as the desired image size. The image size and the frame rate determine the sampling rate or data acquisition time of the imager. Since, for a given image size, fewer measurements are required by compressive sensing reconstruction methods we can use the acquisition time that would have been used for the remaining pixels for further detector integration to reduce noise or to increase the frame rate of the imager.

The imager described here could be improved by improving the RIP property of the measurement matrix. One way to do this is to add another degree of freedom to the measurements device. By letting the holes vary not only in their placement in angle along a constant radius but to vary about that radius, measurement matrices with improved properties may be obtained and produce better reconstructions.

On the processing side, the quality of the images can be enhanced by thresholding the coefficients before transforming them back to the spatial domain. We are currently exploring methods to find the optimum threshold level. Also there is room to improve the role of the sparsity basis so that it is more robust to noise in the signal and other variations. Sparsity in the third dimension (time) can also be explored to further reduce the number of required samples.

## REFERENCES

- [1] Donoho, David "Compressed sensing" IEEE Trans. on Information Theory, 52(4), pp. 1289 - 1306, April 200

- [2] Davenport, Mark Duarte, Marco Eldar, Yonina C. and Kutyniok, Gitta "Introduction to Compressed Sensing" Chapter in Compressed Sensing: Theory and Applications, Cambridge University Press, 2011.
- [3] Candes, Emmanuel Tao, Terence "The Dantzig selector: Statistical estimation when  $p$  is much larger than  $n$ " The Annals of Statistics, 2007
- [4] Chen, S. S. Donoho, David Saunders, M., "Atomic decomposition by basis pursuit", SIAM Journal on Scientific Computing 20 (1) (1998) 33-61.
- [5] R. Tibshirani, "Regression shrinkage and selection via the lasso," J. Royal. Statist. Soc B., vol. 58, no. 1, pp. 267-288, 1996.
- [6] Grant, M. and Boyd, S. "CVX: Matlab software for disciplined convex programming", version 1.21. <http://cvxr.com/cvx>, February 2011.
- [7] Chartrand, Rick Staneva, Valentina "Restricted isometry properties and nonconvex compressive sensing" Inverse Problems pp 035020 2008
- [8] Candès, E. J., Tao, T., Decoding by linear programming. IEEE Trans. Inform. Theory 51 (2005), 4203-4215.
- [9] Mairal, Julien Francis, Bach Ponce, Jean Sapiro, Guillermo "Online dictionary learning for sparse coding" 26th Annual International Conference on Machine Learning - ICML 2009
- [10] Furxhi, Orges Jacobs, Eddie L. "A sub-millimeter wave line imaging device" Image Rochester, N.Y.
- [11] Candès, Emmanuel "Compressive sampling" Int. Congress of Mathematics, 3, pp. 1433-1452, Madrid, Spain, 2006
- [12] Candès, Emmanuel and Michael Wakin "An introduction to compressive sampling" IEEE Signal Processing Magazine, 25(2), pp. 21 - 30, 2008
- [13] Boyd, Stephen Vandenberghe, Lieven [Convex Optimization] Cambridge university press
- [14] Grant, M. and Boyd, S. "Graph implementations for nonsmooth convex programs, Recent Advances in Learning and Control (a tribute to M. Vidyasagar)", V. Blondel, S. Boyd, and H. Kimura, editors, pages 95-110, Lecture Notes in Control and Information Sciences,

# Two-dimensional, real-time, sub-millimeter wave imaging using a spatially selective mask

Orges Furxhi<sup>a</sup>, Eddie L. Jacobs<sup>b</sup>, Robert Hewitt<sup>c</sup>

The University of Memphis, Memphis, TN 38152

## ABSTRACT

In the absence of detector arrays, a single pixel coupled with a spatially selective mask has been shown to be a practical solution to imaging problems in the terahertz and sub-millimeter wave domains. In this paper we demonstrate real-time two-dimensional imager for sub-millimeter waves that is based on a spatially selective image plane mask. The imager consists of a heterodyne source and receiver pair, image forming optics, a spatially selective mask, data acquisition hardware, and image reconstruction software. The optics form an image onto the spatially selective mask and linear measurements of the image are made. The mask must be designed to ensure maximum transmission, measurement linearity, and measurement to measurement independence and our design parameters are presented. Once enough linearly independent measurements are made, the image is reconstructed by solving a system of linear equations that is generated from the mask patterns and the corresponding measurements. We show that for image sizes envisioned for many current applications, this image reconstruction technique is computationally efficient and can be implemented in real time. We present images collected using this system, discuss the results, and discuss other applications for some components of the imager.

**Keywords:** Sub-millimeter waves, terahertz, imaging, spatial light modulator, spatially selective mask, compressive sensing, multi-mode imaging, spectrometry

## 1. INTRODUCTION

Sub-millimeter wave imaging is a useful tool for military and security applications. Sub-millimeter waves can penetrate through many man-made materials and provide high resolution images at stand-off distances while still not suffering tremendously from atmospheric attenuation.<sup>1,2</sup> However, the current state of the art is limited to target space scanning systems that require complicated mechanical mechanisms and hence tend to be bulky, heavy, and not portable. These systems usually make use of a single pixel detector that offers very high signal to noise levels due to the maturity of the technology. Other imaging methods, in particular two-dimensional, that perform well in other modalities such as interferometric arrays in the millimeter wave region<sup>3,4</sup> or focal plane arrays in infrared and visible regimes, have yet to be demonstrated in the sub-millimeter wave regime.

Awaiting the development of focal plane arrays for sub-millimeter wave imaging, other alternatives that exploit the maturity of the single pixel detector need to be explored. We have focused our efforts on Spatial Light Modulators (SLM) for sub-millimeter waves. Spatial light modulators work in reflection mode or in transmission mode. Perhaps the most well known reflective SLM is the Texas Instruments Digital Micro-mirror Device (DMD) known for its use in the Rice University single pixel camera,<sup>5</sup> or in most modern day projectors. An example of transmissive SLM are the Liquid Crystal Optical Modulators (LCOM) common in display applications. The unavailability of high power illumination sources in the sub-millimeter wave regime and the atmospheric absorption suggest special consideration for the efficiency of SLMs for sub-millimeter waves. In this respect, practical implementations of optical systems for SLMs, where the image plane is being modulated, favor transmission mode devices. The energy that passes through the SLM transmission mode device can be collected and channeled to the detector, whereas some of the energy reflected by the SLM reflection mode device will be diffracted away from the detector.

---

<sup>a</sup>ofurxhi@memphis.edu, <sup>b</sup>eljacobs@memphis.edu, <sup>c</sup>rwhe Witt@memphis.edu



An electronically controlled SLM for sub-millimeter waves would be ideal but unfortunately one suitable for imaging has not been developed yet. There have been some efforts to use metamaterials to develop an electronically controlled transmissive SLM<sup>6</sup> but the modulation depth of that device did not exceed 40%, with a minimum transmission coefficient of 0.3 and maximum of 0.7. Higher modulation depths are preferred for most sub-millimeter wave imaging applications. We have developed a mechanically scanned SLM for sub-millimeter waves. Although a mechanically scanned system, our device has low mechanical complexity, provides high modulation levels and high scanning rates, and has low cost. At the core of this device is a rotating disk with holes that spins at a constant speed. The image is formed on one portion of the disk and it is selectively transmitted through the holes onto the receiver. Linear measurements are made on the image as the disk rotates. An image is reconstructed using the knowledge of the hole patterns and the measured signal from the receiver. We call this device a Spatially Selective Mask (SSM).

We have previously presented the electromagnetic analysis and design of this device as well as a working example of a line SSM as part of a line imager.<sup>7,8</sup> In this paper we describe and demonstrate a two-dimensional version of the device that is used to form 64x64 pixel visible light and sub-millimeter wave images. The visible light images are formed in transmission mode and the sub-millimeter wave images are formed in transmission mode and in stand-off reflection mode. In transmission mode the aperture of a object mask is projected onto the device and in stand-off mode the target is placed 10 meters away from the imager and an image of it is formed on the device through an optical system. The paper is organized as follows: Section 2 describes the device and the method of image measurement and reconstruction. In Section 3, we describe the experimental setups. We show and discuss the images collected with each setup in Section 4. In Section 5 we discuss further improvements to the device and additional uses of the SSM. Section 6 concludes the paper.

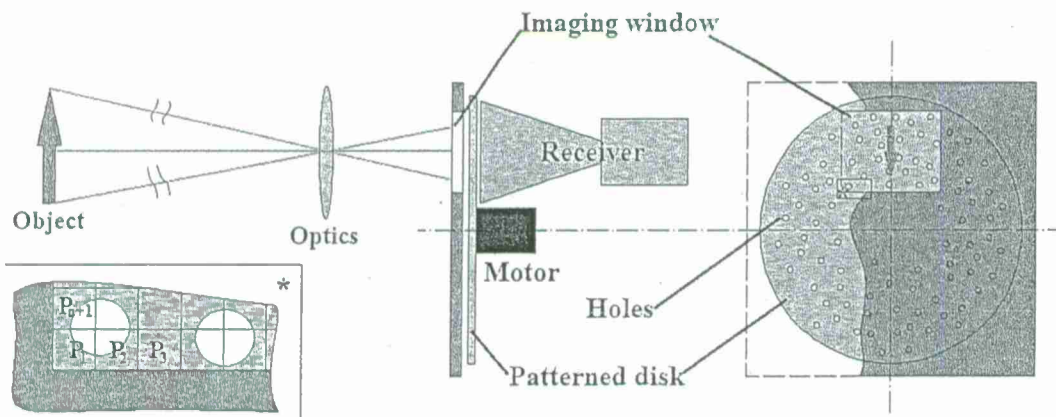


Figure 1. Conceptual drawing of the spatially selective mask placed in the image plane of the imaging system. Insert: arbitrary division of the imaging window into pixels.

## 2. THE TWO-DIMENSIONAL SPATIALLY SELECTIVE MASK AND THE IMAGE RECONSTRUCTION METHOD

A conceptual sketch of the SSM is shown in Figure. 1. The device is placed in the image plane of the imager and an image is formed over the imaging window. The image is scanned with a spinning disk that is patterned with holes. The detector is sampled continuously and each sample is registered with the corresponding pattern of holes in the imaging window at the time of the sample. When the required measurements are recorded, the image is reconstructed. The central component of the SSM is the spinning disk with holes located at random positions. The placement of the holes and their sizes depend on the largest imaging wavelength,  $\lambda_{max}$ . Because of the assumptions of the image reconstruction method, the transmission of each hole must be unity and transmission from many holes must be linear. Electromagnetic analysis<sup>8</sup> has shown that for a disk of thickness around three  $\lambda_{max}$  the minimal hole radius should be greater than  $1.4\lambda_{max}$  and the minimal edge to edge separation between holes should be one  $\lambda_{max}$ . As long as the radius of the holes and the depth increase proportionally, transmission

and linearity are preserved. Another component of importance is the collecting horn placed behind the imaging window and the disk. This collecting mechanism is necessary for coupling all of the energy that makes its way through the holes into the detector. From sub-millimeter wave frequencies to infrared frequencies a horn is preferred because of the low loss and cost, but for frequencies in the visible spectrum a lens can be used instead to focus the energy into the detector. An integrating sphere can also be used. The imaging window is another component. It is an aperture that limits the part of the disk where the image is formed and scanned. The size of the imaging window determines the physical size of the image. The motor spins the disk at a constant rate. For standard video rate imaging (30 frames per second) the disk should spin at 1800 rotations per minute.

For reconstruction purposes, the imaging problem is posed as a linear system of equations and is presented in matrix notation

$$\overline{\overline{M}} \overline{p} = \overline{m} \quad (1)$$

For an image of  $n \times n$  pixels, the column vectors  $\overline{m}$ , and  $\overline{p}$  have dimensions  $n^2 \times 1$  and the matrix  $\overline{\overline{M}}$  is a square matrix of dimensions  $n^2 \times n^2$ . The vector  $\overline{p}$  is composed of the values of the intensity of each image pixel. The vector  $\overline{m} = \overline{m'} + \overline{\eta}$  is composed of the values of each measurement and is called the measurement vector;  $\overline{m'}$  is the noiseless measurement and  $\overline{\eta}$  is the measurement noise. The matrix  $\overline{\overline{M}}$  is called the measurement matrix and each of its rows encodes the pattern of holes over the imaging window for each measurement. Referring to the insert in Figure 1, each entry of each row of the measurement matrix is calculated as the fraction of the area of the corresponding pixel covered by holes. For instance,  $M_{1,1} = 0.23$ ,  $M_{1,2} = 0.27$ ,  $M_{1,3} = 0$ , and so on. The entries of the measurement matrix can also be interpreted as the contribution of each pixel to the measurement. The sizes of the pixels are arbitrary; therefore the imaging window can be divided into as many pixels as desired. However, as the number of pixels increases the probability that the rows of the measurement matrix remain linearly independent decreases. The linear independence of the rows of the measurement matrix is assumed in order to solve Equation 1.

In constructing the measurement matrix in Equation 1 we make the following assumptions. Each measurement is collected as the pattern of holes in the imaging window is stationary. All the energy that passes through the holes is collected and measured by the detector. The measured energy is the sum of the energy passing through each hole. All of these assumptions are broken in the actual implementation. The disk is rotating at a constant speed and each measurement is collected as the disk rotates. The majority, but not all, of the energy that goes through the holes is collected and measured. The holes can be considered as radiators by the detector and the measured energy is not the same as the sum of the energies from each hole because of interference.<sup>9</sup> However, in the current implementation the error or noise introduced because of these assumptions is overshadowed by the measurement noise. In Section 5, we discuss how some of the error introduced by our assumptions can be mitigated.

Equation 1 can be solved simply by inverting the measurement matrix  $\overline{\overline{M}}$  and multiplying the result with the measurement vector  $\overline{m}$ ; however, the unique solution that is obtained is different from the desired vector  $\overline{p}$  because of the measurement noise. In addition, the measurement matrix might be ill-conditioned which would augment that difference. To obtain the desirable solution many inverse imaging algorithms<sup>10</sup> can be used to solve Equation 1, as well as compressive sensing methods.<sup>11</sup> We use a closed form regularized least-squares method.<sup>10</sup> It provides an instantaneous solution and allows the inclusion of some a priori information about the solution in the form of regularization parameters and matrix operators. Although iterative solutions are more flexible and allow more a priori information to be used (an important example is the non-negativity constraint) they are slow to produce solutions with regard to video-rate imaging.

The regularized least squares solution is written as

$$\overline{p'} = \left[ \overline{\overline{M}}^T \overline{\overline{M}} + \alpha \overline{I} + \sum_i \beta_i \overline{H}_i^T \overline{H}_i \right]^{-1} \overline{\overline{M}}^T \overline{m} \quad (2)$$

where  $\overline{p'}$  is the approximate solution, the superscript T denotes the matrix transpose, the regularization parameter  $\alpha$  controls the degree of the minimization of the norm of the solution, the matrix operators  $\overline{H}_i$  are linear operators on the solution  $\overline{p'}$ , and the regularization parameters  $\beta_i$  control the degree of minimization of the matrix vector



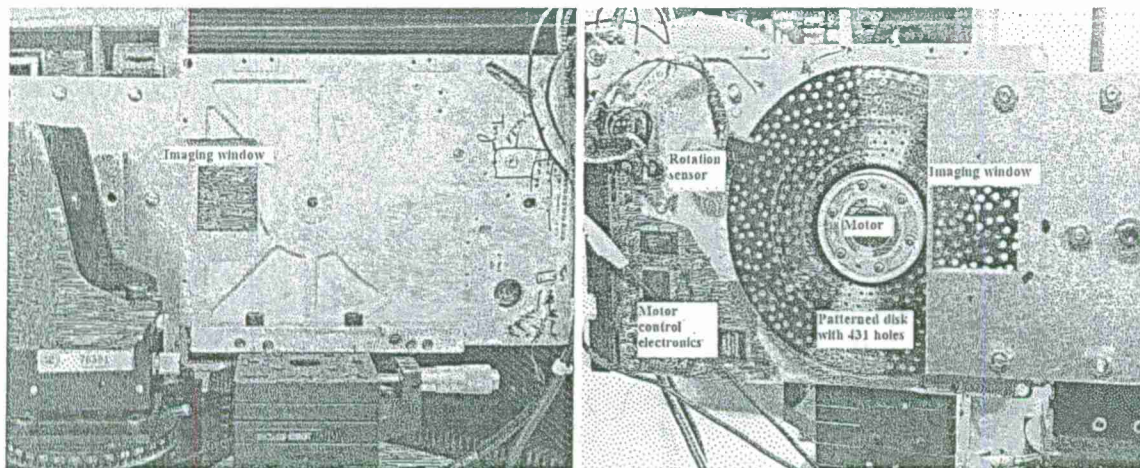


Figure 2. Implementation of the SSM, front (left), and back (right) views.

product  $\overline{H_i} \overline{p}$ . The matrix operators  $\overline{H_i}$  are used to enforce the a priori information on the solution. For instance, if we know a priori that the solution is smooth, we can minimize the first and second derivatives of the solution. In this case the matrices  $\overline{H_i}$  are the Sobel or Prewitt (first order derivatives) and the Laplacian (second order derivative) operators.<sup>12</sup> These are the matrix operators that we have implemented in this work. Because of the system optics and large wavelength, the images that are formed on the SSM are smooth. The regularization parameters can be optimized and several methods for doing this exist<sup>10</sup> however, in the work presented here the regularization parameters were chosen ad-hoc to produce a satisfactory qualitative solution. The optimal regularization parameters as well as other matrix operators will be investigated in the future.

The number of pixels in the image can be increased since the pixels are non-physical, however a  $64 \times 64$  pixel image is sufficient for most stand-off applications of interest. Assuming an F/1 optical system with one meter aperture and a Rayleigh wavelength product  $1.22\lambda = 0.5\text{mm}$ , the angular resolution of the imager is 0.5 milliradian. In object space at 100 meters away this translates to a 5 cm resolution spot. Assuming one pixel sampling for resolution spot (two per airy disk) a  $64 \times 64$  pixel imager would image an object space area of  $3.2 \times 3.2$  meters square. This object space area is sufficient to scan a highway lane, a few human targets, the trunk of a tree, or a helicopter landing site.

### 3. EXPERIMENTAL SETUPS

The spatially selective device was implemented using parts of a 5.25 inch hard drive. One of the platters of the hard drive was used as the spinning disk. The radius of the holes and their minimal separation were designed for operation at 640GHz. A hole radius of 1 mm and a minimal separation of 2 mm were chosen to guarantee unity transmission, linearity, the structural integrity of the disk, and the availability of standard tools. With these parameters as restrictions, a random pattern of 431 holes was generated and the holes were drilled on a CNC mill. The case of the hard drive was cut and modified for access to the disk and for easy mounting on the optical stages. The electronics of the motor driver were also modified so that the disk could be rotated at 3000 rotations per minute (RPM). An emitter diode and phototransistor pair were placed in the proximity of the disk to register the measurement samples with the corresponding hole patterns in the imaging window. A  $34\text{mm} \times 34\text{mm}$  imaging window aperture was machined on two slabs of aluminum and they were mounted to sandwich the disk. Figure 2 shows a picture of the front and back of the device with all the components described above labeled.

The SSM device was used to form images in three different configurations. In the first configuration the device was paired with a visible light detector to form a visible light imager. Although this setup was intended to help debug of all the issues related to the device without concern for the sub-millimeter wave image formation and phenomenology (invisibility to the bare eye, specular nature of the active sub-millimeter wave imaging, optical

alignments, etc), it shows the frequency independence of this device. A conceptual sketch and picture of the setup for visible light are shown in Figure 3. This imager works in transmission mode. A red laser source (400nm – 700nm) was collimated and was masked by object masks to form images over the imaging window. A lens was placed behind the disk and the imaging window to focus the energy into an N-Type Silicon PIN Photodetector. The optical path from the collecting lens to the photodetector was enclosed by a dark tube to eliminate stray light reaching the detector. The detector signal was amplified and then sampled using a 16-bit data acquisition card from Measurement Computing. For each revolution of the disk 5000 samples were recorded, triggered by the rotation sensor, and then were filtered in Matlab using a low pass filter. The disk was rotated at a constant rate of 50 rotations per second. We used 4096 consecutive measurements of the 5000 that were recorded to reconstruct a  $64 \times 64$  pixel image using Equation 2.

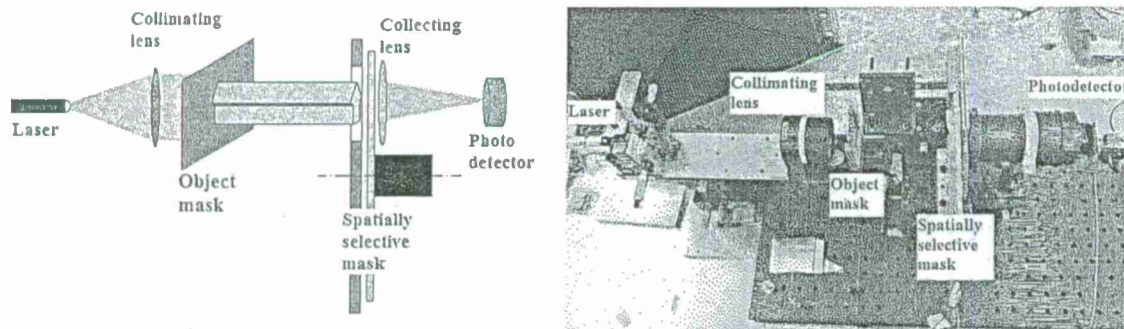


Figure 3. Visible light setup, sketch (left) and actual implementation (right).

In the second configuration, the device was paired with the sub-millimeter wave receiver to form images in transmission mode. A sketch and picture of this setup are shown in Figure 4. We use a heterodyne source and receiver pair from Virginia Diodes. The source and receiver operate at 640 GHz. In this configuration, the 640 GHz source is placed one meter in front of the device and is flood illuminating the imaging window. An object mask is placed right before the imaging window and the projected image is scanned by the spinning disk. The 640 GHz receiver is placed behind the disk and measures the energy passing through the holes. The intermediate frequency (IF) of the receiver was down converted from 4.8 GHz to 2.2 GHz and this new IF was supplied to a spectrum analyzer. The spectrum analyzer was used to band-pass filter and amplify the signal. A time sweep of the signal triggered for each rotation was generated and the video output of the spectrum analyzer was sampled using a 16-bit data acquisition card from Measurement Computing. Here also 5000 samples are recorded per rotation as the disk rotates at 50 rotations per second and then the signal is low-pass filtered in Matlab and 4096 consecutive samples are used to reconstruct a  $64 \times 64$  pixel image using Equation 2.

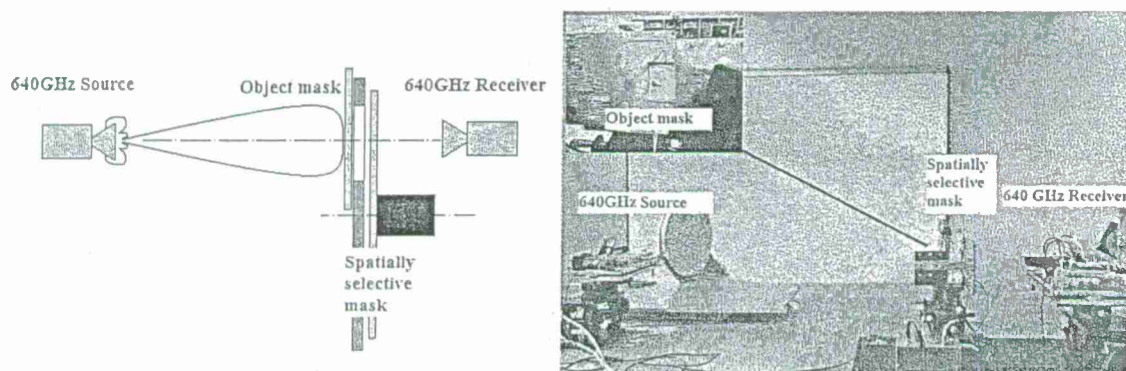


Figure 4. Sub-millimeter wave setup in transmission mode, sketch (left) and actual implementation (right).



In the third configuration, the device was paired with the sub-millimeter wave receiver to form images in stand-off mode. A sketch and picture of this setup are shown in Figure 5. The 640 GHz source is located approximately two meters from the target and flood illuminates it. The energy reflected by the target is collected by the imaging mirror (in the implementation the beam is folded by two flat mirrors) 10 meters away. This mirror is a section of an ellipsoid of rotation with one focus at one meter and the other at 10 meters. The image is formed on the one meter side. The system has an effective diameter of 0.3048 meters (12 inch), effective focal length of 0.9091 meters, resulting in a  $F\#$  of 2.9826. The magnification of the system is 0.1, the depth of focus for coherent radiation is 0.01062 meters, and the depth of field for incoherent radiation is 1.0162 meters. The airy disk diameter is 3.75 millimeters for a wavelength of  $468.43 \mu\text{m}$ , corresponding to the illumination frequency of 640 GHz. The imaging mirror forms an image of the target in the imaging window of the SSM. The image is then scanned by the spinning disk and the energy that goes through the holes is measured by the 640 GHz receiver. The same data collection setup as in the second configuration is used to sample the received signal and reconstruct a  $64 \times 64$  image using Equation 2.

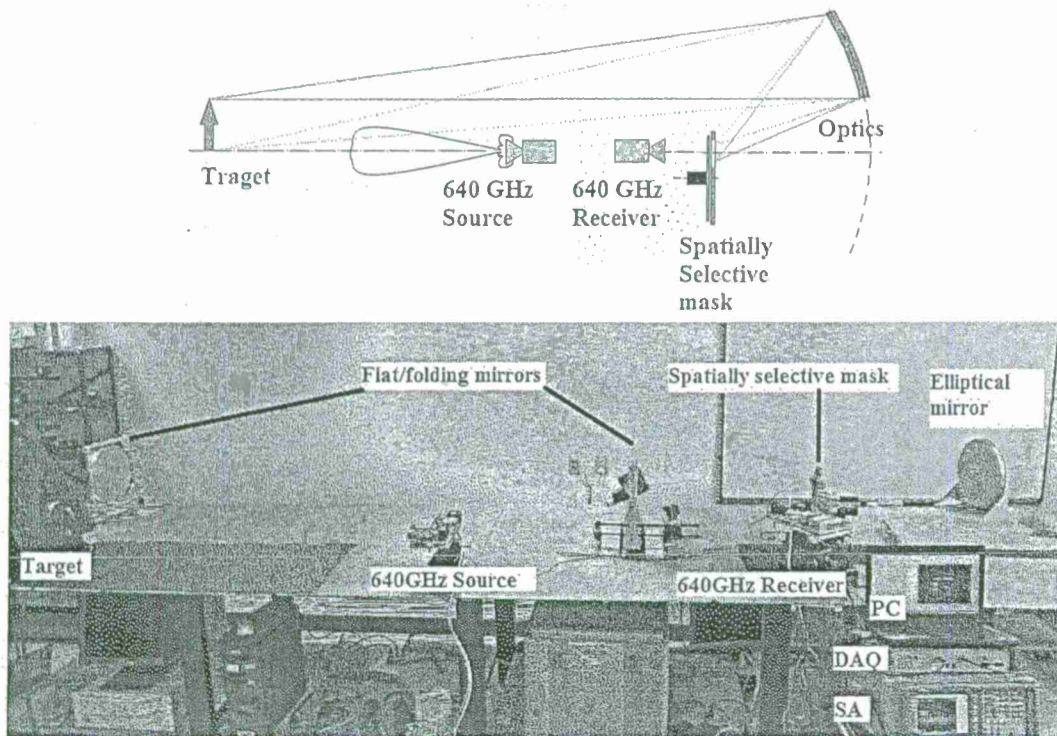


Figure 5. Sub-millimeter wave setup in stand-off mode, sketch (top) and actual implementation (bottom)

#### 4. RESULTS

For all three imager configurations the reconstruction was performed using Matlab software. The Matlab Data Acquisition Toolbox was used to acquire the data from the data acquisition device. Code was written to implement Equation 2 and to calculate the matrices therein. The disk is rotated at a rate of 50 rotations per second and therefore allows image formation at 50 frames per second (fps). However, the data acquisition speed of the current implementation is only 10 fps and when an image is reconstructed and displayed on the screen the image rate is 6 fps. These slower frame rates are due to the implementation in Matlab. On a laptop PC (processor: Intel(R) Core(TM)2 Duo CPU T6670 @ 2.2GHz), the data reconstruction step (`matrix[4094 \times 4096] vector[4096 \times 1] product`) in the current Matlab implementation takes only 30 milliseconds and the rest of the loop

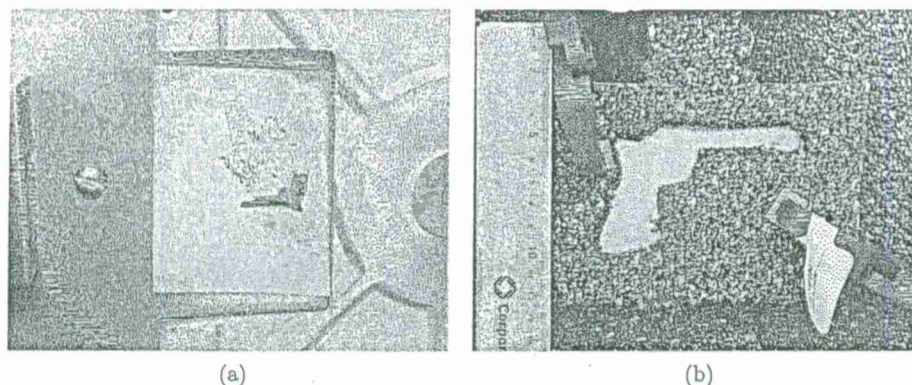


Figure 6. Targets for the imager configurations; (a) target mask used for the visible light and sub-millimeter wave transmission mode configurations, (b) target for the sub-millimeter wave stand-off mode configuration.

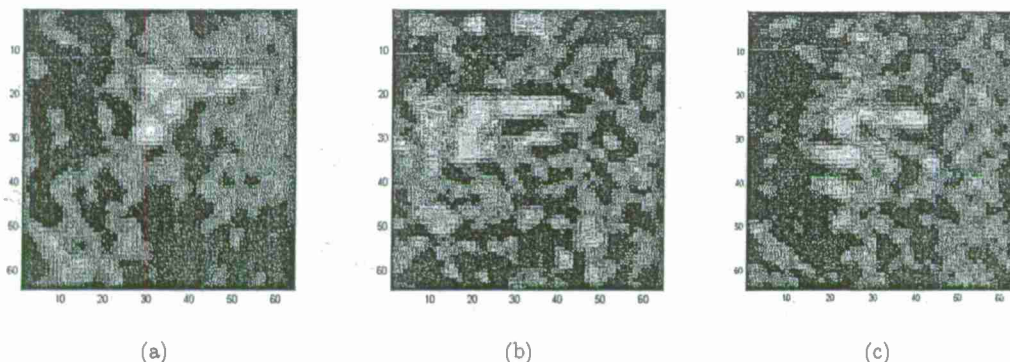


Figure 7. Image reconstructions from each configuration; (a) reconstruction from the visible light configuration, (b) reconstruction from the sub-millimeter wave transmission mode configuration, (c) reconstruction from the sub-millimeter wave stand-off mode configuration.

time is occupied by the data acquisition, image reshaping, filtering, and image display. All these steps can be made faster using a compiled implementation and dedicated processing.

For the transmission mode configurations we used the same mask for both visible and sub-millimeter wave imagers; the mask is shown in Figure 6a. An aperture in the shape of a hand gun was cut on an aluminum sheet and the sheet was placed in front of the SSM as shown in Figures 3 and 4. For the stand-off configuration an aluminum plate was made rough and a piece of carpet with an aperture in the shape of a hand gun was placed over it. This target is shown in Figure 6b. The target was placed 10 meters from the image forming mirror, as shown in Figure 5, and an image was formed on the SSM.

The results of the reconstruction are shown in Figure 7. In all three cases the shape of the gun can be distinguished clearly. The image quality for the transmission mode configurations is better than for the stand-off configuration. One of the reasons for this difference is the optical system. Another reason is the specular nature of active imaging. Both contribute to the non-uniformity of the image intensity on the image plane. We note that in order to acquire the image in stand-off mode (Figure 7c), the object must be positioned precisely. A slight angular movement, with respect to the optical axis, causes one part of the object to be imaged with higher intensity than the other parts and only it can be imaged.

Of the three imager configurations the only configuration where all the radiation was collected by the detector was the visible one. Because of this feature we can reconstruct images regardless of where on the imaging window they are formed. The sub-millimeter wave configurations were missing the energy collection mechanism therefore,



only the central part of the imaging window could be used to form images. In order to use the extent of the imaging window an energy collecting mechanism similar to the collecting lens in Figure 3 is necessary.

All three reconstructions in Figure 7 contain reconstruction noise. This noise is an effect of the measurement noise, the non-linearity of the measurement, and the assumption of static hole patterns during the detector integration time. Of these, the measurement noise dominates. The reconstruction noise appears in the form of low spatial frequency noise because the signal  $\overline{m}$ , that contains the measurement values, is low pass filtered prior to obtaining the solution using Equation 2. In addition, the measurement matrix  $\overline{M}$  is ill-conditioned therefore the regularization parameters are large. Large regularization parameters result in low pass filtering as well. As it was mentioned previously, the regularization parameters that were used were not the optimal parameters. The optimal reconstruction parameters as well as additional regularization operators will be investigated in the near future.

## 5. FURTHER IMPROVEMENTS AND USES

The results from all three imager configurations provide insights into the future improvements needed for a practical stand-off imager. They also suggest further uses of the SSM. In this section we discuss the required improvements further uses of the device.

When the device is used in the visible imager configuration the whole imaging window can be utilized to form images, as contrasted to the sub-millimeter wave configurations where only the central part of the window can be used. The difference is the energy collection mechanism. Being able to collect all the energy that passes through the holes is a must for the full utilization of the SSM. In addition all parts of the imaging window should be coupled to the detector equally. We will investigate mechanisms that can be used to achieve this in the near future.

In this implementation of the spatially selective disk a random pattern of holes was generated and the holes were drilled on the disk. The only constraints that were enforced to generate the random pattern of holes were the minimal hole spacing and hole diameter. There are additional constraints that should be imposed on the generation of the hole pattern: (1) the hole pattern should result in a measurement matrix with low condition number, (2) the hole pattern should maintain a uniform hole area over the imaging window as the disk spins, and (3) the hole area over the imaging window should be maximized. The first constraint improves the robustness to measurement noise. The second constraint improves the uniformity of the image sampling and allows full utilization of the imaging window. The third constraint increases the amount of energy that is measured by the detector thereby increasing the signal to noise ratio of the measurement.

Although non-random patterns of holes that satisfy the three additional constraints mentioned above might exist, random patterns are preferred. Random patterns improve the linearity of the device. To the receiver each hole appears as a radiating source and the pattern of holes can be considered to be an antenna array.<sup>13</sup> Due to this antenna array an interference effect as a function of hole separation is observed in the total detected energy. This interference is minimized when the hole separations are random.

The measurement matrix  $\overline{M}$  is currently constructed by making the assumption that the hole pattern is stationary during the measurement. This assumption is clearly incorrect as we are spinning the disk continuously. A back of the envelope calculation shows that the error introduced by the inaccurate assumption is at most less than 1% for pixels at the edge of the disk, when the disk spins at 50 fps, the hole diameter is 2 mm, the disk diameter is 130 mm, and the integration time of the measurement is 1  $\mu$ s. For pixels located toward the center of the disk the error decreases as a ratio of the circumference of the disk at that position with the circumference at the edge of the disk. This error will be mitigated in the future by including the non-stationary assumption in the calculation of the measurement matrix. This error can also be decreased by slowing down the disk, decreasing the hole diameter, or by decreasing the integration time.

Another very important component of the imager is the optical system. The optical system that is currently being used was designed for conjugate point imaging and was not intended for wide area imaging. The current system suffers from several aberrations and is also an off axis system. These factors contribute to a non-uniform intensity distribution in the image and therefore parts of the image are less bright then others although they

might be on the same object plane. We are currently designing a symmetrical multi-surface optical system with smaller aberrations.

The SSM was designed for operation at 640 GHz and it was also used to form images in the visible part of the spectrum. This suggests that the SSM can be used in other parts of the spectrum as well. Using this device and reflective optics we can build a multi-band imager that provides optically registered images. The frequency independence of the device also suggests the use of the device to build a spectrometer. The SSM can be used to scan a spectrum of the scene mapped spatially across the mask using diffracting optical elements. This spectrometer is similar to a Hadamard spectrometer<sup>14,15</sup> the only difference being the scanning mask (pattern on the disk). Also, the SSM and optics can be configured such that an imager and spectrometer utilize the same SSM and optical system. This device would produce images of the scene as well as the spectrum of the scene but not a spectral image. The spectrometer devices require a wide band receiver. These devices are currently being investigated.

## 6. CONCLUSIONS

We have built a spatially selective mask device for image space scanning with high modulation levels, high scanning rates, low mechanical complexity, and low cost. The design parameters that were identified in our earlier publications<sup>7-9</sup> as well as some reconstruction methods presented there were used to build the device and reconstruct  $64 \times 64$  pixel images. We introduced here an additional method for reconstruction. Through a simple calculation we concluded that a  $64 \times 64$  pixel image is sufficient for most applications of interest. We demonstrated the use of this device in three different configurations and presented images collected and reconstructed for each configuration. The imagers as configured can scan images at 50 fps; they can record images at 10 fps; they can scan, reconstruct, and display images at 6 fps. The data acquisition and image reconstruction chains are currently implemented on a personal computer using Matlab interpreted code. The processes of data acquisition, image reconstruction, and image display can be accelerated to produce images at a rate of 50 fps if the code is compiled and a dedicated computer is used. We also discussed further improvements necessary for a practical stand-off video rate imager and also suggested further uses of the spatially selective mask device. Based on the results shown in this paper we suggested that the device can be used as part of a multi-mode imager, as part of a spectrometer, and as part of an imager spectrometer.

## REFERENCES

- [1] Petkie, D. T., Casto, C., Lucia, F. C. D., Murrill, S. R., Redman, B., Espinola, R. L., Franck, C. C., Jacobs, E. L., Griffin, S. T., Halford, C. E., Reynolds, J., O'Brien, S., and Tofsted, D., "Active and passive imaging in the thz spectral region: phenomenology, dynamic range, modes, and illumination," *J. Opt. Soc. Am. B* 25(9), 1523-1531 (2008).
- [2] Appleby, R. and Wallace, H., "Standoff detection of weapons and contraband in the 100 ghz to 1 thz region," *IEEE Transactions on Antennas and Propagation* 55(11), 2944-2956 (2007).
- [3] Prather, D., Biswas, I., Schuetz, C., Martin, R., and Mirotznik, M., "Multiple aperture imaging of millimeter sources via image-plane interferometry," *Geoscience and Remote Sensing Symposium, 2007. IGARSS 2007. IEEE International*, 2967-2970 (July 2007).
- [4] Schuetz, C. A., Mirotznik, M. S., Shi, S., Schneider, G. J., Murakowski, J., and Prather, D. W., "Applications of optical upconversion to sparse aperture millimeter-wave imaging," *Technologies for Optical Countermeasures II; Femtosecond Phenomena II; and Passive Millimetre-Wave and Terahertz Imaging II* 5989(1), 59891C, SPIE (2005).
- [5] Takhar, D., Laska, J. N., Wakin, M. B., Duarte, M. F., Baron, D., Sarvotham, S., Kelly, K. F., and Baraniuk, R. G., "A new compressive imaging camera architecture using optical-domain compression," *Computational Imaging IV* 6065(1), 606509, SPIE (2006).
- [6] Chan, W. L., Chen, H.-T., Taylor, A. J., Brener, I., Cich, M. J., and Mittleman, D. M., "A spatial light modulator for terahertz beams," *Applied Physics Letters* 94(21), 213511 (2009).
- [7] Furxhi, O. and Jacobs, E. L., "A sub-millimeter wave line imaging device," *Passive Millimeter-Wave Imaging Technology XIII* 7670(1), 76700L, SPIE (2010).



- [8] Furxhi, O. and Jacobs, E. L., "A sub-millimeter wave line scanning imager," *Millimetre Wave and Terahertz Sensors and Technology III* 7837(1), 78370D, SPIE (2010).
- [9] Furxhi, O., *Spatially Selective Mirrors and Masks for Submillimeter Wave Imaging*, PhD thesis, The University of Memphis, <http://www.memphis.edu/etd/> (2010).
- [10] Bertero, M. and Boccacci, P., [*Introduction to Inverse Problems in Imaging*], Institute of Physics Publishing, Bristol and Philadelphia (1998).
- [11] Donoho, D., "Compressed sensing," *IEEE Transactions on Information Theory* 52(4), 1289–1306 (2006).
- [12] Gonzalez, R. and Woods, R., [*Digital Image Processing*], Prentice Hall, Upper Saddle River, N.J (2008).
- [13] Balanis, C., [*Antenna Theory : Analysis and Design*], John Wiley & Sons, Inc., New York (1997).
- [14] Swift, R. D., Wattson, R. B., John A. Decker, J., Paganetti, R., and Harwit, M., "Hadamard transform imager and imaging spectrometer," *Appl. Opt.* 15(6), 1595–1609 (1976).
- [15] Harwit, M. and Sloane, Neil, J., [*Hadamard Transform Optics*], Academic Press, New York (1979).

# Spatially Selective Mask for Single Pixel Video Rate Imaging

Orges Furxhi and Eddie Jacobs

*University of Memphis*

*Department Of Electrical and Computer Engineering*

*206 Engineering Science Bldg., Memphis, TN 38152*

*[ofurxhi@memphis.edu](mailto:ofurxhi@memphis.edu)*

*[eljacobs@memphis.edu](mailto:eljacobs@memphis.edu)*

**Abstract:** We present a spatially selective mask that is used with a single pixel detector to reconstruct images in real-time. Reconstructed image sizes are variable; the mask works in multiple electromagnetic regimes. Experimental results are shown.

OCIS codes: (110.3010) Image reconstruction techniques; (110.6795) Terahertz imaging; (110.1758) Computational imaging

## 1. Introduction

Single pixel imagers find utility in the parts of the electromagnetic spectrum where focal plane arrays are nonexistent or are expensive to fabricate, such as in the Terahertz band (300GHz – 3THz). One method used to form images with a single detector is to scan either the detector over the image or the image across the detector using moving optics [1]. Real-time or video rate, imagers utilizing these methods are possible at high frequencies but as the frequencies decrease the optical components and the detectors become large and more difficult to move.

An alternative imaging configuration is image space scanning. Examples of this configuration can be traced back to the early days of television with the Nipkow disk [2]. The Reticle systems work in a similar way [3]. Another example is the spatial light modulators for millimeter waves developed by Jacobs in the 1960s [4]. The Jacobs devices were frequency dependent and also were not developed beyond laboratory demonstrations. One modern device is the digital multi-mirror device (DMD) developed by Texas Instruments. The DMD was used successfully to implement a compressive sensing imager at visible light frequencies [5]. However, because of its size and limiting physical capabilities on its driving mechanisms the DMD cannot be used at frequencies such as terahertz.

We have developed a spatially selective mask for terahertz that can also be used for higher frequencies. The device is implemented using a spinning disk with randomly placed holes. The mask is placed in the image plane of the imager and the detector is placed behind the mask to collect all the energy that goes through the holes. One image is formed for each revolution of the disk. The reconstruction method allows for variable image pixel sizes and performs at video rates. The device can also be used to implement compressive sensing.

The device and the image reconstruction methodology have been described in detail previously [6], and are briefly described next for completeness. We present a laboratory prototype of the device that was designed for terahertz frequencies. While we wait for the construction of some additional components needed to build a terahertz imager, we paired the device with a visible light detector for proof of concept and to verify the frequency independence property of this device. We were able to reconstruct simple images of 32x32 and 64x64 pixels. Those images are presented and the results are discussed.

## 2. The spatially selective mask and image reconstruction method

A conceptual sketch of the spatially selective mask is shown in Fig. 1. The mask is placed in the image plane of the imager and an image is formed over the imaging window. The image is scanned with a spinning disk that is patterned with holes. The detector is sampled continuously and each sample is registered with the corresponding pattern of holes in the imaging window at the time of the sample. Once enough measurements are recorded, the image is reconstructed.

The central component of the mask is the spinning disk with holes located at random positions. The placement of the holes and their sizes depend on the largest imaging wavelength,  $\lambda_{\max}$ . Because of the assumptions of the image reconstruction method, the transmission of each hole must be unity and transmission from many holes must be linear. Electromagnetic analysis [6], has shown that for a disk of thickness around three  $\lambda_{\max}$  the minimal hole radius should be greater than  $1.4 \lambda_{\max}$  and the minimal edge to edge separation between holes should be one  $\lambda_{\max}$ . As long as the radius of the holes and the depth increase proportionally, transmission and linearity are preserved.

Another component of importance is the collecting horn placed behind the imaging window and the disk. This collecting mechanism is necessary for the coupling all of the energy that makes its way through the holes into the detector. From terahertz to infrared frequencies a horn is preferred because of the low loss and cost, but for frequencies in the visible spectrum a lens can be used instead to focus the energy into the detector. The imaging window is another component. It is an aperture that limits the part of the disk where the image is formed and

scanned. The size of the imaging window determines the physical size of the image. The motor spins the disk at a constant rate. For standard video rate imaging (30 frames per second) the disk should spin at 1800 rotations per minute.

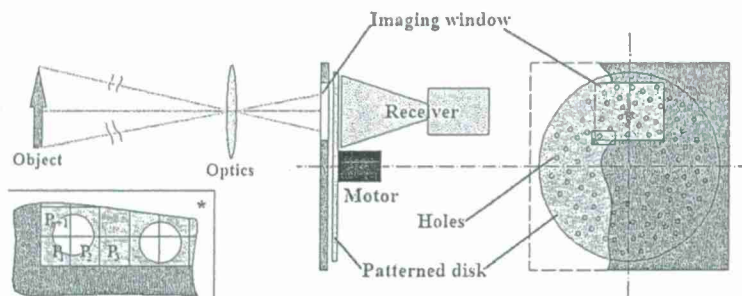


Fig. 1. Conceptual drawing of the spatially selective mask placed in the image plane of the imaging system. Insert: arbitrary division of the imaging window into pixels.

For reconstruction purposes, the imaging problem is posed as a linear system of equations as shown in Eq. 1.

$$\bar{m} = \bar{M} \bar{p} \quad (1)$$

For an image of  $n$  by  $n$  pixels, the column vectors  $\bar{m}$  and  $\bar{p}$  have dimensions  $n^2$  by 1 and the matrix  $\bar{M}$  is a square matrix of dimensions  $n^2$  by  $n^2$ . The vector  $\bar{p}$  is composed of the values of each image pixel. The vector  $\bar{m}$  is composed of the values of each measurement and is called the measurement vector. The matrix  $\bar{M}$  is called the measurement matrix and each of its rows encodes the pattern of holes over the imaging window for each measurement. Referring to the insert in Fig. 1, each entry of each row of the measurement matrix is calculated as the fraction of the area of the corresponding pixel covered by holes. For instance,  $M_{1,1} = 0.23$ ,  $M_{1,2} = 0.27$ ,  $M_{1,3} = 0$ , and so on. The entries of the measurement matrix can also be interpreted as the contribution of each pixel to the measurement.

The sizes of the pixels are arbitrary; therefore the imaging window can be divided into as many pixels as desired. However, as the number of pixels increases the probability that the rows of the measurement matrix remain linearly independent decreases. The linear independence of the rows of the measurement matrix is assumed in order to solve Eq. 1. For a more in-depth discussion of the image reconstruction methodology refer to reference [6].

### 3. Laboratory implementation of the device and results

The spatially selective device was implemented using parts of a 5.25 inch hard drive. One of the platters of the hard drive was used as the spinning disk. The radius of the holes and their minimal separation were designed for operation at 640GHz. A hole radius of 1mm and a minimal separation of 2mm were chosen to guarantee unity transmission, linearity, the structural integrity of the disk, and the availability of standard tools. With these parameters as restrictions, a random pattern of 431 holes was generated and the holes were drilled on a CNC mill.

The case of the hard drive was cut and modified for access to the disk and for easy mounting on the optical stages. The electronics of the motor driver were also modified so that the disk could be rotated at 3000 rotations per minute. An emitter diode and phototransistor pair were placed in the proximity of the disk to register the measurement samples with the corresponding hole patterns in the imaging window. The imaging window aperture was machined on two slabs of aluminum and they were mounted to sandwich the disk.

Although the device was designed for operation at terahertz frequencies, we paired it with a visible light detector to form a visible light imager. This shows the proof of concept and the frequency independence of the device. A picture of the setup for visible light is shown in Fig. 2. A red laser source (400nm – 700nm) was collimated and was masked by object masks to form images over the imaging window. A lens was placed behind the disk and the imaging window to focus the energy into an N-Type Silicon PIN Photodetector. The optical path from the collecting lens to the photodetector was enclosed by a dark tube to eliminate stray light reaching the detector. The detector signal was sampled using a 16-bit data acquisition card from Measurement Computing.

Three object masks were imaged and the reconstructed images for two pixel resolutions are shown in Figs. 3 and 4. For each revolution of the disk 5000 samples were recorded and filtered in Matlab using a low pass filter. For the 32x32 image, 1024 staggered measurements were chosen and used to solve Eq. 1 for the unknown pixel values. For the 64x64 image 4096 consecutive measurements were used. Equation 1 was solved by regularized matrix inversion which effectively acts as a low pass filter.



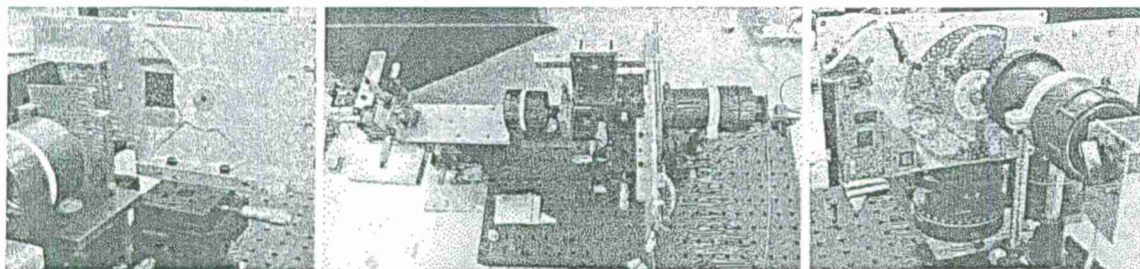


Fig. 2. Pictures of the imager setup for visible light. Left- collimating lens, object mask, imaging window. Center-the whole setup. Right- patterned disk, collecting lens, tube enclosure, detector.

When displaying the images, the negative values are truncated (dark spots in the images). The negative values in the reconstruction and the low spatial frequency noise are attributed to signal noise, filtering (and regularization), and the error in the manufacturing of the disk which is manifested in an incorrect measurement matrix. Minimizing noise and manufacturing errors relaxes filtering and regularization and improves reconstruction.

As the pixel resolution increases, image reconstruction improves. This is expected because the finer sampling of the image decreases the pixel-image ambiguity. It should be noted that the images are acquired, reconstructed and displayed at video rates. The images can also be reconstructed using compressive sensing methods and a portion of the measurements. This is currently being investigated.

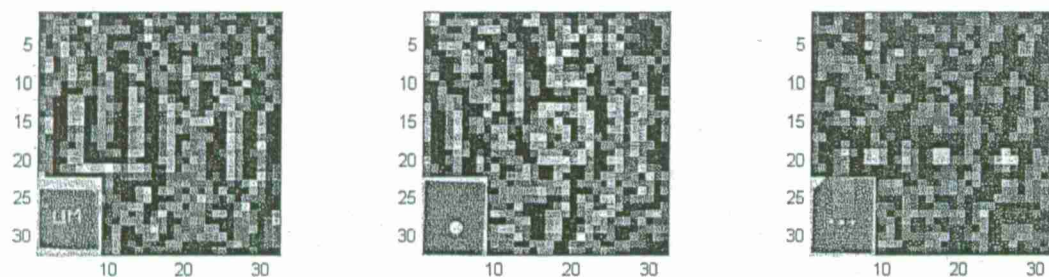


Fig. 3. Image reconstructions of 32x32 pixels for the three object masks, the images are normalized; object masks are shown in the inserts.

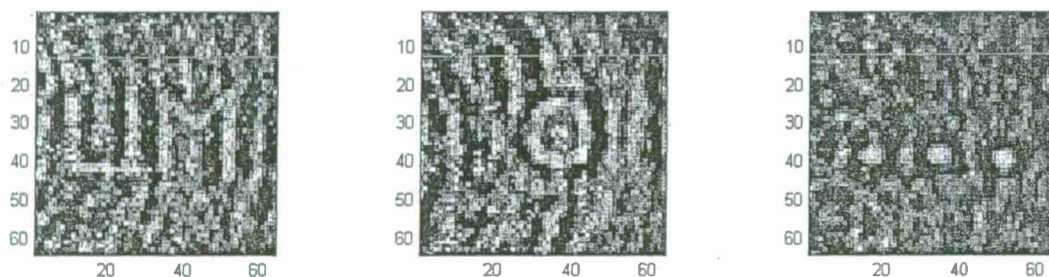


Fig. 4. Image reconstructions of 64x64 pixels for the three object masks, the images are normalized.

The authors would like to thank Robert Hewitt, Rick Voyles, and Robert Jordan for their help in manufacturing some of the components.

#### 4. References

- [1] K. B. Cooper, R. J. Dengler, N. Llombart, A. Talukder, A. V. Panangadan, C. S. Peay, I. Mehdi, and P. H. Siegel, "Fast high-resolution terahertz radar imaging at 25 meters," (SPIE, 2010), vol. 7671, p. 76710Y. 1, D.2
- [2] [http://en.wikipedia.org/wiki/Nipkow\\_disk](http://en.wikipedia.org/wiki/Nipkow_disk), accessed 3 March 2011.
- [3] R. Driggers, Encyclopedia of Optical Engineering (Marcel Dekker, New York, (2003).
- [4] H. Jacobs, R. Hofer, G. Morris, and E. Horn, "Conversion of millimeter-wave images into visible displays," J. Opt. Soc. Am. 58, 246-247 (1968).
- [5] M. Duarte, M. Davenport, D. Takhar, J. Laska, T. Sun, K. Kelly, and R. Baraniuk, "Single-pixel imaging via compressive sampling," Signal Processing Magazine, IEEE 25, 83-91 (2008).
- [6] O. Furukhi and E. L. Jacobs, "A sub-millimeter wave line scanning imager," Millimetre Wave and Terahertz Sensors and Technology III 7837(1), p. 78370D, SPIE, 2010.



# A Sub-Millimeter Wave Line Scanning Imager

Orges Furxhi<sup>a</sup> and Eddie L. Jacobs<sup>b</sup>

The University of Memphis, Memphis, TN 38152

## ABSTRACT

In this paper, the design and implementation of a sub-millimeter line scanning imager using a novel image-forming device is described. The system consists of a coherent illuminator, an optical system, an image plane mask, and a coherent detector. The image plane mask is formed by making a sequence of holes along a constant radius of a metal disk. Spinning the disk scans the holes through the image formed on it. A detector placed behind the spinning disk collects radiation passing through the holes. The holes are arranged in a pseudo-random pattern. At each detector sample time, energy from a different pattern of holes is collected. A rigorous electromagnetic analysis shows that, for a certain minimum size and spacing of holes and certain disk thicknesses, these measurements constitute a linear measurement of the energy in the image formed on the disk. Using techniques reminiscent of those used in compressive sensing, the image is then reconstructed by applying an inverse linear matrix transform to these measurements. We show how simulation can be used to optimize the design of the disk. We demonstrate a laboratory version of this device and discuss future efforts to systematize it. Extensions to full two-dimensional imaging are also discussed.

## 1. INTRODUCTION

The development cycle of imaging devices is a recurring one. First, a single detector is developed that allows the conversion of radiation to a form that can be digitized by a computer or perceived by a human. Next, comes the challenge of reducing the cost of the detector and making it more compact so that staring arrays can be built. This turns out to be a difficult challenge. Therefore, in the meantime, scanning systems are developed that facilitate the formation of images at the expense of mechanical complexity, system size and weight, and image formation rates. Finally, the goal of building staring arrays is achieved and scanning systems become obsolete. However, scanning systems play an important role because they fill the time gap between the development of the single detector and the staring array. Some examples of this cycle are visible light imagers, infrared imagers, and submillimeter wave imagers. To our knowledge, focal plane arrays in the submillimeter wave regime have not been demonstrated yet, although a method for building compact linear heterodyne receiver arrays has been proposed and is in the first stages of development.<sup>1</sup>

The complexity of developing scanning systems for sub-millimeter waves is greater than it is for the scanning systems in other regimes, such as visible and infrared. First, the wavelength is larger therefore the size and weight of these systems are greater. Second, the radiation is not as abundant. Current scanning systems for sub-millimeter waves are large in size and have image formation rates of less than one frame per second.<sup>2</sup> We have developed a novel image forming device that can be packaged into a handheld box and is capable of scanning and forming images at video rates.

The system consists of a coherent illuminator, an optical system, an image plane mask, and a coherent detector. The image plane mask and the image formation methodology associated with it are the novel parts of the system. The image plane mask is formed by making a sequence of holes along a constant radius of a metal disk. Spinning the disk scans the holes through the image formed on it. A detector placed behind the spinning disk collects radiation passing through the holes. The holes are arranged in a pseudo-random pattern. At each detector sample time, energy from a different pattern of holes is collected. These measurements constitute a linear measurement of the energy in the image formed on the mask. This process can be formalized mathematically and is expressed as

---

<sup>a</sup>ofurxhi@memphis.edu, <sup>b</sup>eljacobs@memphis.edu

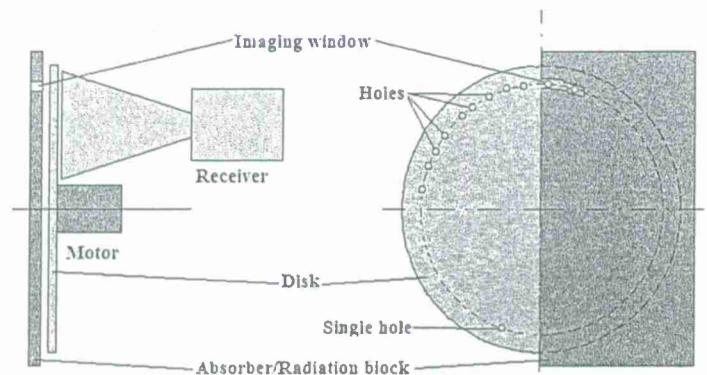


Figure 1: Conceptual sketch of the image plane mask and the coherent detector.

$$\bar{m} = \bar{M} \bar{p} \quad (1)$$

where  $\bar{m}$  is a vector the elements of which contain the values of the measurements,  $\bar{M}$  is a full rank matrix that encodes the pattern of the holes on the disk for each measurement, and  $\bar{p}$  is the unknown vector that contains the pixel intensities. In compressive sensing terminology,  $\bar{M}$  is the measurement matrix and  $\bar{m}$  is the measurement vector. The image is reconstructed by solving this equation for  $\bar{p}$ . Because  $\bar{M}$  is a full rank matrix, the solution is easy to compute. This device and the image measurement and reconstruction technique are described in more detail in a previous publication.<sup>3</sup> A conceptual sketch of the image plane mask and the coherent detector is shown in Figure 1.

The imager is configured similarly to a system with a focal plane array and the image plane mask is positioned where the focal plane array would be. Because the system is still a scanning system, the available integration time per measurement per detector is much less than the integration time available to the focal plane array detectors. This is mitigated in part by the presence of many scanning holes per measurement allowing more energy to go through and be measured by the detector. In addition, if compressive imaging techniques are used, the image can be reconstructed by taking less measurements than desired image pixels.<sup>4,5</sup> This increases the integration time available per measurement. The drawback of this technique is the slow reconstruction time associated with the iterative compressive sensing algorithms. This approach is not employed in this research, rather the number of measurements is made equal to the number of desired pixels allowing instantaneous reconstruction.

In this paper, we present the results of a three-dimensional analysis that aids in the design of the image plane mask. The linearity of the mask is investigated. The reasons for the non-linearity of the mask and a method by which this mask is made nearly linear are discussed. Following this introduction we briefly present the electromagnetic analysis methods used in this paper. The results of the analysis are discussed and the design parameters are given. Next, we describe the implementation of the system and show experimental results considering the results of the electromagnetic analysis. We discuss our approach to systematizing the device so that the images can be scanned and reconstructed at video rates. We also discuss the extension to a two-dimensional imager. The paper concludes with a summary.

## 2. THEORETICAL METHODS

To design the image plane mask we utilize a three-dimensional electromagnetic analysis. The three-dimensional structure of interest is assumed to be a perfect electric conductor (PEC). The field incident on the structure is an elliptically polarized tapered Gaussian beam given by Braunisch.<sup>6</sup> The observables of interest are the power incident on the structure, the power reflected from the structure, and the power transmitted by the structure. The powers are obtained once the far incident and scattered fields are known. The far incident field is derived using the stationary phase approximation.<sup>7</sup> Using the incident field on the structure we solve the Electric Field Integral Equation (EFIE) for the currents using the Method of Moments (MoM) technique. The currents are

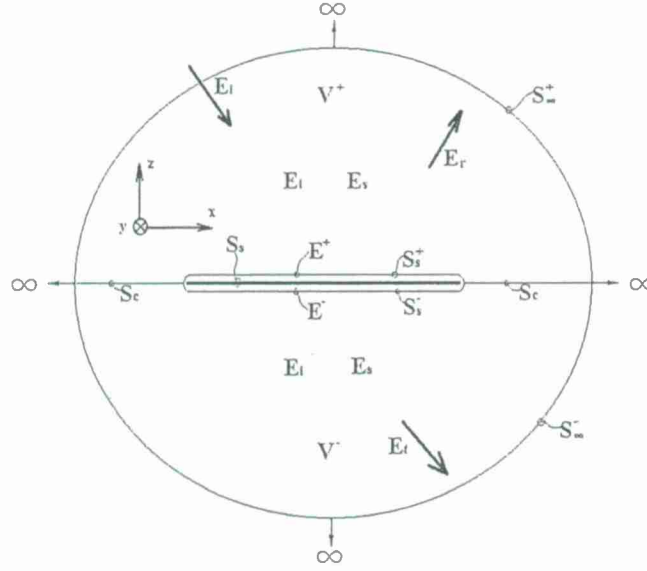


Figure 2: Cross-section cut of the scattering geometry.

used to find the far scattered fields with the help of the far field approximation. Below we summarize the main equations used in the analysis. For the complete derivations of the equations and the numerical techniques used see.<sup>8</sup>

To formalize the problem the scattering object is assumed to be an open scatterer. The open scatterer can be extended and deformed to adhere to the scattering structure of interest. A cross-section of the scattering geometry is shown in Figure 2. The scatterer is illuminated with the Gaussian tapered beam from above ( $z > 0$ ). The incident field induces currents on the scatterer which radiate. Therefore, the total field anywhere in space is composed of the incident field and the scattered field radiated by the scatterer

$$\underline{E}(\underline{R}) = \underline{E}_i(\underline{R}) + \underline{E}_s(\underline{R}) \quad (2)$$

The EFIE for the structure is obtained in the following manner. The well-known vector wave equation is transformed into an integral equation using the well-known vector form of Green's theorem and the free space Green function dyad  $\underline{\underline{G}}_0$  given by<sup>9</sup>

$$\underline{\underline{G}}_0(\underline{R}, \underline{R}') = (\underline{\underline{I}} + \frac{1}{k^2} \nabla \nabla) \frac{e^{ik|\underline{R}-\underline{R}'|}}{4\pi|\underline{R}-\underline{R}'|} \quad (3)$$

where  $\underline{\underline{I}} = \hat{x}\hat{x} + \hat{y}\hat{y} + \hat{z}\hat{z}$ , is the unit dyad (or idem factor),  $k^2 = \omega^2 \epsilon_0 \mu_0$  is the free space wave number,  $\underline{R} = x\hat{x} + y\hat{y} + z\hat{z}$  is a vector in Cartesian space noting the observation point,  $\underline{R}'$  is a vector noting the source point, and  $\nabla = \hat{x}\frac{\partial}{\partial x} + \hat{y}\frac{\partial}{\partial y} + \hat{z}\frac{\partial}{\partial z}$  is the gradient operator. The Green function dyad satisfies the wave and radiation equations.<sup>9</sup> Using this fact and applying vector identities,<sup>10</sup> we obtain

$$\underline{E}(\underline{R}) = -\oint_S [i\omega\mu_0(\hat{n} \times \underline{H}(\underline{R}')) \cdot \underline{\underline{G}}_0(\underline{R}', \underline{R}) + (\hat{n} \times \underline{E}(\underline{R}')) \cdot \nabla' \times \underline{\underline{G}}_0(\underline{R}', \underline{R})] ds' \quad (4)$$

where  $\underline{E}(\underline{R})$  is the electric field in a volume  $V$  enclosed by the surface  $S$ ,  $\hat{n}$  is the outward normal to  $S$ ,  $\underline{H}(\underline{R}')$  is the magnetic field on the surface contour.

Referring to Figure 2, Equation 4 is applied to the following fields in the respective regions: the scattered field in the volume  $V^+$  enclosed by  $S_s^+$ ,  $S_c$ , and  $S_\infty^+$ ; the incident field in the volume  $V^-$  enclosed by  $S_s^+$ ,  $S_c$ , and  $S_\infty^-$ ; the total field in the volume  $V^-$  enclosed by  $S_s^-$ ,  $S_c$ , and  $S_\infty^-$ . In all three cases, the integral over  $S_\infty^{+/-}$  vanishes because the scattered and incident fields satisfy the radiation condition in the respective regions. Combining and adding the three resulting equations as the contours  $S_s^+$  and  $S_s^-$  approach  $S_s$  and using equation 2, results in

$$\begin{aligned} \underline{E}_s(\underline{R}) = & \int_{S_s} \left[ i\omega\mu_0(\hat{n}' \times (\underline{H}^+ - \underline{H}^-)) \cdot \underline{G}_0 \right. \\ & \left. + (\hat{n}' \times (\underline{E}^+ - \underline{E}^-)) \cdot \nabla' \times \underline{G}_0 \right] ds' \quad \underline{R} \in V^- \cup V^+ \end{aligned} \quad (5)$$

Equation (5) gives the scattered field in the volumes  $V^-$  and  $V^+$  in terms of the fields on the scatterer surface  $S_s$ . The superscripts  $+$  and  $-$  indicate fields above and below the scatterer and  $\hat{n}'$  is the unit normal pointing into  $V^+$ . This equation is made more specific by applying the well-known PEC boundary conditions<sup>11</sup> of the scatterer

$$\underline{E}_s(\underline{R}) = i\omega\mu_0 \left( \underline{I} + \frac{1}{k^2} \nabla \nabla \right) \cdot \int_{S_s} \underline{J}_s(\underline{R}') \frac{e^{ik|\underline{R}-\underline{R}'|}}{4\pi|\underline{R}-\underline{R}'|} ds' \quad \underline{R} \in V^- \cup V^+, \quad (6)$$

where  $\underline{J}_s$  is the surface current on the scatterer and the free space Green function dyad is written explicitly. Equation (6) is used to find the scattered field in the volume  $V$  once the surface currents are known. The final form of the EFIE is obtained using Equation 2 in Equation 6 and evaluating Equation 6 on the boundary of the PEC scatterer

$$\hat{n}' \times \underline{E}_i(\underline{R}) = -\hat{n}' \times \left\{ i\omega\mu_0 \left( \underline{I} + \frac{1}{k^2} \nabla \nabla \right) \cdot \int_{S_s} \underline{J}_s(\underline{R}') \frac{e^{ik|\underline{R}-\underline{R}'|}}{4\pi|\underline{R}-\underline{R}'|} ds' \right\} \quad \underline{R} \in S_s \quad (7)$$

The unknown currents are obtained by solving Equation 7 using the Method of Moments.

The incident field on the scatterer is given by<sup>8</sup>

$$\begin{aligned} \underline{E}_i(\underline{R}) = & \int_0^{2\pi} d\phi \int_0^{\pi/2} d\theta k^2 \sin \theta \cos \theta \times \\ & \exp \{ ik [x \sin \theta \cos \phi + y \sin \theta \sin \phi - z \cos \theta] \} \times \\ & \psi(\theta, \phi) \underline{e}(\theta, \phi) \end{aligned} \quad (8)$$

This is a Gaussian beam with spatial center at the origin of the coordinate system and  $\underline{e}(\theta, \phi)$  and  $\psi(\theta, \phi)$  are the polarization vector and Gaussian spectrum respectively, given in.<sup>6</sup>

The far incident field is calculated from Equation 8 using the method of stationary phase for double integrals as presented in Mandel and Wolf.<sup>7</sup> For  $z > 0$ , and  $0 < \theta_s < \pi/2$ ,  $0 < \phi_s < 2\pi$ , the far incident field is given by

$$\underline{E}_i(\theta_s, \phi_s) \sim \frac{\exp[-ikr]}{r} \underline{F}_i(\theta_s, \phi_s) \quad (9)$$

Similarly, the far incident field for  $z < 0$ , and  $\pi/2 < \theta_s < \pi$ ,  $0 < \phi_s < 2\pi$ , is given by

$$\underline{E}_i(\theta_s, \phi_s) \sim \frac{\exp[ikr]}{r} \underline{F}_i(\theta_s, \phi_s) \quad (10)$$

where

$$\underline{F}_i(\theta_s, \phi_s) = \begin{cases} \frac{2\pi i}{k} \cos(-\theta_s) k^2 \psi(-\theta_s, \phi_s) \underline{e}(-\theta_s, \phi_s) & 0 < \theta_s < \pi/2 \\ -\frac{2\pi i}{k} \cos(\theta_s - \pi) k^2 \psi(\theta_s - \pi, \phi_s - \pi) \underline{e}(\theta_s - \pi, \phi_s - \pi) & \pi/2 < \theta_s < \pi \end{cases} \quad (11)$$



is the far incident field amplitude and it is assumed that  $0 < \phi_s < 2\pi$ .

The far field is obtained by approximating Equation (6) for the large argument  $|\underline{R} - \underline{R}'|$  and making the far field approximation.<sup>12</sup> The far scattered field is given by

$$\underline{E}_s(r, \theta, \phi) = \frac{e^{ikr}}{r} \underline{F}_s(\theta, \phi) \quad (12)$$

where

$$\underline{F}_s(\theta, \phi) = i \frac{\omega \mu_0}{4\pi} \int_{S_s} (\underline{J}_s(\underline{R}') - \hat{\phi} \hat{\phi} \cdot \underline{J}_s(\underline{R}')) e^{-ik(\underline{R}' \cdot \hat{\phi})} d\underline{s}' \quad (13)$$

is the far scattering field amplitude. The unit vector  $\hat{\phi}$  is in the direction of the observation and is given by

$$\hat{\phi} = \hat{x} \sin \theta \cos \phi + \hat{y} \sin \theta \sin \phi + \hat{z} \cos \theta \quad (14)$$

Because of the conservation of energy, the power incident on the structure is equal to the sum of the powers reflected by and transmitted through the structure. Because the structure is a PEC, there is no absorbed power. Therefore<sup>8</sup>

$$P_I = P_T + P_R \quad (15)$$

where  $P_I$  is the incident power given by

$$P_I = \frac{1}{\eta_0} \int_0^{\pi/2} d\theta \sin \theta \int_0^{2\pi} d\phi |\underline{E}_i|^2 \quad (16)$$

$P_R$  is the reflected power given by

$$P_R = \frac{1}{\eta_0} \int_0^{\pi/2} d\theta \sin \theta \int_0^{2\pi} d\phi |\underline{E}_s|^2 \quad (17)$$

$P_T$  is the transmitted power given by

$$P_T = \frac{1}{\eta_0} \int_{\pi/2}^{\pi} d\theta \sin \theta \int_0^{2\pi} d\phi |\underline{E}_i + \underline{E}_s|^2 \quad (18)$$

For the numerical solution of Equation 7 the structure of interest is modeled using triangular patches. The famous Rao-Wilton-Glisson (RWG) basis functions<sup>13</sup> are used as basis and testing functions for the MoM. The resulting matrix equation is solved using available software such as Matlab. Once the surface currents on the structure are found, the desired power quantities are calculated with the help of the equations presented above. For detailed explanation of the equations presented above and the numerical methods associated with them refer to.<sup>8</sup>

### 3. ELECTROMAGNETIC ANALYSIS RESULTS AND DESIGN PARAMETERS

The analysis method presented above is used to design the parameters of the scanning holes. We are interested in the radius, depth, and minimal proximity of the holes. From previous results,<sup>8</sup> the depth of the holes does not have a noticeable effect on the transmission of the radiation through the holes as long as the radius of the hole is larger than the first cutoff radius of a circular waveguide and the depth is comparable to the diameter of the hole. For holes with radii less than the cutoff radius, transmission decreases exponentially with depth. As it will be shown in the results presented below, we are only interested in holes with large radii. Therefore, from a design perspective, the hole depth is a free parameter. The thickness of the disks available to us is approximately  $2.7112\lambda$ , where the wavelength  $\lambda = 468.43\mu m$ , corresponding to a frequency of  $640GHz$ . Because of this restriction, the hole depth parameter is fixed.

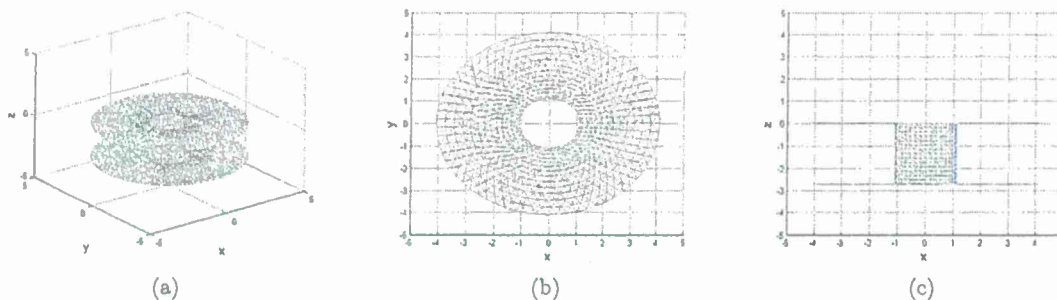


Figure 3: Three-dimensional geometry of the hole structure. The units are in normalized  $\lambda$ .

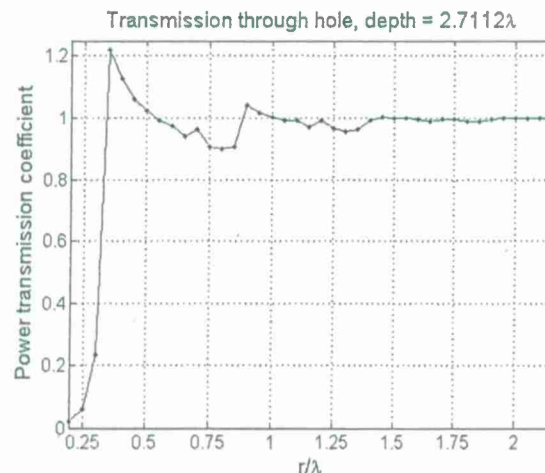


Figure 4: Power transmission coefficient as a function of hole radius for hole depth of  $2.7112\lambda$ .

The power transmission coefficient of the holes with depth  $2.7112\lambda$  is investigated as a function of the hole radius. The three-dimensional geometry of the structure used in this analysis is shown in Figure 3. The geometry is finite and has a diameter of  $8\lambda$ . The incident field has a tapering of  $1.5\lambda$  (the tapering parameters is related to the variance of the Gaussian taper), is normally incident, and is circularly polarized. The incident beam resembles a blur spot approximately  $5\lambda$  in diameter. Because the incident field is tapered, the structure can be made finite and the transmission of the hole can be measured. The radius of the hole is varied from  $0.2\lambda$  to  $2.05\lambda$  in steps of  $0.05\lambda$ . The power transmission coefficient is calculated as the ratio of the incident power on the top aperture of the hole to the power transmitted in the lower hemisphere ( $z < 0$ ). The results are shown in Figure 4.

The transmission coefficients for certain radii are greater than unity. The reason for this is that only the power incident on the hole aperture from above is used as the input power reference. The fields radiated by the edge currents at the hole apertures are not included in the input power reference but they are accounted for in the far field measurement. Hence, the calculated power transmission coefficient is greater than unity. The edge current effects become less evident as the radius increases. When the radius is larger than  $1.4\lambda$  these effects are almost unnoticeable and therefore the far field measurement results only from the power incident on the hole aperture. In this case, the holes are said to scan the image formed on the image plane mask. This is the desired effect because we need the radiation associated with the part of the image formed on the hole to pass and the part of the image outside the hole to be blocked.

Another important parameter is the proximity between two holes. This affects the linearity of the structure. Cross-sections of the geometries used to investigate the minimal proximity are shown in Figure 5. The depth of the holes is  $2.7112\lambda$  and the radius of the holes is  $1\lambda$ . For these hole parameters the transmission coefficient is

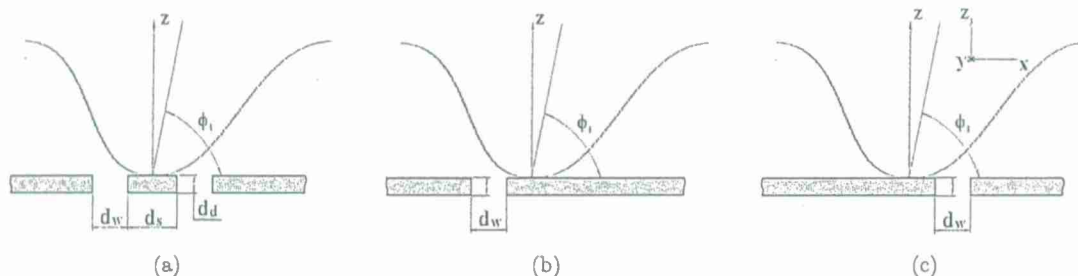


Figure 5: Cross-sections of the geometries used to investigate the minimal proximity between holes. In the three-dimensional simulation the depth of the holes is  $2.7112\lambda$  and the radius is  $1\lambda$ . The incident field is the same as in the radius analysis.

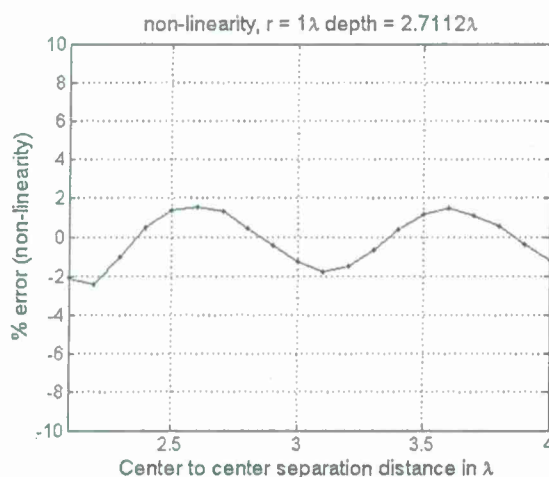


Figure 6: Percent linearity error as a function of the center to center separation of two identical holes.

unity. For a linear structure, the measurement from the structure in Figure 5a should be equal to the sum of the measurements from the structures of Figures 5b and 5c. Because the source and the detector are coherent the power measurement is not expected to be linear.

To investigate the linearity of the structure as a function of the separation distance we introduce the percent linearity error metric. The percent linearity error is calculated as the difference of the measurement from the structure in Figure 5a with the sum of the measurements from the structures of Figures 5b and 5c. Then, the result is divided by the the sum of the measurements from the structures of Figures 5b and 5c and multiplied by 100%. The results are shown in Figure 6.

Except when the holes are very close to each other (edge to edge separation  $< \lambda$ ) the linearity error oscillates around zero with a period of  $1\lambda$ . This error is predicted by the array factor of this structure<sup>8</sup> because the structure resembles two identical radiating antennas separated by a distance.<sup>14</sup> The error can be eliminated if many holes are placed at random distances from each other. This is advantageous because it not only improves the linearity of the structure but it also does not require any modification of the scanning technique. The holes in the line imager are placed in random fashion as required by the reconstruction technique.

From the results of the electromagnetic analysis, we can conclude design parameters for the holes in the image plane mask. The radius of the holes needs to be greater than  $1.4\lambda$  but other radii are also possible such as  $1\lambda$ . In all these cases the far field measurement results from the field incident on the hole, and not from the edge currents. In this case the holes are effectively scanning the image formed on the mask. The edge to edge separation of the holes is recommended to be greater than  $1\lambda$ . This separation assures that the only non-linearity is due to the array factor of the structure. The depth of the holes was determined from the available disk for the



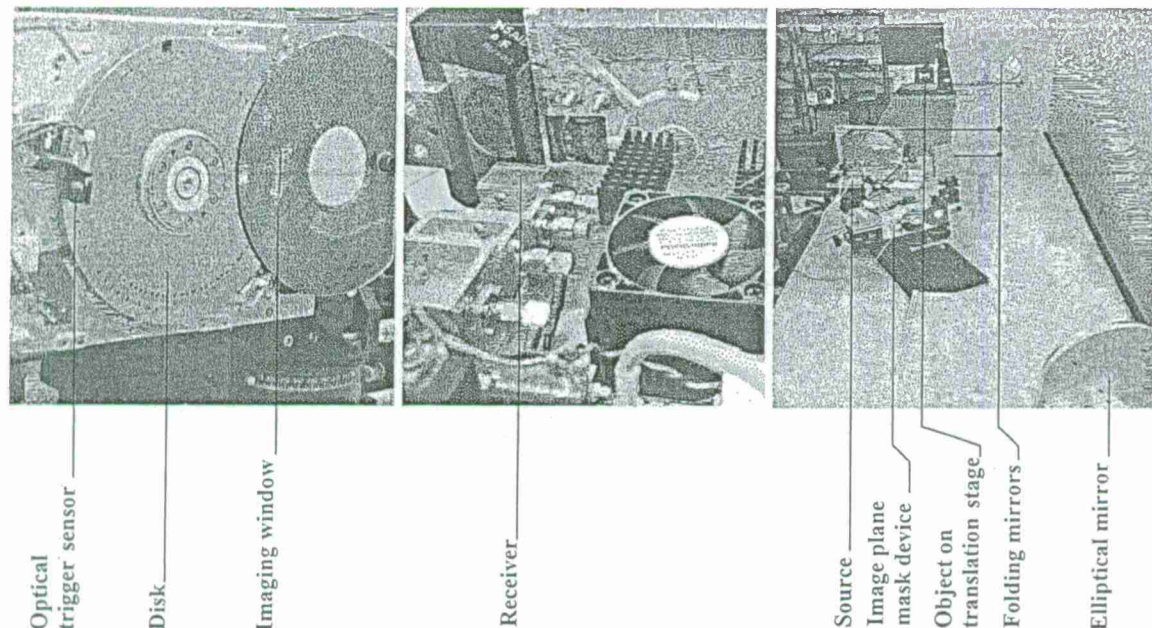


Figure 7: Grouping of pictures illustrating the imaging system and its parts.

production of the mask, however if the depth parameter is to be designed it should be chosen comparable with the diameter of the holes and such that it does not introduce resonances (i.e. edge currents).

#### 4. IMPLEMENTATION OF THE IMAGING SYSTEM

A grouping of pictures illustrating the descriptions presented in this section is shown in Figure 7. A laboratory prototype of the image plane mask device has been implemented using parts from a 5.25 inch hard drive. The hard drive platters are made of conducting materials and are balanced and flat. They are used as the disks on which the scanning holes are drilled. The motor can be driven at a constant rate and the disk is already mounted on it. We have designed some electronics that can drive the motor at three revolutions per second. The motor can rotate at speeds up to 90 rotations per second using other electronics. The front cover of the hard drive is removed and a window is placed in front of the scanning disk. This is the imaging window and the optical system forms the image onto it. The extent of the imaging window is 22 millimeters long. An opening is made in the back of the case so that the radiation is allowed to pass onto the receiver. An optical sensor is mounted in the vicinity of disk edge. This sensor is used to trigger a measurement for each rotation of the disk and facilitates the registration of the measurements with the position of the disk. The receiver and source are from Virginia Diodes and operate at  $640\text{ GHz}$ . The signal is detected from the receiver and is down-converted to  $4.8\text{ GHz}$ . The down-converted signal is measured using a spectrum analyzer (Agilent SCA Spectrum Analyzer AN1996A). The measurement data is transferred remotely to a computer where it is stored and later post-processed to reconstruct the image. For each rotation of the disk 1000 data points are collected.

The optical system consists of a main elliptical reflective surface with a focus at one meter and the other at 10 meters. The image is formed on the one meter side. The system has an effective diameter of 0.3048 meters (12 inch), effective focal length of 0.9091 meters, resulting in a  $F\#$  of 2.9826. The magnification of the system is 0.1, the depth of focus for coherent radiation is 0.01062 meters, and the depth of field for incoherent radiation is 1.0162 meters. The diffraction spot diameter is 3.75 millimeters for a wavelength of  $468.43\text{ }\mu\text{m}$ , corresponding to the illumination frequency of  $640\text{ GHz}$ . The system is folded using two flat mirrors. The source is placed three meters away from the object to flood illuminate it.

Holes have been drilled on the disk in a constant radius of 58 millimeters. This radius and the extent of the imaging window were chosen to minimize the curvature of the scan. A single hole of radius 0.5 millimeters



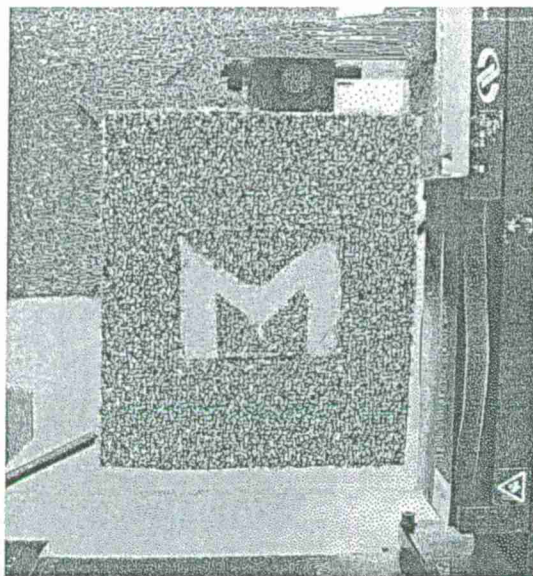


Figure 8: Picture of the target.

( $1.06 \lambda$ ) is drilled at a distance from other holes that have a radius of 1 millimeter ( $2.12 \lambda$ ) and are placed in the vicinity of each other at a random order respecting the design parameters presented above. The single hole is used to perform a raster scan of the image formed on the imaging window. The radius of half a millimeter allows high transmission (over 98%) and high scan resolution. The disk is 1.27 ( $2.7112 \lambda$ ) millimeters thick.

The imaging window is placed over the disk so that the image is scanned vertically. For demonstration purposes, the object is placed on a translational stage and is scanned horizontally. Vertical lines of the image of the object are scanned by the image plane mask as the object is moved horizontally and an image of it is reconstructed when the measured data is post-processed. The results are shown in the next section.

## 5. EXPERIMENTAL RESULTS

For this experiment we chose to form an image of the letter "M". A picture of the target mounted on the translational stage is shown in Figure 8. The object letter is formed by placing a piece of carpet with a cutout of the letter "M" over a plate of aluminum. The plate of aluminum was made rough to minimize specular reflections. The contour of the letter "M" was approximately 15 to 20 millimeters wide. The height of the letter was 60 millimeters. Because of the characteristics of the optical system, the image is expected to be one tenth of the object in size and highly blurred. The target was made small to ensure that it was illuminated uniformly by the source. We did not use illumination optics hence, the wavefront reaching the object was not planar and images of large objects were not formed properly.

The results of the raster scan (single hole) and linear measurement scan (plurality of holes) are shown in Figure 9a and Figure 9b respectively. Referring to the raster scan image which will be used as the reference, the image is severely blurred. However, the structure of the letter "M" can be identified. The blur is expected given the characteristics of the optics. From the measurements the image has a height of 25 samples corresponding to 9.1 millimeters (the radius where the holes are placed is 58 millimeters and 1000 data points are collected per rotation). This is consistent with the calculation from the parameters of the optical system, resulting in an object size of approximately 60 millimeters.

Figure 9b shows the reconstructed image using the linear measurements made on the image plane. There is a clear resemblance between the reconstructed image and the raster scan image of Figure 9a. The technique used to reconstruct the image is described in detail in<sup>3,8</sup> To reconstruct the image it was necessary to use regularization when inverting the measurement matrix. This is necessary because of the error in the knowledge

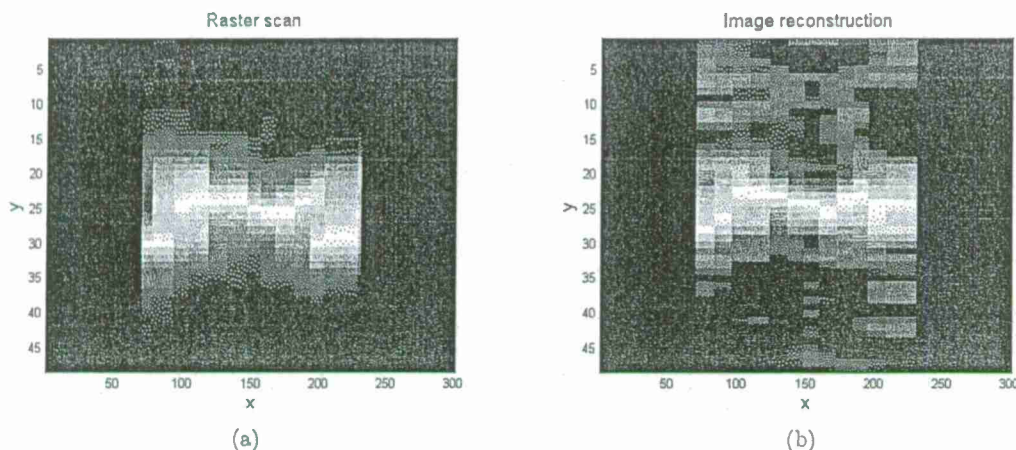


Figure 9: Images of the object in Figure 8. 9a Image reconstructed from the raster scan, 9b image reconstructed from the linear measurement.

of the exact positions of the holes on the disk for each data sample. Analysis shows<sup>8</sup> that the quality of the reconstruction will improve if all of the energy that goes through the holes is measured. Currently, only part of the energy is measured. The proper way of collecting all of the energy will be investigated in the future.

## 6. FUTURE EFFORTS

Currently, the imager can perform line scans at rates of three frames per second and the data is post-processed to reconstruct the images. The optical system was designed for a conjugate point scanning imager and is not appropriate for the current imaging system. In the current implementation, only part of the energy that goes through the holes is collected by the receiver antenna. In addition, the image plane mask device is not properly guarded against stray radiation from the different reflective materials in the room. We plan to address all of these issues in the near future.

New electronics will be built to drive the hard drive spindle motor so that the disk can be spun at least 30 revolutions per second. This will facilitate video rate imaging. The use of additional down-converters and an analog to digital conversion card interfaced to a computer will facilitate the collection of the measurement data and the real time image reconstruction. We are in the process of designing new optics for the imager and illumination systems. This will facilitate uniform plane wave illumination of the scene and the minimization of aberrations. To collect all the energy that passes through the holes we plan to build a lens that will be placed behind the holes. The lens will focus the energy on the horn of the receiving antenna.

One of the factors that affect the quality of the reconstructed image is the uncertainty of the location of the holes. To mitigate this, we will use precision machining to drill the holes at known locations. This and the addition of the lens behind the holes are expected to improve the quality of the reconstruction. The sensitivity of the imager can be improved if the image plane mask is shielded properly from stray radiation that makes its way into the receiver. This will allow us to form images of objects that have low reflectivity coefficients. Also, by increasing the size of the imaging window we can form larger images. Because more randomly placed holes will be contributing to the measurement, the linearity of the measurement will improve. This will improve the quality of the reconstruction.

The imager can be extended to full two-dimensional imaging simply by replacing the slit imaging window with a rectangular one and by adding more randomly placed holes on the disk. The image reconstruction technique is the same as for the line image and has been described in detail in previous publications.<sup>3,8</sup> Preliminary analysis<sup>8</sup> shows that we will be able to generate enough random patterns in one revolution of the disk to reconstruct a 32 by 32 pixel image from linear measurements. When the line imager has been optimized and all associated issues have been resolved, we will implement the full two-dimensional imager.

## 7. CONCLUSIONS

We have presented the results of a rigorous three-dimensional electromagnetic analysis and used them to design the image plane mask. For the available disk thickness the optimal hole radius was greater than  $1.4\lambda$ . We also investigated the linearity of the mask and concluded that the mask is made nearly linear if the scanning holes are placed randomly on the disk and separated by at least  $1\lambda$  from each other. We described the implementation of the system in detail. Two images of the same object formed using the line imager were presented. The first image was formed using raster scanning as the object was moved horizontally on a translation stage. This image was used as a reference. The second image was reconstructed from linear measurements made on the image plane and was compared against the first image. There was clear resemblance between the two images. Finally, we discussed our approach to systematizing the device so that the images can be scanned and reconstructed at video rates. We also discussed the necessary changes that need to be made to improve the image reconstruction from linear measurements. These improvements will facilitate the successful implementation of the full two-dimensional imager.

## REFERENCES

1. I. Mehdi, B. Thomas, C. Lee, G. Chattopadhyay, R. Lin, E. Schlecht, A. Peralta, J. Gill, K. Cooper, N. Llombart, and P. Siegel, "Radiometer-on-a-chip: a path toward super-compact submillimeter-wave imaging arrays," *Terahertz Physics, Devices, and Systems IV: Advanced Applications in Industry and Defense* 7671(1), p. 767105, SPIE, 2010.
2. K. B. Cooper, R. J. Dengler, N. Llombart, A. Talukder, A. V. Panangadan, C. S. Peay, I. Mehdi, and P. H. Siegel, "Fast high-resolution terahertz radar imaging at 25 meters," *Terahertz Physics, Devices, and Systems IV: Advanced Applications in Industry and Defense* 7671(1), p. 76710Y, SPIE, 2010.
3. O. Fuxhi and E. L. Jacobs, "A sub-millimeter wave line imaging device," *Passive Millimeter-Wave Imaging Technology XIII* 7670(1), p. 76700L, SPIE, 2010.
4. M. Duarte, M. Davenport, D. Takhar, J. Laska, T. Sun, K. Kelly, and R. Baraniuk, "Single-pixel imaging via compressive sampling," *Signal Processing Magazine, IEEE* 25, pp. 83–91, march 2008.
5. J. Romberg, "Imaging via compressive sampling," *Signal Processing Magazine, IEEE* 25, pp. 14–20, march 2008.
6. H. Braunisch, Y. Zhang, C. Ao, S.-E. Shih, Y. Yang, K.-H. Ding, J. Kong, and L. Tsang, "Tapered wave with dominant polarization state for all angles of incidence," *Antennas and Propagation, IEEE Transactions on* 48, pp. 1086–1096, Jul 2000.
7. L. Mandel, *Optical Coherence and Quantum Optics*, Andrews McMeel, Kansas City, 1995.
8. O. Fuxhi, *Spatially Selective Mirrors and Masks for Submillimeter Wave Imaging*. PhD thesis, The University of Memphis, <http://www.memphis.edu/etd/>, 2010.
9. C. Tai, *Dyadic Green's Functions in Electromagnetic Theory*, Andrews McMeel, Kansas City, 1971.
10. J. Jackson, *Classical Electrodynamics*, Oxford University Press, Oxford Oxfordshire, 1999.
11. J. Volakis, *Finite Element Method for Electromagnetics*, Andrews McMeel, Kansas City, 1998.
12. A. Ishimaru, *Electromagnetic Wave Propagation, Radiation, and Scattering*, Andrews McMeel, Kansas City, 1991.
13. S. Rao, D. Wilton, and A. Glisson, "Electromagnetic scattering by surfaces of arbitrary shape," *Antennas and Propagation, IEEE Transactions on* 30, pp. 409–418, may 1982.
14. C. Balanis, *Antenna Theory*, Oxford University Press, Oxford Oxfordshire, 1997.



# A Sub-Millimeter Wave Line Imaging Device

Orges Furxhi<sup>a</sup> and Eddie L. Jacobs<sup>b</sup>

The University of Memphis, Memphis, TN 38152

## ABSTRACT

In this paper we present a single mode active device for sub-millimeter wave line imaging. The illuminated scene is imaged through focusing optics onto a device we have developed and have dubbed a spatially selective mask (SSM). This device transmits parts of the image onto a heterodyne receiver. Currently the SSM is capable of transmitting user-selectable parts of one line of the image that is focused on it. Multiple patterns are used to sample a line in the image. The voltage in the receiver resulting from each pattern constitutes an independent measurement of the illuminated scene along a line. A one dimensional image is reconstructed from the measurement results and a priori knowledge of the patterns using methods derived from the theory of compressive sensing. The theory behind the device and the design principles we use are reviewed. We show line images obtained at 640 GHz. Extension of this technique to two dimensional imaging is discussed.

## 1. INTRODUCTION

The usefulness of sub-millimeter wave imaging in military and security applications needs no introduction. Sub-millimeter waves can penetrate through many manmade materials and provide high resolution images at stand-off distances while still not suffering tremendously from atmospheric attenuation.<sup>1,2</sup> However, the current state of the art is limited to target space scanning systems that require complicated mechanical mechanisms and hence tend to be bulky, heavy, and not portable. These systems usually make use of a single pixel detector that offers very high signal to noise levels due to the maturity of the technology. Other imaging methods that perform well in other modalities such as interferometric arrays in the millimeter wave region<sup>3,4</sup> or focal plane arrays in infrared and visible regimes, have yet to be demonstrated in the sub-millimeter wave regime.

Scanning the image space is an alternative to scanning the target space. The image space is smaller than the target space and the scanning mechanisms can be made small, thereby eliminating the bulkiness of the imager. Current efforts are going on at Rice University to develop a electronically controlled mask that can be used to scan the image field.<sup>5</sup> Although promising, they have not been able to achieve the high modulation levels needed to bring the signal to noise ratio to acceptable levels for image formation. We have developed a method of image space scanning with high modulation levels, high scanning rates, low mechanical complexity, and low cost. At the core of this method is a rotating disk with holes that spins at a constant speed. The image is formed on one portion of the disk and it is selectively transmitted through the holes onto the receiver. Linear measurements are made on the image as the disk rotates. An image is reconstructed on a screen using the knowledge of the hole patterns and the measured signal from the receiver.

The paper is organized as follows. Section 2 describes the device and the method of image reconstruction in more detail. In Section 3, we present the theoretical formulation and numerical methods used for the performance and electromagnetic analysis of the device. Results of the analysis that pertain to the design of the device are shown in Section 4. The image simulation results and the experimental image results are shown in Section 5. Section 6 discusses the extension of the imaging methodology to two dimensional images. Section 7 concludes the paper.

---

<sup>a</sup>ofurxhi@memphis.edu, <sup>b</sup>eljacobs@memphis.edu



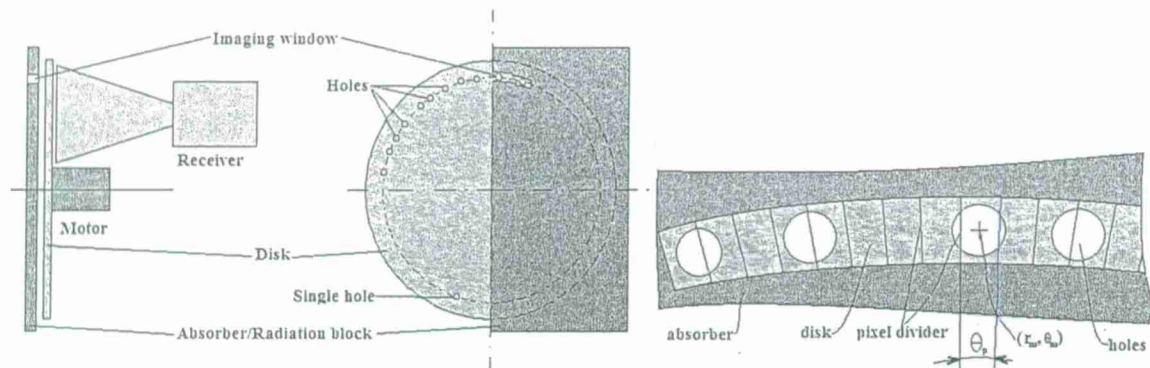


Figure 1. (Left) Conceptual sketch of the line imaging device, (right) pixel block divisions.

## 2. THE SPATIALLY SELECTIVE MASK AND IMAGE RECONSTRUCTION

Figure 1 shows a conceptual sketch of the line imaging device that utilizes a spatially selective mask. This device is placed in the image plane of the imager and the image of the scene is formed on it. The device consists of a rotating disk that contains holes along a constant radius. The image is formed only on a part of the disk and that part is referred to as the imaging window. For the line imager this window resembles a slit. The receiver is placed behind the disk and all the energy from the image that passes through the holes is collected. At any given time several holes are found in the imaging window. These holes sample the image that is formed on the imaging window by allowing only the energy from the part of the image where the holes are located to be measured. A number of measurements are made as the disk is rotated and the pattern of holes inside the imaging window changes.

In order to reconstruct the image from these measurements the imaging window is divided into conceptual (imaginary) blocks. These blocks are the image pixels and the reconstruction process will produce the average value of the intensity in each of them. If the number of measurements made is less than the number of pixels inside the imaging window, the image can be reconstructed using compressive sensing algorithms as presented in.<sup>6</sup> Although a lot of research is being dissipated into compressive sensing algorithms, their performance with respect to time is still below that required for video rates because they use iterative methods. As will be shown, one of the advantages of our technique is that it allows us to take as many linearly independent measurements as there are pixels in the image, given that the positions of the holes on the disk have been carefully chosen. This advantage can be exploited in the reconstruction process as presented below.

Our imaging problem can be cast into a matrix equation of the form

$$\bar{m} = \bar{M} \bar{i} \quad (1)$$

where  $\bar{m}$  is a vector the elements which contain the measurement values corresponding to each pattern of holes in the imaging window as the disk is rotated.  $\bar{M}$  is a full rank square matrix called the measurement matrix. The vector  $\bar{i}$  contains the pixel values of the image formed on the imaging window and is the unknown quantity. Each row on the measurement matrix corresponds to one pattern of holes on the imaging window and is to be registered with the measurement values  $m_n$  corresponding to that pattern. Each entry in the rows corresponds to a pixel. The numerical value of each entry is the portion of the pixel corresponding to that entry that is transmitted through the hole.

Assuming that the holes on the disk are placed so that each measurement matrix row is linearly independent of the others equation 1 can be solved for  $\bar{i}$ ,

$$\bar{i} = \bar{M}^{-1} \bar{m} \quad (2)$$

Equation 2 can be solved in parallel since each entry of  $\bar{i}$  can be computed simply through addition and multiplication operations on the elements of  $\bar{M}^{-1}$  and  $\bar{m}$ . This is very important when the technique is extended to two dimensions where the number of computations increases greatly. The series of measurements  $m_n$ , elements of  $\bar{m}$ , can be collected at the same rotational positions of the disk for each image frame. Hence, the elements of  $\bar{M}^{-1}$  need to be computed only once. Once a full set of measurements is made and the entries of the measurement vector  $\bar{m}$  are known, the image can be reconstructed almost instantaneously by solving equation 2. A full set of measurements can be collected during one full rotation of the disk. If the disk is rotated at a constant rate of 1800 rotations per minute the imager will produce images at a video rates of 30 lines (or frames) per second.

For the line imager an appropriate pixel block can have the shape of an area element on the  $r - \theta$  plane of a cylindrical coordinate system as shown in Figure 1(right). In that implementation the entries of the measurement matrix can be calculated using geometrical formulas given that we know the centers of each hole ( $r_m, \theta_m$ ) with respect to the revolution axis, their diameters, and the angular extent of the pixels ( $\theta_p$ ). Each pattern of holes in the imaging window corresponds to one row of the measurement matrix. We obtain different patterns at different rotational positions of the disk. For each pixel the geometrical formulas are used to determine the area of intercept of that pixel with the holes inside the imaging window. The ratio of the area of intercept to the area of the pixel becomes the numerical entry on the row of the measurement matrix corresponding to that pattern and pixel.

### 3. ANALYSIS METHODS

It is natural to ask several questions when constructing a device such as the one described above. What is the optimal number of holes inside the imaging window at any given time? What is the minimum dimension of the holes? What is the minimal distance between holes? What is the optimal depth of the holes? All but the first question require a rigorous three-dimensional electromagnetic analysis. The first question is answered by observing the condition number of the measurement matrix as we change the number of random holes inside the imaging window. The condition number of the measurement matrix indicates how noise is amplified in the reconstruction process and is given in equation 3.

$$\kappa = \left\| \bar{M} \right\| \left\| \bar{M}^{-1} \right\| \quad (3)$$

The condition number is always greater than one, with one being the lower limit signifying a well-conditioned matrix and infinity signifying a singular matrix. Obviously the number of holes that can be placed in a limited space, i.e. the image window, is determined by the dimensions of the holes and the minimal proximity between any two holes.

Transmission through the cylindrical holes of the disk has characteristics similar to transmission through a cylindrical waveguide.<sup>7</sup> The transmission depends on the dimensions of the cylindrical hole. The waveguide behavior of the cylindrical holes becomes evident when the thickness of the disk is made finite. For example, as the diameter of the hole is increased through the cutoff value, large jumps in transmission are noticed and then the transmission decreases until the cutoff value of another mode is reached and then another jump, and so on. Also, if the hole diameter is kept constant and the thickness of the disk is varied, one notices sinusoidal variations in the transmission through the hole. The transmission of the hole for hole diameters less than the cutoff diameter, decreases exponentially as a function of thickness.<sup>7</sup> The same relationships between transmission through the aperture and aperture dimensions are preset with thick slits.<sup>8</sup> Thick slits behave like parallel plate waveguides and can be analyzed using a two-dimensional electromagnetic analysis.

Although the two-dimensional electromagnetic analysis of the structure would reveal the same relationships between the structure parameters and the power transmitted to the receiver, it can not be used to obtain design parameters. The reason is the difference between the cutoff frequencies of a parallel plate waveguide and the cutoff frequencies of a cylindrical waveguide (due to the boundary conditions). The design parameters can be obtained through a three-dimensional analysis. A three-dimensional analysis is being implemented and will be the subject of another publication.

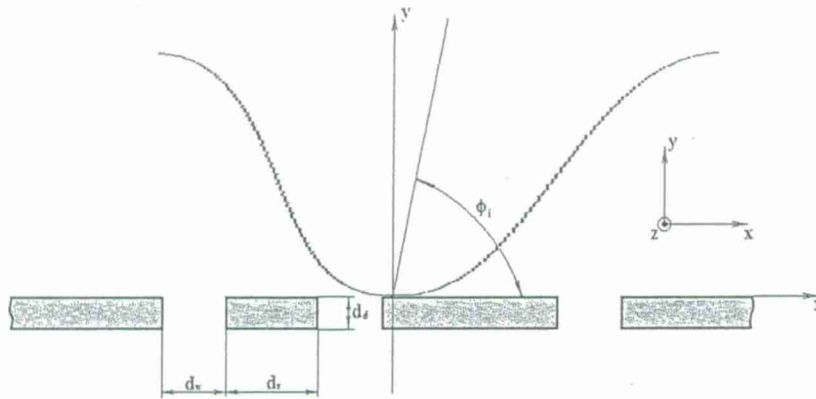


Figure 2. Electromagnetic analysis geometry

The two-dimensional analysis can give us insight into the qualitative behavior of our imager as observed by experiment. For this purpose we implemented a two-dimensional electromagnetic simulation using a Method of Moments technique. The geometry for the simulations is shown in Figure 2. The width of the slits is noted by  $d_w$ , the slit separation is noted by  $d_s$ , the slit depth is noted by  $d_d$ , and the angle of incidence of the incident field is noted by  $\phi_i$  and is measured with respect to the  $x$ -axis. The  $z$ -axis is pointing out of the page. As will be delineated next, the currents on the contours of the structure are the primary quantities that need to be calculated. All the other unknown quantities are obtained from the currents. Since the contours are taken on the surface of the structure the calculated currents are also physical currents. The theoretical formulation of the electromagnetic equations used to analyze the structures of interest has been presented previously.<sup>9</sup> The main equations are summarized below.

The total electric field at any point in space is given by the sum of the incident and scattered fields

$$\Psi(\underline{x}) = \Psi_i(\underline{x}) + \Psi_s(\underline{x}) \quad (4)$$

where  $\underline{x}$  is a vector in the  $x, y$  plane. These fields satisfy the Helmholtz wave equations. The Incident electric field is assumed to be polarized in the  $z$ -direction and is propagating towards the structure in the negative  $y$ -direction. The scattered field satisfies the radiation condition in all directions, while the incident field satisfies it for the lower half space since it is incident from the top half space. For several reasons made clear below, the incident field is modeled as a superposition of tapered Gaussian beams and is defined as

$$\Psi_i(x, y) = \sum_n a_n \int_0^\pi W_n(\alpha - \phi_i) e^{-ik_0((x-x_{0n})\cos\alpha + (y-y_{0n})\sin\alpha)} d\alpha \quad (5)$$

where  $k_0$  is the free space wave number for the wavelength of interest,  $a_n$  is the amplitude of the  $n$ th beam,  $x_{0n}$  and  $y_{0n}$  are the spatial shifts of the beam on the structure, and  $W_n(\alpha)$  is the Gaussian spectrum function of the  $n$ th beam and is given by<sup>10,11</sup>

$$W(\alpha) = \frac{1}{\sqrt{\pi}\Omega} e^{-\frac{\alpha^2}{\Omega^2}} \quad \Omega = \frac{2}{k_0\tau \sin\phi_i}$$

The tapering factor of the beam is represented by  $\tau$  and the angle of incidence, measured with respect to the positive  $x$  axis, is represented by  $\phi_i$ , as shown in Figure 2. Gaussian tapering is convenient for several reasons. It makes possible the calculation of the transmitted field because the incident field is almost finite in extent at the structure. It minimizes the erroneous effects of a finite structure since the incident field at the ends of the structure tends towards zero. It can be used to simulate the diffraction-limited image of one or more point sources because of its similarity with the Sombrero function. This allows the simulation of the structure of interest as part of an imaging system and is very useful when analyzing the resolution properties of the system.

Using Green's theorem on the fields and the Green's function for two dimensions, and applying the boundary conditions on the structure, we express the scattered and incident fields in terms of the currents on the structure.

The far field for the incident field is calculated using the stationary phase approximation.<sup>12</sup>

$$\Psi_i(\underline{x}) = F_i(\phi) \begin{cases} g(|\underline{x}|) & 0 \leq \phi < \pi \\ g^*(|\underline{x}|) & \pi \leq \phi < 2\pi \end{cases} \quad (6)$$

$$F_i(\phi) = \sqrt{\frac{2\pi}{k_0}} \begin{cases} \sum_n a_n W_n(\phi - \phi_i) e^{ik_0(x_{0n} \cos(\phi) + y_{0n} \sin(\phi))} & 0 \leq \phi < \pi \\ \sum_n a_n W_n(\phi - \phi_i - \pi) e^{ik_0(x_{0n} \cos(\phi - \pi) + y_{0n} \sin(\phi - \pi))} & \pi \leq \phi < 2\pi \end{cases} \quad (7)$$

$$g(|\underline{x}|) = \frac{e^{-i(k_0|\underline{x}| - \pi/4)}}{\sqrt{|\underline{x}|}} \quad (8)$$

The scattered field in the far region is given by

$$\Psi_s(\underline{x}) \approx g(|\underline{x}|) F_s(\phi) \quad (9)$$

$$F_s(\phi) = -\eta_0 \left( \frac{k_0}{8\pi} \right)^{1/2} \int_{C_s} J_z(\underline{x}') e^{-ik_0 \hat{\underline{x}} \cdot \underline{x}'} dl' \quad (10)$$

$$g(|\underline{x}|) = \frac{e^{i(k_0|\underline{x}| - \pi/4)}}{\sqrt{|\underline{x}|}} \quad (11)$$

where  $F_s(\phi)$  is the scattering amplitude,  $\hat{\underline{x}} = \hat{x} \cos \phi_s + \hat{y} \sin \phi_s$  is a unit vector in the observation direction and  $g(|\underline{x}|)$  is the propagation phase and attenuation.

Because of the conservation of energy the power of the incident field should be equal to the sum of the reflected power and transmitted power.

The incident power is given by

$$P_i = \frac{1}{\eta_0} \int_0^\pi |F_i(\phi)|^2 d\phi \quad (12)$$

the reflected power is given by

$$P_r = \frac{1}{\eta_0} \int_0^\pi |F_s(\phi)|^2 d\phi \quad (13)$$

and the transmitted power is given by

$$P_t = \frac{1}{\eta_0} \int_\pi^{2\pi} |F_i(\phi) + F_s(\phi)|^2 d\phi \quad (14)$$

The transmission power coefficient is calculated as the ratio of the transmitted power to the incident power.

A numerical solution for the currents can be obtained using the Method of Moments. The details of the MoM solution have been presented previously in.<sup>9</sup> Once the currents are known we can calculate the far scattered field using the discrete form of equation 10. The far incident field is calculated directly from equation 7. The powers, hence the transmission coefficient, can be calculated using equations 12, 13, and 14, once the far fields are known.



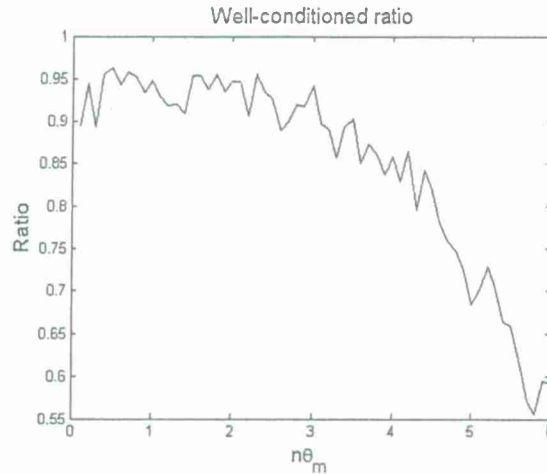


Figure 3. Ratio of well-conditioned measurement matrices to total number of measurement matrices

#### 4. SIMULATION RESULTS AND DISCUSSION

To investigate the performance of the reconstruction process as a function of the number of holes inside the imaging window, we simulated the scenario illustrated in Figure 1(right). The image window is divided into twenty pixels of equal angular extent  $\phi_p = \pi/200$ , the angular extent of each hole was about  $\pi/170$ , corresponding to a hole diameter of 1 mm positioned at a radial distance from the center of revolution of about 58 mm. The holes were positioned at a random angular distance from each other on a constant radius. The random angular distance was generated as follows

$$\theta_s = n\theta_m + \Theta \quad (15)$$

where  $\theta_s$  is the angular separation distance,  $\theta_m$  is the angular extent of the holes,  $n$  is a number between 0.1 and 6,  $\Theta$  is a uniformly distributed random variable that takes values between  $0.1\theta_m$  and  $6\theta_m$ . The term  $n\theta_m$  determines the minimum angular separation distance between two holes. A sequence of 30 holes was generated. Several measurement matrices were calculated as the patterns moved across the imaging window and their condition number was recorded. Each measurement matrix had dimensions of 20 by 20. For a given minimum separation distance not all of the calculated measurement matrices were well-conditioned. We calculated the ratio of well-conditioned measurement matrices to the total number of measurement matrices for each minimum separation distance  $n\theta_m$ . The results are shown in Figure 3.

We defined a well-conditioned matrix to have a condition number,  $\kappa$ , of less than 500. Although this is a large condition number it is less than half the average condition number of a 20 by 20 matrix with random elements. In addition the mean  $\kappa$  of the matrices with  $\kappa$  smaller than 500 was around 90 for all of the minimum separations, more than 10 times better than a matrix of random coefficients.

The plot in Figure 3 shows that the number of well-conditioned measurement matrices that can be generated given a random placement of holes is larger when the separation between adjacent holes is small, i.e. the number of holes in the imaging window is large. This result is to be expected since the variation in the patterns increases as the total perimeter length of the the holes inside the imaging window.

For the line imager we only need to have one measurement matrix so the result above might seem unnecessary given that a well-conditioned measurement matrix can be found for any value of  $n\theta_m$ , however for a two dimensional imager the result of Figure 3 is important. It demonstrates the ability of the rotating disk to implement equation 1, since many linearly independent measurement matrix rows can be generated in one rotation.

One infers from the result of Figure 3 that the number of possible well-conditioned measurement matrices can be increased by decreasing the size of the holes so that more of them can be placed in the imaging window.

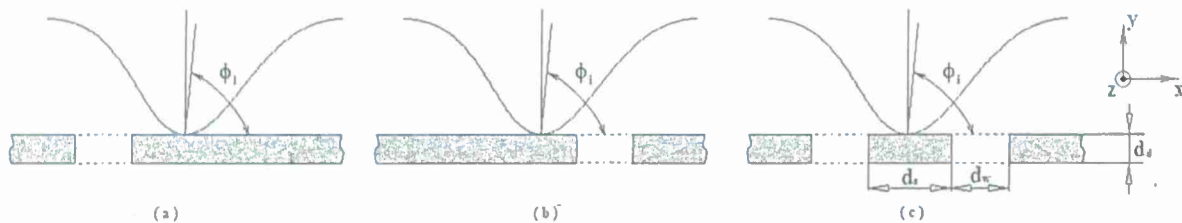


Figure 4. Structures for the simulation of the non-linearity of the mask

However, both the size of the holes and their minimum separation distance are limited by the physics of the structure. As it is shown in<sup>7</sup> and in<sup>13</sup> choosing a smaller hole diameter limits transmission through the hole and some diameters have better transmission than others. Also, as the holes are placed closer to each other, mutual coupling between the holes adversely affects the linearity of the mask assumed by equations 1 and 2. These same effects are observed for thick slits.<sup>8</sup>

The two dimensional analysis presented in Section 3 pertains to a slit geometry. Therefore, it cannot be used to obtain design parameters for our device, such as the diameter of the holes, the thickness of the disk, or the minimal separation distance for which the linearity is still preserved. We can however, at least qualitatively, observe the effect of the hole separation distance on the non-linearity of the measurement.

We simulated the linearity of a slit mask for the configuration shown in Figure 4.c. The transmitted power from the structures in Figures 4.a. and 4.b. was calculated using equation 14. The sum of the two was compared with the power transmitted from the structure in Figure 4.c. The depth of the slits  $d_d$  was set to  $2.7\lambda$ , the width of the slits  $d_w$  was set to  $2.1\lambda$ , and the separation distance  $d_s$  was varied from  $0.1\lambda$  to  $10\lambda$ . These values were chosen to match the dimensions of the experimental setup. We could have selected some other values since the two dimensional simulation is only qualitatively and not quantitatively equivalent to the physical structure with holes. The extent of the structure was  $40\lambda$ . The incident field was normally incident ( $\phi_i = \pi/2$ ) with a tapering factor  $\tau = 5\lambda$  and spatially centered at the origin.

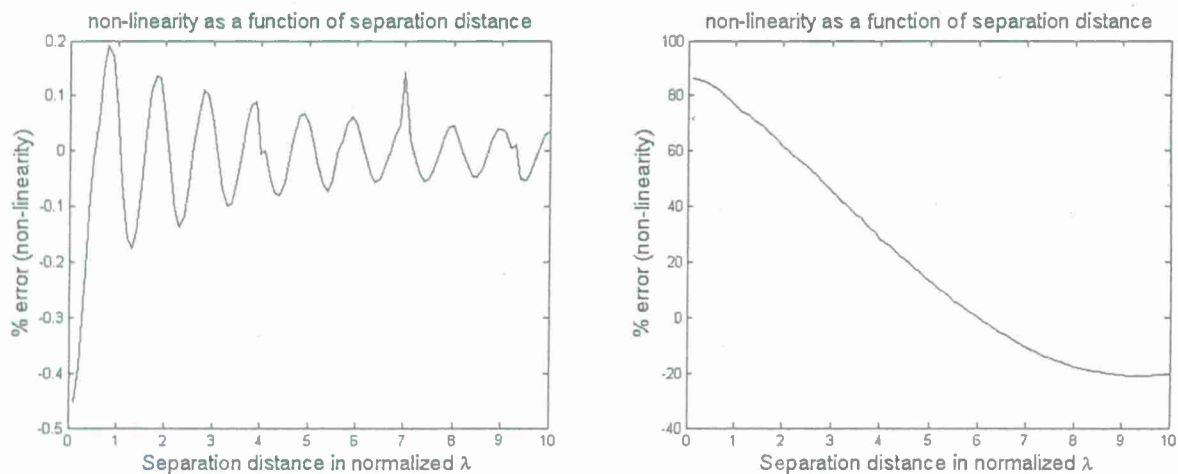


Figure 5. Results of the linearity analysis (left) when all of the transmitted power is compared; (right) when the transmitted power between 262.8 and 277.2 degrees is compared.

Figure 5 shows the results of the linearity analysis. On the right side we have plotted the percent error when the total power transmitted through the structure is collected. This is the linearity error and is computed by taking the difference of the transmitted powers and normalizing them by the sum of the powers from the structures a and b. The difference is very small with a maximum of two tenths of a percent. We notice that the

error oscillates around zero with some separations being linear (error is approximately zero) and some not. The period of oscillations is one wavelength. The cusps are numerical artifacts due to the large condition number of the MoM matrix for the given geometry of structure c. The linearity error decreases as the separation of the slits increases indicating that the slits decouple. In<sup>13</sup> the authors conclude that the coupling between holes becomes insignificant when the ratio of the separation, measured from the centers of the holes, to the radius of the holes is about six.

Figure 5(right) shows the linearity error when only the power between 262.8 and 277.2 degrees of the far field is collected. This error is extremely large but decreases as the distance between separations increases. This result is expected since the sum of the powers transmitted through structures a and b ignores the interference pattern of the two slits and the far field pattern will be a Gaussian. The power transmitted through structure c will display an interference pattern in the far field. Therefore, the transmitted powers will differ in a particular section. As the separation distance increases the zeros of the interference pattern come closer together and the power is concentrated more and more in the center of the far field, and the difference between the transmitted powers decreases.

Using the linearity results presented in Figure 5(left) we can construct a image scanning scenario where the majority of the holes are spaced such that the mask is non-linear (worst case scenario). In the following discussions we will refer to the slits in the simulation as holes. In order to have a reference to compare the reconstructions with, a single hole was placed at some distance from the others (approximately  $40\lambda$ ) so that we could simulate raster scanning. The structure length was  $40\lambda$ . The field incident on the structure was composed of two normally incident beams with tapering factor of  $\tau = 3$  and spatial centers at  $x_1 = -5\lambda$ ,  $y_1 = 0$  and  $x_2 = 3\lambda$ ,  $y_2 = 0$ .

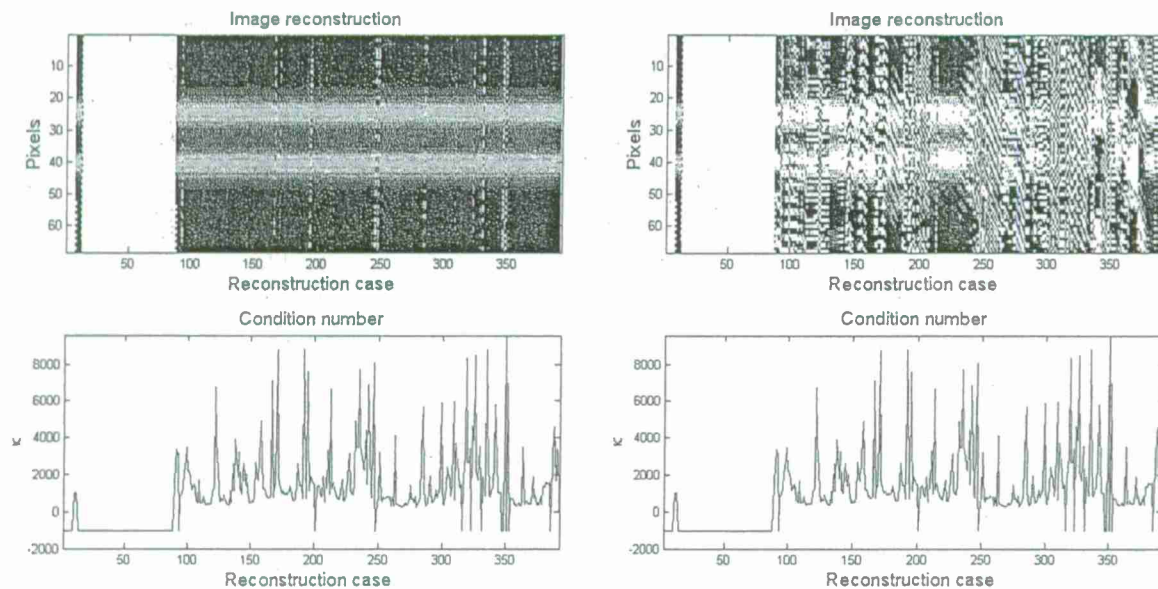


Figure 6. Results of the image reconstruction simulation using power measurements; (left) when all of the transmitted power is collected; (right) when the transmitted power between 262.8 and 277.2 degrees is collected.

The results of this simulation, when the measurement data used in the reconstruction consists of all of the transmitted power, are shown in Figure 6(left). The top image in Figure 6(left) shows the reconstructions for different measurement matrices using the corresponding measurement data. Each column of the image represents a reconstruction of the line image. To the left we see the result of the raster scan. The image is normalized by the maximum of the raster scan image. The white space that separates the raster scan images from the



reconstructed images corresponds to the part of the scan that did not contain holes, hence, the measurement matrix was singular. The bottom plot shows the condition number of the measurement matrix, the negative values correspond to condition numbers greater than  $10^4$ . The reconstruction is generally very good and the worst reconstruction cases correspond to measurement matrices with a very large condition number. The reconstruction however is not perfect and this is attributed to the non-linearity of the measurements.

If the measurement data used for the reconstruction consists only of part of the transmitted power, the reconstruction deteriorates. Figure 6(right) shows the results of this reconstruction. The measurement data consists of the transmitted power collected between 262.8 and 277.2 degrees of the far field. Some reconstructions are qualitatively similar to the raster scan. The reason for those reconstructions, although the linearity error as shown in Figure 5(right) is large, is attributed to the presence of more than two holes diffracting the incident energy. The main lobe from the interference pattern of more than two holes is more narrow than the one for two holes. Also, more of the energy is concentrated in the main lobe. Hence the collected energy represents more of the main lobe and the main lobe represents more of the total energy. Therefore, the non-linearity error is less than the error in Figure 5(right). As it is to be expected the reconstructions from the measurement matrices with larger condition number are affected the most.

## 5. EXPERIMENTAL MEASUREMENTS AND RESULTS

Using scrounged materials we built a line imager in our lab. The imager and its components are shown in Figure 7. We used the spindle motor and disk from a 5.25 inch Quantum Bigfoot hard drive. Holes were drilled on the disk at a constant radius of 58 mm. A 1 mm drill bit was used to drill 15 holes spaced at random with separation distances between 2.3 mm and 5.3 mm. Another hole was drilled about 50 mm arc away from the others. This single hole was used for raster scanning. The disk was 1.27 mm thick. We removed the top cover and cut a rectangular aperture on the back of the hard drive case so that the signal could be let into the receiver. The motor was rotated at a constant velocity of 180 revolutions per minute so that about 750 measurements are captured for one revolution. A photo-diode detector was placed in the proximity of the edge of the disk. A piece of dark tape was placed on the edge of the disk to obtain a pulse for every revolution. The pulse was used to trigger a sweep of the spectrum analyzer (Agilent SCA Spectrum Analyzer AN1996A ) so that we could register the measurements with the positions of the holes. The operating frequency of the source receiver pair was 640 GHz. The signal from the receiver was down-converted to 4.8 GHz and supplied to the spectrum analyzer. The optical system consisted of an elliptical mirror with one focus at 1 m and the other at 10 m. The line imager was placed on the 1 m side of the mirror with the receiver positioned approximately 100 mm behind the rotating disk. The target consisting of a mask in front of the receiver was placed on the side of the 10 m focus. The source was placed approximately 0.5 m behind the mask. The mask consisted of two holes cut in a piece of carpet. The image of the mask was focused on the line imager and a sweep of data was saved manually onto a flash drive from the spectrum analyzer. The saved data was post-processed.

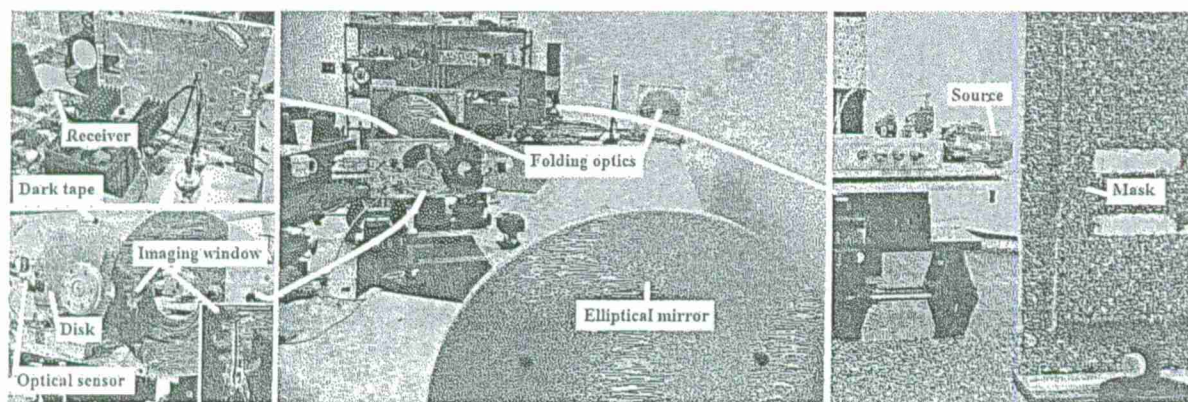


Figure 7. Picture of the line imager.



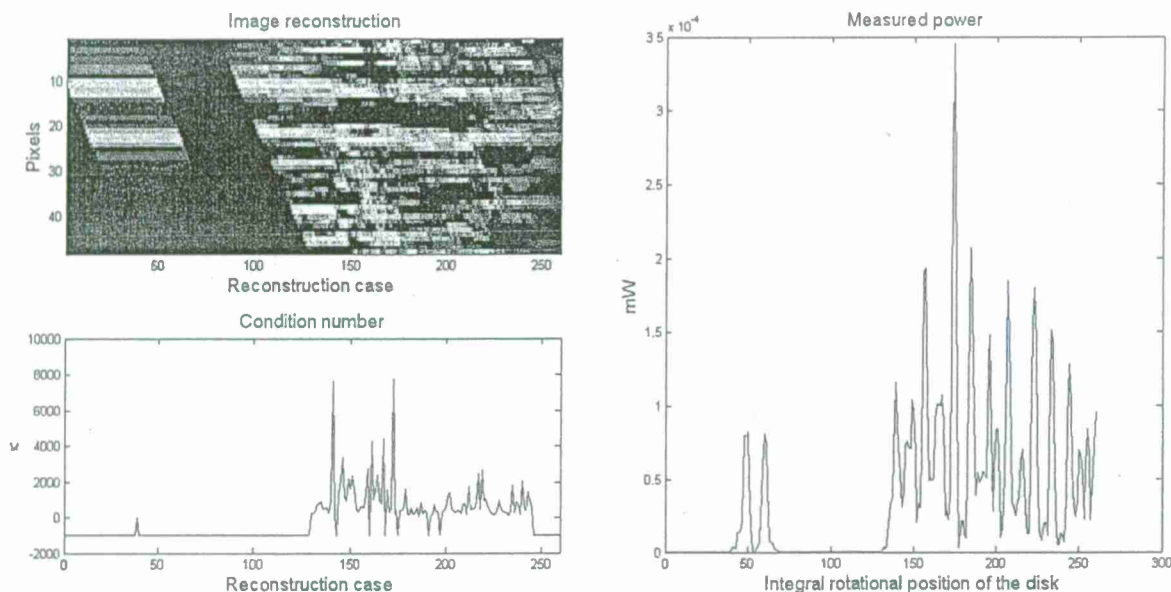


Figure 8. (Left) results of the image reconstruction using experimental data; (right) corresponding measurement data

Figure 8(left) shows the results of the reconstruction. The measurement data used for the reconstruction are shown to the right. We used regularization when calculating the inverse measurement matrix. This was necessary to obtain decent reconstruction. Just like with the simulation results shown in Figure 6, each column of the image on the top (left) figure represents a reconstruction of the line image. The partial reconstructions that give the appearance of a slant are due to the use of regularization.

The quality of the reconstruction can be attributed to a couple of factors. Only part of the power is collected therefore the reconstruction is noisy. These results agree with the simulations presented in Section 4. Another source of error was the wobbling of the disk, although small. Yet another source of error was the lack of accuracy in the knowledge of the exact positions of the holes on the disk, leading to inaccurate measurement matrices. The holes on the disk were marked at the desired locations and drilled on a 12 inch drill press while the disk was held on the bench by hand. Needless to say this was not a precise manufacturing process, and it is a wonder that we can reconstruct the image at all.

It was observed (results not shown here) that the quality of the reconstruction improved when the diameter of the holes was increased to 2 mm. This can be attributed to the increased signal (more power was let through the holes) and to the fact that the larger holes diffract less than the small ones, so the power was directed more towards the receiver.

## 6. EXTENSION TO TWO DIMENSIONS

Figure 9 shows a conceptual sketch of the spatially selective mask device for imaging in two dimensions. Equation 1 is valid for both the one-dimensional and two-dimensional imaging problems. In the line image setup the arranging of the measurement matrix row elements was obvious. For the two dimensional image the two dimensional array of pixels is linearized; each row of the array is concatenated to the end of the previous row. Just like for the line imager a full set of measurements can be collected during one full rotation of the disk. Therefore, if the disk is rotated at a constant rate of 1800 rotations per minute the imager will produce images at a video rates of 30 frames per second.

An appropriate pixel block for this implementation would be a square. In that case the entries of the measurement matrix can be calculated by the following method. The imaging window is divided into conceptual

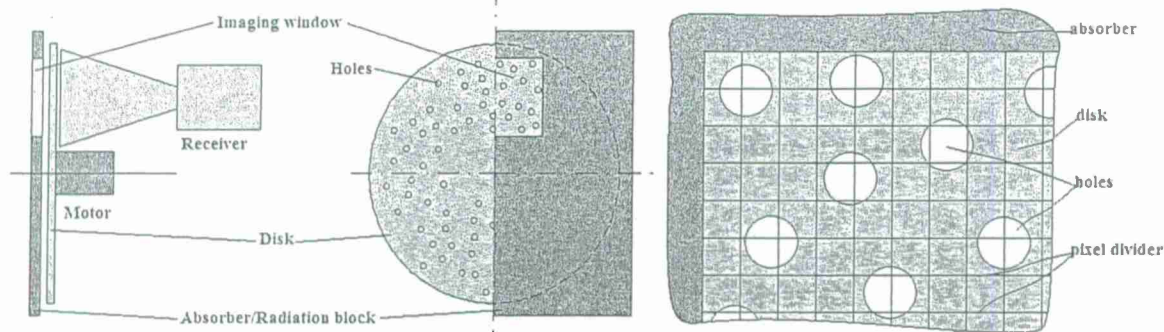


Figure 9. (Left) Conceptual sketch of the two dimensional imaging device, (right) pixel block divisions

square blocks as shown in Figure 9(right), each corresponding to an image pixel. Each pattern of holes in the imaging window corresponds to one row of the measurement matrix. We obtain different patterns at different rotational positions of the disk. For each pixel a Monte Carlo integration method is used to determine the area of intercept of that pixel with the holes inside the imaging window. The ratio of the area of intercept to the area of the pixel is the entry on the row of the measurement matrix corresponding to that pattern and pixel.

## 7. CONCLUSIONS

We have shown simulation and experimental results supporting a method of image space scanning with high modulation levels, high scanning rates, low mechanical complexity, and low cost. We observed that randomly placing the holes close to each other and having many of them in the imaging window, produces more well-conditioned measurement matrices than does placing them far and having less of them in the imaging window. However, as the holes come closer to each other non-linearity effects are observed. Also the transmission through the holes is limited by the waveguide-like behavior. Simulations of linear measurements on a image were performed using a two dimensional electromagnetic analysis approximating the holes with infinite slits. Although the electromagnetic analysis could not be used to design the device it satisfactorily explained the experimental observations qualitatively. From the results of Figures 6 we conclude that for the best performance we need to collect all of the energy that is transmitted through the holes. The same image formation methodology used for the line imager can be extrapolated to a two-dimensional imager and we have introduced the required adaptations to do so.

## REFERENCES

1. D. T. Petkie, C. Casto, F. C. D. Lucia, S. R. Murrill, B. Redman, R. L. Espinola, C. C. Franck, E. L. Jacobs, S. T. Griffin, C. E. Halford, J. Reynolds, S. O'Brien, and D. Tofsted, "Active and passive imaging in the thz spectral region: phenomenology, dynamic range, modes, and illumination," *J. Opt. Soc. Am. B* **25**(9), pp. 1523-1531, 2008.
2. R. Appleby and H. Wallace, "Standoff detection of weapons and contraband in the 100 ghz to 1 thz region," *Antennas and Propagation, IEEE Transactions on* **55**, pp. 2944-2956, nov. 2007.
3. H. Jacobs, J. Schumacher, and D. Register, "Multiple aperture imaging of millimeter sources via image-plane interferometry," *Electron Devices, IEEE Transactions on*, pp. 2967-2970, July 2007.
4. C. A. Schuetz, M. S. Mirotznik, S. Shi, G. J. Schneider, J. Murakowski, and D. W. Prather, "Applications of optical upconversion to sparse aperture millimeter-wave imaging," in *Society of Photo-Optical Instrumentation Engineers (SPIE) Conference Series*, D. H. Titterton, S. M. Kirkpatrick, R. Stoian, R. Appleby, J. M. Chamberlain, & K. A. Krapels, ed., Presented at the *Society of Photo-Optical Instrumentation Engineers (SPIE) Conference* **5989**, pp. 396-407, Nov. 2005.
5. W. L. Chan, H.-T. Chen, A. J. Taylor, I. Brener, M. J. Cich, and D. M. Mittleman, "A spatial light modulator for terahertz beams," *Applied Physics Letters* **94**(21), p. 213511, 2009.

6. J. Zheng and E. L. Jacobs, "Video compressive sensing using spatial domain sparsity," *Optical Engineering* 48(8), p. 087006, 2009.
7. A. Roberts, "Electromagnetic theory of diffraction by a circular aperture in a thick, perfectly conducting screen," *J. Opt. Soc. Am. A* 4(10), pp. 1970-1983, 1987.
8. K. Hongo and G. Ishii, "Diffraction of an electromagnetic plane wave by a thick slit," *Antennas and Propagation, IEEE Transactions on* 26, pp. 494 - 499, may 1978.
9. O. Furxhi and E. L. Jacobs, "Design and analysis of a spatially selective mirror for submillimeter-wave imaging," *Passive Millimeter-Wave Imaging Technology XII* 7309(1), p. 73090K, SPIE, 2009.
10. E. I. Thorsos, "The validity of the kirchhoff approximation for rough surface scattering using a gaussian roughness spectrum," *The Journal of the Acoustical Society of America* 83(1), pp. 78-92, 1988.
11. E. Jacobs and R. Lang, "Scattering, transmission, and absorption by a rough resistive sheet - e polarization," *Antennas and Propagation, IEEE Transactions on* 50, pp. 1567-1576, Nov 2002.
12. D. S. Jones, *Acoustic and Electromagnetic Waves*, Oxford University Press, New York, first ed., 1986.
13. Y. Park and H. Eom, "Electromagnetic transmission through multiple circular apertures in a thick conducting plane," *Antennas and Propagation, IEEE Transactions on* 52, pp. 1049 - 1055, april 2004.



## **Appendix B. Unpublished papers in support of this contract**

Copies of three unpublished papers produced as part of this cooperative agreement are provided following this page.

## Equation Chapter 1 Section 1 Information Theoretic Model of a Profiling Sensor

Carl Halford, Professor Emeritus, Department of Electrical and Computer Engineering, University of Memphis, Memphis, TN 38152

Ronald B. Sartain, Army Research Laboratory, Adelphi, MD

### Abstract

The performance of a binary output beam break sensor is characterized by its information rate per pixel. A physics based model utilizes target and noise spectra to establish the channel capacity and the realizable rate. This model enables the determination of a system of sensors performance metric, suitable for optimizing system performance. A method of optimizing sensor design within the system of sensors is discussed. Numerical results from the model illustrate the process for a beam break sensor such as one used on garage door openers. Also, the numerical results coupled with classification performance data may quantify the value of information for such a sensor, as discussed in the paper. An uncertainty analysis is presented for a beam break sensor used to estimate a target's height to width ratio, useful for human/other classification. The uncertainty analysis suggests some quantitative method of determining the minimum number of pixels desired.

### Introduction

Beam break sensors are an example of a class of sensors that provide profile information about a target [Russomanno, 2010]. Such profiling sensors may provide sufficient information for some applications or they may be part of a system of sensors. It is important for optimizing performance of a system of sensors that a system performance metric be available. Such a metric enables system performance optimization for many aspects of the system. Examples include sensor selection from a suite of available sensors, sensor design within given types of sensors for the network or algorithm choices for automatic processing of some sensor outputs.

In general, systems of sensors are likely to utilize automated processing at a variety of levels. Such processing might be in the form of image enhancement, image fusion for human observers or classifiers that provide cues for human observers. This paper on profiling sensors considers the use of a classifier but does not consider image fusion or enhancement.

Two metrics are often used for imaging sensors [Driggers, 1998]. NIIRS (National Imagery Information Rating Scale) is often used in surveillance applications, and the Targeting Task Performance metric is often used for tactical imagers. An information theoretic metric (information rate in bits/pixel) is also commonly used. At their foundations lie the same sensor parameters, resolution and signal to noise ratio. All are also active areas for research [Irvine, 2007, Westover, 2008, Vollmerhausen, 2006]. Each

has its own domain of applicability, with some overlap. For the beam break sensor presented here, we use information rate as the metric for modeling the beam break profiling sensor. One reason is that information rate does not implicitly incorporate a model for the human observer. However, some researchers have modeled human observer performance in terms of information rate. This flexibility allows one to model algorithms and human observers within a system. Furthermore, the point of view is not from above (as with NIIRS) and the task is not quite in the realm of detection/recognition/identification (as with Targeting Task Performance metric). So among existing metrics information rate is the metric immediately applicable to profiling sensors as part of a system. Imaging sensors and other types of sensor can also be modeled using information rate as a metric within the information theoretic framework [Huck, 1996]. This facilitates system level modeling by utilizing a common metric. Also the end numerical results in bits per pixel have a more general understanding than most other metrics.

In summary the work presented in this paper represents a significant step in the direction of modeling a system of sensors that includes sensors of various types. These types are likely to include an imaging sensor supplemented perhaps by profiling, radar, seismic and acoustic sensors as well as intelligence information. We expect the system of sensors to include automated processing of sensor output as well as human observers using imagery. Specifically the paper presents the modeling process for the information rate of a binary output beam break profiling sensor. Numerical results illustrate the model. Additional discussions show how the results are important to sensor system modeling and optimization.

### **Binary Output Beam Break Sensor**

As with imaging sensors there are many configurations of profiling sensors. Each has its own unique characteristics as well as sharing characteristics with a general profiling sensor. The binary output beam break sensor is chosen as being representative of the broader class of profiling sensors. The model presented here captures the more general aspects of profiling sensors. The model has sufficient fidelity, accuracy and complexity to illustrate the behavior of the sensor within a system of sensors. This desire for a system level model leads to an information theoretic model. Any sensor can be modeled from that viewpoint, making information rate a common metric for any sensor in the network.

A binary output beam break sensor has a two state output indicating that a beam is blocked or not blocked. It was proposed as a low cost sensor that could distinguish humans from animals by assessing their profiles. Several other versions of profiling sensors have been built, generally passive versions. The two state profiles can also result from applying a threshold to detector outputs with greater bit depths. However, the original beam break sensor was inspired by the common garage door safety detector, and the notional sensor modeled here is that type of profiling sensor. It consists of a transmitter module and a detector module whose output is either high or low. We arbitrarily choose the presence of the target to be a high state and the absence of the target to be the low state.

In its simplest implementation the transmitter/detector module pair is replicated in the vertical direction, creating a linear array of detectors. Other deployments are also possible. The binary detector outputs are sampled in time. The target must move through the beams to create its profile. Targets are assumed to move in the horizontal direction, breaking the separate beams as the target passes through



the sensor. The temporal sampling coupled with the spatial sampling in the vertical direction produces data that is easily interpreted as a two dimensional target profile.

Each detector and transmitter has its own field of view. Figure 1 depicts a general situation where the detector and transmitter fields of view differ. For our example sensor the two are the same. The figure shows a slice of the three dimensional field of view cones. That means the vertical arrows are slices of an edge. For discussion we choose to think of Figure 1 as a top view. That means a vertical edge is being moved horizontally into the field of view (at one of three locations in Figure 1.) For an analog system the detector response diminishes as soon as the edge reduces the received radiation. Figure 2 shows a simulated analog edge response with added noise. It also demonstrates the one-to-one relationship between edge position within the field of view and the analog detector output. A binary output sensor does not show any change until the moving edge has blocked a threshold amount of radiation. Fifty percent blockage is a convenient threshold since the output change occurs with the edge at or near the optical axis. Therefore, the binary output toggles as the edge reaches the optical axis. Figure 1 illustrates that the amount of edge movement within the analog edge response varies with the edge location between the transmitter and the detector. It also shows that the maximum field of view has an upper bound of the larger angular field of view times half the separation distance between transmitter and receiver.

The geometrical complications are minimized in our example system which has equal detector and transmitter fields of view. And we choose to locate the target edge midway between the transmitter and receiver. A fifty percent threshold is also assumed. These conditions match the experimental conditions for the garage door opener safety switch used to obtain numerical results.

In an array of such transmitter/detector pairs, the fields of view of adjacent pairs may overlap. This overlap increases the transmitted power seen by any particular detector. The additional power from other transmitters varies with the configuration chosen for the array. Detectors near the middle of a linear vertical array (our notional sensor array) receive extra optical radiation from transmitters above and below. Those detectors near the top or bottom receive radiation that is not symmetrical in the vertical direction. Regardless of the total received power, the binary output sensor toggles when the power is reduced by fifty percent of its unblocked value. Therefore our notional model assumes the detector/transmitter pairs are isolated from the other pairs that form the profiling sensor array.

The sensor output can be used as input to an automated classification algorithm [Chari, 2008.] However, viewing it in an image format provides insight to typical uses. Figure 3 shows three profile images for illustration purposes and to help understand the validity of assumptions made in the analytical modeling process that follows.

### **Model for Binary Output Beam Break Sensor**

The discussion above suggests the following characteristics for the binary output sensor and targets in our model. Sampling in the vertical direction is achieved by separate transmitter/detector pairs. Sampling in the horizontal direction occurs by temporally sampling the binary output state of the detectors. Block targets move only horizontally while passing the vertical line of sensors. The detectors

change states when the block obscures half of the optical power being received by the detectors with no obscuration. Targets too small to block half of the received radiation will not be detected by the profiling sensor and result in no information from the sensor. We arbitrarily choose the blocked state to be binary output 1 and the unblocked state to be 0. The threshold response changes the analog edge response of Figure 2 to a sharp transition from 0 to 1 at the optical axis (0.5 position in Figure 2).

These properties imply a two dimensional output from the array, a spatial output in the vertical direction and a temporal output. Instead of using spatial/temporal pixels, the horizontal motion of the target coupled with the temporal sampling is modeled as a spatial pixel. Pixel size in the horizontal direction is determined by the sample rate and the speed of the target. In effect the model equivalently locates a stationary target within a horizontal field of view. The equivalent horizontal field of view is determined by the speed of the target, the sample rate, and the period of time being considered. The period is conveniently chosen to include both edges of the target. Most often this sensor is used for automated human/other classification. Therefore, numerical examples will draw from this scenario.

### Information Rate Equivalents for Sensors

Information rate as we use the term does not include the actual communication channel used to transmit information from the sensor to the user. Models for the communication channel are highly developed and therefore not addressed here. Our interest is in the sensor's effect on the information in a spatial scene as that spatial information is converted from optical radiation to an electronic signal. Consequently, spatial frequency domain techniques provide the tools for characterizing the information capabilities of imaging sensors and profiling sensors. The two dimensional character of the information is modeled by assuming separable dimensions.

The major factors in information transfer by an imaging sensor include blur, noise and dynamic range. In addition to imaging blur, blur is sometimes used to model atmospheric effects such as turbulence. Blur is also intimately linked to resolution which leads to the critical parameter of pixels on the target. Noise arises from a number of sources, but includes detector noise, temporal quantization noise, spatial sampling noise and can include speckle for laser illuminated scenes. Noise at the system level is affected by temporal factors such as frame rate/integration time. Dynamic range can be affected by blur, but is also impacted by pedestal removal and automatic gain control. Many modern imaging sensors use sophisticated algorithms to process images and usually include automated control of the dynamic range. These factors must be included in our model for the binary output beam bread sensor. Some are treated by our assumptions that establish the domain of applicability for the information theoretic model. For example we assume the noise to be additive white noise.

Traditional imaging sensors with focal plane arrays for detectors are well modeled by the information rate metric [Huck, 1996]. Both the information rate and channel capacity arise from the following fundamental expression for the information rate. The expressions here are for a single sided bandwidth  $B$ .

$$H = \iint_B \log \frac{S_{\text{tgt}}(\xi, \eta)}{N(\xi, \eta)} d\xi d\eta \quad (1.1)$$

$H$  is the average information rate in bits for each pixel (with the base 2 logarithm).  $S_{tgt}(\xi, \eta)$  is the power spectral density of the region of interest or target as displayed (or in the image plane) including noise and sensor degradations.  $N(\xi, \eta)$  is the power spectral density of the "noise." Noise represents the threshold level of the signal and can be treated as this more general term. For example, if the above equation is applied with human observers, the denominator term might become the contrast threshold function rather than just detector or system noise.  $\xi, \eta$  are the spatial frequency variables in appropriate units such as cycles per pixel.  $B$  represents the two dimensional bandwidth. For digital imagery the bandwidth is limited by the half sample frequency (0.5 cycles/pixel in each dimension.) Note that for separable functions (horizontal and vertical directions) the total information rate is the sum of the rates for each dimension.

The channel capacity results from the information rate under ideal assumptions. These assumptions are never met by real images since the target spectrum is assumed to be constant across the bandwidth. Such a spectrum is white noise to an observer with each pixel being uncorrelated with the adjacent pixels. A white spectrum might be approached by an ensemble of images or targets.  $S$  is assumed to consist of a signal spectrum with additive noise and no sensor degradation. Under the channel capacity assumptions, the upper bound of  $H$  becomes the following.

$$C = B \log(1 + SNR^2) \quad (1.2)$$

$C$  is the channel capacity and  $SNR$  is the signal to noise ratio. The square of  $SNR$  is the power signal to noise ratio. In this case the term signal does not include the additive noise. The one accounts for the additive noise. This equation implies the physical information limit for the system is the number of resolvable levels of signal (signal power divided by noise power) times the bandwidth of the channel. The encoding of the information is ideal and  $C$  is in bits/pixel.

For the binary output beam break sensor it is convenient to think of locating an edge in one dimension. The sensor output encodes the time that the edge passes the detector. From an information standpoint this action is equivalent to locating the edge in space. Refer to Figure 2 to translate location into detector output. The threshold results in digital output with an edge at the optical axis, but that location is made uncertain by the noise. Since the detector binary output toggles at the midpoint of the analog edge response, the signal level corresponds to half of the beam width. The channel capacity represents the limit to which we can know the location within the analog edge response. Keep in mind that the channel capacity assumes a white spectrum which is equivalent to locating a multitude of edges within the analog edge response. No location information results when the detector output remains fixed in either state, blocked or unblocked. Edge location information only results from a transition. Channel capacity then represents the number of bits required to encode the maximum number of different positions within the analog edge response that the sensor can isolate based on signal level and noise level.

### Information Rate Model for Binary Output Beam Break Sensor

The information theoretic model is based on Eqn. 1. As suggested above we choose to represent the horizontal direction as spatial pixels. The target speed times the sample period determines the size of

the pixels. Therefore Eq. 1 is directly applicable to our beam break sensor. The linear systems model requires some assumptions regarding the threshold process which is not linear. For our region of interest, we choose the target itself with only enough background pixels to model the transitions from unblocked to blocked. Our target is a rectangular block that moves in the horizontal direction only. While an edge target is interesting, it results in a spectrum that violates assumptions inherent in Eq. 1, namely having a form that has a defined logarithm. One could blur the ideal edge, but the block shape more nearly matches the typical applications of classification based on a profile. With these thoughts in mind, the information rate metric for the horizontal direction is given by the following.

$$H_x = \int_0^{0.5} \log_2 \left\{ \frac{[TGT_x^2(\xi) + N_x^2(\xi)] MTF_x^2(\xi)}{N_x^2(\xi)} \right\} d\xi \quad (1.3)$$

The limits on the integral are in cycles per pixel where the upper limit is the half sample frequency. Consequently, a similar expression is also used for  $H_y$ , the information rate metric for the vertical direction. The separable system assumption means the total information rate is the sum of the two directional rates. In practice the pixel size is rarely the same in the two directions, but the limits are the same in cycles per pixel.  $TGT$  is the target spectrum and the square represents the power density. For an ideal block target, the spectrum is the familiar *sinc* function. The same convention is used for the noise spectrum  $N$  and  $MTF$  represents the sensor degradations such as blur.

The threshold process model is incorporated through the following approach. Figure 2 represents the analog output edge response and shows the typical blur. However, the digital output with a threshold at fifty per cent blocked is a sudden transition, say from 0 unblocked to 1 for blocked condition. As a result the blur does not impact the digital output. Therefore, if one is using an automated classification algorithm, the sensor degradation function is set to one across the spectrum. If one converts the digital output to analog, a reconstruction blur occurs. But the blur is mostly within a single sample period except for some ringing. Its apparent from the example system discussed below that the threshold process significantly reduces the effect of blur, even for analog outputs.

## Example Beam Break Sensor

Eqn. 3 provides a general model for determining the information rate metric for a binary output beam break sensor. This section applies Eqn. 3 to an example system. While the chosen system is typical, the ensemble of possible sensors, detector transmitter separation, etc. is large. However, the purpose of illustrating the process is well served by a numerical example.

Experiments to determine sensor parameters include a repeated trials approach. An edge target (tall, wide block) is moved through the sensor repeatedly and the position that changes the binary state of the sensor output is recorded. The standard deviation of the edge location that toggles the sensor is the edge location uncertainty. For vertical uncertainty the vertical location of the block is varied. The variance of the edge location that toggles an adjacent detector is the vertical edge location uncertainty.



Actual measurements on a garage door safety sensor confirm the advantages of a binary output device in reducing edge location uncertainty. This particular sensor uses 1.8 cm diameter apertures for transmitter and detector/receiver, which are spaced 2.7 m apart. The threshold level is approximately 50%, an optimum choice for detection at the optical axis independent of target location between the transmitter and receiver. Both the field of view of the detector and the beam width from the transmitter are approximately 1 m full width at 2.7 m distance. The uncertainty in edge location is 0.5 mm ( $\pm 0.2$  mm). The symmetry of the device means this uncertainty is the same for both horizontal and vertical directions. The edge location lies on the optical axis, within the uncertainty of the determining the position of the optical axis ( $\pm 1$  mm).

Additional uncertainty arises from the temporal sampling of a moving target (horizontal) and the spatial sampling from using an array of separate detectors (vertical.) For the horizontal direction assume a 1 m/sec speed. This is a reasonable speed for walking and it is also easy to scale to different speeds. Sampling at one thousand samples per second yields an equivalent spatial pixel size of 1 mm. Assuming a uniform distribution of edge location about any given sample, the variance is then 1 mm squared divided by twelve. The variances add since sampling uncertainty is independent of the edge location variance.

Sampling in the vertical direction is accomplished by different sensors, so pixel size is the physical distance between the sensors. We assume a typical value of 100 mm as the sample spacing. Therefore, the variance is  $100\text{ cm}^2$  divided by twelve. The sampling uncertainty in the vertical direction is also independent of the edge location uncertainty. The variances add, but the sampling uncertainty is the dominant uncertainty for the vertical direction.

Eqn. 2 for the channel capacity can now be used for the example sensor. We assume a linear relationship between location of the edge and the analog detector output (see Figure 2). One can then transform edge location into fractional signal level. In Eqns. 2 and 3 all powers occur in ratios. Therefore, fractional signal level (edge location) is sufficient information for calculating channel capacity and realizable information rates. The beam size/detector field of view at the midpoint location is 500 mm. The detector output toggles at with the edge at 250 mm from the beam edge, that is, it toggles at optical axis. Therefore the signal level is half of the unblocked radiation level, or 0.5 fractional signal level. The noise is the standard deviation of the measured values from the previous paragraphs. For the horizontal direction, the noise is 0.315 mm ( $6.3 \times 10^{-4}$  fractional signal). Eqn. 2 then yields 9.6 bits per pixel for the channel capacity.

The channel capacity for the vertical direction is obtained from the same signal level, but an increased noise from the larger sample spacing. The signal level (in position units) is 250 mm while the noise is 28.9 mm (100 mm detector separation). This yields a channel capacity of 3.1 bits per pixel. With a separable model the two add for a total channel capacity of 12.7 bits per pixel.

Eqn. 3 for the realizable rate is applied through selecting a target and including the sensor degradation if appropriate. The channel capacity is based on a white spectrum which is unrealistic for a profiling sensor. Consequently, we choose a block with typical size (700 mm wide by 1400 mm high) for

human/other animals to illustrate the model and obtain a typical realizable rate. We first consider a digital output and set the MTF to 1 for all spatial frequencies. The integration indicated in Eqn. 3 is carried out numerically and results in a realizable rate of 0.9 bits per pixel for the horizontal direction and 0.5 bits per pixel for the vertical direction.

Sensor degradations are included through the *MTF* function. To illustrate we now consider an analog output and use a reconstruction blur for the degradation. The blur is assumed to be only between the digital edge (pixel value 1) and the nearest off pixel (value 0.) The fidelity of the reconstruction improves only slightly as the number of pixels on the target increase from a few to several hundred. With our numerical assumptions we have 500 pixels on the target in the horizontal direction and 14 samples in the vertical direction. We use the following Gaussian function fit to the reconstructed analog signal between the two pixels defining the edge.

$$MTF_x(\xi) = \exp\left(-2\pi^2 \sigma_{blurx}^2 \xi^2\right) \quad (1.4)$$

The notation is for the horizontal direction and a similar function is used for the vertical direction. The fit determines the best value of  $\sigma_{blurx}$ . To within the accuracy of measured values, the best fit is the pixel separation divided by 2.5, for either vertical or horizontal directions. Figures 4 and 5 illustrate the signal spectrum and the  $MTF^2$  for the horizontal and vertical directions respectively. The target plus noise spectra have no zeros at the minima, seen more clearly in Figure 5. Applying the degradation does reduce the SNR below 1 near some of the minima. Those regions are excluded from the integration since the logarithm is undefined there. The resulting realizable rates with this reconstruction blur degradation are 0.7 bits per pixel in the horizontal direction and 0.4 bits per pixel in the vertical direction.

The average information rate coupled with the number of pixels on the target provides an estimate of the information content. The minimum number of pixels for successful classification will be discussed below.

### Additional Results of Interest from the Information Theoretic Model

Quantifying the value of information might be accomplished by the process described next. Consider a two sensor system that includes a highly capable intelligence/surveillance/reconnaissance (ISR) imager. The second sensor is much more limited, perhaps a profiling sensor as modeled above. We choose to think of the second sensor as augmenting the information from the ISR imager and we attempt to quantify the value of the additional information.

Our notional ISR sensor has one million pixels and a ground sample distance of 0.5 meters. A single static image can be analyzed for the average information rate within a region of interest that includes the profiling sensor. With just this single static image, it is difficult to even locate a human in the image. However, suppose the profiling sensor has classified an object as a human just prior to the acquisition of the ISR image. This additional information perhaps enables one to classify a blob of pixels as a human.

The information theoretic model presented here estimates the information rate for a profiling sensor. Such sensors have provided excellent classification accuracy in hundreds of examples of human/animal data. Consequently, the data rate coupled with the number of pixels required provides an estimate of the information value of the added classification result from the profiling sensor. This increased information could also be modeled as an increased ISR resolution, perhaps an equivalent ground sample distance of 0.1 meters within that small region of interest. This approach to establishing the value of information can be further developed, as discussed in the conclusion as a future effort. Of course if the ISR sensor video stream is available, one can detect a moving object the size of a human without additional sensors. However, the typical ISR sensor view point is from above, making human/other classification somewhat harder. The example is chosen to illustrate the value of added information from additional sensors, not to discuss sensor selection.

The information rate from the information theoretic model is given as an average per pixel, so one must consider how many pixels are required to execute a task such as classification. One approach to establishing the number of pixels required for classification is to use uncertainty analysis. The primary feature for human/animal classification is the height to width ratio. This means the number of pixels required can be estimated from the required accuracy of measuring the height and width. One uses the same "noise" estimates to get the standard deviation used in uncertainty discussions. Our example system will be used for the numerical results. Our goal is uncertainty of the ratio of height to width, not the individual parameters of height and width.

In equation form, the following equation describes the uncertainty for the height to width ratio. First order uncertainty of the ratio adds the fractional uncertainties of the height and width.

$$\frac{h + \Delta h}{w + \Delta w} = \left( \frac{h}{w} \right) \left( \frac{1 + \frac{\Delta h}{h}}{1 + \frac{\Delta w}{w}} \right) = \left( \frac{h}{w} \right) \left( 1 + \frac{\Delta h}{h} + \frac{\Delta w}{w} + H.O.T. \right) \quad (1.5)$$

$h$  and  $w$  are height and width,  $\Delta h$  and  $\Delta w$  are the uncertainties, and *H.O.T.* denotes terms of second order and higher in the fractional uncertainties  $\Delta h/h$  and  $\Delta w/w$ . A minus sign in front of the width fractional uncertainty has been replaced by a plus sign, appropriate for combining uncertainties. Two edges must be located to measure height and width although the ground might form one edge for height. For numerical purposes we assume the uncertainty for each edge location measurement is independent of the uncertainty for any other edge location measurement.

Our example system provides an abundance of samples in the horizontal direction so the uncertainty is dominated by the vertical uncertainty where  $\Delta h$  is 40.8 mm (two edges). For some insight the minimum size required to block 50% of the radiation is somewhat less than 150 mm (136 mm by analysis.) Four pixels (400 mm) of height reduces the vertical fractional uncertainty to approximately 0.1 or 10%. The minimum number of pixels in the horizontal direction is overdesigned in the example system. Therefore for estimating the minimum number of pixels, we create a notional system with a horizontal pixel spacing of 100 mm. This redesigned pixel size will have the same horizontal uncertainty as the vertical

direction. So it is suggested that one use four pixels minimum, corresponding to a 400 mm target size. Such a design accommodates height to width ratios with a maximum of 4 and a minimum of  $\frac{1}{4}$ . This 4 x 4 pattern yields 16 pixels total and a reasonable uncertainty. Few moving objects are square, so fewer than 16 pixels might suffice. A 3x3 pattern is obtained using Johnson's criteria for recognition [Johnson, 1958] with Holst's modification for low clutter [Holst, 1995]. The typical sized block target used in this effort produces 14 x 7 pixels with 100 mm horizontal pixels or approximately 100 pixels. The system used for data collections is intentionally overdesigned to accomplish studies that classify more than two classes, e.g. humans, animals, humans with backpacks or humans with weapons.

These considerations, uncertainty analysis and minimum target sizes that are detected, suggest that 16 pixels or fewer may be sufficient. However, the pixels must be sized such that approximately 4 pixels are across each dimension of the target. The edges are the significant feature. Adding many more pixels that are highly correlated does not add much information. The number of pixels on target has a slightly different connotation with profiling sensors as contrasted with imaging sensors. More pixels in an imaging system may provide useful intra-target information. In a profile there is essentially no intra-target information. Obviously more pixels and smaller pixels can provide more detail in the outline of the target, even in the profiling sensor [Chari, 2010].

## Conclusion and Future Effort

This paper describes a process for obtaining the information rate per pixel of a profiling sensor. In effect, a profiling sensor provides information at transitions. For example, the binary output beam break sensor makes a transition from 0 to 1 or from 1 to 0. The location of these transitions represents the information content so a finer sampling produces more information, but the sampling is limited by the noise level. A block target is used to illustrate the process and numerical results are given.

One motivation for developing the information theoretic model is to enable the optimization of sensor design within a system of sensors. One approach to the optimization is suggested by the convex optimization technique [Joshi, 2009]. One considers a new design to simply be an additional sensor available to be "selected" for use by the system. Variations of a particular parameter create new sensors that are possibly available. The optimization technique then chooses from all the possible designs being considered as a sensor selection process. Information rate is envisioned as the metric that ties all of the sensors together in a system. This enables one to "design" a particular sensor so that the system level performance is optimum, at least by some chosen criterion.

Future efforts include expanding the model to include passive profiling sensors. This category includes different approaches, one of which is in effect an image processing technique. Consequently, the information throughput for an image processing algorithm can result from the modeling effort. Other approaches utilize linear arrays. As shown here the moving targets are scanning themselves when they pass through the field of view of the linear array. Therefore, the process presented in this paper should be directly applicable to this particular type of passive sensor.

In some sense the numerical results coupled with classification algorithm performance may provide an estimate of the value of information for this classification task. This points the way to creating a table of



tasks with the estimated value of information associated with successful completion of the task. One could use the table to estimate the value of information not directly in the table. The user either finds an equivalent task in the table or "brackets" the task by finding a task slightly easier and another slightly harder from the table. The NIIRS metric is often structured this way. One could develop such a table by utilizing human perception studies, both existing results and new ones conducted for this purpose.

## References

- S. Joshi and S. Boyd, "Sensor selection via complex optimization," *IEEE Trans. Signal Processing*, 57, pp. 451-462, 2009.
- F.O. Huck, C.L. Fales and Z. Rahman, "An information theory of visual communication," *Phil. Trans.: Math., Phys. & Engr. Sci.*, 354, pp. 2193-2248, 1996.
- R. Driggers, P. Cox, J. Lechtenauer, R. Vollmerhausen and D. Scribner, "Targeting and intelligence electro-optical recognition modeling: a juxtaposition of the probabilities of discrimination and the general image quality equation," *Optical Engineering*, 37, pp. 789 – 797, 1998.
- J. Irvine, A. Aviles, D. Cannon, C. Fennimore, D. Haverkamp, J. Israel, G. O'Brian and J. Roberts, "Developing an interpretability scale for motion imagery," *Optical Engineering*, 46, pp. 117401-1 – 12, 2007.
- M.B. Westover and J.A. O'Sullivan, "Achievable rates for pattern recognition," *IEEE Trans. Information Theory*, 54, pp. 299-320, 2008.
- D.J. Russomanno, S. Chari, E. Jacobs and C. Halford "Near-IR Sparse Detector Sensor for Intelligent Electronic Fence Applications," *IEEE Sensors Journal*, 10, Number 6, pp. 1106-1107, 2010.
- S.K. Chari, C.E. Halford and E.L. Jacobs, "Human target identification and automated shape based target recognition algorithms using target silhouettes," *SPIE Proceedings*, 6941, Orlando, FL., April, 2008.
- S. Chari, F.A. Smith, R.B. Sartain, C.E. Halford and J.M. Brooks, "Range and velocity independent classification of humans and animals using a profiling sensor," *SPIE Proceedings*, 7694, Orlando, Florida, April, 2010.
- R. H. Vollmerhausen and T. Bui, "Using a targeting metric to predict the utility of an EO imager as a pilotage aid," *SPIE Proceedings*, 6207, Orlando, Florida, May, 2006.

J. Johnson, "Analysis of image forming systems," *Proc. of the Image Intensifier Symposium*, pp.249-273, U.S. Army Research and Development Laboratory, Ft. Belvoir, VA, 1958.

G. Holst, *Electro-Optical Imaging System Performance*, p. 421, JCD Publishing, Winter Park, FL, 1995.

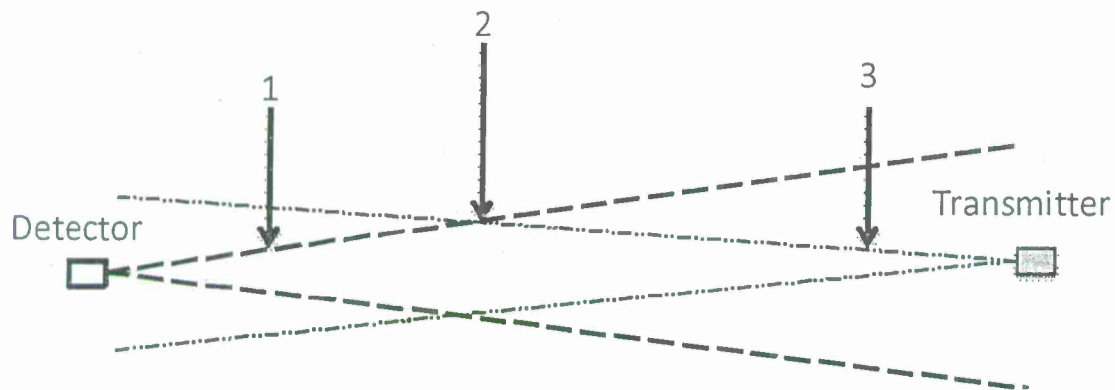


Figure1 A top view depicts the detector field of view and the transmitter beam width for a beam break sensor. The arrows represent edges being moved into the field of view. At position 1 the detector field of view limits the edge detection. At position 3 the transmitter beam width is the limit. It is apparent the amount of edge movement required for a detector output change depends on the edge location between the detector and the transmitter.

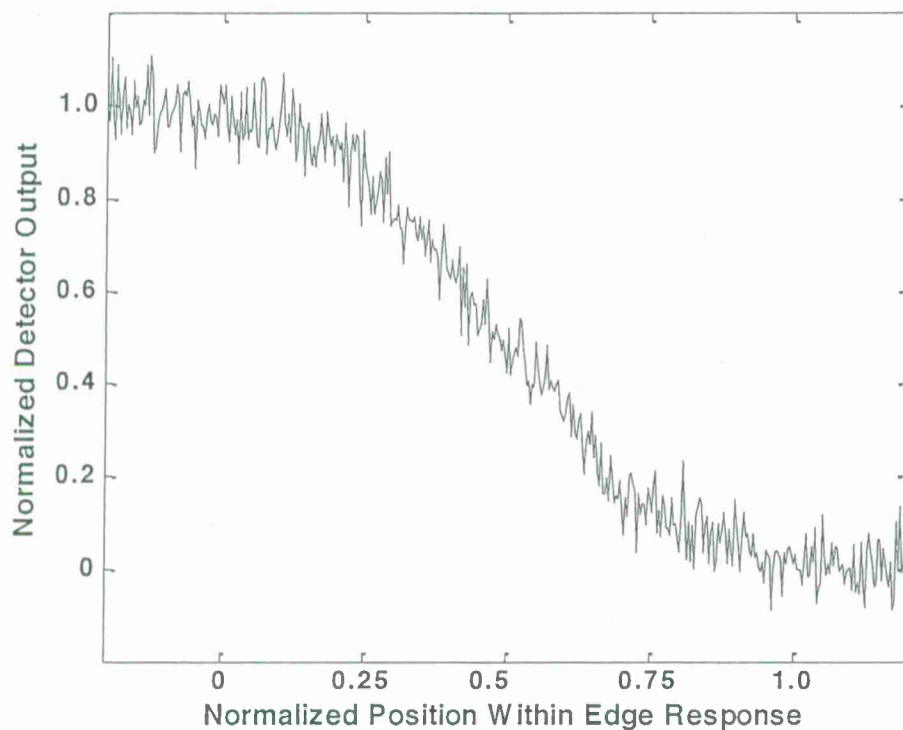
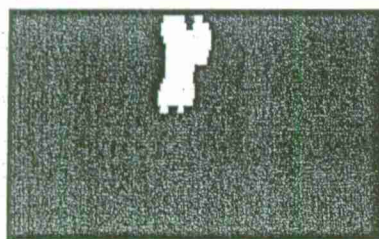
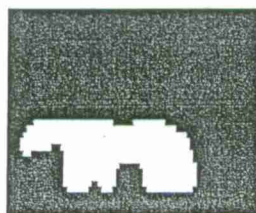


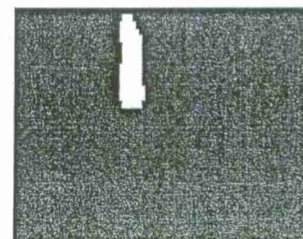
Figure 2 This figure simulates the analog detector response to an edge moving across the field of view with added noise. It demonstrates that edge position within the field of view has a one-to-one relationship with fractional optical power, except for noise.



Human with backpack



Pony



Human without backpack

Figure 3 Output from the binary output beam bread sensor is displayed in a two dimensional format. Hundreds of these examples have been collected for testing profiling sensors and classification algorithms for processing their output data.

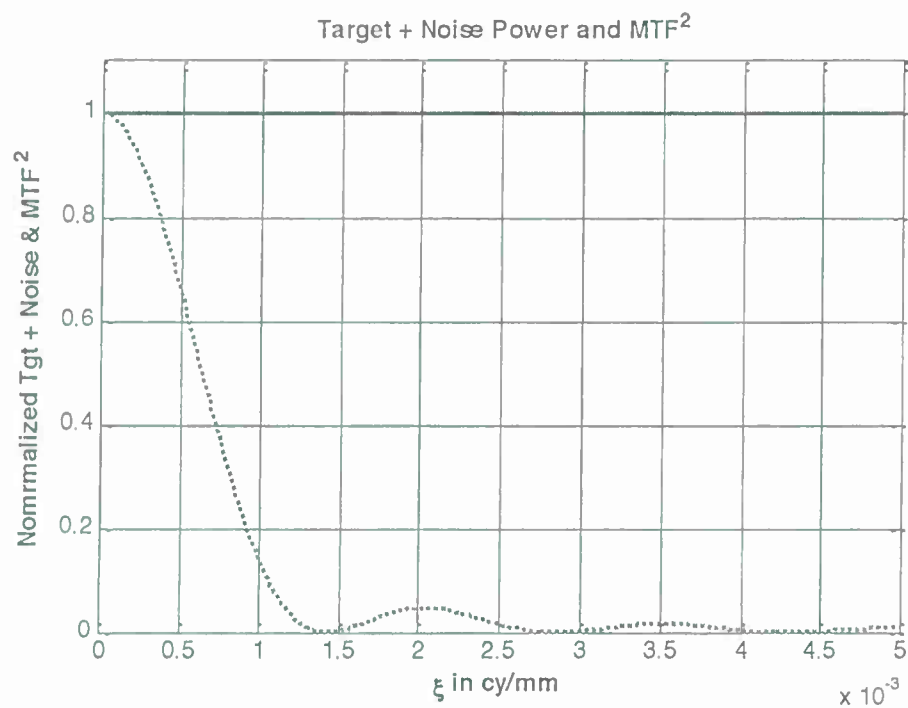


Figure 4 This figure illustrates the example system quantities used to find a numerical value for the information rate. The target plus noise power spectrum is normalized to one for illustration (actual peak is  $250^2 \text{ mm}^2$ .) The horizontal axis stops at 0.005 cy/mm whereas the integration goes to 0.5 cy/mm. The horizontal scale as chosen matches that for the vertical direction shown in Figure 5. The solid blue curve is the MTF<sup>2</sup> and the dotted red curve shows the target spectrum normalized to a peak value of 1.



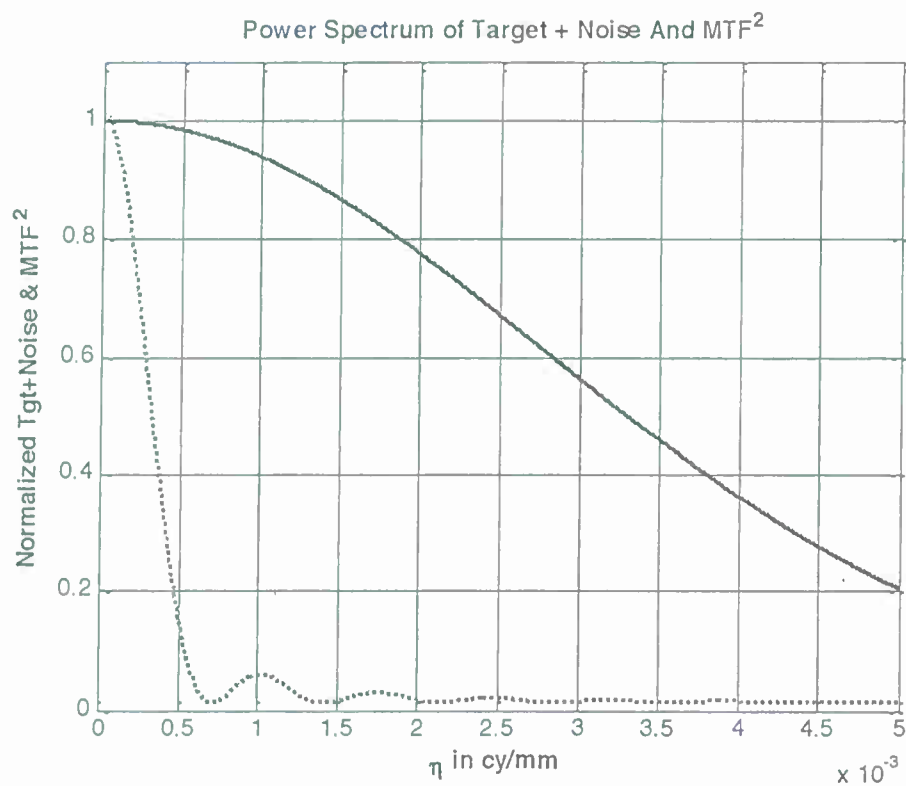


Figure 5 The solid blue curve is the square of the MTF and the dotted red curve is the target power plus the noise power. For this vertical direction the integration ends at  $5 \times 10^{-3}$  cycles per millimeter.

## Equation Chapter 5 Section 5 Performance Model for Micro-resonator Sensors Leading to Information Rate

A common feature to many micro resonator based sensors is a sphere being deformed. That deformation changes the resonant wavelength. The resulting change in resonant wavelength is then detected. The detection is accomplished by noting the resonant wavelength shift from before and after the deformation. The resonance wavelength is the point of greatest loss from the transmitted beam.

The relationship between the deformation and the individual "force" being measured must be modeled. Here "force" means field quantity being sensed as well as force. This elasticity model depends on materials and the resonator geometry. Much of this elasticity modeling is already available and is summarized well in [1]. Their model relates the force being measured to the change in wavelength of the resonant cavity. Essentially this is the model of the common feature to those sensors of interest.

The model presented in [1] does not treat the statistical aspects of the sensor. For example, what are the noise sources in laser source including its current driver? How much wavelength jitter can be expected from the laser diode? Similarly, we need to model the detector noise.

We want to also to model the digitization issues of bit depth and dynamic range and sampling noise. The actual signal processing reported in [1] is a correlation of the model pattern before the force and after the force. The correlation will reveal the shift and this shift can be expressed as a wavelength shift. The model as presented in [1] is an analog model.

Shapes other than spherical have been studied for potential use in micro-resonator sensors. Perhaps one can be creative with the basic spherical shape. Is there an optimal shape that might even be different for different sensing modalities?

The model in [1] uses a first order ray model for the resonance. A more sophisticated (complicated) model would use the electromagnetic fields inside the resonator so that any mode effects on the resonance are included. The em fields inside the cavity for some cavity shapes are available in the literature [2]. For example, prolate (and oblate) spheroidal shapes are two important cases that are already solved [2]. However, the first order ray model appears to be very successful. This is likely due to the fact that the spheres being used are much larger than the resonant wavelength. If future work involves smaller spheres, the ray model might not be as successful. The smallest mode volume theoretically possible is on the order of  $\lambda^3$  [3].

To summarize, the performance model for microresonator sensors has three parts, the elasticity model relating force to deformation, the resonance model relating deformation to wavelength change, and the signal processing and noise model.

## 5.1 Elasticity Model

Ioppolo et al. summarize the elasticity of the sphere and its response to a force from rigid plates that are diametrically opposite[1]. The solutions they reference are for a fairly rigid material and/or a small force and do not apply where the plates touch the sphere (squashed flat region). In Ioppolo's coordinate system (typical spherical coordinates), there is symmetry with respect to  $\phi$  and variation in the polar angle  $\theta$  and the radius  $r$ . What is varying is the displacement  $u$  of a given point within the sphere and the pressure plates are at the poles,  $\theta = 0$  and  $\theta = \pi$ .

They begin with the Navier equation for the displacement (strain) of a given point.

$$\nabla^2 u + \frac{1}{1-2\nu} \nabla \nabla \cdot u = 0 \quad (5.1)$$

$\nu$  is the Poisson ratio. The Poisson ratio relates stress and strain in directions perpendicular to the force. Squashing at the poles causes bulging at the equator,  $\theta = \pi/2$ , and the Poisson ratio models that effect.

With the azimuthal symmetry the solution is given by

$$u_r = \sum_{n=0}^{\infty} [A_n (n+1)(n-2+4\nu)r^{n+1} + B_n n r^{n-1}] P_n(\cos \theta) \quad (5.2)$$

$A_n$  and  $B_n$  are determined from boundary conditions, but will be related to another constant,  $H_n$ , before applying the conditions.  $P_n(\cos \theta)$  denote the Legendre polynomials of order  $n$ .

The resonance condition for the micro resonator is that a phase shift of an integral multiple of  $2\pi$  occur within the resonator. The authors use the ray model and the assumption that the circumference of the sphere is the path. That leads to the following equation.

$$2\pi n_0 a = k\lambda \quad (5.3)$$

$a$  is the radius of the sphere and  $\lambda$  is the freespace wavelength. Since we are interested in shifts in the resonant wavelength, the authors take the differential change and write the following.

$$\frac{d\lambda}{\lambda} = \frac{dn_0}{n_0} + \frac{da}{a} \quad (5.4)$$

The change in the index of refraction is a result of a force (stress) at the point being considered. Consequently, the strain result and the shear modulus of the material are used to obtain the stress. Eqn.(5.5) shows only the  $rr$  component. The other components are not relevant under the assumptions for this analysis.

$$\sigma_{rr} = 2G \sum_{n=0}^{\infty} [A_n (n+1)(n^2 - n - 2 - 2\nu)r^n + B_n n(n-1)r^{n-2}] P_n(\cos \theta) \quad (5.5)$$

By considering the interface between the plates applying the force and the sphere itself, there is no "rolling" of the material. This means the boundary conditions are as follows.

$$\sigma_{rr}(a) = \begin{cases} -p(\theta) & 0 \leq \theta \leq \theta_0 \text{ and } \pi - \theta_0 \leq \theta \leq \pi \\ 0 & \theta_0 \leq \theta \leq \pi - \theta_0 \end{cases} \quad (5.6)$$

$\theta_0$  is the greatest value of  $\theta$  for which the contacting plate touches the sphere. Similarly,  $a_0$  is the radius of the contact area between the plates and the sphere, that is, from the polar axis to point on the surface of the sphere where the pressure plate contact ends. The expression for  $a_0$  follows.

$$a_0 = \left[ \frac{3Fa(1-\nu^2)}{4E} \right]^{1/3} \quad (5.7)$$

$E$  is Young's modulus for the material and  $a$  is the radius of the sphere. The expression for pressure distribution under the contacting plate is given by the following.

$$p(\theta) = \frac{3F}{2\pi a_0^3} \sqrt{a_0^2 - a^2 \sin^2(\theta)} \quad (5.8)$$

The symmetry of this arrangement yields a deformation that does not vary with the azimuthal angle  $\phi$  and is an even function with respect to  $\theta$  (about  $\theta$  equal to  $\pi/2$ ). As a result the expansion of Eqn (5.9) uses only the even orders of the Legendre polynomials.

$$\sigma_{rr}(a) = \sum_{n=0}^{\infty} H_n P_n(\cos \theta) \quad (5.9)$$

The coefficients  $H_n$  are found by invoking the orthogonality of the Legendre polynomials. The result follows.

$$H_n = (4n+1) \frac{3F}{2\pi a_0^3} \int_{\theta_0}^0 \sqrt{a_0^2 - a^2 \sin^2(\theta)} P_n(\cos \theta) \sin \theta d\theta \quad (5.10)$$

The integral is evaluated numerically for a specific example. Some details of the numerical evaluation are presented in Appendix A for this chapter.

Once the set of  $H_n$  is obtained, the  $A_n$  and  $B_n$  in Eqn (5.2) can be found. The following expressions for  $A_n$  and  $B_n$  are obtained by using Eqn (5.9) and Eqn(5.5) to satisfy the boundary conditions in Eqns (5.6), (5.7) and (5.8).

$$A_n = \frac{H_n}{2Ga^n \left[ (n+1)(n^2 - n - 2 - 2\nu) - n(n^2 + 2n - 1 + 2\nu) \right]} \quad (5.11)$$



$$\begin{aligned}
B_n &= \frac{H_n}{2G \left[ (n+1)(n^2 - n - 2 - 2\nu) - n(n^2 + 2n - 1 + 2\nu) \right]} \\
&\times \frac{(n^2 + 2n - 1 + 2\nu)a^{2-n}}{(n-1)} \\
&= A_n \frac{(n^2 + 2n - 1 + 2\nu)a^2}{(n-1)}
\end{aligned} \tag{5.12}$$

The  $a^{-n}$  factor in both  $A_n$  and  $B_n$  is associated with the  $r^n$  factor in Eqn (5.5) to avoid a numerical disaster as  $n$  increases. For the cases of interest,  $a$  is on the order of hundreds of micrometers. Therefore, as  $a$  is raised to higher and higher powers of  $n$ , the values of  $A_n$  and  $B_n$  grow larger and larger.

## 5.2 Signal Processing and Noise Model

The feature extracted from the signal is the resonant wavelength shift caused by a force. The shift is obtained by processing the output from the photodetector. That output shows more than a single mode, so there is a pattern of minima in the detector output. The ramp in the output due to the current ramp is removed from the data. The entire pattern shifts as a force is applied to the resonator. Correlation is used to measure the amount the pattern shifts in response to the force. Most published results use a large signal so that signal processing uncertainty and noise is not likely significant. For field applications, however, minimizing power may result in operating with a low signal-to-noise ratio. Hence, the current section models the major contributors to the uncertainty in the data output.

Actually, wavelength is not measured, but rather a current level from a ramp used to drive the laser diode. Expressing the shift in wavelength is the traditional way of expressing the change. As a result of this choice, temporal noise (in the laser driver and in the photodetector) is converted to wavelength through the calibration curve relating current and wavelength for the laser. For illustration purposes the conversion factor of 5 picometers per milliamp will be used.

The graphic below illustrates the major factors included in the signal processing and noise model.



## Signal Processing & Noise Model

Laser Source	Detector/Processing
<ul style="list-style-type: none"> <li>• Laser Noise (Current is constant)</li> <li>• Driver Noise (Noise due to ramp in current)</li> <li>• Sampling Noise (Sample rate and phasing issues)</li> </ul>	<ul style="list-style-type: none"> <li>• Detector Temporal Noise (Constant irradiance)</li> <li>• Sampling Noise (Sample rate and phasing issues)</li> <li>• Dip Separation (Correlation process accuracy limitations)</li> </ul>

**Figure 5.1** This overall view shows the factors included in the signal processing and noise model.

For combining noise sources, the independence of the various sources of noise allows us to add the individual fractional variances. Or, if each noise is converted to the same units (such as nm), the variances may be added. The overall standard deviation is then the square root of the variances. In the example below, all noise terms are converted to equivalent wavelength. Eqns (5.13), (5.14) and (5.15) summarize the noise and uncertainty in the signal processing and noise model. Other terms can be added and some of these can be deleted as the model is applied to specific cases.

$$\begin{aligned} laserNoiseVar = & powerNoiseVar + freqNoiseVar + \\ & driverNoiseVar + sourceSamplingNoiseVar \end{aligned} \quad (5.13)$$

$$\begin{aligned} detSigProcVar = & detTempNoiseVar + sampleNoiseVar \\ & +dipSeparationProcessingVar \end{aligned} \quad (5.14)$$

$$var = laserNoiseVar + detSigProcVar \quad (5.15)$$

This model implicitly assumes that the signal processing takes place at the sensor. That means the output of the signal processing step is the end of the model. There is not a transmission model for the noise and corruption that occurs in transmitting the data. Other modes of operation such as transmitting the detector output are possible. The model can be adapted to end the sensor part of the model at the appropriate step. One may need to add a transmission model.

The divisions in the model are arbitrary. The dip separation is the feature extracted from the sensor. It is the shift in wavelength of the dips or minima in the power measured by the detector.

### 5.3 Sources of Noise and Uncertainty

A brief summary of the signals involved helps identify the sources of uncertainty in the microresonator sensor. A ramp of current is used to drive the laser diode and subsequent signals are compared in time to the ramp. A calibration curve converts the current values to wavelengths. For this diode, the temperature is set by a thermoelectric cooler since temperature changes result in wavelength changes even without any change in current. The microresonator changes its shape in response to a force, which causes a shift in the resonant wavelength. These resonances are detected as losses in signal strength from the photodiode. By noting where the resonances occur in the current ramp, one can determine wavelengths and therefore the amount of the wavelength shift.

Seeking the wavelength shift entails two types of uncertainty, one being temporal noise and the other being frequency noise (wavelength noise). The spectral linewidth of the laser represents frequency noise. Temporal noise arises from both the driver for the laser diode and from the photodiode. Since we are interested ultimately in wavelength, we will convert temporal noise into an equivalent frequency noise. The calibration curve relating current to wavelength for a typical laser diode is linear. Therefore, the two end points are used to approximate the slope,  $\Delta\lambda/\Delta i$ . For one laser diode this slope or ratio is 5 picometers/milliamp.

Figure 5.2 below illustrates the conversion of temporal noise into a current equivalent (or temporal equivalent) which can then be converted to wavelength uncertainty. The calibration between current and wavelength (for example, 5 picometers per milliamp) converts the current uncertainty into a wavelength uncertainty.



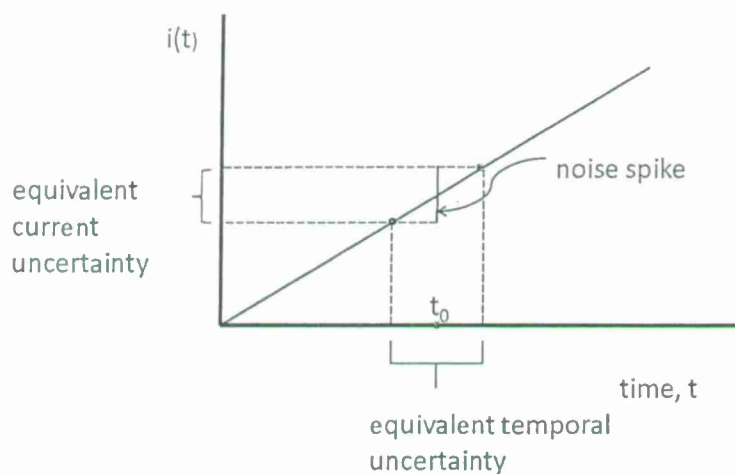


Figure 5.2 This illustrates the conversion of temporal amplitude noise into an equivalent wavelength uncertainty. Suppose a noise spike changes the amplitude instantaneously at time  $t_0$  during the ramp of current. Since the ramp is used to determine wavelength, the extremities of the spike then yield an equivalent uncertainty in current. If time during the ramp is used to determine wavelength, then the equivalent temporal uncertainty shown in the figure can be used.

In general sampling uncertainty is well modeled as a noise. The noise level is the variance which is modeled as arising from a uniformly distributed probability density function. The width of the density function is the least significant bit converted to the quantity being measured. The Example Calculations section illustrates the process with a numerical example.

#### 5.4 Detector Noise Model

Noise in detectors is a mature field of study, with many detailed models available. The application area is the major consideration in choosing a model for reasonable results. The model often used for photodiodes in fiber optic applications is chosen here. In essence, four physical phenomena are included in the model. Major noise sources are shot noise driven by the signal level itself and background power, dark current noise and thermal noise in the load resistance. The fourth phenomenon is that the signal level is often measured with the noise included. Therefore, a fraction of the signal power is added to the noise terms to account for that phenomenon. The end result is given as Eqn (5.16) below for the SNR. This is considered to be an analog signal, so sampling noise is not included, or equivalently, the signals are well sampled. Other assumptions are that the noise spectra are flat within the electronic bandwidth, so integrations over the band result in a multiplication by the bandwidth. This model also requires modification for avalanche photodiodes.

$$SNR = \frac{i_s^2}{i_N^2} = \frac{\left(\frac{\eta q P_s}{h\nu}\right)^2}{\left(\frac{2q^2\eta}{h\nu}\right)(P_s + P_B)\Delta f + 2qi_d\Delta f + \left(\frac{4kT}{R_L}\right)\Delta f + \left(\alpha\frac{\eta q P_s}{h\nu}\right)^2} \quad (5.16)$$

The notation is:  $i_s$  and  $i_N$  are signal and noise currents,  $\eta$  is the quantum efficiency of photon-to-electron conversion,  $q$  is the electron charge in Coulombs,  $P_s$  is the signal power in watts (possibly plus the noise power),  $h$  is Planck's constant,  $\nu$  is the frequency of the light,  $P_B$  is the background power that reaches the detector,  $\Delta f$  is the electronic bandwidth of the detection circuit,  $k$  is Boltzmann's constant,  $T$  is the temperature in degrees Kelvin,  $R_L$  is the load resistance, and  $\alpha$  is the fraction of the signal power within the electronic frequency bandwidth that results from the noise. The first three terms in the denominator are the shot noise variance, the dark current variance and the thermal noise variance. The fourth term in the denominator is the correction factor for the signal actually being signal plus noise.

Vendors commonly quote  $i_d$ , the dark current. At low signal power (perhaps less than 10  $\mu$ W), the thermal noise and the dark current noise dominate. Since thermal noise and dark current noise do not increase with power, the signal to noise ratio improves as signal power is increased. At some power level (perhaps  $\sim 10 \mu$ W) the shot noise and/or the fourth term in the denominator become significant. If the shot noise is dominant, the SNR will increase with increasing signal power, but only linearly rather than as the square. If the fourth term dominates, the SNR does not increase any further with increasing signal power.

Vendors often quote the responsivity in amps/watt instead of the quantum efficiency. The responsivity is given by the following.

$$\mathcal{R} = \frac{\eta q}{h\nu} \quad (5.17)$$

Using Eqn (5.17) in Eqn (5.16) results in a more practical expression that follows.

$$SNR = \frac{i_s^2}{i_N^2} = \frac{(\mathcal{R}P_s)^2}{2q\mathcal{R}(P_s + P_B)\Delta f + 2qi_d\Delta f + \left(\frac{4kT}{R_L}\right)\Delta f + (\alpha\mathcal{R}P_s)^2} \quad (5.18)$$

## 5.5 Example Calculations

As an example of sampling noise, suppose the current is being measured and the dynamic range is required to span 20 mA. A 16 bit A/D converter resolves the 20 mA dynamic range into 65536 bins. Therefore the least significant bit corresponds to 20/65536 mA or approximately 0.3  $\mu$ A. With the uniform probability density function, the variance is given by  $(0.3 \mu\text{A})^2/12$  or approximately  $7.7 \times 10^{-15} \text{A}^2$ , or a standard deviation of 0.88  $\mu$ A. This standard deviation in wavelength terms is  $(5 \text{ pm/mA} \times 0.88 \times 10^{-3} \text{ mA})$  or  $0.44 \times 10^{-3} \text{ pm}$ . Another sampling process, a temporal one, takes place as the current ramp progresses. The uncertainty associated with the temporal sample rate is discussed below.

Specifications are not often detailed for laser diodes, so the following numbers are selected for illustrating the process of determining wavelength uncertainty. The operating power level is typically in the mW to tens of mW range, so we assume 8 mW of laser output power. At that level, the spectral or frequency noise is quoted as 10 MHz, so we will use 0.06 pm as the equivalent frequency noise. Amplitude noise arises from sources such as the laser diode itself, driver current noise and temperature noise. The Agere 2300 laser specifications quote the relative intensity noise as  $-145$  dB/Hz. No separate specifications were available for driver noise, but it is small based on the overall noise amount. Also, the power output stability of the laser itself was not specified and that too is small. Temperature variations will manifest themselves as a change in wavelength, indistinguishable from a change in current. The laser diodes are usually cooled by a thermoelectric cooler. The temperature fluctuations may be slow enough to amount to drift more than noise. In any case the small overall intensity noise suggests the thermoelectric cooler holds the temperature steady without adding significant noise. Consequently, for illustration purposes the total intensity noise of the laser source will be  $-145$  dB/Hz.

A typical responsivity is 0.8 mA/mW so the signal level will be 6.4 mA.

The background power reaching the detector is assumed to be negligible ( $P_B = 0$ ) as will the signal fraction resulting from noise ( $\alpha = 0$ ).

Thermal noise current squared with  $T = 300$  deg K is  $1.66 \times 10^{-20}$  amps squared ohms per Hertz. So this number is multiplied by the ratio of the bandwidth in Hertz to the load shunt resistance in ohms. For illustration we choose a 1 MHz bandwidth and a 1 kilohm resistor. This yields  $1.66 \times 10^{-17} \text{ A}^2$  for the thermal noise current squared.

A typical detector dark current noise of 1 nA will be used for numerical illustration. The dark current noise squared is  $3.2 \times 10^{-19}$  times the dark current times the bandwidth. Using 1 nA for the vendor specified dark current and 1 MHz for the bandwidth results in  $3.2 \times 10^{-22} \text{ A}^2$  for the dark current noise squared.

The shot noise current squared is  $3.2 \times 10^{-19}$  times the responsivity times the signal power times the electronic bandwidth. Our assumed responsivity is 0.8 mA/mW and the laser output power is 8 mW. Again, with a 1 MHz bandwidth, the shot noise current squared is  $2 \times 10^{-15} \text{ A}^2$ .

It is typical that shot noise dominates the noise for the detector and our assumed parameters illustrate that condition. The noise current squared numbers obtained as examples are added to get the total noise, which will be approximately equal to just the shot noise. The total detector noise current is 45 nA. Converted to equivalent wavelength by using 5 picometer/milliampere, the detector noise is equivalent to  $2.2 \times 10^{-4}$  picometers.

Polarization noise results from the source varying the output polarization. The reflections (and perhaps some parameters) inside the micro resonator depend on polarization, so the variations in the polarizations yield different losses inside the resonator. Consequently the power measured by the photodiode may change if the polarization changes.

Uncertainty in the wavelength separation of the two dips, one before stimulus and the other after stimulus, involves sampling and other previously discussed uncertainties. There are at least two effects that interact to affect the separation uncertainty. The laser linewidth is a fundamental uncertainty that limits accuracy. The Agere 2300 laser diode previously mentioned has a linewidth of 10 MHz. This translates to a wavelength uncertainty of approximately 0.06 picometers at  $\lambda_0 = 1.312 \mu\text{m}$  wavelength. In effect, this is the width of the tool used to measure the resonant dips, so its width is a limit on defining the shape of a resonance dip. The Q of the cavity describes the width of the resonance dip. See Appendix B for the resonant linewidth model. In terms of wavelength, the Q is equivalent to  $\Delta\lambda/\lambda_0$  where  $\Delta\lambda$  is the full width at half maximum and  $\lambda_0$  is the resonant wavelength. See references 3 through 5 for more detailed discussions. For  $Q = 10^6$  the resonant linewidth is 1.3 picometers. That means the maximum number of uncorrelated samples within the full width half maximum resonance width is  $1.3/0.06$  or approximately 22 samples. However, because of the scanning the temporal sampling rate must also be considered. It is the second of the two effects under discussion.

The temporal sampling rate affects a number of performance issues in addition to the uncertainty. Each ramp can be thought of as a "sample" unto itself since we assume a detection of a resonance shift occurs only once during a given ramp. For example, suppose one wants to check for a shift 400 times per second. That means a scan or ramp must complete within 2.5 milliseconds. If the stimulus is changing with time, the 2.5 millisecond separation must be satisfactory for the intended application. The next issue affecting temporal sampling rates is the range of wavelengths to be search for the resonance shift. The wavelength range can be guided by the free spectral range of the resonator. For example, consider a  $100 \mu\text{m}$  diameter sphere. The wavelength that resonates in the sphere must have an integral number of wavelengths around the circumference. With PMMA index of refraction is 1.492 and with PDMS the index is 1.4. Near  $1.312 \mu\text{m}$  wavelength, the free spectral range is slightly less than 4 nm for either material ( 3.7 nm for PMMA or 3.9 nm for PDMS. Let us choose the laser linewidth of 0.06 pm to be our sampling distance. To span 4 nm, we need 67,000 samples. With 400 scans per second, our temporal sampling rate must be approximately 27 M samples per second.

The choice of the laser linewidth as the sample spacing is somewhat arbitrary. A larger sample spacing provides fewer data points so the resonance line shape is not as well resolved. From an uncertainty viewpoint the laser linewidth is already an uncertainty whereas the sample spacing must be converted to uncertainty as was done for the amplitude digitization. The two effects are independent so the net uncertainty is the square root of the sum of the squared individual uncertainties. If we choose the sample spacing of 0.06 pm, the sampling uncertainty is 0.017 pm. This yields a net uncertainty from these two effects of 0.062 pm. The laser linewidth dominates the sampling uncertainty.

## 5.6 Information Rate

The microresonator sensor has a one dimensional signal output which is the detector output as a function of wavelength, although other equivalent variables can be used. As shown above the driving current for the laser diode can be used instead of wavelength shift, or time during the ramp can also be used. Consequently, the information rate is modeled by the following equation.



$$H = \int_B \log \frac{S(\xi)}{N(\xi)} d\xi \quad (5.19)$$

H is the information rates in bits per measurement (with log implying base 2 logarithm), S is the signal power spectral density (including noise, in general) and N is the noise power spectral density.  $\xi$  is the frequency so that B is the bandwidth (single sided).  $\xi$  and B have appropriate units, e.g. cycles per m with our choice of wavelength as the independent variable for the signal.

### 5.6.1 Information Rate for Detection of Dip

There are various features that can be extracted from the data. One of these is simply detecting the dips and noting the time separation of the minima. The signal for this feature extraction is modeled as follows. The basic signal prior to signal processing is the detector output. The detector output (in amps) is linearly related to the optical power from the fiber. The laser input to the fiber is an increasing power over time resulting from the current ramp driving the laser diode. As the current changes along the ramp the output wavelength changes, with 5 picometers per milliamp being our example value. The power output dips in the vicinity of a resonance of the micro resonator. The width and shape of the dip are discussed in Appendix B.

The first step in processing is to remove the unimportant ramp in the detector output. After that, the remaining feature is the sharp dip denoting the resonance. There can be more than one resonance within each scan of wavelengths. However for signal spectrum purposes, we assume a single dip before the stimulus is applied and a single dip after the stimulus is applied. We assume the dips are identical except for their locations in wavelength. The signal power is then the square of the detector output in amps to yield a power signal in  $A^2$ , consistent with our prior noise power calculations.

The same signal to noise ratio holds if the dips are considered pulses with peaks instead of dips. Therefore, we use the following as our signal.

$$g(\lambda) = \frac{MA \left( \frac{\Delta\lambda}{2} \right)^2}{\left( \frac{\Delta\lambda}{2} \right)^2 + (\lambda - \lambda_0)^2} \quad (5.20)$$

MA is the peak of the current signal in amps, which is the fractional dip times the responsivity times the optical power. The constant A will adjust the amplitude to the proper value and the proper units.

We need the transform of the signal squared. Recall that the transform of the signal magnitude squared is the cross correlation of the transform with its complex conjugate. The transform is given by the following.

$$\begin{aligned}
I(\xi) &= \frac{MA\pi\Delta\lambda}{2} F \left\{ \frac{1}{\pi} \frac{\frac{\Delta\lambda}{2}}{(\lambda - \lambda_0)^2 + \left(\frac{\Delta\lambda}{2}\right)^2} \right\} \\
&= \frac{MA\pi\Delta\lambda}{2} \exp(-j2\pi\lambda_0\xi) \exp(-\pi\Delta\lambda|\xi|)
\end{aligned} \tag{5.21}$$

The signal power spectrum is then as follows.

$$S(\xi) = \left( \frac{MA\pi\Delta\lambda}{2} \right)^2 \exp(-2\pi\Delta\lambda|\xi|) \tag{5.22}$$

For a single sided power spectrum the symmetry of the above power spectrum yields the following single sided expression.

$$S(\xi) = 2 \left( \frac{MA\pi\Delta\lambda}{2} \right)^2 \exp(-2\pi\Delta\lambda\xi) \tag{5.23}$$

The noise power spectrum is the denominator in Eqn (5.18). Often the shot noise from the detection process dominates the noise.

### 5.6.2 Information Rate for Detection of Dip: A Numerical Example

We use Eqn (5.19) with some assumptions to provide a numerical example of the information rate when detection of a dip is the goal. Our prior example values are used except that we increase the temporal bandwidth consistent with a 27 million samples per second sampling rate. We assume the detector shot noise is the noise power spectrum.

The signal power spectrum is given in Eqn (5.23) and the shot noise spectrum has that same spectral shape. Thus the ratio of the two spectra is constant. As the spectra approach zero, other noise terms come into play. We choose to limit the spectrum to a band where the two spectra are significant compared to zero. For integration purposes for Eqn(5.19) we are integrating a constant from zero out to a band limit. The following numerical results illustrate the process.

The peak signal current arises from 8 mW of optical power, converted to current by a responsivity of 0.8 mA/mW, and a fractional peak of 0.6, or 3.84 milliamps. This yields a peak squared signal current of  $4.1 \times 10^{-5}$  amps<sup>2</sup>. The resulting shot noise current squared is  $2(1.6 \times 10^{-19})(3.84 \times 10^{-3}) \Delta f$ . We have chosen the electronic bandwidth to be 50 MHz. Note that the electronic bandwidth is not the bandwidth for the integration in Eqn (5.19). With this electronic bandwidth the shot noise current squared is equal to  $6.14 \times 10^{-14}$  amps<sup>2</sup>.

In Eqn (5.19) the signal spectrum is assumed to include additive noise. The integrand is then  $\log_2(1+S/N)$  where S is signal only, and for our example is equal to 29.3. This large number results from the small

noise with a modest optical power. In essence, the information rate is driven by the number of equivalent noise levels found in the signal, hence the large value.

The bandwidth for the integral is the final issue to be considered. We have used wavelength as the independent variable for our signal, so our frequency variable  $\xi$  has units of  $\text{m}^{-1}$  or some equivalent convenient unit. The decaying exponential in Eqn (5.23) will be considered zero when the following bandwidth is reached.

$$\Delta\xi = \frac{3}{2\pi\Delta\lambda} \quad (5.24)$$

$\Delta\lambda$  is found from the Q of the resonator (assume  $Q = 10^6$ ) and the laser wavelength of  $1.3 \mu\text{m}$ . The result is  $\Delta\xi = 0.36$  cycles per picometer.

The information rate is then 10.7 bits per picometer per measurement.

Intuitively this information rate suggests one can resolve roughly 1000 positions within a picometer. This is true if one considers the shot noise as the limiting factor. A more realistic approach is to use the total uncertainty expressed in picometers. As an example the uncertainty caused by the laser linewidth is a larger uncertainty ( $\approx 0.06 \text{ pm}$ ) than the noise ( $\approx 0.0012 \text{ pm}$ , a factor of 50 smaller). With the laser linewidth uncertainty we would expect to resolve approximately 16 spots within  $1 \text{ pm}$ . This is approximately 4 bits per picometer per measurement. This estimate does not account for the different spectral shape of the laser linewidth uncertainty, but the estimate provides further intuitive meaning for what the information rate means physically.

### 5.6.3 Using Cross Correlation to Determine Separation of Dips

The actual signal processing consists of measuring the shift in the resonant frequency rather than just detecting the presence of a dip. One technique for determining the shift is to locate the peak value in the cross correlation of the before stimulus signal and the after stimulus signal. To proceed with a numerical example, the details of the cross correlation of two Lorentzian functions is presented in Appendix C. The before stimulus signal and the after stimulus signal are assumed to be the same except for the shift in the resonant wavelength. While the actual signal is a dip, we first focus on just the part that varies with wavelengths. Then the constants will be considered. From the appendices the two signals are given by the following.

$$g(\lambda) = \frac{MA\left(\frac{\Delta\lambda}{2}\right)^2}{\left(\frac{\Delta\lambda}{2}\right)^2 + (\lambda - \lambda_0)^2} \quad (5.25)$$

$$g_1(\lambda) = \frac{MA\left(\frac{\Delta\lambda}{2}\right)^2}{\left(\frac{\Delta\lambda}{2}\right)^2 + (\lambda - \lambda_1)^2}$$

Their cross correlation is then expressed as follows.

$$C(\delta) = \frac{M^2 A^2 \pi (\Delta\lambda)^3}{4} \frac{1}{[\delta - (\lambda_1 - \lambda_0)]^2 + (\Delta\lambda)^2} \quad (5.26)$$

$\delta$  is the shift or lag independent variable for the cross correlation,  $C$ .  $\Delta\lambda$  is the full width half maximum of the lineshape. Usually this is estimated from the Q of the resonator and the operating wavelength given the following.

$$Q = \frac{\lambda}{\Delta\lambda} \quad (5.27)$$

M is the fractional depth of the dip that is normalized to be between 0 and 1. So our normalized signals are just a constant  $-g(\lambda)$  and the same constant  $-g_1(\lambda)$ . The cross correlations of these two signals then adds the square of the constant minus the mean values of  $g$  and  $g_1$  to  $C(\delta)$ . Under our assumptions of identical lineshapes, the mean values of  $g$  and  $g_1$  are the same, and are equal to  $MA\pi(\Delta\lambda/2)$ . The constant A will be adjusted to make the peak of the cross correlation equal to the peak signal current squared.

In locating the dip what matters is the change in the signal as we move one or more samples away from the dip. Therefore we get that information by working from Eqn (5.26) as a peaked function. The constant additive terms discussed above do not affect the result. If our change in signal is smaller than the noise, the noise can cause an uncertainty in location.

The sample spacing relative to the width  $\Delta\lambda$  is critical in determining the accuracy of peak location. Using our example numbers the linewidth of the laser limits our resolution to something greater than 0.06 pm whereas the FWHM of the resonator line shape function is approximately 1.3 pm. With an adequate temporal sample rate (27 M samples per second) the lineshape function is reasonably well sampled. There will be approximately 22 samples within the FWHM portion of the line shape. We will treat this well sampled condition and not consider a poorly sampled case.

There is always a phasing or synchronization issue as to whether the peak is centered within a sample. We will make that assumption for our calculations. Therefore, the sample at the peak itself extends 0.03 pm to either side of the peak. The adjacent sample is centered 0.06 pm from the peak itself. As one moves from the peak sample, the adjacent samples change by factors of 0.0021, 0.0083, 0.0185, 0.0497, etc. That means that the noise or uncertainty has to exceed 0.21 percent of the peak value to cause a one sample uncertainty in peak location. Continuing with our example numbers the peak current from the detector is 8 mW of optical power times a responsivity of 0.8 mA/mW or 6.4 mA. The resonance will dip below this by the fraction factor M for which we have used 0.6 as an example. That means at the depth of the dip the current is 0.4 times 6.4 or 2.56 mA. The uncertainty must cause a rise of 0.0021 time 2.56 mA or 0.0269 pm (using 5 pm/mA for wavelength vs. current slope for laser).



The shot noise associated with a signal of 2.56 mA is  $4.1 \times 10^{-14} \text{ A}^2$ . This is equivalent to a current of  $2.02 \times 10^{-4} \text{ mA}$ , which is 0.001 pm. The shot noise is approximately 4 % of the signal level change in moving from the minimum to an adjacent sample.

A process has been presented and illustrated regarding uncertainty in locating a dip using cross correlation. As expected with the large signal level and the very small shot noise, the shot noise does not impact the sample selection for the minimum. The shot noise is only about 4% of what would cause a single sample uncertainty in the minimum location.

## References

1. T. Ioppolo, U. Ayaz and M.V. Otugen, "High-resolution force sensor based on morphology dependent optical resonances of polymeric spheres," J. Appl. Phys., vol 105, pp. 0135351-9, 2009.
2. J.A. Stratton, *Electromagnetic Theory*, McGraw-Hill, 1941.
3. B.E. Little, J.S. Foresi, G. Steinmeyer, E.R. Thoen, S.T. Chu, H.A. Haus, E.P. Ippen, L.C. Kimerling, and W. Greene, "Ultra-compact Si-SiO<sub>2</sub> microring resonator optical channel dropping filters," IEEE Photon. Technol. Lett, vol. 10, pp 549-551, 1998.
4. T. Ioppolo, M. Kozhevnikov, V. Stepaniuk, M.V. Otugen, and V. Sheverev, "Micro-optical force sensor concept based on whispering gallery mode resonators," J. Appl Optics 47, pp. 3009-3014, 2008.
5. A.Naweed, G. Farca, S. Shopova, and A. Rosenberger, "Induced transparency and absorption in couple whispering gallery microresonators," Phys Rev A 71, pp. 043804-1 – 4, 2005.

## Equation Section 1 Appendix A Numerical Integration

Eqn (5.10) can be expressed in different algebraic forms, so a different form was chosen. Basically it is obtained by letting  $\cos\theta$  be  $x$  and replacing  $\cos^2\theta_0$  by  $(a^2 - a_0^2)/a^2$ . The end result is the following expression for the  $H_n$  coefficients.

$$\begin{aligned} H_n &= -\frac{3(4n+1)F\sqrt{a^2 - a_0^2}}{2\pi a_0^3} \int_{\cos\theta_0}^1 \left( \frac{x^2}{\cos^2\theta_0} - 1 \right)^{1/2} P_n(x) dx \\ &= -\frac{3(4n+1)F}{2\pi a_0^3} \int_{\cos\theta_0}^1 \sqrt{x^2 a^2 - (a^2 - a_0^2)} P_n(x) dx \end{aligned} \quad (\text{A.1})$$

Only even values of  $n$  will be used, so one can use  $2n$  as the subscript of  $H$  and for the order of  $P$ , the Legendre polynomial. In that case, for loops one uses an increment that advances by 1. Here, we use an index that begins with 0 and increments by 2. Using Matlab, one cannot use a subscript of 0 for an array, so we used  $nn = n+1$  where  $n$  advances by an increment of 2.

The convergence of the integral towards zero is slow, so that the power of  $x$  in the Legendre polynomials gets high. This can create numerical noise without a robust algorithm for generating the Legendre

polynomials. Consequently, the built in function `legendre.m` was used and was successful. `legendre.m` generates the associated Legendre polynomials recognized as  $P_n^m(x)$ .  $P_n(x)$  is the  $m=0$  associated Legendre polynomial, which is the Matlab subscript 1 array from the  $m=0$  to  $m=n-1$  associated arrays generated. The code snippet below illustrates the approach, where  $x$  is an array of values from  $\cos\theta_0$  to 1. Note that odd orders are also generated even though they are not used. The 1001 vectors contain the  $P_n(x)$  values needed for the integration.

```
%%%%%%%%%%%% Legendre Polynomials
%Generate the Legendre Polynomials. Use legendre which generates the
%associated Legendre Polynomials, Psub n superscript m (x). The m=0
%(Matlab subscript of 1)array is the ordinary Legendre Polynomials
for n=0:1:1000 %Generate more than twice the n loop limit below since
    %this function uses a backward recursion algorithm. That is, both
    %even and odd orders are generated. The code below outside this loop
    %selects the even orders. Start with n=0 to get P sub 0 array. Note that
    %P starts with an index of 1, which is P sub 0 array.
    Ptemp=legendre(n,x); %Generates the associated Leg Poly's
    P(n+1,:)=Ptemp(1,:); %selects the m = 0 array to keep
    clear Ptemp
end %end n loop
```

The integral from Eqn (A.1) was accomplished using a Simpson's rule approach, modified slightly to eliminate a trivial imaginary part to the first value in the integration. The code below creates 401 even order values for the integral. This will subsequently be multiplied by the term outside the integral in Eqn (A.1). This code uses an  $x$  array described earlier, the sphere radius  $a$  and a calculated radius of the rigid plate contact area.

```
%%%%%%%%%%%% Integral Calculation %%%%%%%%%%%%%
for nn=1:401
    intgrnd(nn,:)=sqrt((x(1,:).^2)*a^2-(a^2-a0^2)).*P(2*nn,:);
    %The true Simpson's rule is commented out because the term
    %int(nn,1) causes a complex result. Removing it doesn't change the
    %values and the imaginary part was very small. I chose to use the
    %magnitude or abs(int(nn,1), but it doesn't really matter.
    integral(nn)= dx/3*(abs(intgrnd(nn,1))+ 2*sum(intgrnd(nn,3:2:end-2))...
        + 4 *sum(intgrnd(nn,2:2:end))+ intgrnd(nn,end));

    %integral(nn)= dx/3*(intgrnd(nn,1)+2*sum(intgrnd(nn,3:2:end-2))...
    %+4*sum(intgrnd(nn,2:2:end))+intgrnd(nn,end));
end %end nn loop
```

## Equation Section 1 Appendix B Model for Resonance Dip

A number of authors state that the resonance dip is well approximated by a Lorentzian lineshape. There are a variety of different expressions used for this line shape that depend on normalization mostly. We choose to work in wavelengths (rather than frequency), so our expression follows in Eqn (B.1).

$$g(\lambda) = A \frac{M \left( \frac{\Delta\lambda}{2} \right)^2}{\left( \frac{\Delta\lambda}{2} \right)^2 + (\lambda - \lambda_0)^2} \quad (\text{B.1})$$

A is a constant that will be adjusted to make the peak power correct and to have correct units. In this form M represents the fractional peak value or the depth of the dip if we subtract  $g(\lambda)$  from 1 or the constant signal. That is, evaluating at  $\lambda_0$  yields M times A. M has a value between 0 and 1.  $\Delta\lambda$  is the full width at half maximum as can be seen by evaluating  $g(\lambda)$  at  $\lambda = \lambda_0 \pm \frac{\Delta\lambda}{2}$ . The total area under the function in this form is  $\pi$  times  $\Delta\lambda/2$  times M times A.

The parameters are measured from data as follows. The resonant wavelength  $\lambda_0$  is found by locating the minimum value of the transmitted power. The ramp resulting from the current ramp can be removed from the signal prior to processing.  $\Delta\lambda$  is measured as the full width at half max on the dip. M is the depth of the dip.

There are other quantities that relate to these parameters. For example, the Q of the system is equal to  $\Delta\lambda/\lambda_0$ . Naweed et al. [5] give the following expression for M.

$$M = \frac{4 \frac{T}{\alpha l}}{\left( 1 + \frac{T}{\alpha l} \right)^2} \quad (\text{B.2})$$

T represents the coupling transmission from the fiber to the sphere and  $\alpha l$  is the loss in the sphere.

Unfortunately, it is not easy to separate these two loss quantities from usual data. Consequently Eqn (B.2) is offered for theoretical interest. Notice however that the depth increases ( $1 - M$  gets smaller) with increasing T and decreases with increases in  $\alpha l$ .

## Equation Chapter 3 Section 1 Appendix C Crosscorrelation of Lorentzian Lineshape Functions

The Fourier transform of  $e^{-\beta|x|}$  is given by the following expression.

$$F\{e^{-2\pi\beta|x|}\} = \int_{-\infty}^{\infty} e^{-2\pi\beta|x|} e^{-j2\pi\xi x} dx = \int_{-\infty}^0 e^{2\pi\beta x} e^{-j2\pi\xi x} dx + \int_0^{\infty} e^{-2\pi\beta x} e^{-j2\pi\xi x} dx \quad (C.1)$$

By expanding the exponential with an imaginary argument into cosines and sines, then changing the dummy variable of integration on the first integral to  $\alpha = -x$ , one obtains the following, after consulting a table of integrals.

$$\begin{aligned} F\{e^{-2\pi\beta|x|}\} &= 2 \int_0^{\infty} \cos(2\pi\xi\alpha) \exp(-2\pi\beta\alpha) d\alpha \\ &= \frac{1}{\pi} \frac{\beta}{\xi^2 + \beta^2} \end{aligned} \quad (C.2)$$

$\beta$  is a constant and the independent variable is  $\xi$ . This Lorentzian function and its transform can be used to obtain the cross correlation of the lineshape functions of interest.

We use the same functional shape before stimulus and after stimulus except for a shift of the resonance. Eqn (B.1) describes the resonance lineshapes that we will use. Without loss of generality we set  $\lambda_0$  to 0 as the before stimulus response. The after stimulus response will shift the resonance to  $\lambda_1$  so our second lineshape is also obtained from Eqn (B.1) with  $\lambda_0$  replaced by  $\lambda_1$ . The term inside the brackets below matches the form of Eqn (C.2).

$$g_1(\lambda) = MA\pi \frac{\Delta\lambda}{2} \left[ \frac{1}{\pi} \frac{\left(\frac{\Delta\lambda}{2}\right)}{(\lambda - \lambda_1)^2 + \left(\frac{\Delta\lambda}{2}\right)^2} \right] \quad (C.3)$$

In the transform domain, the product of the two functions is the following.

$$M^2 A^2 \pi^2 \left(\frac{\Delta\lambda}{2}\right)^2 \left[ \exp\left(-2\pi \frac{\Delta\lambda}{2} |x|\right) \right] \left[ \exp(j2\pi\lambda_1 |x|) \exp\left(-2\pi \frac{\Delta\lambda}{2} |x|\right) \right] \quad (C.4)$$

The bracketed terms show the individual functions in the transform domain. Combining the two identical decaying exponential terms and bringing the result out of the transform domain yields the cross correlation,  $C(\delta)$ .

$$\begin{aligned} C(\delta) &= M^2 A^2 \pi^2 \left(\frac{\Delta\lambda}{2}\right)^2 \left[ \frac{1}{\pi} \frac{2\left(\frac{\Delta\lambda}{2}\right)}{(\delta - \lambda_1)^2 + 4\left(\frac{\Delta\lambda}{2}\right)^2} \right] \\ &= \frac{M^2 A^2 \pi (\Delta\lambda)^3}{4} \frac{1}{(\delta - \lambda_1)^2 + (\Delta\lambda)^2} \end{aligned} \quad (C.5)$$



Generalizing to a  $\lambda_0$  not zero, replace  $\lambda_1$  by  $\lambda_1 - \lambda_0$ . Some liberty was taken with signs since the cross correlation of these even functions is an even function. Somewhat as expected the cross correlation is a Lorentzian function with twice the FWHM value of the individual lineshapes. We finally write the following for our basic signal arising from the cross correlation. While the signals actually dip, the noise and uncertainty and SNR will be the same if we use these peaked functions.

$$C(\delta) = \frac{M^2 A^2 \pi (\Delta\lambda)^3}{4} \frac{1}{[\delta - (\lambda_1 - \lambda_0)]^2 + (\Delta\lambda)^2} \quad (C.6)$$

The constant A will be adjusted so that the peak value is the signal current squared in amps squared. For example, with 8 mW of optical power, detector responsivity of 0.8 mA/mW, A will be 6.4 mA times 2 divided by the square root of pi times  $\Delta\lambda$  with units of mA per m to the one half power.

# Profile Sensing Using Sensor Atoms

Eddie L. Jacobs

*Abstract*—The concept of a sensor atom as a fundamental unit of sensing is introduced. The properties of one particular type of sensor atom, the Bernoulli sensor atom, are derived.

## I. INTRODUCTION

Profiling sensors have been demonstrated to provide sufficient information about a moving object to perform many useful classifications such as whether or not the object is a human, an animal, or a vehicle. A profiling sensor extracts basic shape information about a moving object and classifies it into two or more categories. These types of sensors could be a low cost alternative to imaging sensors for applications involving border and perimeter security. To date, these sensors have been built using linear arrays of sensors. The linear arrays have either been a single integrated component or collections of several discrete components.

Atoms are the fundamental unit of matter. Atoms in combination form all the stuff we see. A large part of modern physics has been devoted to studying the properties of atoms and how they interact to form molecules. The concept of a sensor atom presented in this research is an attempt to leverage some of the principles of modern atomic physics and apply them to the problem of sensor design with particular application to the profiling sensor. The main result of this research will be a software/hardware infrastructure that facilitates the development of complex sensing systems from simple elements.

Sensor atoms are sensors. Hence, the properties of sensors are the properties of sensor atoms. In general sensors sense some sensible quantity and output some other sensible quantity. For instance, a typical electro-optic detector senses light and outputs a current or voltage. Sensible quantities can be described in terms of domain modes. Domain modes are functions that describe the behavior of the sensor with respect to some domain. As an example, an electro-optical sensor may only sense energy from a certain angular region of space and over a limited spectral bandwidth. As a result, an electro-optical sensor will have a spatial domain mode (or simply spatial mode) and a spectral mode. The sensor may be more sensitive to one polarization of light than another and will have a polarization mode. It will also be limited in how fast it can respond to changes in light energy<sup>1</sup> and will have a temporal mode. These modes may be independent or may be coupled. For instance, if a sensor has no sensitivity to polarization, the spatial and polarization modes will be independent. On the other hand, as is often the case, polarization sensitivity may vary spatially and as a result the polarization and spatial modes will be coupled.

Within an element atoms are described fairly simply and all are the same. However, the properties of a material are more strongly determined by the configuration of the atoms rather than the atoms themselves.

<sup>1</sup>The temporal mode is restricted to time variations that are slow with respect to the mean frequency of the light.

Carbon atoms arranged in one way form the lead in a pencil. Arranged another way they form a diamond. Similarly, sensor atoms when combined together will have properties that are not only governed by the individual properties of the atoms but also by the rules by which they interact. Rules established for the interaction of sensor atoms presume the existence of some mechanism for facilitating the interaction such as a communication channel and protocol. This mechanism is also properly a property of the sensor atom.

As a simple example of the interaction of sensor atoms, suppose two simple break-beam sensors (atoms) are positioned horizontally some distance apart. These sensors send out an optical beam that strikes a reflecting surface and returns to the receiver which is co-located with the beam transmitter. The output of each sensor is one of two states; "OPEN" if the beam is not broken and "CLOSED" if it is. As an object passes by it will break one beam and then the other. If the distance between the sensors is sufficiently short, objects of interest will at some time be breaking both beams during transit. Assume each sensor atom can report its own state (open or closed) and has knowledge of the state of other sensor at all times. Each atom now has enough information to report something more than just whether it is open or closed. A proper choice of interconnection rules of the atoms will allow each atom to report the direction of travel of the object. An example of an interconnection rule would be that if a sensor (say the left one) changes state from open to closed and knows that the right sensor is in a closed state then the object is traveling from right to left and the atom will report that the direction of travel is "LEFT". This is something more than either sensor can discern alone and is possible due to the interaction of both sensors.

This example, while trivial, provides some insight

into the power of interconnected sensor atoms. Sensors of minimal complexity joined together by appropriate interconnection rules allow sensors to be developed that are robust, optimal for their intended tasks, and make efficient use of power and bandwidth resources. This research explores some aspects of this capability using theoretically simple and physically realizable sensor atoms. The remainder of the paper is organized as follows. The next section describes a particular type of sensor atom termed the Bernoulli sensor atom.

## II. A BERNOULLI SENSOR ATOM

### A. General Theory

Consider a simple sensor whose functional block diagram is as shown in Figure . Input to the sensor produces a sensed signal  $S(t)$  which is corrupted by additive noise  $N(t)$  to produce the signal  $V(t)$  which is sampled every  $T$  seconds to produce the random sequence  $V_n$  where  $n$  is the index of the  $n$ th sample. Each value of  $V_n$  is compared with a threshold value  $\gamma$  to produce the following binary sequence.

$$B_n = \begin{cases} 1 & V_n > \gamma \\ 0 & V_n \leq \gamma \end{cases} \quad (1)$$

The sequence  $B_n$  is a Bernoulli sequence characterized to first order by the probability  $p$  where

$$p = P[B_n = 1] = P[V_n > \gamma] = P[V(nT) > \gamma] \quad (2)$$

If  $V(t)$  is a stationary random signal, then

$$p = \int_{\gamma}^{+\infty} f_V(v) dv \quad (3)$$

where  $f_V(v)$  is the first order probability density function (PDF) of the random variable  $V(t)$ . Note that because of its binary nature,  $E[B_n] = p$ .

The second order statistics of  $B_n$  are described by If  $\mu_V = 0$  and  $\gamma = 0$  then  $Z_n$  is the output of a classic hard limiter and  $R_Z(k) = \frac{2}{\pi} \arcsin \rho_k$  yielding

$$R_B(k) = E[B_n B_{n+k}] = P[B_n = 1, B_{n+k} = 1]. \text{ If } V_1 = V(nT) \text{ and } V_2 = V(nT + kT) \text{ then} \quad R_B(k) = \frac{1}{2\pi} \arcsin \rho_k + \frac{1}{4} \quad (9)$$

$$R_B(k) = \int_{-\gamma}^{+\infty} \int_{-\gamma}^{+\infty} f_{V_1 V_2}(v_1, v_2) dv_1 dv_2 \quad (4)$$

where  $f_{V_1 V_2}(v_1, v_2)$  represents the joint PDF of the signal  $V(t)$  at times  $nT$  and  $nT + kT$ . Further development requires knowledge of the first and second order densities of  $V(t)$ .

### B. The Gaussian Assumption

If  $V(t)$  is assumed to be a non-periodic Gaussian process with autocorrelation  $R_V(\tau)$  then

$$f_V(v) = G(v; \mu_V, \sigma_V) = [2\pi\sigma_V^2]^{-\frac{1}{2}} \exp \left\{ -\frac{1}{2} \left( \frac{v - \mu_V}{\sigma_V} \right)^2 \right\} \quad (5)$$

and

$$f_{V_1 V_2}(v_1, v_2) = \left[ 2\pi\sigma_V^2 \sqrt{1 - \rho_k^2} \right]^{-1} \exp \left\{ -\frac{1}{2\sigma_V^2(1 - \rho_k^2)} \left[ (v_1 - \mu_V)^2 - 2\rho_k(v_1 - \mu_V)(v_2 - \mu_V) + (v_2 - \mu_V)^2 \right] \right\} \quad (6)$$

where  $\mu_V^2 = \lim_{\tau \rightarrow \infty} R_V(\tau)$ ,  $\sigma_V^2 + \mu_V^2 = R_V(0)$ , and  $\rho_k = \frac{R_V(kT) - \mu_V^2}{R_V(0) - \mu_V^2}$ . It is convenient to re-write equation 6 using the definition of conditional probability as

$$f_{V_1 V_2}(v_1, v_2) = f_{V_2}(v_2) f_{V_1/V_2}(v_1) = f_V(v_2) f_{V_1/V_2}(v_1) \quad (7)$$

where  $f_{V_1/V_2}(v_1) = G(v_1; \mu_C(v_1), \sigma_C)$  with  $\mu_C(v_1) = \mu_V + \rho_k(v_1 - \mu_V)$  and  $\sigma_C = \sigma_V \sqrt{1 - \rho_k^2}$ . Using this definition then equations 3 and 4 can be written in terms of the cumulative normal function or  $p = 1 - \Phi\left(\frac{\gamma - \mu_V}{\sigma_V}\right)$  and

$$R_B(k) = p - \int_{-\gamma}^{+\infty} f_V(v) \Phi\left(\frac{\gamma - \mu_C(v)}{\sigma_C}\right) dv \quad (8)$$

with  $\Phi(x) = \frac{1}{\sqrt{2\pi}} \int_{-\infty}^x e^{-\epsilon^2/2} d\epsilon$ . A useful particular result can be obtained by defining the auxillary random variable  $Z_n = 2B_n - 1$ . Then  $R_B(k) = \frac{1}{4} R_Z(k) + p - \frac{1}{4}$ .



